Julius-Maximilians-Universität Würzburg
Graduate School of Science and Technology

**Doctoral thesis**
for the doctoral degree
**Doctor rerum naturalium (Dr. rer. nat.)**

# Poly(2-oxazine) Based Biomaterial Inks for the Additive Manufacturing of Microperiodic Hydrogel Scaffolds

*Poly(2-oxazine) Basierte Biomaterialtinten für die Additive Fertigung von Mikroperiodischen Hydrogelstrukturen*

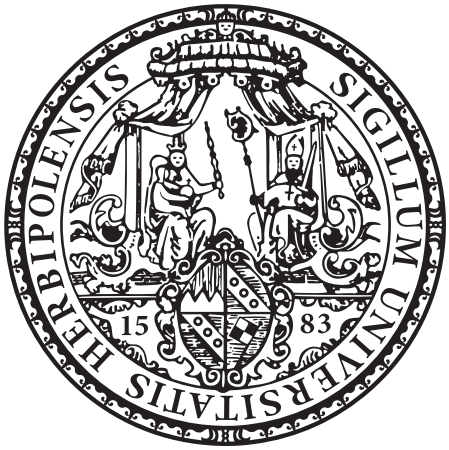


Submitted by
**M.Sc. Daniel Nahm**
from
Tübingen

Würzburg, 2021

Submitted on / *Eingereicht am:* .....

Stamp / *Stempel* Graduate School

**Members of thesis committee / *Mitglieder des Promotionskomitees***

Chairperson / Vorsitz: .....

1. Reviewer and Examiner / 1. Gutachter und Prüfer: .....

2. Reviewer and Examiner / 2. Gutachter und Prüfer: .....

3. Examiner / 3. Prüfer: .....

Additional Examiners / Weitere Prüfer: .....

.....

Day of thesis defense / *Tag des Promotionskolloquiums:* .....

This work was conducted from March 2017 until December 2020 at the Chair for Advanced Materials Synthesis at the University of Würzburg under supervision of Prof. Dr. Robert Luxenhofer.

# Danksagung

Im Folgenden möchte ich mich bei all denen bedanken, die zum Gelingen dieser Arbeit beigetragen haben.

Zunächst möchte ich meinem Doktorvater Prof. Dr. Robert Luxenhofer und meinem zweiten Betreuer Prof. Dr. Paul D. Dalton für die Möglichkeit danken, meine Promotion am Lehrstuhl für Chemische Technologie der Materialsynthese in der Gruppe Polymere Funktionswerkstoffe und am Lehrstuhl für Funktionswerkstoffe der Medizin und der Zahnheilkunde in der Gruppe Biofabrikation durchzuführen. Danke dafür, dass ihr immer ein offenes Ohr hattet und nie müde wurdet, über fachliche und nicht-fachliche Themen zu diskutieren. An dieser Stelle sei auch erwähnt, dass ich weiterhin der Meinung bin, dass ein großer Unterschied zwischen Spätzle und Knöpfle besteht. Insbesondere möchte ich mich auch für die großen Freiheiten bei der Themen- und Projektwahl bedanken, die ihr mir ermöglicht habt. In diesem Zuge möchte ich mich auch bei Prof. Dr. Katrin Heinze für die Betreuung meiner Promotion an der GSST und viele bereichernde Diskussionen bedanken.

Allen Kollegen und Mitarbeitern des LCTM Lehrstuhls danke ich für die angenehme und motivierende Arbeitsatmosphäre. In diesem Zusammenhang möchte ich mich bei Niklas Gangloff, Thomas Lorson, Sebastian Halupczok, Jochen Löblein, Michael Lübtow, Mengshi Yang, Chen Hu, Lukas Hahn, Stefan Forster, Claudia Stauch, Julian Heck, Robin Bissert, Mira Rupp und im Besonderen bei meinen Bürokolleginnen Solomiia Borova und Christine Schlutt für eine wirklich großartige Zeit bedanken. Nicht vergessen möchte ich Christian May, der mit seiner tatkräftigen Unterstützung bei den alltäglichen Laborproblemchen und seiner freundlichen und hilfsbereiten Art ein unersetzlicher Teil des Lehrstuhles ist. Meinen Studenten und Hiwi‘s, Lukas Nickel, Sven Heilig, Andreas Helbig, Paul Otto, Andreas Züge, und Larissa Kessler danke ich für die fruchtvolle Zusammenarbeit.

Auch bei allen Mitgliedern der Biofabrikations Gruppe möchte ich mich für die schöne Zeit bedanken. Hier auch speziellen Dank an Andrei Hrynevich und Christoph Böhm für die Unterstützung an den MEW Druckern sowie die Hilfe beim Schreiben der G-Codes. Vielen Dank auch an Kelly O’Neill. Die Zusammenarbeit mit dir hat wirklich sehr viel Spaß gemacht.

Franziska Weigl, Dr. Ana Sancho und Prof. Dr. Jürgen Groll danke ich für die Zusammenarbeit im Rahmen der Fluid-FM Messungen. Dr. Natascha Schaefer und Prof. Dr. Carmen Villmann danke ich für die Zellexperimente mit den Hydrogel Scaffolds. Andreas Frank und Prof. Dr. Hans-Werner Schmidt danke ich für die Durchführung der ESEM-Aufnahmen. Philipp Stahlhut möchte ich für die REM und Cryo-REM Aufnahmen danken. Vielen Dank auch an Michael Bartolf-Kopp, Mehmet Taskin und Dr. Tomasz Jüngst für die Unterstützung in der Fertigung von Tubular-Scaffolds und beim Solution Elektrospinning. Für die MALDI-TOF Messungen möchte ich Niklas Gangloff und Christine Schlutt danken.

Meiner Familie möchte ich für den nie endenden Rückhalt während meiner ganzen Studienzeit und auch während der Promotion danken. Danke, dass ihr es möglich gemacht habt, dass ich diesen Weg gehen konnte.

Zu aller letzt gilt mein größter Dank meiner Freundin Laura für die seelische und moralische Unterstützung abseits des Arbeitsalltages. Danke, dass du mich durch alle Höhen und Tiefen dieser Zeit begleitet hast und bis zum Schluss an mich geglaubt hast. Ohne dich wäre diese Zeit um einiges schwieriger gewesen. Tausend Dank auch für deine unermüdliche und akribische Unterstützung bei den Korrekturarbeiten. – Danke für alles!

# List of publications

"Poly(2-oxazoline)s based biomaterials: A comprehensive and critical update"
Thomas Lorson and Michael M. Luebtow and Erik Wegener and Malik S. Haider and Solomiia Borova and Daniel Nahm and Rainer Jordan and Marina Sokolski-Papkov and Alexander V. Kabanov and Robert Luxenhofer
*Biomaterials*, **2018**, *178*, 204-280.

"A versatile biomaterial ink platform for the melt electrowriting of chemically-crosslinked hydrogels"
Daniel Nahm, Franziska Weigl, Natascha Schaefer, Ana Sancho, Andreas Frank, Juergen Groll, Carmen Villmann, Hans-Werner Schmidt, Paul D. Dalton, Robert Luxenhofer
*Materials Horizons*, **2020**, *7*, 928-933.

# Table of Contents

# Abbreviations

| | |
|---|---|
| AM | additive manufacturing |
| AN | acetonitrile |
| BN | benzonitrile |
| CAN | covalent adaptable network |
| CDI | 1,1'-carbonyldiimidazole |
| CLIP | continuous liquid interface production |
| COSY | correlation spectroscopy |
| Cryo-SEM | cryogenic scanning electron microscopy |
| CS | collector speed |
| $CS_x$ | collector speed in x direction |
| $CS_y$ | collector speed in y direction |
| CTS | critical translation speed |
| DA | Diels-Alder |
| DCC | N,N'-dicyclohexylcarbodiimide |
| DF | degree of functionalization |
| DIC | N,N'-diisopropylcarbodiimide |
| DMF | dimethylformamide |
| DP | degree of polymerization |
| DSC | differential scanning calorimetry |
| ESEM | environmental scanning electron microscopy |
| EtOx | 2-ethyl-2-oxazoline |
| EtOzi | 2-ethyl-2-oxazine |
| EWC | equilibrium water content |
| FD | fibre distance |
| FDM | fused deposition modeling |
| GPC | gel permeation chromatography |
| $HD_e$ | experimental hydrolysis degree |
| $HD_t$ | theoretical hydrolysis degree |
| HMBC | heteronuclear multiple-bond correlation spectroscopy |
| HSQC | heteronuclear single-quantum correlation spectroscopy |
| $IC_{50}$ | half maximal inhibitory concentration |
| IR | infrared |
| LCROP | living cationic ring opening polymerization |
| LCST | lower critical solution temperature |
| M/I | monomer to initiator ratio |

| | |
|---|---|
| MALDI-TOF | matrix-assisted laser desorption/ionization time-of-flight mass spectrometry |
| ML | mass loss |
| MeOTf | methyl trifluoromethanesulfonate |
| MeOx | 2-methyl-2-oxazoline |
| MeOzi | 2-methyl-2-oxazine |
| MEW | melt electrowriting |
| NMR | nuclear magnetic resonance |
| NT | needle temperature |
| Ox | 2-alkyl-2-oxazoline |
| Ozi | 2-alkyl-2-oxazine |
| PBS | phosphate-buffered saline |
| PC | polymer composition |
| PCL | poly($\epsilon$-caprolactone) |
| PEG | poly(ethylene glycol) |
| PEI | poly(ethylene imine) |
| PEtOx | poly(2-ethyl-2-oxazoline) |
| PEtOzi | poly(2-ethyl-2-oxazine) |
| PHEMA | poly(2-hydroxyethyl methacrylate) |
| PMeOx | poly(2-methyl-2-oxazoline) |
| PMeOzi | poly(2-methyl-2-oxazine) |
| POx | poly(2-oxazoline) |
| POzi | poly(2-oxazine) |
| PPrOx | poly(2-n-propyl-oxazoline) |
| PPrOzi | poly(2-n-propyl-oxazine) |
| rDA | retro Diels-Alder |
| RGD | arginylglycylaspartic acid |
| RT | room temperature |
| SEM | scanning electron microscopy |
| SES | solution electrospinning |
| SID | scaffold identification number |
| SR | swelling ratio |
| ST | syringe temperature |
| TE | tissue engineering |
| TGA | thermogravimetric analysis |
| UCST | upper critical solution temperature |
| UV | ultraviolet |

# Symbols

| | |
|---|---|
| $a$ | intercept |
| $\alpha$ | printing angle |
| $A_0$ | initial monomer concentration |
| $A^\star$ | concentration of the active chain ends |
| $A_t$ | current monomer concentration |
| $b$ | slope |
| Đ | polydispersity |
| $d$ | collector distance |
| $I_0$ | initiator concentration |
| $k_p^{app}$ | apparent propagation rate |
| $k_h^{app}$ | apparent hydrolysis rate |
| $G''$ | loss modulus |
| $\bar{M}_n$ | number average molar mass |
| $\bar{M}_w$ | mass average molar mass |
| $p$ | pressure |
| $G'$ | storage modulus |
| $T_{CP}$ | cloud point temperature |
| $T_g$ | glass-transition temperature |
| $T_m$ | melting temperature |
| $V$ | voltage |

# 1 Introduction

Giants only exist in fairy tales. This statement was also valid in the scientific field of chemistry for a long time. Molecules consisting of thousands or even millions of atoms were considered to be fantasy by most scientists. Then, just about 100 years ago, the German chemist Hermann Staudinger described for the first time a completely new class of materials: Macromolecules.[1] Thirty-three years later in 1953, this discovery was awarded with the Nobel prize in chemistry. Today, polymers are commonly referred to as "plastics" and modern society has been transformed by them. They are essential components of almost every modern technology, and the automotive, multimedia and food industry now rely on them. Today, we are able to process polymers into complex three-dimensional structures using additive manufacturing (AM) also known as 3D printing. These manufacturing techniques can be described as the computer controlled deposition of materials in a layer-by-layer fashion, with the result of a 3D object based on a digital model.[2] The high degree of flexibility, the enormous degree of freedom in the geometrical designs, and the ability to rapidly prepare constructs that are simply not accessible by traditional subtractive fabrication techniques, are the main advantages of AM. Currently it is believed that AM is an essential technology for a new industrial revolution, often referred to as Industry 4.0.[3]

The scientific fields of scaffold-based tissue engineering (TE) as well as biofabrication rely strongly on the principles of AM. These two related disciplines aim to regenerate and restore the function of damaged biological tissue.[4] A notable example are patient specific implants for the treatment of calvarial defects. These constructs are commercially available under the trademark Osteoplug™. They are approved by the medical authorities and are already in clinical use.[5] Still, despite some successful examples, the use of tissue transplantation is still the gold standard to repair or replace damaged tissue. However, such therapies are not without risk. Drawbacks like infections, disease transmission or the potential for complement reaction, which might lead to the rejection of the implant, must be considered. And above all, suitable donor tissue needs to be available as well. With regard to demographical changes and an ageing population, the need for artificial alternatives to replace or repair biological tissue will continue to rise.[6,7]

However, constructs which fully mimic the complex geometry, the hierarchy and especially the function of human tissue or organs are still dreams of the future.[8] To get closer to achieving this goal, the manufacturing techniques and especially the biomaterials still require further development. In general, TE scaffolds should provide a suitable environment for cells to grow, migrate and establish their biological function. It is essential that the support structures provide the required mechanical, biological as well as structural cues to stimulate cells to regenerate a specific tissue. However, structuring biomaterials in a predefined manner and with high precession is a challenging task.[9,10]

Poly(2-oxazoline)s (POxs) and their higher homologue poly(2-oxazine)s (POzis) are a promising polymer platform for the synthesis of biomaterials in general. These polymers are available via living cationic ring opening polymerization (LCROP) with high control over their molar mass and its distribution. By carefully choosing the amide side chains, it is possible to tune their physico-chemical properties over a wide range.[11] Also functional groups for crosslinking and the incorporation of biological stimuli are readily realized. So far, POxs have been reported to show excellent cytocompatibility and they are under research for a large variety of biomaterial applications. Within the scope of this thesis, investigations for a new biomaterial platform based on POx and POzi for the AM of hydrogel structures with defined low micron sized features will be presented.

# 2 State of Knowledge

In the following, the basic principles, important for the understanding of this thesis, are discussed. Based on this state of knowledge, the importance of further research will be made clear and the novelty of the thesis will be elaborated. In this context, the literature published until 01.09.2018 will be considered. All advances published past this date will be addressed within the main body of this thesis at the respective text passages of interest. The material developed in this work is intended for, but not limited to the use in biomedical applications. However, as biological applications are envisioned, special focus will be set on the concepts relating to the field of biology. In addition, this dissertation has a strong interdisciplinary character and not all relevant subjects can be discussed in full detail, as this would go beyond the scope of this introduction.

## 2.1 Biofabrication and Scaffold-Based Tissue Engineering

Biofabrication is a young research discipline and the first attempt to define this field has been made only about ten years ago.[12] This was also shortly after the founding of the first scientific journal dedicated to the subject of biofabrication.[13] Since then, this rapidly growing field of science generated more and more attention and the terminology within the published literature was increasingly inconsistent. This issue was recently addressed by The International Society for Biofabrication and a revised definition was presented. According to this, Biofabrication for Tissue Engineering and Regenerative Medicine is "the automated generation of biologically functional products with structural organization from living cells, bioactive molecules, biomaterials, cell aggregates such as micro-tissues, or hybrid cell-material constructs, through bioprinting or bioassembly and subsequent tissue maturation processes."[14] From this definition, some important implications can be drawn. First of all, "the automated generation" implies the use of computer-aided fabrication techniques, most notably AM techniques. These techniques are either bioprinting or bioassembly. Both of these are presented very detailed in articles by Guillemont *et al.*[15] and Schon *et al.*[16] respectively and will not be further discussed herein. The term "biologically functional

products" implies that the printed constructs need to serve some kind of biological function. This is rather ill-defined and highlights the scope of biofabrication in general.

Scaffold-based Tissue Engineering is a sub discipline of the broad field of TE, which according to Wang *et al.* aims to "restore, maintain, or improve tissue functions that are defective or have been lost by different pathological conditions, either by developing biological substitutes or by reconstructing tissues".[17] TE combines disciplines like cell biology, chemistry as well as material science with the aim to establish new medical therapies. In the classical TE working procedure, the cells of interest are harvested, cultured and expanded *in vitro*. Afterwards, the expanded cells are seeded onto a structural support, the scaffold. The cell-containing scaffold can be further cultivated *in vitro* or bio-functional signals added. Finally, the matured construct can be implanted to the patient as treatment for a medical condition.[18] Ideally the implant is degraded with time and becomes replaced with healthy tissue of the patient. Interestingly, the two disciplines of biofabrication and TE intersect when an additively manufactured scaffold influences cell maturing into tissue equivalent structures.[19] Therefore scaffolds seeded with cells post fabrication can be referred to as biofabricated if they meet the aforementioned condition.

Besides other techniques like gas foaming,[20] cryo structuring,[21] or porogen leaching[22] AM is of major importance for the fabrication of TE scaffolds.[10] This is due to the fact that AM techniques allow the reproducible fabrication of precise and predefined structures. For the fabrication of such scaffolds several factors need to be considered. Among many, this is the biological performance of the material which includes the ability to control cell adhesion and viability as well as the immunogenic properties.[23] For this, it is important to be able to control and tailor the surface chemistry of the scaffold. As mentioned above, it is the objective of TE, to allow the body's own cells to replace the implant with time. Therefore, biodegradability is an important requirement for a TE biomaterial as well. Biodegradability can be realized through chemical groups which are susceptible towards hydrolysis, like ester functions, or through peptides sequences which can be cleaved enzymatically.[24–26] Obviously it has to be assured that the degradation products are also cytocompatible as well as non-carcinogenic. Ideally, the implanted material should also mimic the mechanical properties of the tissue at the implant site. This is due to the fact that cells will respond to the mechanical stimuli they receive from their environment.[27–29] In contrast, from the perspective of a surgeon, the scaffold needs to be stable enough to allow handling during surgery. Finally, the scaffold architecture plays an important role as well. First of all, the scaffold dimension themselves need to be tailored to the respective defect size. This is easily achieved for most of the AM techniques. Additionally, the scaffolds need to have a certain

degree of porosity as well as the interconnection of these pores needs to be ensured. This will allow cell infiltration and the diffusion of waste products and nutrients. Due to the lack of vascularisation, the latter is of special importance. In general, ensuring vascularisation is still a major challenge for TE.[30] As a general rule of thumb, due to diffusion limitation in biological tissues, blood vessels need to be present every 100 to 200 $\mu$m to allow sufficient mass transport.[31] In addition to the porosity, sufficient cell-material-contact needs to be ensured to allow optimal cell adherence. Therefore, the pores need to be large enough to allow cell in-growth but still sufficiently small to establish a high specific surface area within the structure. Also the combination of both parameters needs to be optimized for the respective cell type as well as the engineered tissue.[23] This requires the ability to precisely control the scaffold architecture in a low micrometre level, yet many AM methods lack the structural resolution limit to allow controlling the microstructure in such detail. For instance simple extrusion-based techniques like fused deposition modeling (FDM) typically allow fibre diameters on the range of 400 $\mu$m. This limits the ability to produce structures that combine high porosity with high surface area and fibre density. Exceptions to this include techniques like two-photon-polymerization and melt electrowriting (MEW). The latter is a relatively young but promising tool for TE as well as biofabrication and will be discussed in the following.

## 2.2 Melt Electrowriting

One major factor responsible for the diameter limitation of extrusion-based AM techniques like FDM is the Barus effect, also referred to as die swell.[32] In equilibrium state, the macromolecules in the melt usually take a random coil conformation. This maximizes the entropy of the system. While the polymer melt is pressed through a small diameter nozzle, it is exposed to shear forces and extensional flow. This causes the deformation of the polymer random coil conformation.[33] The result is an alignment of the macromolecules and alongside with a decrease in the entropy of the melt. Due to the viscoelastic nature of polymers, part of the mechanical force is stored elastically. Upon exiting the nozzle, the melt is no longer constrained, the stored energy is released, and the random coil conformation is partially recovered. This conformation has a higher volume requirement, which results in a "swelling" of the extruded polymer stream. While decreasing the nozzle size would allow fibres with a smaller diameter, this will also require increasingly high pressures. Extreme pressure gradients can lead to processing instabilities like melt fracture or even cause damage to the polymers on a molecular level.[34] Generally for extrusion-based techniques, the layer thickness is limited to 100-200 $\mu$m.[35] While smaller fibres are in principle possible, this comes at the cost of a limited throughput.[36] These boundaries can be overcome by

applying an external high voltage field between the nozzle and the collector. The resulting electrostatic phenomenon will force the liquid, exiting the nozzle, into a cone-like structure which is termed the Taylor Cone.[37] High voltage leads to the polarization of the molecules within the extruded liquid and electrical charges are accumulated on the surface of the material, causing Coulomb repulsion. The system tries to increase its surface area leading to the formation of the cone-like structure. As soon as the electrical repulsion between the charges overcomes the surface tension of the extruded liquid, a small diameter jet emerges from the tip of the cone. At this point, the jet already has a much smaller diameter than the nozzle. However, until the fibre is deposited on the collector plate, mechanical as well as electrical forces cause further stretching, which results in a significant reduction of the fibre diameter. This phenomena is the basic principle for all electrohydrodynamic processes and allows the fabrication of fibres with diameters in the nano- and micrometre range.[38,39]

One of the most commonly known electrohydrodynamic processing techniques is solution electrospinning (SES).[40] Here, the processed materials (usually polymers) are dissolved in volatile solvents. During electrospinning, the jet first travels a straight path and then undergoes bending instabilities. These instabilities are termed whipping and are caused by increasing amounts of charges build up on the material surface while the fibre is approaching the collector. Furthermore, also parameters like solvent evaporation or the mechanical properties of the material jet as well as air friction play an important role in the whipping phenomena.[41] Due to these jet instabilities, SES allows the fabrication of randomly distributed non-woven meshes. While there are approaches to induce some degree of preferred fibre direction for instance by electrospinning on patterned collectors or on fast rotating mandrels, SES does not allow the accurate placing of fibres in predefined positions.[42,43] Interestingly, the electrospinning of polymer melts allows much higher control over the material jet compared to polymer solutions. Polymer melts solidify much more rapidly, and they exhibit higher viscosities as well as lower charge densities than polymer solutions.[44,45] This combination makes melt-based jets much more resistant against bending forces and whipping effects than polymer solutions. Thus, compared to SES, it is much easier to maintain a straight jet path for melt electrospinning over long distances. MEW takes advantage of this fact and a chaotic electrospinning process is transformed into a controlled direct writing AM technique.[46]

A MEW device consists typically out of a heated printer head with a pressure and a high voltage supply (Figure 2.1). Furthermore, a collector plate with computer-controlled x/y-axis is required. In addition to a flat collector plate it is also possible to print on a rotating mandrel, which gives access to tubular structures.[47] To prepare for printing, the polymer

is molten in the heated reservoir and extruded through a charged nozzle by the pressurized air or nitrogen. The option to use the inert gas nitrogen is especially beneficial for polymers with high processing temperatures to prevent or retard thermal degradation.[48,49] A Taylor cone is formed at the tip of the nozzle and a straight jet is drawn towards a grounded collector. In order to direct write, the collector plate is moved, and a continuous polymer filament is deposited. In this context, the collector speed (CS) plays a key role in the fibre deposition. Loop or sinusoidal structures are printed when the CS is lower than the speed of the jet.[50] From the point where the CS matches the speed of the jet, it is possible to print straight fibres. This specific CS is called critical translation speed (CTS) and is a characteristic parameter for the MEW process.[46] When the CS is higher than the velocity of the jet, the deposited fibre is stretched, which leads to a decrease in fibre diameter.[51] Generally, MEW can be seen as a bridging technique between traditional SES and FDM. It combines the precise fibre placement capability of FDM with the extensive fibre diameter reduction of a electrohydrodynamic processing technique. Another advantage of MEW compared to solution based processing is the lack of (potentially toxic) solvents. This is especially relevant for the fabrication of biologically relevant structures.

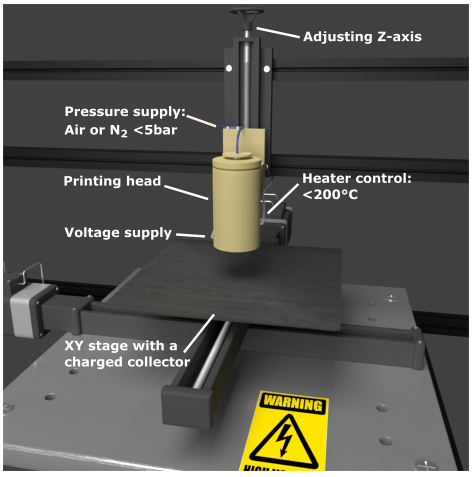


**Figure 2.1:** Schematic illustration of a melt electrowriting device.

The MEW process is influenced by several device related parameters. For instance, the processing temperature has a strong influence on the printing process as it is directly related to the viscosity of the extruded polymer. This influence is especially drastic close to the melting and glass transition temperature of the printed material, as the viscosity changes are most significant in this temperature range.[52] Higher temperatures and therefore lower melt viscosities will lead to smaller fibre diameters. Also the jet velocity is increased, which leads to an increased CTS.[46] Furthermore, at very high temperatures the risk for thermal degradation of the processed material increases. Interestingly, it was found that thermally induced changes during MEW processing can become noticeable even far below

the combustion temperature of the processed polymers.[48] The nozzle diameter has a direct influence on the material flow rate and therefore on the MEW process. Commonly used nozzle sizes range from 50 to 500 $\mu$m (21 G), which allows the printing of fibre diameters between 5 and 50 $\mu$m respectively.[51,53,54] In addition, the feeding pressure is also directly related to the melt flow rate and has major influence on the fibre diameter as well as the processing stability. For a stable printing process, the material flow through the nozzle needs to be matched with the material flow of the polymer jet. Otherwise processing instabilities like fibre pulsing and long-beading may occur, which hinders a precise fibre deposition.[48,55,56] During stable MEW processing, low material flow rates on the range of 5 to 50 $\mu$l/h are typically used.[46] Another important parameter is the electrical field strength, which is defined by the applied voltage and the distance between the nozzle and the collector. During MEW, usually collector distances on the range of a few millimetre are applied, and a higher field strength generally causes a smaller diameter and faster jet.[51,53]

The maximum electrical field strength is physically limited by the spark gap, which is in air approximately 3 kV/mm. For higher values the gas molecules become ionized, resulting in arcing and the breakdown of the electrical field.[57] Furthermore, a stronger electrical field leads to a charge build up in the deposited fibres. Due to the low conductivity of the printed polymer, these charges remain in the construct. This results in repulsive forces and subsequently counteracts accurate fibre placement.[55] On the other hand, a low conductivity of the processed material is required to prevent a short circuit as soon as the charged jet comes into contact with the grounded collector. Therefore, typical conductivity values suitable for melt electrospinning range between $10^{-6}$ and $10^{-8}$ S/m.[58] In general, the fabrication of thin but wide sheet-like structures with a precise microstructure is easily achieved via MEW.[59] However, the continuous character of MEW makes it challenging to control the macro structure of the printed architecture. Opposing to FDM, the deposition of the filament cannot be readily or accurately stopped and restarted. As recently addressed by Paxton and coworkers, commercially available tools, which convert 3D-structures into G-codes commands cannot be used for MEW.[60] Due to the small fibres and the mentioned charge related errors in fibre stacking, structures with large volumes are usually challenging to achieve with MEW. Only very recently, Wunner *et al.* managed to print well-structured scaffolds with more than 300 layers and a total height of over 7 cm.[55] In addition to the electrical properties, the viscoelastic properties of the polymers also play a major role in melt electrospinning. For example, the molar mass as well as its distribution have a strong influence on the melt processing temperature. The polymer chains need to enable sufficient entanglement to resist a jet-breakup, while still allow sufficient mobility of the molecules for a stretching of the jet. This balance was investigated by Lyons *et. al.* for

polypropylene.[61] They found that for very high molar masses ($\bar{M}_n$: 165 kg/mol and $\bar{M}_w$: 580 kg/mol) no Taylor cone formation was possible, and the material was simply extruded through the nozzle. Lowering the molar mass allowed continuous electrospinning and the fibre diameter decreased exponentially with regards to the $\bar{M}_w$. For very low molar masses ($\bar{M}_n$: 5 kg/mol and $\bar{M}_w$: 12 kg/mol) processing instabilities were found. These instabilities were attributed to insufficient chain entanglement. Laboratory experience has also shown that external parameters, such as humidity and ambient temperature, can influence the processing performance during MEW as well. Until now, no detailed studies have been performed on this subject. For poly($\epsilon$-caprolactone) (PCL), currently the gold standard polymer for MEW, molar masses ($\bar{M}_w$) between 45 and 80 kg/mol are commonly processed at temperatures between 70 and 120 °C.[39]

The discussion above highlights that MEW processing is influenced by several internal and external parameters. If these are well-balanced, MEW allows the deposition of continuous polymer filaments with remarkable precision. The fibre diameter can typically be controlled in a range of 2 to 50 $\mu$m with very small deviations.[39] Sub-micron sized fibres have also been achieved, however with less control over the diameter distribution.[62] Due to the small fibre diameter and the highly accurate fibre placing, MEW scaffolds generally have high porosity of more than 87 %.[63,64] The structural resolution of MEW is well in size dimension of cells, which enables the production of cell-instructive architectures.[63] Considering this, MEW is a very promising tool for the fields of biofabrication and scaffold-based TE. Theoretically, every thermoplastic polymer can be processed with MEW, yet most of the available research is currently limited to PCL.[65] While PCL allows the production of scaffolds which enable cell attachment and proliferation, it lacks the option for direct incorporation of bioactive cues.[16,66] Furthermore, the hydrophobic nature of PCL favours unspecific protein adsorption.[67] PCL is a semi-crystalline and stiff polymer, making it a good choice for mimicking hard though tissue like cartilage or bone.[27,66,68,69] While the processing of hydrophilic poly(2-ethyl-2-oxazoline) (PEtOx) has been described before, MEW currently lacks the ability for the fabrication of soft and hydrophilic architectures. However, this would allow to transfer the advantages of melt electrowritten structures to the TE of soft tissue and enable the fabrication of microperiodic hydrogel structures. Such scaffolds could be used for the mimicking of tissues like nerve or liver. In general, hydrogels have several advantages for the application as a biomaterial, which will be discussed in detail in the following section. In addition, other available techniques for the fabrication of microperiodic hydrogel structures will be addressed below as well.

## 2.3 Hydrogels

Due to characteristics like their inherent softness, the hydrophilic character, the potential biocompatibility and the similarity to the native extracellular matrix, hydrogels have been of utmost importance to biomaterial science for many years.[70–72] This dates back to the reports of Otto Wichterle and Drahoslav Lim in 1960 on chemically crosslinked poly(2-hydroxyethyl methacrylate) (PHEMA) for the fabrication of hydrophilic contact lenses.[73] Since then, significant advantages in the synthesis and fabrication of hydrogels have been made and the material class finds applications in regenerative medicine, drug delivery, biosensors, ophthalmology or biofabrication.[14,72,74–76] Important non biological fields of application among others are soft robotics, 4D-printing and mechanical metamaterials.[77–79]

Per definition, a hydrogel is a "polymeric material that exhibits the ability to swell and retain a significant fraction of water within its structure, but will not dissolve in water"[80]. In addition to this, from a rheological point of view hydrogels are viscoelastic materials and therefore exhibit liquid-like as well as solid-like properties. This means, a gel must exhibit no flow in the idle state, yet gels crosslinked via temporary bonds for instance can allow liquefaction (shear thinning) upon mechanical stress. Some characteristics, like the minimal amount of water uptake required to be classified as a hydrogel, are not strictly defined. The ability to adsorb water arises from the hydrophilic nature of the polymeric material. At the same time, the crosslinks between the polymer chains prevent the dissolution of the gel. By nature, hydrogels are porous materials, and the polymer serves as a three-dimensional matrix, which defines the water-filled pores. Generally, the water inside the pores can move freely and this allows the diffusion of small solutes through the network. The degree of crosslinking, the correlation length ($\xi$) as well as the character of the water binding determines the overall mobility of such solutes. An important characteristic of hydrogels is their equilibrium water content (EWC), as this value gives information about the amount of water bound in the polymer network. The EWC can be calculated via Equation 2.1 and by determining the weight of a gel sample in the hydrated (MW) and in the dry state (MD).

$$EWC = \frac{MW - MD}{MW} \times 100 \tag{2.1}$$

Hydrogels can be classified on various characteristics, among others these are the source or the type of crosslinking. Based on the source, hydrogels are divided into two groups, natural or synthetic origin. Naturally derived gels are appealing because of their intrinsic biocompatibility, the cell signalling and instructing properties and most notably the biode-

gradability.[81] Sometimes criticized are batch-to-batch variations, the inability to control degradation and structure as well as the potential immunogenicity. Examples for important naturally derived gels are polysaccharides like chitosan, hyaluronic acid and alginate or proteins like gelatin and chondroitin sulfate.[82] Synthetically derived polymers on the other hand allow control of the chemical microstructure and the mechanical properties. Important polymers of this category are poly(ethylene glycol) (PEG), PHEMA and poly(vinyl alcohol). The incorporation of biological moieties as well as the biodegradability however can be a challenge for synthetic hydrogels.[72,83,84] In the recent years, the borders between synthetic and naturally derived hydrogels are fading and hybrid biomaterials are being explored.[85]

The type of crosslinking is also important, and hydrogels are usually divided into chemical and physical crosslinking. In physically crosslinked gels the polymer chains are connected through weak and reversible bonds like hydrogen bonds, ionic interactions or thermoresponsive/hydrophobic interactions.[81] These types of crosslinks are often established under mild conditions in aqueous solutions and no toxic chemicals are involved. Typical examples for these bonds are gels based on agarose crosslinked via hydrogen bonding, alginate crosslinked via ionic interactions with $Ca^{2+}$ ions or PEG-based gels (e.g Pluronic™) crosslinked via hydrophobic interactions. In chemically crosslinked gels, the polymer chains are linked via covalent and therefore (usually) permanent bonds. Such covalent bonds are commonly established via ultraviolet (UV)-light induced reactions of acrylates. Common examples are PHEMA or methacrylated gelatin-based hydrogels.[72] Furthermore, thiol-ene and Michael chemistry has been applied as well.[86] Generally, chemically crosslinked hydrogels possess higher mechanical stability than their physically crosslinked counterparts making them of interest for load bearing biomedical devices. As a drawback, potential toxic chemicals from the crosslinking procedure can remain within chemically crosslinked gels.

Another important subclass of hydrogel materials are stimuli responsive and most notably thermoresponsive hydrogels. These are gels for which either gelation is triggered by a temperature change (crosslinking based on hydrophobic interactions) or where the EWC is dependant on the temperature. Such materials are produced from polymers, which exhibit a lower critical solution temperature (LCST) or a upper critical solution temperature (UCST). This subclass is of special importance for the fields of bioprinting as well as 4D-printing.[78,87] In addition to the temperature, hydrogels can also be sensitive to pH, light or selected molecules.[85]

Hydrogels are interesting for several biomedical applications as they offer a unique combination of properties. Due to the high water content, these materials are generally soft but can cover a wide stiffness range.[88,89] Furthermore, the material stiffness is easily controlled through the water content. This is important for biomaterial applications, as cells do respond strongly on the mechanical stimuli of their environment.[29] The hydrophilic nature of hydrogels can prevent unspecific protein adsorption and therefore enables target specific cell interactions through incorporation of cell instructive motives.[70] The water filled pores can allow cell in-growth and the transport of nutrients.[83] Hydrogels can also be used to protect cells and fragile substances like proteins, DNA or drugs.[90] Furthermore, due to their high water content they are often biocompatible. However, this statement must be viewed critically, as generalized biocompatibility is often based on simple cytotoxicity experiments with a few selected cell lines. Depending on the analysis, terms like cytocompatible, hemocompatible or biotolerant are often better suited to describe the biological response of the respective material.

## 2.4 Structured Hydrogels

The precise three-dimensional structuring of soft matter is of immense importance for the scientific fields of scaffold-based TE as well as biofabrication.[69,87,91] In this context the precise structuring of hydrogels is, due to their low mechanical strength, especially challenging. However, to provide tissue equivalent structures for soft tissue applications, it is essential to have precise control over the scaffold architecture on a micrometre level.[92,93] When discussing the patterning of soft matter for biological applications, it is important to differentiate these efforts into two categories: techniques that use bioinks and techniques that use biomaterial inks.[87] Bioinks are a mixture of a biomaterial and living cells, and the precise placement of bioinks in 3D is referred to as bioprinting.[14] For bioprinting it is essential to operate under cytocompatible conditions, thus high shear forces, high temperatures or toxic solvents must be avoided throughout the process.[94,95] This limits the number of applicable AM techniques and excludes techniques like FDM, MEW or selective laser sintering. Biomaterial inks are usually used in the context of scaffold-based TE. Here, the biological components (e.g. cells or proteins) can be added post processing and conditions during processing are of less importance. Nevertheless, potentially toxic solvents or chemical triggers have to be removed completely post processing. Additionally, the constructs must be either produced under sterile conditions or allow sterilization before use. In the following section, the focus will be set on techniques for the AM of biomaterial inks. More specific information about bioprinting can be found in several recently published reviews.[87,96–98]

### Light-based Techniques

Light-based AM techniques rely on photocurable resins or fusible powders, which are cured in a layer-by-layer fashion using a laser or a light projection device.[69,99] Resin-based techniques are for example stereolithography or two-photon polymerization. These techniques cure one volume element (a voxel) at a time and allow excellent lateral resolution. In particular, two-photon polymerization is outstanding in this context as it can achieve resolutions as small as 100 nm. However, this comes at the cost of fabrication speed as well as total construct size, as such devices are also commonly limited to overall dimension in the range of 1 $cm^3$.[100] Techniques like digital light processing and continuous liquid interface production (CLIP) are capable of curing complete layers at once. This makes them comparably fast and also allows to cover large total volumes of more than 100 $cm^3$.[101] Usually, non of these techniques allow the simultaneous structuring of multiple materials. Only very recently, Khademhosseini and coworkers addressed this issue by combining microfluidics with an stereolithography device, which enabled multi-material resin-based

bioprinting.[102] They were able to pattern bioinks into complex constructs with potential applications as tissue models. While the overall illumination volume was quite limited (5x5x5 mm), they achieved very defined structures with a planar resolution of 10-25 $\mu$m. Due to its ability to rapidly manufacture complex large volume structures, CLIP is a very versatile AM technique. Recently it was used for the preparation of structured drug-loaded PEG and hydroxyethyl methacrylate-based hydrogel implants for potential drug delivery applications.[103] Here, no toxicity for the HeLa cell line or a human umbilical vein endothelial cell line was found. These two recent studies highlight the potential of light-based AM techniques for the structuring of hydrogels. However, the use of resin-based systems for biological applications is strongly limited by the lack of biocompatible photocurable resins, as usually both, the monomers as well as the photo initiators, are potentially cytotoxic.[104] It is important to point out that photocuring is applied by many researchers for the crosslinking of hydrogels with biological applications and can be performed in a cell-friendly manner.

### Extrusion-Based Techniques

Extrusion-based direct writing techniques are commonly used for the processing of both, bioinks as well as biomaterial inks.[87] For the former, it is essential to maintain cell viability throughout the process.[96] Therefore, shear thinning and physically crosslinked hydrogels are typically used, as this allows to mediate the shear forces during extrusion. For these techniques, the nozzle diameter is the limiting factor for the smallest size feature in the printed construct. However, as small diameter nozzles will lead to extensive shear forces, the extruded filaments size is usually limited to diameters on the range of 150-400 $\mu$m.[105–108] The shape fidelity of the constructs prepared from physically crosslinked hydrogels is also reliant on the gelation kinetics. In contrast to the extrusion of thermoplastics, which allow high shape fidelity due to the rapid solidification upon cooling, hydrogels tend to show material flow post processing. This leads to the fusion of fibre stacks, the spreading of the hydrogel and the loss of the desired architecture.[107,108] In general, physical bonds are comparably weak interactions, which can result in structures that do not allow handling. Also, in biological media, physically crosslinked structures are at risk to be dissolved over time. Both properties can be adjusted via chemical crosslinking of the constructs post printing. Established techniques for this are radical polymerization, Michael addition or enzymatic reactions.[109–112]

In contrast to bioinks, for the extrusion of simple biomaterial inks much higher shear forces can be tolerated. This allows the use of nozzles with smaller diameter and enables the

fabrication of structures with higher resolution, if material spread can be prevented. For biomaterial inks this can be achieved by crosslinking the material during extrusion. Using this approach, the Lewis group was able to prepare hydrogel scaffolds with very high shape fidelity. Due to the outstanding resolution, they termed these structures microperiodic hydrogel scaffolds.[113] The inks consisted out of solutions of PHEMA as macromonomer, N,N'-methylene bisacrylamide as crosslinker and diethoxy acetophenone as initiator. These solutions showed pronounced shear thinning over almost four orders of magnitude, when the shear rate was increased from $10^{-1}$ to $10^{3}\,1/\mathrm{s}$. This allowed the extrusion of these ink through nozzles with diameters between 1 and 10 $\mu$m using moderate pressures of 2 to 5 bar. The ink was crosslinked directly upon exiting the nozzle using UV light, which successfully preserved the fibre shape. Doing this, they prepared multi layered hydrogel scaffolds with a fibre diameter of 5 $\mu$m and defined fibre spacings of 20 $\mu$m at a printing speed of 30 mm/min. The scaffolds allowed to influence cell morphology of 3T3 murine fibroblast. The cells were found to either elongate along the fibre or to integrate themselves into the regions between interconnecting filaments. In a follow-up study, the microperiodic hydrogel scaffolds were investigated as substrates for 3D neuronal cell culture.[93] Box-like scaffolds with a fibre diameter of 10 $\mu$m and varying fibre spacing of 30 to 80 $\mu$m were printed and chemically modified with a polylysine coating. Primary rat hippocampal neurons were seeded and cultured for 7 d. They found that the neuron response was dependent upon the scaffold architecture. For the larger spacing (60 to 80 $\mu$m), the cells fell through the pores and grew primarily on the underlying substrate. For the 30 $\mu$m pores, the cells were located almost exclusively in the top most layers and only few penetrated into the vertical direction. On the scaffolds with 40 $\mu$m pores however, the neurons were fully integrated within the 3D-architecture of the scaffold and created a highly branched 3D-network. Generally, for all architectures, neurite outgrowth was found to be strongly directed along the filaments. Cells wrapped around the fibres, suspended within the pores, or elongated over multiple pores.

Another technique for the fabrication of microperiodic hydrogel scaffolds was also presented by the Lewis group.[114] Here, crosslinking was again induced directly upon extrusion. This time, polyelectrolyte-based inks were printed into a coagulation bath. Using this setup, they were able to prepare hydrogel structures with high precision and fibre diameters as low as 1 $\mu$m.

Structures with similar microperiodicity are accessible via the AM technique MEW (Section 2.2). However, currently this is only possible with stiff and hydrophobic polymers like PCL. New biomaterial inks are required to open the field of hydrogel micro-structuring for MEW.

Interesting in this context is a recent report by Haigh and coworkers, where they used MEW printed microperiodic structures as sacrificial template to prepare hydrogels with hierarchically structured micro pores.[115] This approach resulted in interconnected pores in the gel matrix with channel diameters of around 30 $\mu$m. Such structures are highly desirable for the TE of micro vascular systems.

## 2.5 Poly(2-oxazoline) and Poly(2-oxazine)-Based Biomaterials

POx is a versatile polymer class, which receives increasing attention in biomedical science in the recent years.[116–119] The synthesis of POx was first reported almost simultaneously by four independent research groups about 50 years ago.[120–123] POxs are often referred to as pseudo-peptides, as they are structural isomers of polypeptides.[124] However in contrast to polypeptides, the lack of chiral centres in the backbone as well as the absence of hydrogen bond donors prevents the formation of higher ordered secondary structures. The polymerization of the higher homologue of POx, POzi was reported simultaneously to POx, but has been almost forgotten since then.[120,125] Very recently, several reports suggest an enormous potential of the POzi polymer class for the preparation of biomaterials.[108,126,127] While PEG is currently the "gold-standard" in the field of biomaterials, POx is often presented as a promising alternative. In contrast to PEG, the enormous versatility of the POx and POzi side chains allows this polymer platform to cover a wide range of material properties. Characteristics like solubility, thermal properties and the potential for crosslinking are readily controlled.[119] Currently the application of POx as a biomaterial platform is limited by the lack of approval from authorities like the FDA or EMA. While PEtOx has been approved as a food additive by the FDA, no approved POx- or POzi-based medical product is available. In this context it is important to highlight that a POx containing Parkinson's treatment is currently going through clinical trials and could be the first product to overcome this limitation.[128]

### 2.5.1 The Monomers

The heterocyclic 2-alkyl-2-oxazoline (Ox) monomers are available via various synthesis routes, and only the four most commonly applied strategies are presented in the following. They can be synthesized directly from the non activated carboxylic acids in combination with 2-aminoethanol catalysed by titanium- or iron-based Lewis acids.[129] This reaction requires high temperatures of up to 200°C and is therefore rarely used for lab scale synthesis. This route is still attractive due to the fact that naturally derived fatty acids can be utilized allowing a more sustainable synthesis. Much milder is the Wenker method, which uses activated carboxylic acids such as acid chlorides.[130] In a two-step procedure, the acid chloride is reacted with 2-aminoethanol followed by the conversion with thionyl chloride to replace the hydroxyl groups with a more potent leaving group. The following ring closure proceeds under basic conditions. As a shortcut one can also use 2-chloroethyl amine instead, making the conversion with thionyl chloride redundant. An attractive method for

lab scale synthesis is the Witte-Seeliger method.[131] Here the carboxylic acid is replaced with a nitrile compound. In a one-step synthesis the nitrile is reacted with 2-aminoethanol at 130°C using a Lewis acid like zinc acetate as catalyst. The release of ammonia is the driving force for the ring closure. Starting from 2-methyl-2-oxazoline (MeOx) other Ox monomers are accessible via an $\alpha$ deprotonation reaction.[132,133] Using a strong base like lithium diisopropyl amide, MeOx is readily deprotonated at $\alpha$ position. Following nucleophilic substitution with alkyl bromides enables the formation of a wide variety of Ox monomers. Since MeOx has become commercially available in the recent years, this can be an attractive alternative for the synthesis of more complex Ox molecules. Furthermore, it is also possible to substitute the Ox monomers at 4- and 5-position of the ring, but this reduces the polymerization speed significantly due to steric hindrance.[133] It is also important to note that 2-alkyl-2-oxazine (Ozi) monomers are generally available via the same synthesis routes.[125,126,134] The chemical structures of both 2-substituted-2-oxazolines and 2-substituted-2-oxazines are visualized in Figure 2.2.

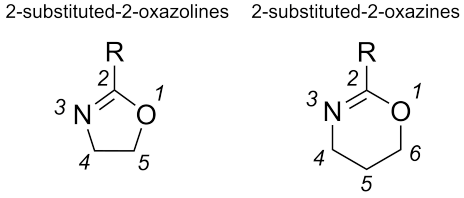


**Figure 2.2:** Chemical structure of 2-substituted-2-oxazolines and 2-substituted-2-oxazines.

## 2.5.2 Polymerization

POx and POzi can be polymerized in a cationic ring-opening polymerization. When performed carefully and under the appropriate conditions, this reaction can proceed in a living manner. This allows the synthesis of polymers with a defined molar mass distribution. For this, the reactants as well as the solvents must be of high purity. No traces of water or other nucleophiles can be tolerated as these will lead to deviations from the living conditions. The polymerization follows a chain growth mechanism and can therefore be divided in three steps: the initiation, the propagation, and the termination.

### Initiation

The initiation step proceeds by the nucleophilic attack of a Ox or Ozi monomer onto the electrophilic initiator (Figure 2.3). While this reaction is strongly exothermic, it is still rather slow at room temperature (RT). An exception to this is the use of very reactive initiators like methyl trifluoromethanesulfonate (MeOTf) or methyl tosylate. In this case the reaction

proceeds rapidly at RT as well.[120,135] Therefore, triflates and tosylates are the most commonly used initiators. Besides these, a large variety of other initiating agents have been explored as well, this includes Lewis acids, alkyl halides or silyl halides.[122,136,137] Please note that the initiating step can be used to introduce functional groups to the polymers as well.[138] An important requirement for the polymerization under living conditions is that the total number of reactive species must be constant throughout the reaction. Apart from the lack of termination or chain transfer reactions, it is therefore desired that the initiation rate ($k_i$) is much larger than the propagation rate ($k_p$). This will favour a simultaneous start of the chain growth and will result in more defined polymers. Using a 1:1 molar ratio of initiator and monomer allows the synthesis and isolation of oxazolinium salts.[139] Due to resonance stabilization, these are remarkably stable and can be used as initiator salt for further polymerization or for basic research on the reactivity of the oxazolinium species. During the initiation, an equilibrium between the cyclic cationic species as well as the linear covalent species is established (Figure 2.3). The position of this equilibrium is mainly determined by the nucleophilicity of the counter ion $X^-$, but also by the solvent and the respective monomer. It was found that the cationic species is more reactive than its covalent counterpart. It has also been concluded that the propagation reaction proceeds almost exclusively through the cyclic species.[119,140] As a result, the equilibrium has major influence on the polymerization kinetics and it is beneficial to keep the concentration of the covalent species low.

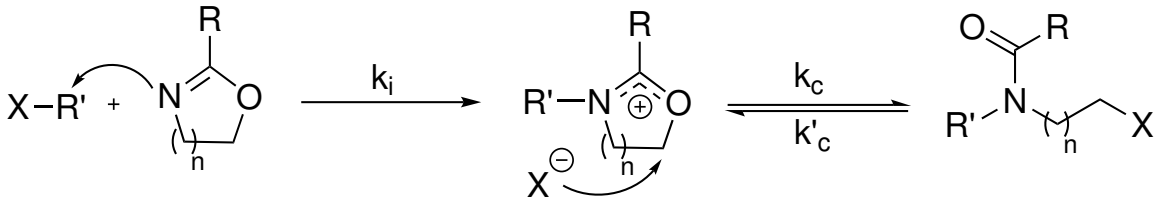


**Figure 2.3:** Schematic illustration of the initiation mechanism for the oxazoline (n=1) and oxazine (n=2) polymerization.

### Propagation

The propagation reaction proceeds through a nucleophilic attack of the imine function of an Ox monomer on the 5-position of the propagating cationic ring species (Figure 2.4). The polymerization chemistry of Ozi has been studied in less detail compared to Ox, but it has been generally accepted that they proceed via the same mechanism.[141–145] Accordingly, the propagation of Ozi proceeds via the nucleophilic attack at 6-position. For both monomer species, this attack leads to the opening of the cationic ring under the formation of a tertiary amide function. Interestingly it was found that the addition of the first

monomer ($k_{p,1}$) is the rate determining step of the whole polymerization reaction, and it is significantly slower than the attack of the following monomers ($k_p$).[146] This can be explained by the formation of a six-membered (oxazoline) or seven-membered (oxazine) ring, where the carbonyl oxygen of the previous repeating unit coordinates to the nitrogen of the propagating end-group (Figure 2.4). This phenomenon has significant influence on the

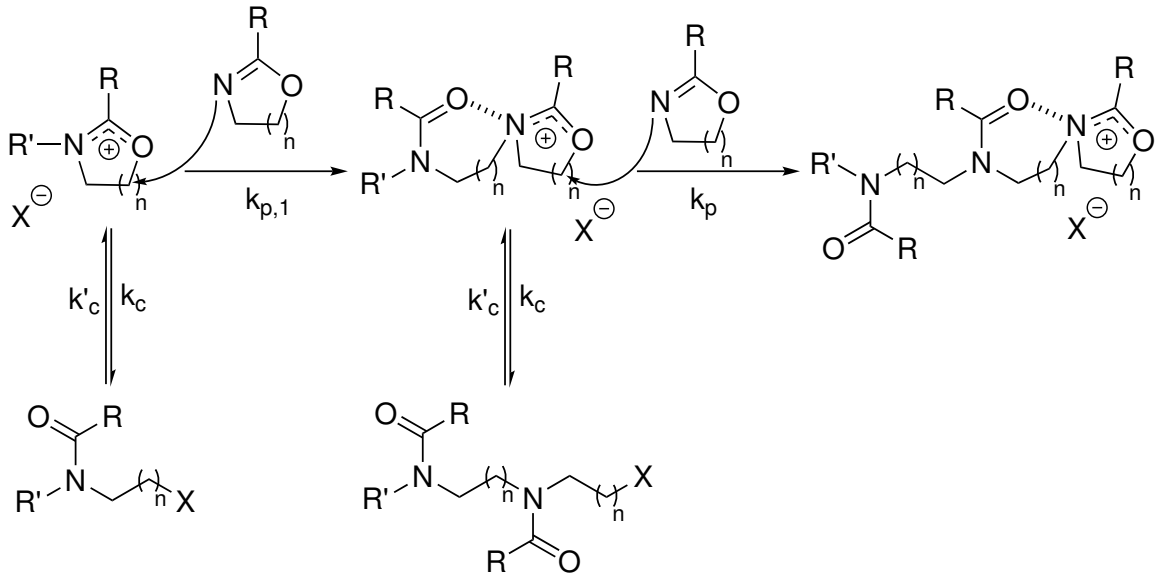


**Figure 2.4:** Schematic illustration of the propagation mechanism for the oxazoline (n=1) and oxazine (n=2) polymerization.

electron density in the active chain end and therefore on its reactivity.[119] Such a coordination is not possible during the attack of the first monomer, which explains the reduced reactivity rate. Under living conditions, the polymerization of Ox and Ozi is characterized by a pseudo-first order kinetics. It was found that the apparent propagation rate ($k_p^{app}$) is highly dependent on the monomer structure as well as the nature of the side chain. However, it has to be highlighted that general reactivity predictions of Ox and Ozi just based on the chemical structure are rather difficult.[119] Concerning the polymerization kinetics, the reaction speed is influenced by stabilization of the positive charge in the active chain end as well as the nucleophilicity of the imine function in the attacking monomer. As an example, side chains with an inductive electron donating effect (e.g. alkyl chains) decrease the reactivity of the cyclic cation, but on the other hand increase the nucleophilicity of the imine functionality. These two effects are contrary to each other and the extend of both contributions to the LCROP is not yet fully understood. Furthermore, steric contributions of the monomers do also influence $k_p^{app}$. Experimentally it was found that $k_p^{app}$ decreases from MeOx over 2-ethyl-2-oxazoline (EtOx) to 2-*iso*-propyl-2-oxazoline. Interesting is that increasing the side chain length from ethyl to *n*-nonyl showed only a minor

influence on the reaction kinetics. This indicates that the sterics play only a minor role for linear alkyl chains.[147] Using side chains with strong electron withdrawing effects like in 2-pentafluoroethyl-2-oxazoline leads to a drastically decreased $k_p^{app}$, which can be attributed to a decrease of the nucleophilicity of these monomers.[148]

The reactivity differences of the Ox monomers has major implications for the statistical copolymerization behaviour. It is important to note that the $k_p^{app}$ values of homopolymerizations can usually not be applied to gain information about the copolymerization behaviour of two monomers. In this context, the copolymerization kinetics and the reactivity ratios need to be determined. However, it was found that Ox monomers tend to retain the homopolymerization $k_p^{app}$ values during copolymerization.[119] This allows the estimation of the copolymer structure based on these values. When polymerizing two monomers simultaneously, a statistical copolymer is formed for monomers with similar reactivity. For example, this has been shown for the monomers EtOx and 2-n-propyl-oxazoline.[149] In the case of a large reactivity difference between two monomers, a statistical gradient polymer is formed. This was observed for the copolymerization of MeOx with 2-phenyl-2-oxazolin.[150]

While the polymerization behaviour of Ox has been studied quite detailed, less research has been done on the polymerization kinetics of Ozi monomers.[145] Generally, it was found that the Ozi monomers show a much slower polymerization speed than their respective Ox counterparts. In comparison to the planar conformation of the oxazolinium cation, the oxazinium cation is non-planar.[142] This causes an increased steric hindrance during the nucleophilic attack of Ozi monomers on the active chain and slows down the polymerization reaction. Also the reduced ring tension of the six-membered Ozi rings makes the ring opening less favourable and thus also decreases the reaction speed. When comparing Ozi monomers with increasing linear side chain length (from 2-methyl-2-oxazine (MeOzi) to 2-*iso*-propyl-2-oxazine), a similar decrease of the $k_p^{app}$ was found as for the Ox monomers. In the early stages of this thesis, no study about the statistical copolymerization of Ox and Ozi was available in literature. Only block copolymers of Ox and Ozi monomers had been studied and promising material properties were found.[108,127] Therefore, many opportunities might arise from studying the statistical copolymerization of Ox and Ozi as well. Due to the living character of the Ox and Ozi polymerization, a second monomer can be added after full conversion of the first monomer. This will result in defined block copolymers and most importantly, when the monomers are added sequentially, little attention must be paid to the reactivity ratios. For Ox, this was first reported by Seagusa *et al.* for the synthesis of amphiphilic block copolymers.[151] Since then a large variety of Ox-based di- and triblock copolymers have been reported, yet only little research was done

on Ox/Ozi block copolymers.[108,127,151] In general, copolymerization allows the synthesis of polymers with interesting properties and many of those polymers have been proposed for biomedical applications in the fields of bioprinting, drug delivery, hydrogels or antifouling surfaces.[108,117,127,152–154]

Even though, the polymerization of Ox can be performed under living conditions, chain transfer and chain coupling reactions are still known to occur. When the polymerization is performed carefully and the degree of polymerization (DP) is kept below 200, such reactions are most of the times negligible. However, for certain monomers as well as when high molar mass polymers are prepared, these side reactions will lead to increasingly broad molar mass distributions and compromised end-group functionalization.[155,156] Bloksma *et al.* report similar observations for the polymerization of several Ozi monomers.[126] Notably was that in this study side reactions occurred even for low monomer to initiator ratios of 50, and high dispersities of up to 1.42 were found. Therefore, the synthesis of POzi with narrow molar mass distributions is still a challenge. The underlying mechanism of the side reactions has been proposed to proceed via a $\beta$-elimination or imine-enamine tautomerism respectively (Figure 2.5). Through this process, two unwanted species are formed. On the one hand a "dead" enamine chain end and on the other hand a proton-initiated oxazolinium cation. The enamine species can react with another growing polymer and this will cause chain coupling and formation of a branched polymer. Simultaneously, the proton initiated cation can induce the growth of a new chain.

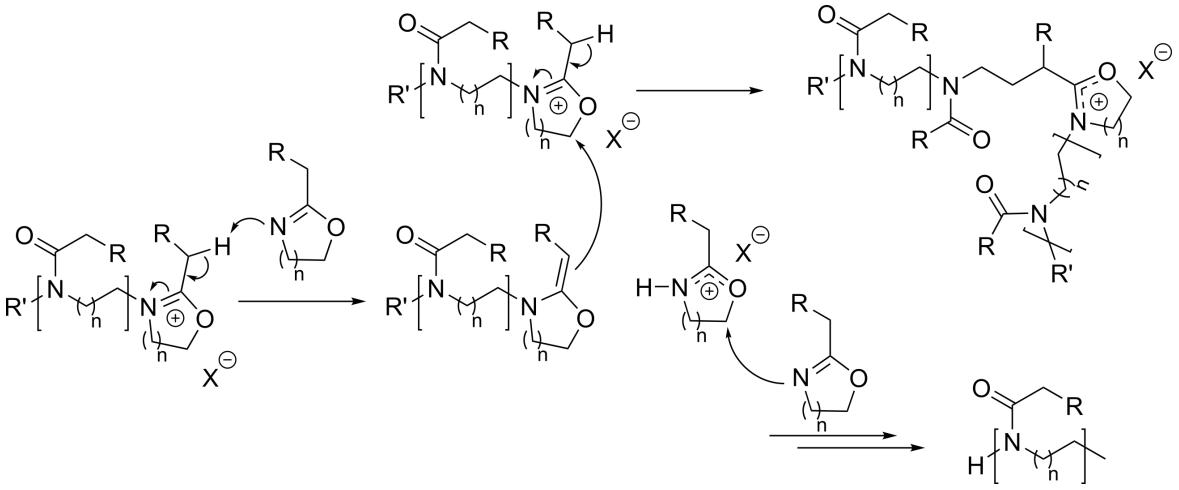

**Figure 2.5:** Schematic illustration of the chain transfer as well as the chain coupling mechanism during the polymerization of oxazolines (n=1) or oxazines (n=2).

Interestingly, signs for chain transfer were also found for the polymerization of monomers, which do not contain a $\beta$-proton, like 2-phenyl-2-oxazoline.[155] Clearly, the presented mech-

anism cannot be applied in these cases. This indicates that other reaction pathways might also take place. Furthermore, impurities as well as the polymerization solvent itself have been found to induce or favour chain transfer reactions.[119]

### Termination

In general, the polymerization of Ox and Ozi can be terminated with any nucleophile. The active chain end has two electrophilic positions, and terminating reagents may add to the *2*- or the *5*-positions of POx (Figure 2.6). While some studies about the termination of POx are published,[139] to date no detailed research has been published for POzi. Assuming a similar reactivity as POx, the termination of POzi should proceed at *2*- or *6*-position respectively. It has been proposed that the position of termination can be rationalized via the hard and soft acids and bases theory.[119] While soft nucleophiles like water (neutral conditions) or potassium carbonate have the tendency to terminate at *2*-position, hard reagents like KOH in MeOH or amines will add preferentially in *5*-position. In case of the attack at *2*-position an acetamide-acetal like structure is formed first. For the most reagents (secondary amines or alcohols), a ring opening of this compound is not possible and without further workup, only the reverse reaction to the oxazinium ion can occur. Interestingly, when water is used as a reagent, ring opening and the formation of an amino ester compound does occur.[139] In literature, often piperidine as well as methanolic solution of KOH are used as terminating agents as both are reported to give trustworthy termination in *5*-position. Similar to the initiator, the terminating reagent can be used to introduce a wide variety of functional groups as well. Among others these are alkyne or azide functions, alkenes, or maleimides.[157–159]

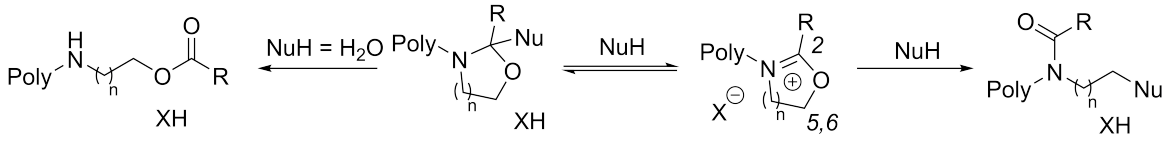


**Figure 2.6:** Schematic illustration of the termination mechanism in *2*- (left) and *5*-position (right) during the polymerization of oxazolines (n=1) or oxazines (n=2).

However, the termination behaviour of POx is still not fully understood. Recently an interesting study about the formation of primary amine end-groups during the termination of PEtOx has been published.[160] In a very detailed study the authors present convincing proof about the unexpected reactivity of the oxazolinium cation with ammonia. Kobayashi *et al.* and later other groups claim that the termination with a solution of $NH_3$ in MeOH will result in termination at *5*-position, which results exclusively in primary amine termina.[161] In their study, Kosakowska *et al.* show that these conditions will in fact lead

to termination in *2*-position and the exclusive formation of hydroxyethylamino end-groups. As they report a procedure under water free conditions, they also propose a water free mechanism of this process involving the formation of a nitrile component. However, if amine terminating agents contain residual water, the formation of $OH^-$ nucleophiles in the termination solution is likely. $OH^-$ is a very potent nucleophile and can compete with remaining amines in the termination procedure. In the case of the undesired $OH^-$ addition, the reaction can occur in *2*- or *5*-position. While both pathways will not produce the desired amine terminus, the addition in *2*-position will also lead to the formation of hydroxyethylamino end-groups.

### 2.5.3 The Properties

The combination of an immense library of available monomers, as well as the straight forward copolymerization allows the tuning of the physical properties of POx over a broad range. This versatility is one reason for current popularity surge of POx. It can be assumed that POzi offers a similar diversity as POx however currently little data is available to support this claim.

#### Thermal Properties

Generally, degradation temperatures of 300 °C and higher have been found for POx. This suggests the potential for application over a wide temperature range. In this context it is important to note that thermally induced ageing of polymers can occur at much lower temperatures than the degradation temperature. Depending on the nature of the side chain, POx can be either amorphous or semicrystalline. In the case of linear side chains, the polymers poly(2-methyl-2-oxazoline) (PMeOx) to poly(2-n-propyl-oxazoline) (PPrOx) are amorphous and poly(2-n-butyl-oxazoline) is the first semicrystalline derivative, which shows a melting temperature ($T_m$) of 150 °C.[162] Interestingly, the $T_m$ was found to be virtually independent for increasing length of n-alkyl side chains. Furthermore, using cyclic side chains results in performance polymers with $T_m$ values of up to 306 °C.[163] In addition, there are also hints for possibility to induce crystallinity for short alkyl chains by isothermal heating over prolonged time periods.[123] In contrast to the $T_m$, the glass-transition temperature ($T_g$) was found to be strongly dependant on the number of carbon atoms in n-alkyl side chains. For instance, a linear dependency from 80 °C for PMeOx to 24 °C for poly(2-n-butyl-oxazoline) was found.[147,162] Due to less pronounced alignment, utilizing branched side chains also results in fully amorphous polymers with low $T_g$.[164,165] It has been shown that statistical copolymerization allows straight forward control over both, the $T_g$ and the $T_m$. For instance via the combination of amorphous poly(2-phenyl-2-oxazoline) and semi-

crystalline poly(2-nonyl-2-oxazoline), the $T_g$ could be controlled between 110 and 50 °C, whereas the $T_m$ increased from 120 to 150 °C.[166] In another example, the two amorphous polymers PEtOx and poly(2-(3-ethylheptyl)-2-oxazoline) were combined.[164] A predictable linear dependency of the $T_g$ ranging between 58 and -5 °C degrees was found. The $T_g$ of POzi was generally found to be about 50 °C lower than the corresponding POx.[125] This has been attributed to the increased flexibility resulting from the additional $CH_2$ group in the polymer backbone. For instance, a $T_g$ at 16 and 8 °C was found for poly(2-methyl-2-oxazine) (PMeOzi) and poly(2-ethyl-2-oxazine) (PEtOzi), whereas their respective Ox counterparts exhibit a $T_g$ at 80 and 60 °C. As, no studies about the influence of copolymerization on the $T_g$ and $T_m$ are published for POzi, a behaviour comparable to POx copolymers can only be assumed.

### Solubility

Similar to the $T_g$, the solubility of POx and POzi is strongly dependant on the chemical nature of the side chain. With POx it is generally possibly to cover the full solubility spectrum from hydrophilic, for short side chains like methyl and ethyl, to hydrophobic, for long side chains with four or more carbon atoms.[167] When perfluoroalkyl substituents are used, even fluorophilic polymers are accessible.[148] For biomedical applications, the water solubility and hydrophilicity is of special importance. With the exception of PMeOx all water soluble POxs show an LCST behaviour.[168] Interestingly enough, it was hypothesized that PMeOx is even more hydrophilic than PEG.[169] With the additional $CH_2$ group in the side chain, PEtOx in less hydrophilic than PMeOx and LCST values between 60 and 100 °C have been reported.[170,171] This wide range shows clearly that beside the side chain the polymer end-groups and the DP play a major role for the solubility properties. Copolymerization of hydrophilic and hydrophobic monomers results in amphiphilic polymers, which can self-assemble into larger structures like micelles. Due to the thermoresponsiveness, micelle formation can be triggered by temperature if the polymer concentration is above the critical concentration. Such micelles have been extensively studied for applications in the field of drug delivery.[117,127,172,173] The solubility of Ozi has not been studied in detail yet. One publication however reports a similar trend as seen for POx. While PMeOzi showed no LCST, an LCST was found for PEtOzi and poly(2-n-propyl-oxazine) (PPrOzi) at 56 and 11 °C respectively. Poly(2-n-butyl-2-oxazine) on the other hand was found to be insoluble in water. Currently two potential applications of POx/POzi block copolymers that utilize the tunable hydrophilicity, have been reported. Lorson *et al.* use a PPrOzi-b-PMeOx copolymer for the preparation of hydrogels for bioprinting and Luebtow *et al.* use POx/POzi triblock copolymers for the preparation of micelles for drug delivery.[108,127]

### Biological Properties

Concerning biological applications, POxs are often reported to show excellent biocompatibility.[11] Such a general statement has to be viewed critically as most of the currently available research does not go beyond simple *in vitro* cell cytotoxicity tests. Furthermore, large portions of the respective research focused only on the hydrophilic PMeOx and PEtOx. Indeed for those two POx species, excellent cyto- and hemocompatibility was found.[174–176] Novel POx biomaterials however, are often based on copolymers. As differences in the polymer composition (PC), the molar mass and the polymer end-groups can alter the biological response, it is essential to always evaluate the potential toxicity of a new material. However, many copolymers incorporating either MeOx or EtOx have been already evaluated on their cytotoxicity and overall no signs for cytotoxicity were found.[108,177–180] In addition to simple toxicity tests, it is a must for new biomaterials to understand the biodistribution mechanism. For POx homo- and copolymers *in vivo* radiolabelling studies in mice revealed a rapid clearance of these polymers from the bloodstream.[181,182] Further studies found that only for a molar mass below 20 kg/mol the polymers are excreted via the kidneys.[183] Therefore, especially for polymers with high molar mass, the biodegradability is of importance. While the POx side chains are easily cleaved off via hydrolysis in concentrated acidic or base, this mechanism is not really relevant under physiological conditions.[184] Even in simulated gastric fluid no significant hydrolysis was observed.[180] Furthermore, the POx backbone is not readily degraded. Some hints were found that degradation via reactive oxygen species or enzymes might be relevant for POx, but so far no significant biological degradation pathways have been found.[24]

## 2.5.4 Hydrolysis of Poly(2-oxazoline) and Poly(2-oxazine)

While the chemical stability of the POx and POzi backbone is relatively high, the amide side chains can be cleaved under strong basic or acidic conditions. This was first reported by Tomalia *et al.* in 1966, where they hydrolysed PMeOx to linear poly(ethylene imine) (PEI) using sulphuric acid as a prove for the chemical structure of POx.[122] Today, the hydrolysis of POx is an established path for the synthesis of linear PEI, which is rather difficult to prepare by other routes.[185] The first characterization of linear PEI prepared from POx was presented by Saegusa *et al.* and a crystalline product with a $T_m$ of 58 °C and a $T_g$ of -23 °C was found.[186] Since then, several reports about the acidic and alkaline hydrolysis of POx for the synthesis of PEI have been reported.[187,188] Interesting is also the partial hydrolysis of PEtOx-based on enzymatic degradation reported by Wang and coworkers.[189] In biomedical research, linear PEI is commonly applied for the transfection of cells, despite its pronounced cytotoxicity.[190] It is currently under investigation, if par-

tially hydrolysed POx could allow high transfection activity with lower cytotoxicity. Here it might also be helpful to know more about the hydrolysis behaviour of POzi, as POx/POzi copolymers could help balancing cytotoxicity and transfection activity. In particular, since poly(propylenimine) was found to exhibit lower toxicity values than PEI.[191] In contrast to POx, the hydrolysis of POzi has not been investigated in detail. However, it was found that it also proceeds under basic as well as acidic conditions and presumably follows a comparable mechanism.[145,192] In addition to its biological use, linear PEI finds application in the textile industry to enhance the adsorption of dye onto fibres or the construction industry to control the water retention of cements.[193,194]

In general, the hydrolysis of POx is a rather slow reaction and hydrolysis times from several hours up to days have been reported.[188] Under basic conditions, the reaction proceeds via the attack of an $OH^-$ nucleophile at the carbonyl group (Figure 2.7 top). The intermediate product is deprotonated, and the respective carboxylic acid is eliminated from the polymer. The full reaction mechanism follows $2^{nd}$ order kinetics and the final step is virtually irreversible. It is important to highlight that there are reports for backbone degradation under basic hydrolysis conditions.[195] This phenomenon might have been overlooked by earlier reports due to the challenging analysis via gel permeation chromatography (GPC) caused by strong polymer column interactions. Under acidic conditions the hydrolysis reaction proceeds much more rapidly.[196] This reaction is usually performed using a large excess of HCL and under these conditions the reaction follows a pseudo-first order kinetic.[184] The mechanism is believed to proceed via the activation of the amide by protonation of the carboxyl oxygen (Figure 2.7 bottom). This facilitates the attack of water, which is also the rate determining step of the reaction. The formed intermediate product dissociates under the formation of the secondary amine and the respective carboxylic acid. Lambermont-Thijs *et al.* present a detailed study of the acidic hydrolysis of PMeOx and PEtOx. For PEtOx they found a linear dependency of the hydrolysis degree on the reaction time for low to medium conversions. For hydrolysis degrees of 60 % and higher, the polymer solubility decreased, resulting in partial precipitation and slight deviation from the linear dependency. Also, no significant influence of the molar mass on the reaction kinetics was found. In direct comparison, PMeOx was hydrolysed more rapidly than PEtOx. This was attributed to the reduced steric hindrance as well as to the increased hydrophilicity. The hydrolysis kinetics was found to be independent of the total amide concentration, but in a follow-up study it was shown that it is strongly dependant on the reaction temperature.[180] Under acidic conditions the reaction may be influenced by the formation of an intermolecular seven-membered ring. In the case, where an already hydrolysed group is located next to an amide function (Figure 2.7 inset), the susceptibility towards hydrolysis of the neighbouring

amide is increased.[180] This reactivity is evidenced by an acceleration of the hydrolysis speed in the first minutes of the reaction. In addition, such a phenomenon might favour the formation of block-like hydrolysed compartments within the polymer backbone.

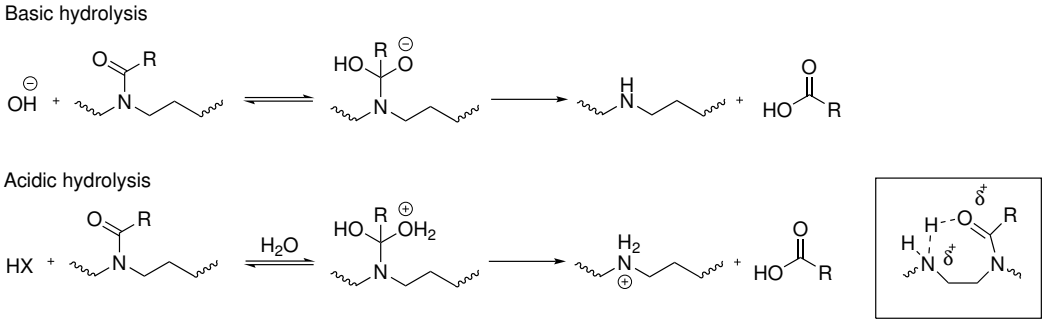


**Figure 2.7:** Illustration of the chemical mechanism of the POx hydrolysis under basic and acidic conditions. In the square, the seven-membered transition state, responsible for the accelerated hydrolysis under acidic conditions, is visualized.

Using predefined hydrolysis kinetics, it is also possible to control the hydrolysis degree via the reaction time. This allows the synthesis of partially hydrolysed POx with a defined amine content.[180] Utilizing the strong dependency of the hydrolysis kinetics on the steric demand of the Ox side chain also allows the selective partial hydrolysis of Ox block copolymers. This was shown by using poly(2-undecyl-2-oxazoline)-block-PEtOx polymers.[197] Furthermore, partial hydrolysis has been successfully used as a starting point for polymer analogue modification. The formed secondary amines in the polymer backbone are readily converted with carboxylic acids, Michael acceptors or isocyanates (Figure 2.8). This allows the introduction of chemical functions to the polymers, which would not be compatible with the LCROP, and therefore this method is extensively used for the synthesis of Ox-based functional polymeric materials.[198] Furthermore, it is also a viable method for the introduction of bulky side chains, as it allows to bypass the synthesis of the respective Ox monomer. Especially, since it is often challenging to achieve the required quantity as well as purity for complex monomers. Examples for the use of polymer analogue functionalization of POx are presented by Chujo and coworkers. They used partially hydrolysed PMeOx for the synthesis of hydrogels based on various different covalent crosslinking methods.[199–204] These were among others bi-functional isocyanates, which resulted in redox sensitive hydrogels or carboxylic acid derivatives of furan and maleimide, which gave thermally reversible hydrogels. The latter approach will be discussed in the following section in greater detail. Also, Saegusa *et al.* functionalized partially hydrolysed PEtOx with methacrylic acid, which resulted in polymers with carboxylic acid side chains.[205]

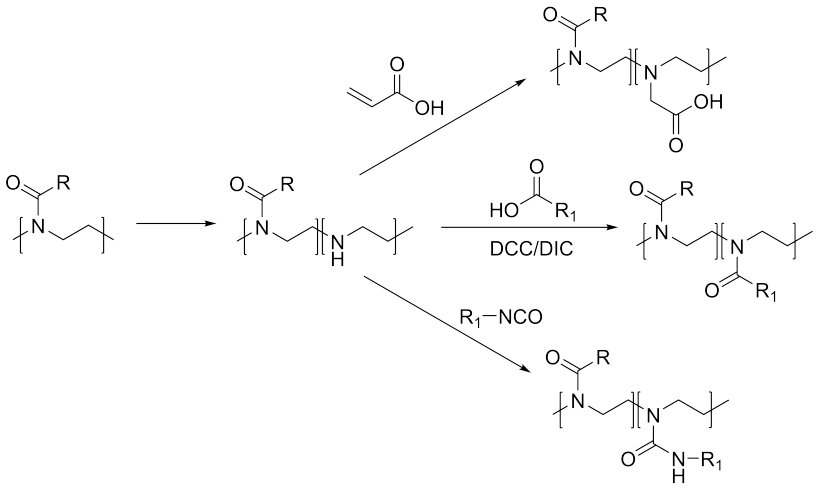


**Figure 2.8:** Illustrative overview of the post-polymerization modification strategies for partially hydrolysed POx.

## 2.5.5 Hydrogels Based on Poly(2-oxazoline)

In the preceding sections, a discussion of general details about hydrogels was presented. However, to contextualize this thesis, it is also important to learn more about the state of art concerning POx-based hydrogels. This subject was pioneered by Chujo *et al.* in the early 1990's in a series of publications[199–204]. At the same time, these publications lay the basis for this thesis. For the preparation of all hydrogels, Chujo *et al.* utilized polymer analogue modification of partially hydrolysed PMeOx. The respective functional groups for the crosslinking of the polymers were introduced via simple amine acid coupling. Among other techniques, the crosslinking was achieved via isocyanates, thiols and most importantly via the thermally reversible Diels-Alder (DA) reaction of furan and maleimide. The latter is also the first time thermally reversible covalent crosslinking was used for the synthesis of hydrogels. Until today, many researchers adopted this system and the DA chemistry enjoys increasing popularity in the field of biomaterials.[206] In the respective publication, Chujo and coworkers synthesized PMeOx with a molar mass of 15.8 kg/mol (monomer/initiator ratio: 190). The polymers were partially hydrolysed using sodium hydroxide to a degree between 2.5 and 23 %. The two polymeric components required for the DA crosslinking were synthesized separately via N,N'-dicyclohexylcarbodiimide (DCC) supported amine acid coupling of 3-(2-furyl)propionic acid and 3-maleimidopropionic acid to the polymer backbone. The crosslinked material was prepared by mixing the two components in MeOH followed by evaporation of the solvent at RT. The resulting films were then cured for 3 or 7 d at RT and under light exclusion. The DA reaction proceeded under these conditions in bulk without any further external stimuli, and most of the samples were insoluble afterwards. Interestingly, for the lower functionalization degrees of 2.5 and 4 %,

the films still dissolved after 3 d of curing. When the curing period was extended to 7 d, the material functionalized to 4 % also resulted in a non-soluble samples. This indicated that the critical degree of functionalization (DF) required for the complete crosslinking of the two components is around 4 %. Furthermore, the extended incubation time emphasizes a slow kinetics of the DA reaction. This could be due the limited mobility of the reactive functions in the solidified bulk material. Upon swelling in water, transparent hydrogels with a swelling degree between 110 and 1480 % depending on the DF were recovered. While stable in liquid medium at RT, the gels were readily dissolved within 1 h in hot solvents. This highlights the thermally reversible nature of the DA crosslinks. The cleaved polymers could be recovered as a reactive mixture. Upon incubation for 7 d, these samples resulted in hydrogels with comparable properties as before dissolution. Despite these promising results, the authors of this study reported no follow up work.

In addition to the use of functional side chains, two other main routes for the synthesis of POx hydrogels have been reported so far. These are the copolymerization of multivalent monomers or the macro-monomer method.[207–213] Commonly used multivalent monomers for the copolymerization approach are two Ox monomers connected by an aliphatic or a benzylic spacer. During polymerization, the chemically crosslinked 3D-network is formed insitu. After workup, swelling in water will result in the formation of a hydrogel.[208] Using a 2,2'-tetramethylenebis(2-oxazoline) allowed the synthesis of highly swollen non-ionic hydrogels. They reported swelling degrees of 3600 and 2800 % for the copolymerization with MeOx and EtOx respectively.[152] The macro-monomer approach usually uses polymers with allyl end-group functionalities. These functions can be introduced during the initiation or the termination step of the polymerization. In a following step, the allyl groups are crosslinked via radical reaction. This results in a crosslinked polymer network, which can be swollen in water.[208,212,213] In addition to the covalent crosslinking, the polymer network can also be established through physical bonds. These kind of hydrogels are much less frequently reported. This is because their formation is hard to predict and the discovery is often mere luck. Currently the only physical hydrogel, which consists purely out of POx and POzi, was reported by Lorson and coworkers.[108] This material shows pronounced shear thinning properties and the application as a bioink is envisioned. For the use as advanced biomaterials, it is necessary that the hydrogels allow the introduction of cell adhesive and cell instructive cues. Such options have been explored for POx-based gels as well. For instance, thiol-ene chemistry was applied to incorporate the cell adhesion sequence arginylglycylaspartic acid (RGD) into the gel material.[210] As expected, this led to a strong increase in cell adhesion. Farrugia *et al.* went further and encapsulated fibroblasts in a PEtOx hydrogel matrix, which was crosslinked via UV induced thiol-ene reaction in

phosphate-buffered saline (PBS).[214] After optimization of the curing time and the photo initiator concentration, the cell viability remained high (80-90 %) after the UV-based cross-linking procedure. The resulting gels were relatively dense and lacked degradation sites, therefore no cell migration was possible within the material.

## 2.6 Diels-Alder Chemistry

The ability to covalently couple functional molecules is a key challenge in the field of biomaterials and drug delivery. The underlying reactions need to be rapid, efficient, proceed under mild conditions and require no toxic trigger.[86,215] Many reactions from the scientific field of click chemistry fulfil these requirements. The term "click chemistry" was coined in 2001 by Sharpless and defines a group of "spring-loaded" reactions that proceed in a highly selective manner.[216] In addition, click reactions are applicable to various materials and chemical environments. It is therefore not surprising that click chemistry has already been used for the synthesis of hydrogels with the focus on biomedical applications.[86,200,217–219] The most outstanding of those reactions is probably the copper(I)-catalysed azide-alkyne Huisgen cycloaddition (CuAAC). This reaction reaches quantitative conversion in both, aqueous and organic media and simultaneously allows a very high level of selectivity. Obviously, the potential toxicity of the catalysts is a major concern for the use in biological applications.[86,158] The DA reaction of furan and maleimide on the other hand is a cycloaddition reaction that has also been classified as click chemistry and requires no catalyst or external trigger, except a temperature gradient.[206] This reaction was pioneered by Otto Diels and Kurt Alder in 1928 and this discovery was later rewarded with the Nobel prize in chemistry.[220] The DA reaction offers predictable and trustworthy stereoselectivity, it is atom economical and highly efficient. This makes this reaction a powerful tool for organic chemistry in general and especially for the synthesis of unsaturated six-membered rings.[221] The DA reaction was also described as bioorthogonal, meaning it can be carried out in living systems without disturbing the biological processes.[222–225] This makes the DA reaction a promising candidate for pharmaceutical and biomedical applications, which is also reflected by its increasing popularity in those research fields.[218,219,226–229] The DA reaction is the [4+2] pericyclic reaction of a diene and an alkene (often termed dienophile). During their reaction, 6 $\pi$-electrons are rearranged, two new covalent carbon-carbon bonds are formed, and a six-membered ring (Figure 2.9) is established. The DA reaction is concerted, meaning it has only one transition state and no intermediated products are formed.[230,231] The most simple example of a [4+2] reaction is the reaction of 1,3-butadiene with ethylene, yet this is more of a theoretical example as the reaction between these two molecules proceeds only under high temperature and pressure. The reaction kinetic depends drastically on the

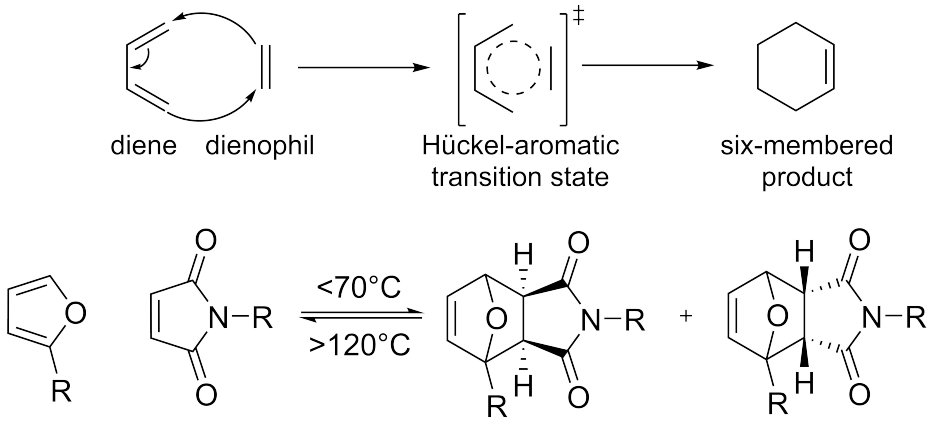


**Figure 2.9:** Schematic illustration of the Diels-Alder reaction.

electronic environment of the educts. Generally, a favourable reaction can be achieved by using electron rich dienes and electron poor dienophiles.[206] The furan and maleimide pair is particularly outstanding in this context.[216] Due to the electron donating capabilities of the oxygen atom furan, is a rather electron rich heterocyclic compound. Contrary to its related five-membered ring compounds, pyrrole and thiophene, furan shows a rather low aromaticity. Therefore, it is the only representative of this series that shows significant diene reactivity. For instance thiophene, which is highly aromatic, only undergoes DA reaction under drastic conditions of up to 8000 bar.[232] The C=C double bond of maleimide on the other hand is very electron poor. This is due to the electron withdrawing effect of the carbonyl groups and makes maleimides very susceptible for pericyclic reactions. At this point it should also be mentioned that the DA reaction can proceed with very electron poor dienes and electron rich dienophiles. This subcategory is termed inverse electron-demand DA reaction. The DA reaction has immense potential in organic chemistry as it allows the design of up to four stereocentres in one reaction step.[233] Furthermore, the reaction is stereoselective as well as stereospecific, meaning it allows exact prediction of the formed stereoisomer via the Woodward-Hoffmann rules. However most importantly, for certain diene and dienophile pairs, the DA reaction is readily reversed at elevated temperatures via the retro Diels-Alder (rDA) reaction (Figure 2.9). This offers exciting design possibilities for materials that can exploit the dynamic DA equilibrium.[234,235] Important DA pairs that establish dynamic equilibrium under relatively mild conditions are listed in Figure 2.10.[236] Several characteristics make the DA reaction of furan and maleimide a promising candidate for the synthesis of functional materials in general and also with focus on biomedical applications. For instance, a variety of furan and maleimide derivatives are commercially available or easily synthesized. Reactive furan deviates like furfuryl alcohol or furfuryl amine readily react with carboxylic acids. On the other hand, 2-furfuryl chloride or carboxylic acid

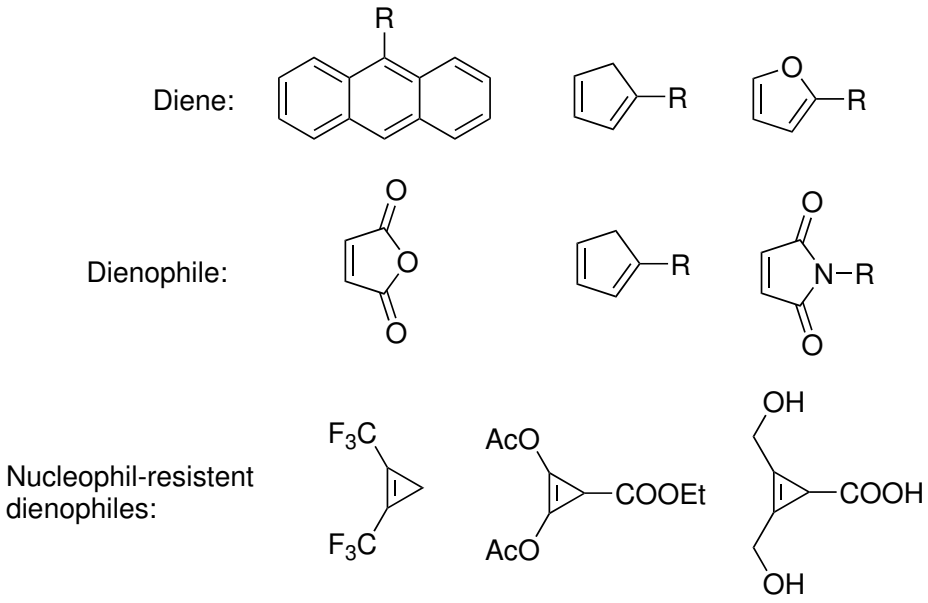


**Figure 2.10:** Schematic illustration of interesting dienes and dienophiles for the DA reaction.

derivatives of furan, like 3-(2-furyl)propionic acid can be readily reacted with amines or alcohols.[200] The same is valid for maleimides, which are readily utilized via the respective carboxylic acid derivatives. Such acid derivatives are either commercially available or can be synthesized by conversion of maleic acid with amino acids.[237] The reaction between furan and maleimide can proceed either in aqueous solutions or in bulk without any external stimuli.[200,218,219,235,238] Therefore, no toxic solvents or chemical triggers are required, which also makes purification redundant. Interestingly, due to a hydrophobic effect, the reaction actually proceeds faster in water than in organic solvents.[236] While the reaction does proceed to high levels of conversion at RT, it has to be stated that the kinetics are rather slow. For instance, at 25 °C in aqueous solution, a conversion of 92 % was found after 47 h.[239] The DA reaction has been extensively used for the synthesis of functional polymeric systems. Its dynamic nature allows to prepare materials, which combine the character of thermoset and thermoplastic materials. In the cooled state they possess properties that resemble a thermoset, such as mechanical stability, creep/chemical resistance as well as the insolubility in solvents. However, at elevated temperatures, they allow plasticity or material flow and can be dissolved in suitable solvents. Such systems are also referred to as covalent adaptable networks (CANs).[240] Generally, CANs are divided into two categories, the dissociative and the associative CAN. In the dissociative networks, crosslinks (chemical bonds) are first broken and then formed again at another place in the material. This means, upon a temperature increase the total number of crosslinks is decreased, which causes a loss of network integrity. These materials can achieve geometrical changes like stress relaxation or flow. The loss of crosslinking density due to

the temperature increase can result in sudden viscosity drops similar to what is observed for common thermoplastic materials. Networks based on DA crosslinks are classified as dissociative CANs. In the second group, the associative CANs, a crosslink (chemical bond) is only broken, when a new bond is established. This means, upon a temperature increase, the total number of crosslinks within the network remains unchanged. The temperature merely influences the frequency of the bond exchange and such systems therefore show a more gradual change of the viscosity. A common example for an associative CAN is a network based on carboxylate transesterification.[240]

Up to now, the DA reaction has been used for the synthesis of numerous materials with and without focus on biomedical applications. Some excellent reviews about this topic can be found in literature.[206,225,234,241,242] In the following only some selected examples, which are of special interest for this work, will be presented. For instance, Goepferich, Brandl and coworkers have published a series of papers on a PEG-based hydrogel.[218,219,243–245] They developed a platform based on star-shaped PEG macro monomers with a molar mass between 10 and 20 kg/mol, which they functionalized with maleimide and furan.[218] Upon mixing the two components in water, a hydrogel was formed without any external trigger. The gelation time ranged between 25 and 175 min depending on the polymer concentration, the molar mass, and the branching factor. Furthermore, these factors also influenced the mechanical properties of the material. For instance the stiffness, which was determined via oscillatory rheology experiments, was found to be influenced between 5 and 40 kPa. The degradation of these gels was strongly dependant on the temperature as well as the pH.[243] Under acidic conditions (pH 3 to 5.5) the material showed little degradation over an extended time period of over 300 d. Under neutral or basic conditions however, rapid degradation within 5 to 20 d was found. The degradation mechanism was attributed to the basic hydrolysis of the maleimide ring. By introducing short lysine containing peptide sequences as linkers, they also enabled enzymatic degradation of the DA-based gels as well.[219] This was used to investigate the *in vitro* drug release of bevacizumab as potential treatment for age-related macular degeneration. By increasing the hydrophobicity of the DA units, it was possible to significantly shorten the gelation times to 25 min.[244] This also affected the hydrogel properties such as mesh size, crosslinking density and degradability. Consolidating on this, they prepared a physically gelating system, which reinforces itself *in situ* and without external trigger by chemical DA bonds.[245] In addition, to the synthesis of functional hydrogels the DA reaction was also used to functionalize surfaces. For instance, for the mediation of cell attachment and spread, RGD sequences have been introduced to surfaces.[246] Other groups have used the mild DA reaction for the bioconjugation of DNA or antibodies on nanoparticle surfaces for drug delivery applications.[247,248]

Apart from potential biological applications, the thermoreversible nature of the DA reaction has been extensively used for the synthesis of materials with self-healing properties.[242,249] Self-healing describes the ability of a material/construct to (partially) recover its mechanical properties from breaks or cracks. The DA reaction is an ideal candidate for such applications, as it allows to re-establish chemical bonds at the defect without additional stimuli.[238,250,251] For instance, Chen *et al.* report about a remendable material based on multifunctional low molar mass furan and maleimide components. They found that after healing a fracture at elevated temperatures the material recovered 57 % of its original fracture load. The recovery could be initiated by simply heating a construct to elevated temperatures. This initiates the partial fusing at the defect side and upon cooling covalent bonds are established. Oehlenschlaeger *et al.* present a self-healing material based on a hetero DA system. After curing of a fracture, the specimen exhibited even higher toughness than before the treatment.[250]

Another interesting approach by Yang *et al.* utilizes the dynamic covalent chemistry to improve the interlayer adhesion of FDM printed constructs. The printing ink was a polymer blend of poly(L-lactide) with up to 25 % of multifunctional low molar mass furan and maleimide components. Using this system, they were able to increase the interlayer adhesion in printed parts by more than 95 %, while also decreasing the anisotropy within the constructs. Interestingly they report about a "save-temperature" (which unfortunately is not further specified) beyond this they observed a loss of reversibility of the material. Literature known, temperature induced, side reactions in relation to DA chemistry are the aromatisation of the DA adduct, the ring-opening of the furfuryl rings and the homopolymerization of the maleimide.[252–256] Each of those reactions leads to the loss of the reversibility of the crosslinked system. Interestingly, most of the remendable DA systems consist out of at least one low molar mass component.[238,250,251,257,258] Much fewer systems are based on two high molar mass polymer unimers.[200,251,259] Throughout literature, these self-healing systems are usually only kept at elevated temperatures for short time periods. Therefore, potential side reactions might often remain undetected and are seldom reported. An exception to this is a report by Bose and coworkers.[251] They investigated the use of furan and maleimide functionalized poly(lauryl-methacrylate) for materials with self-healing properties. Polymers containing both, furan and maleimide, allowed several liquefaction-solidification cycles by heating the material up to 160 °C. Also, such materials could be kept liquefied for four hours with little change in the storage modulus ($G'$) and loss modulus ($G''$) at 100 °C. However, when the polymers contained only maleimide groups, they found rapid and irreversible solidification upon heating to 160 °C. They attributed this solidification to the thermally induced homopolymerization of maleimide.

However, the use of the DA reaction also comes with some other challenges. One of them is the slow reaction kinetics at RT. This phenomenon basically excludes the use of DA chemistry for situations, where a rapid reaction is required, for instance for the preparation of *in situ* forming hydrogels. If needed, the reaction speed can be increased by a higher ambient temperature or the addition of Lewis acids such as $AlCl_3$.[260] Much more impactful are the potential side reactions that may proceed with the educts furan and maleimide. As stated above, the C=C double bond of the maleimide has a pronounced electron deficit. This makes it an excellent dienophile, but also highly susceptible towards nucleophilic attacks. Such nucleophiles might be water, alcohol-groups, amines or thiols. These can undergo a Michael-type reaction with the maleimide, which results in a irreversible covalent bond.[222] In particular, the reaction with thiols proceeds very rapidly and efficient to an extend where it has been classified a "click-type" reaction as well.[261] This has strong implications for biomedical applications of maleimides, as amines and thiols are abundant functions in biological environments. It can lead to unwanted conjugation of proteins with the DA material and lead to unspecific protein adsorption onto the surface of the material. Undesired complement reaction might be the result of this. Furthermore, the formed adduct cannot perform a DA reaction anymore. This has a strong impact for applications that utilize the dynamic nature of the reaction. It is generally very challenging to separate the reactivity as a Michael acceptor from the reactivity as a dienophile. An interesting theoretical study was presented by Tang and coworkers.[222] They calculated the free Gibb's activation energy of the Michael addition and the DA reaction of several dienes using a density functional theory method. What they found was that N-methylmaleimide has a very low energy barrier of 3.4 kcal/mol towards the Michael addition of methanethiol. In contrast to this, for the DA reaction with 1,3-butadiene an energy barrier of 20.9 kcal/mol was found. Unfortunately, they did not investigate more potent dienes. Interestingly, this problem cannot be solved by increasing the electron demand of the dienophiles, as this does also always facilitate the Michael addition. However, it is known that the relief of ring strain has a strong effect on the DA reaction.[262] For instance cyclopropene (high ring strain) has a lower DA barrier than cyclobutene and the barrier further increases with the size of the ring system. Based on this knowledge they were able to design several dienes, which have higher activation barriers towards Michael-type additions than to cyclo addition reactions. These are all based on substituted cyclopropenes and some of these are displayed in Figure 2.10. As an example, for 1,2-bis(hydroxymethyl)-3-carboxycyclopropene the activation energy for the addition of methanethiol was 26.2 kcal/mol and for the cycloaddition of 1,3-butadiene it was 24.2 kcal/mol. While the authors point out possible literature known synthesis routes of the substituted cyclopropenes, none of these are viable options for a large-scale production. Also, the difference in the activation energy is not

very pronounced, so both reactions will still proceed in an environment, where both thiols as well as dienes are present. Nonetheless, if the downsides and pitfalls can be managed, the DA reaction is a promising candidate for the synthesis of remendable thermoset materials. Furthermore, its biocompatible nature allows the use in biological environments, which makes it a promising reaction for the synthesis of functional biomaterials.

# 3 Motivation

MEW allows the fabrication of architectures with a unique feature set. This includes the accurate deposition of a single continuous low micron sized polymer filament. In addition to this, the fibre diameter can be controlled with high precision on a range from 5 to 50 $\mu$m. This enables the fabrication of tailor-made microperiodic constructs, which combine a high surface area with a high porosity. Furthermore, as MEW is a melt-based process, volatile and potentially toxic organic solvents are not required. These distinct features are highly desirable for the fabrication of constructs for biological applications or medical implants. Currently, only a limited selection of polymers is explored for MEW and most commonly PCL, a hydrophobic and stiff polymer, is used. While constructs made from PCL are very promising for applications in stiff tissue environments like bone or cartilage, MEW lacks the ability to process soft materials. Due to a high water content, hydrogels are a material class, which intrinsically provide a soft environment. Therefore, they are often used to mimic soft tissues like nerve or liver. However, the rapid fabrication of precise 3D hydrogel architectures with defined low micron sized features is still inherently challenging. This is due to the fact that upon extrusion of physically crosslinked hydrogels the material still tends to flow, and the printed structure loses shape. This can be prevented by reinforcing the material during extrusion for instance by UV-crosslinking or by coagulation.[113,114] In contrast to this, during melt processing, the printed fibres rapidly cool down after extrusion, they solidify and maintain high shape fidelity.

In order to overcome this shortcoming, this project aims to prepare a polymeric ink for the fabrication of hydrogels with low micron sized fibres via MEW. To prevent potential cytotoxicity, this material should allow crosslinking post printing without any external stimuli. Due to the hydrophilic nature of the polymer backbone, the printed filaments will swell in water, which results in the formation of hydrogel microfibres. For this purpose, POx and POzi will be investigated as the polymer basis for this biomaterial ink. These polymers can be prepared in large quantities and with precise control over the molar mass. The polymer platform offers excellent biological performance and allows to adjust the physico-chemical properties over a wide range without changing the polymerization chemistry. Most importantly, the polymers show high thermal stability and functional groups for the preparation

of a crosslinked network are readily introduced. Concerning the crosslinking method, there are three major requirements, that should be met. First, the method needs to be compatible with the demanding environment of melt processing and secondly, it should provide covalent bonds. This second point is required to assure high shape fidelity and to allow the handling of the hydrogel microfibres. Finally, the crosslinking should not require any external chemical to trigger the reaction. Apart from their potential cytotoxicity, such chemicals often show high reactivity and could interfere with the melt processing. This set of requirements is matched by the field of dynamic covalent chemistry and in this context especially the DA reaction of furan and maleimide stands out. While at RT the equilibrium is shifted significantly to the side of the bicyclic adduct, the reaction is readily reversed for temperatures above 120 °C. This is well in the range of commonly used MEW processing temperatures. This particular reaction is classified as a "click-type" reaction and it is therefore highly efficient and selective. A network crosslinked by DA chemistry will establish a CAN and combine the features of thermosets with the features of thermoplastics. In the cooled state the material will offer the mechanical stability, the creep and chemical resistance as well as the insolubility in solvents of thermosets. In contrast to this, in the heated state it will resemble a thermoplastic and allow material flow as well as melt processing. All in all, it has the potential to consolidate chemical crosslinking with MEW processing to manufacture hydrogels – a new class of material for this AM technology.

This project will therefore significantly broaden the application range of the young AM technique MEW. It will allow to utilize the benefits of the MEW technology for the engineering of soft tissue. In summary, the aim of this thesis defined in one sentence is: "the preparation of a biomaterial ink for the fabrication of chemically crosslinked hydrogel scaffolds with low micron sized features by using MEW". This thesis will be divided in three chapters. The first chapter presents an exploration of the general chemistry of POzi. Special focus was set on the homo- and copolymerization, the termination behaviour as well as a general evaluation of the melt processability. All these characteristics are currently not well investigated for POzi. In the second chapter, polymer analogue modification will be utilized to synthesize a POzi-based dynamically crosslinkable polymer platform. The MEW processability of this material will be evaluated and microperiodic hydrogel scaffolds will be prepared. Afterwards, the mechanical and biological properties of these constructs will be assessed. The third chapter will emphasize on the opportunities arising from this innovative material platform for the field of biofabrication and MEW.

# 4 Results and Discussion

## 4.1 Exploring the Polymer Platform

Thermal degradation of polymers at elevated temperatures in melt processing applications such as MEW is a major challenge. This is of special importance when reactive chemical functions are a vital part for the application of the processed material.[49,50] Polymer properties such as the $T_g$ and the molar mass have a strong influence on the melt flow behaviour and therefore on the melt processing temperature. The work described in the following chapter was aimed to investigate the homo- and copolymerization of 2-ethyl-2-oxazine (EtOzi) and EtOx. Basic research about the polymerization and termination behaviour was conducted and the properties of the resulting copolymers were analysed. This specific set of monomers was selected since their homopolymers combine moderate to high hydrophilicity with a low to moderate $T_g$. It was hypothesized that copolymerization would allow to control the polymer properties for MEW. Accordingly, the impact of the polymer properties on MEW processing can be evaluated. This will allow the identification of a promising polymer basis and will lay the foundation for the preparation of a first generation of MEW processable DA crosslinkable polymers.

### 4.1.1 Synthesis of Poly(2-oxazoline) and Poly(2-oxazine) Homo- and Copolymers

At the beginning of this work, no studies regarding the statistical copolymerization of POzi and POx could be found in literature. To study this matter, a library of five polymers with a DP of 100 and a varying EtOzi to EtOx monomer ratio was synthesized according to the schematic shown in Figure 4.1 a). In order to ensure a rapid and quantitative initiation, MeOTf was used as initiator. After polymerization in benzonitrile (BN), the polymers were terminated using a 1 M solution of KOH in MeOH. This condition was reported as a straightforward method for the introduction of "OH" termini to POx.[119,139] In this context, a more detailed discussion about the termination of POzi will be presented in section 4.1.3. Here, the "OH" termini were favoured over the more commonly used amine termination, as a higher thermal stability during melt processing was hypothesized. All

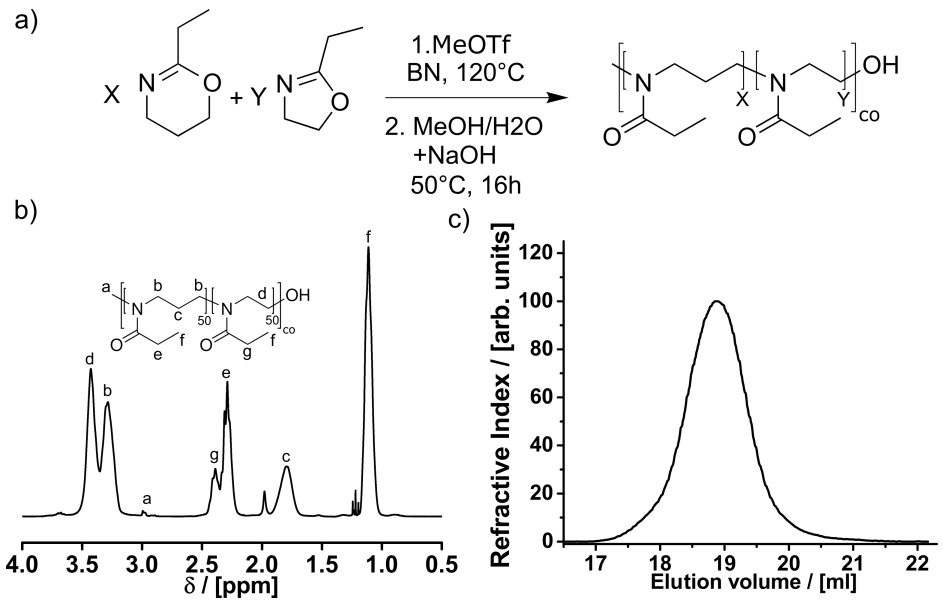


**Figure 4.1:** a) Schematic illustration of the polymer synthesis. b) $^1$H-NMR spectrum (300MHz, 298 K, $CDCl_3$) and c) GPC elugram of the P(EtOzi-co-EtOx) copolymer **P3** with a monomer feed ratio of 1:1.

polymers were characterized using $^1$H-nuclear magnetic resonance (NMR) spectroscopy, GPC and (if possible) matrix-assisted laser desorption/ionization time-of-flight mass spectrometry (MALDI-TOF) (Table 4.1). The $^1$H-NMR spectrum of **P3** is shown in Figure 4.1 b) as an representative example. All peaks can be assigned and the $CH_3$ signals of the initiating methyl group can be used to approximate the DP as well as the copolymer composition. For all copolymers, the calculated values matched well with the respective monomer feeds (Table 4.1). The representative GPC elugram of **P3** (Figure 4.1 c) as well as the overall low polydispersity values (Đ) (Table 4.1) indicate a narrow molar mass distribution of all polymers. This highlights that the copolymerization of EtOzi and EtOx was well controlled and resulted in defined polymers. Noteworthy is the discrepancy between the DP determined via $^1$H-NMR and the $M_n$ value determined via GPC. This can be explained by the nature of the GPC method, where only sample retention times depending on the hydrodynamic radius of the respective polymer are measured. Without universal calibration no absolute molar mass can be determined and the obtained values are, under ideal conditions, solely dependant on the applied calibration and solvent. In this particular case PEG standards in HFIP were used. Presumably, due to a more compact coiling, the POzi and POx molecules with a molar mass around 10 kg/mol eluate at a similar retention time as PEG molecules with 5 kg/mol. It should also be appreciated that the monomer mass of PEG and POx differ. Analysis with GPC was still required as it allowed straight forward access to informations about the molar mass distribution and the dispersity Đ. In particular, since MALDI-TOF analysis of the copolymers resulted undefined spectra, which

prohibited detailed analysis and the calculation of $M_n$ and Đ from the respective spectra. For the PEtOzi and PEtOx homopolymers, the MALDI-TOF spectra were well resolved

**Table 4.1:** Synthesized EtOzi- and EtOx-based homo- and copolymers with respective analytical data.

| **Polymer** | ID | DP | $M_n^c$ | $M_n^a$ | Đ | $T_g^d$ | ML$^e$ 5 % | ML$^e$ 50 % |
|---|---|---|---|---|---|---|---|---|
| $PEtOzi_{100}$ | **P1** | $100^a$ | 5.1 | 11.4 | $1.01^a$ | 25 | 351 | 417 |
| P($EtOzi_{75}$-co-$EtOx_{25}$) | **P2** | $77/29^b$ | 4.8 | – | $1.15^c$ | 33 | 356 | 414 |
| P($EtOzi_{50}$-co-$EtOx_{50}$) | **P3** | $47/48^b$ | 4.5 | – | $1.18^c$ | 37 | 353 | 411 |
| P($EtOzi_{25}$-co-$EtOx_{75}$) | **P4** | $26/82^b$ | 4.1 | – | $1.22^c$ | 48 | 361 | 408 |
| $PEtOx_{100}$ | **P5** | $106^a$ | 5.1 | 10.5 | $1.00^a$ | 61 | 358 | 404 |

Determined by: $^a$ MALDI-TOF in [kg/mol]; $^b$ $^1$H-NMR analysis in [%]

Determined by: $^c$ GPC(HFIP) in [kg/mol]; $^d$ by DSC in [°C]; $^e$ by TGA in [°C]

(Figure 8.1), and the $M_n$ and Đ values could be calculated. The derived DP and $M_n$ values were well in line with the theoretical molar mass and the dispersities were low. These results again support the controlled polymerization of both monomers.

The thermal properties of the homo- and copolymers were analysed using thermogravimetric analysis (TGA) and differential scanning calorimetry (DSC) (Figure 4.2 a, b). The DSC trace of **P3** was representative for all polymers discussed in this chapter, and showed a single $T_g$ and no $T_m$, indicating that the sample is completely amorphous. This is in agreement with literature, as generally POx requires longer side chains to allow crystallization.[162] These results also indicate the absence of microphase separation and highlight the chemical compatibility of the EtOx and EtOzi monomers. It has to be stated that this does not necessarily mean that a blend of PEtOx and PEtOzi homopolymers would be fully miscible. Schoolaert *et al.* showed very recently that blends of PEtOx and PPrOx homopolymers with a molar mass of more than 10 kg/mol are immiscible. Contrary to this, the respective statistical copolymers did not show microphase separation.[263] In this context it is also important to note that PPrOx and PEtOzi are structural isomers. Due to the higher mobility of the polymer backbone, POzis generally possess a lower $T_g$ than their respective POx counterparts. While the $T_g$ of **P5** ($PEtOx_{100}$) compares well with the reported value for PEtOx (54 °C)[149], the $T_g$ of **P1** ($PEtOzi_{100}$) is higher than the value reported by Hoogenboom and coworkers (8 °C).[145] The discrepancy of the latter could be due to various reasons including differences in the molar mass distribution or the polymer end-groups. With increasing EtOzi content, the $T_g$ of the copolymers decreased linearly from 57.9 to 20.4 °C. This allows the prediction of the copolymer $T_{g,co}$ depending on the monomer weight fraction ($w_{Ozi}$;$w_{Ox}$) using the simple Fox equation (Equation 4.1). While

this behaviour has been observed for Ox copolymers[164,166], this has not been reported for Ox/Ozi copolymers.

$$T_{g,co} = T_{g,Ozi} * w_{Ozi} + T_{g,Ox} * w_{Ox} \tag{4.1}$$

TGA revealed high thermal stability for all homo- and copolymers and a mass loss (ML) of 5 % was found in the temperature range of 351-361 °C. This is in agreement with literature, reporting degradation temperatures around 300 °C for POx in general.[264] In summary,

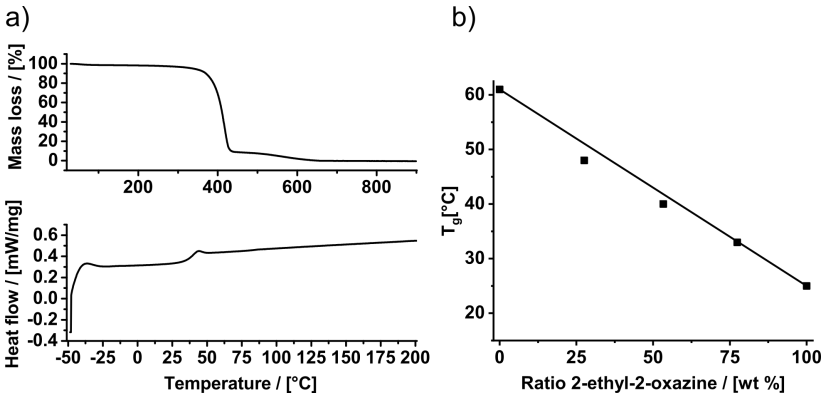


**Figure 4.2:** a) DSC and TGA traces of **P3**. b) Glass-transition temperature of the polymers **P1**, **2**, **3**, **4**, **5** depending on the polymer composition. The black line shows the theoretical dependency of the glass-transition temperature according to the Fox equation.

in this section it was shown that POx and POzi copolymers with defined molar mass distribution can be synthesized via simple copolymerization. The polymers are thermally stable up to a temperature range far beyond the expected MEW processing temperature (see Section 4.1.4). Most importantly, the $T_g$ of the copolymers can be predicted via the Fox equation, which allows to control the $T_g$ when required.

### 4.1.2 Polymerization Kinetics

During the execution of the polymerization reactions discussed in the previous chapter, indications for unexpected monomer reactivities were found. In a statistical copolymerization the chemical microstructure of the resulting polymers is determined by the relative reactivity (relative rate constants) of the different monomers. The chemical structure of polymers can have a strong influence on the physical and chemical properties. For example, this could be of particular importance for the partial hydrolysis of polymers. To elaborate on this topic, the copolymerization behaviour of several combinations of EtOzi, EtOx, MeOzi and MeOx were studied using $^1$H-NMR analysis. The polymerizations were carried out in a round bottom Schlenk flask using BN as solvent and MeOTf as initiator. A $^1$H-NMR spectrum was taken immediately after the components were fully mixed, and this gave the initial monomer concentration ($A_0$). In the following, the reaction mixture was heated to 120 °C, samples were taken manually at set time intervals, $^1$H-NMR spectra were taken rapidly thereafter, and the current monomer concentration ($A_t$) was determined. The change of the monomer concentration over time is directly correlated to the $A_t$ and the concentration of the active chain ends ($A^\star$). If the polymerization of Ox is performed under living conditions, $A^\star$ can be regarded as constant and equal to the initiator concentration ($I_0$). Because of this, the monomer consumption can be described by a pseudo-first order kinetic using Equation 4.2 and its integrated form Equation 4.3.

$$-\frac{d[A_t]}{dt} = k_p^{app}[I]_0[A]_t \tag{4.2}$$

$$ln\left(\frac{[A]_0}{[A]_t}\right) = k_p^{app}[I]_0 t \tag{4.3}$$

Therefore, under ideal conditions, plotting the fraction $ln\left(\frac{[A]_0}{[A]_t}\right)$ vs. $t$ gives a linear dependency. As $I_0$ is known, one can calculate the $k_p^{app}$ from the slope of a simple linear fitting of the data points. Figure 4.3 a) shows the linearised first order kinetic plots of the homopolymerization of MeOx, EtOx, MeOzi and EtOzi with the respective linear fits. The derived $k_p^{app}$ are listed in Table 4.2. Comparing MeOx, EtOx and EtOzi reveals a decreasing $k_p^{app}$ in that respective order. The reactivity ratio of the Ox monomers $\frac{k_{p,MeOx}^{app}}{k_{p,EtOx}^{app}}$=1.3 is in good agreement with literature, where a ratio of 1.4 is reported.[147] In literature it is often argued that the increased electron donating character of the ethyl side chain leads to a decrease in the electrophilicity of the propagating ethyl oxazolinium salt. This could explain the reduced polymerization rate of EtOx compared to MeOx. The reduced polymerization rate of EtOzi compared with EtOx can be attributed to the more pronounced steric hindrance during the nucleophilic attack of an oxazine monomer at the six-membered

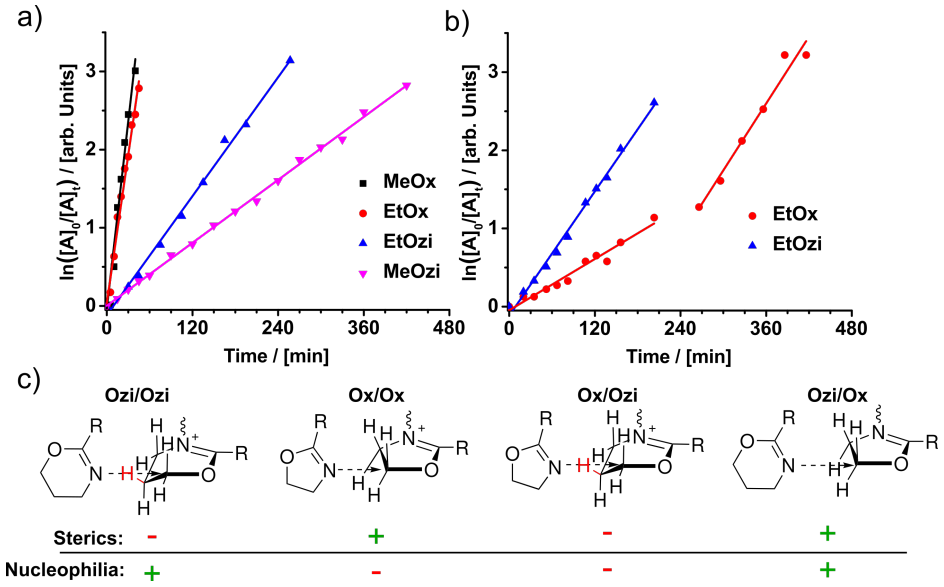


**Figure 4.3:** a) First order kinetic plots of the homopolymerization of MeOx, EtOx, MeOzi and EtOzi. b) First order kinetic plot of the copolymerization of EtOx and EtOzi (Ratio: 1:3). c) Qualitative evaluation of the reactivity between Ox and Ozi (adapted from [265]).

configuration of the propagating oxazinium cation (Figure 4.3 c). Unexpected is the almost two times lower rate constant ($\frac{k_{p,EtOzi}^{app}}{k_{p,MeOzi}^{app}} = 1.9$) for MeOzi compared to EtOzi. Based on the results of the Ox monomers, the opposite ratio would be expected. It has to be highlighted that general reactivity predictions of Ox and Ozi, just based on the chemical structure, are rather difficult. For instance, the increase of the electron density within an Ox or Ozi monomer caused by an electron donating side chain decreases the reactivity of the active cationic species (decreasing contribution to $k_p^{app}$). At the same time this effect increases the nucleophilicity of the attacking imine functionality of the monomer (increasing contribution to $k_p^{app}$).[119] Also, the extent of both contributions is heavily influenced by the reaction conditions e.g. the used solvent or initiator. It is important to point out that Hoogenboom *et al.* report an opposing observation for the comparison of EtOzi and MeOzi ($\frac{k_{p,EtOzi}^{app}}{k_{p,MeOzi}^{app}}$=0.66).[126] However, in these investigations Bloksma and coworkers used a different set of reaction conditions, such as acetonitrile (AN) as solvent and methyltosylate as initiator, and this prevents a direct comparison. More in depth investigation of the LCROP mechanism of Ozi is required to explain the observations made for the reactivity of EtOzi and MeOzi. Theoretical modelling of the system might be helpful to shine light in this matter, but this would be well beyond the scope of this thesis.

From the homopolymerization a reactivity ratio for EtOzi and EtOx of $\frac{k_{p,EtOzi}^{app}}{k_{p,EtOx}^{app}} = 0.2$ was derived, surprisingly a reversal of this reactivity was observed for the statistical copolymerizations of those monomers at three different Ox to Ozi ratios (Figure 4.3 b, Figure 8.2 a,

b, Table 4.2). In a 1:3 mixture, EtOzi reacted almost unhindered, which was reflected by a $k_{Co,Ozi}$ similar to the homopolymerization. In contrast, the reactivity of the EtOx monomer was decreased by roughly one order of magnitude ($\frac{k_{p,EtOx}^{app}}{k_{Co,Ox1}} = 11.3$). The deceleration of the EtOx kinetics was pronounced to such an extend that even for a Ox to Ozi ratio of 3:1, EtOzi was consumed before the Ox monomer (Figure 8.2 a). While these studies were performed, Hoogenboom *et al.* reported very comparable observations for the copolymerization behaviour of MeOzi with 2-butyl-2-oxazoline and 2-n-propyl-2-oxazoline.[265] Based

**Table 4.2:** Comparison of the apparent rate constants found for the homopolymerization of EtOzi, EtOx, MeOzi and MeOx as well as for the copolymerization of selected combinations.

| **Monomers** | $k_p^{app}$ | $k_{Co,Ozi}$ | $k_{Co,Ox1}$ | $k_{Co,Ox2}$ |
|---|---|---|---|---|
| MeOx | 44 | – | – | – |
| EtOx | 35 | – | – | – |
| MeOzi | 3.8 | – | – | – |
| EtOzi | 7.2 | – | – | – |
| $EtOx_{25}/EtOzi_{75}$ | – | 7.4 | 3.1 | 7.9 |
| $EtOx_{50}/EtOzi_{50}$ | – | 4.3 | 2.4 | 7.1 |
| $EtOx_{75}/EtOzi_{25}$ | – | 8.1 | 4.3 | 21 |

$I_0$ = [0.03 mol/l]; $k_p^{app}$ $[1 \times 10^{-3} \frac{l}{mol \times s}]$

$k_{Co,Ozi}$ describes the $k_p^{app}$ of the Ozi fraction during copolymerization.

$k_{Co,Ox1}$ describes the $k_p^{app}$ of the Ox while there is still Ozi detectable by $^1$H-NMR.

$k_{Co,Ox2}$ describes the $k_p^{app}$ of the Ox monomer after no Ozi is detectable by $^1$H-NMR.

on these kinetic investigations together with the data presented here, one can postulate that the nucleophilic attack of an EtOzi molecule onto an oxazinium chain end is faster than the attack of the EtOx monomer on said chain end. These effects can be explained by a combination of sterics and nucleophilicity (Figure 4.3 c). While Ozi monomers are generally better nucleophiles than their Ox counterparts, in a homopolymerization scenario the Ozi reaction is sterically hindered by the nonplanar configuration of the oxazinium chain end. Experimental data showed that under these circumstances steric hindrance overcomes nucleophilicity, which explains the lower $k_p^{app}$ values of Ozi.[142] In a copolymerization scenario of Ox and Ozi, if the propagating species is an oxazinium cation, both monomers are sterically hindered and therefore the attack of the better nucleophile (Ozi) is favoured. In the context of the data presented here, the increased nucleophilicity of EtOzi compared to EtOx should lead to an excess of oxazinium cations as chain starters.[142] Therefore, in the propagation phase the attack of the EtOzi monomers is favoured over the EtOx monomers and proceeds with similar speed compared to its homopolymerization. Interesting is that according to the same sterics vs. nucleophilicity argument the attack of an EtOzi monomer onto an oxazolinium chain end should also be favoured over the attack of

the EtOx monomer (Figure 4.3 c). According to this argument, the EtOzi/EtOx reaction should be even faster than the EtOzi/EtOzi reaction. Therefore, an acceleration of the EtOzi monomer consumption in the copolymerization compared to the homopolymerization might be expected. Very interesting is that Hoogenboom *et al.* reported this effect in combination with a deviation from the ideal LCROP, since for their investigations the monomer consumption did not follow pseudo-first order kinetics for the copolymerization of MeOzi with 2-butyl-2-oxazoline.[265] Conversely, for the kinetics of EtOzi/EtOx presented here, a strictly linear dependency was found (Figure 4.3 b, Figure 8.2 a, b). It might be possible that this effect is less pronounced for EtOzi and that it is masked by the experimental error of the kinetic measurement itself. Also, EtOzi is sterically more hindered than MeOzi, which could lead to a less pronounced acceleration. Striking however was that in preliminary copolymerization studies of the monomer combinations MeOzi and EtOx as well as MeOx with EtOzi, the respective Ozi components also showed deviations from a pseudo-first order kinetic (Figure 8.3). Therefore, this phenomenon might only occur for monomer combinations with different side chains.

Once the EtOzi monomer was consumed, the $k_{Co,Ox2}$ of the EtOx monomer increased but did not reach the value determined for its homopolymerization. The reason for the incomplete recovery could be that the total monomer conversion at this state of the reaction was usually above 90 %, which makes a precise analysis challenging. Also residual EtOzi (beyond the detection limit of the NMR) could still hamper the polymerization. Very interesting are the implications for the resulting copolymer structures that can be drawn from these findings. Against intuition, the EtOzi/EtOx copolymers will have very EtOzi rich domain containing little to no EtOx units in the beginning. The chain end however will be an EtOx rich block structure. Therefore, the copolymers will show major deviations from the ideal statistical copolymer and rather express a block-like structure. Based on these results, for certain monomer combinations also a complete block structure formation is imaginable. Depending on the copolymer parameters this could allow straight forward access to Ox/Ozi block copolymers. These findings are also important for the subsequent work, as the polymers will be partially hydrolysed before functionalising the hydrolysed units with reactive moieties allowing crosslinking. The distribution of the hydrolysed units within the polymers will therefore govern the distribution of the crosslinking units. While the hydrolysis kinetics will be discussed in section 4.2.1, the literature reports a major difference in the hydrolytic activity of Ozi and Ox units. Therefore, a inhomogeneous monomer distribution in the polymer will be translated to an inhomogeneous distribution of the reactive crosslinking units. This might influence the crosslinking kinetics and efficiency and therefore ultimately the performance of the biomaterial ink.

Summarizing this section, unexpected reactivity trends were found for the EtOzi and MeOzi homopolymers as well as in the statistical copolymerizations of Ozi and Ox monomers. These findings question the current presumption in the oxazoline community that Ozi molecules show similar reactivity as their Ox counterparts. Further research needs to be done to shine more light into the chemistry of Ozi. These findings also suggest deviations from a perfect statistical copolymer structure, and a more block-like nature of the Ozi and Ox copolymers was postulated.

### 4.1.3 Termination

While the termination behaviour of POx has already been studied, there are no studies specifically investigating the reactivity of POzi in the context of the termination. While it is generally assumed that POzi shows similar reactivity to POx[119,120,125,126], clear deviations have been found in the polymerization behaviour. Interestingly, early into this work, hints for unexpected termination behaviour of PEtOzi were noticed. This was expressed by signals in the $^1$H-NMR spectrum of polymers which appeared after termination. These peaks could be attributed to secondary amines being present after termination with 1 M KOH in methanol. It has to be highlighted that for the termination of POx, this terminating reagent has been reported to reliably yield "OH" termini through a nucleophilic attack at the *5*-position of the active 5-membered ring.[139] The presence of secondary amines could indicate a different reactivity of the 6-membered cationic POzi ring. Secondary amines have been reported to be the result of the nucleophilic attack at the *2*-position of the propagating species (Figure 4.4). In general, end-group functionalization is of major importance for controlling the physical and chemical properties of polymers. Therefore, the work presented in the following chapter aims to investigate the termination reaction of a selection of Ox and Ozi polymers. Due to the reduced relative number of end-groups it

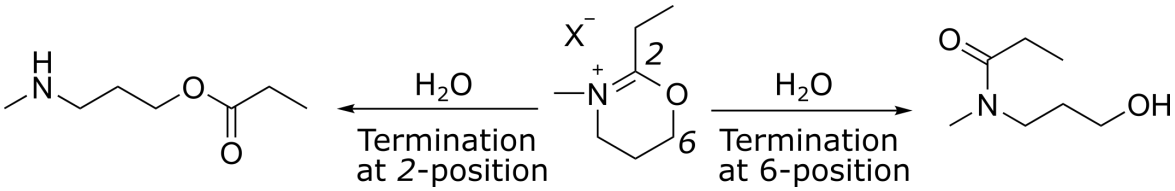


**Figure 4.4:** Schematic illustration of the reaction of a EtOzi initiator salt with water. The kinetically driven attack on *2*-position (left) leads to the formation of an amino ester compound. The thermodynamically driven reaction at *6*-position (right) results in an amide compound.

is challenging to study such a phenomenon with polymer molecules. Using the oxazinium salt as a model compound however, allows a more straight forward analysis. The reactivity of EtOzi, EtOx as well as MeOzi salts with the literature known terminating agents water, aqueous KOH and methanolic KOH was analysed, and the reactivity will be discussed in context to the literature reports. The structure of these molecules, as well as the abbreviations for the compound used in the following, are listed in Figure 4.5 a). Furthermore, the potential products of the reaction of the EtOzi salt with the used reagents are listed in Figure 4.5 b). For these products, all protons are labelled with small letters and all carbon atoms are labelled with capital letters. For this study, all reactions were performed directly inside an NMR tube. First, the respective initiator salt was dissolved in deuterated solvent, then a threefold excess of termination reagent was added. The first $^1$H-NMR spectrum was taken shortly after. However, due to handling and instrument limitations usually a

period of 5-10 min passed between addition of the reagent and the acquisition of the first spectrum. Due to this, it was not possible to resolve very fast reactions.

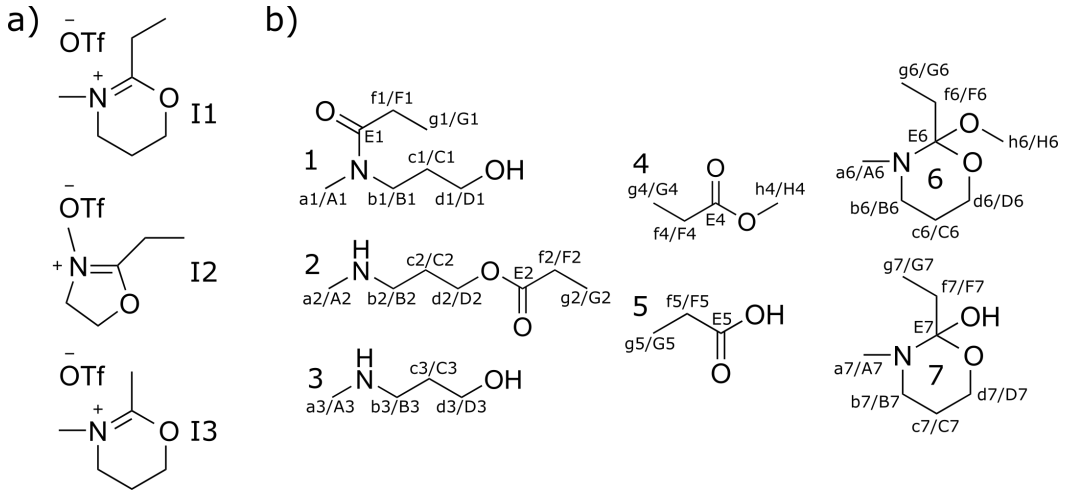


**Figure 4.5:** a) Chemical structure of the investigated oxazolinium and oxazinium initiator salts labelled **I1**, **I2** and **I3**. b) Selection of possible products formed in the reaction of **I1** with water, aqueous and methanolic KOH. In the respective products, all carbon atoms (capital letters) and hydrogen atoms (small letters) are labelled.

At first, water was used as termination reagent. Under neutral conditions, water is a weak nucleophile and according to literature reacts with oxazolinium cations preferentially at *2*-position, leading to the formation of an amino ester compound (Figure 4.4). Accordingly, the reactivity of the initiator salts against water was investigated by dissolving the respective compounds in $D_2O$. Therefore, in this experimental setup $D_2O$ served as both, NMR solvent and reactant. Under these conditions all studied salts reacted exclusively to the respective amino ester compound. As a representative example, the detailed 1D- and 2D-NMR analysis of the hydrolysis product of the salt **I1** is shown in Figure 4.6. The results of heteronuclear single-quantum correlation spectroscopy (HSQC) (Figure 4.6 a) allows correlation of all protons with the respective carbon atoms. In particular, the high chemical shift of the triplet **d2** at 4.22 ppm supports the formation of the amino ester **2**, since this is a typical chemical shift for a -$CH_2$-O group bound to an ester. Furthermore, the absence of a syn/anti split-up of the proton signal **a2** (see below) rules out the formation of the amide product **1**. Considering the vast excess of terminating reagent, the reaction proceeded surprisingly slow. For example in the case of **I1** full conversion was reached only after more than six days. Referencing the signals of the remaining initiator salt with the signals of the slowly forming ester allowed determination of the respective hydrolysis kinetics (Figure 4.6 c). This revealed that the oxazoline-based salt **I2** was much more rapidly converted than the two oxazine-based salts. This is in line with the higher

reactivity as seen previously (Section 4.1.2). Rather unexpected was the pronounced reactivity difference of **I1** and **I3**. In direct comparison, **I3** is sterically less hindered, a stronger electrophile as well as more hydrophilic (better solubilisation). All three aspects should in fact result in a faster hydrolysis reactivity. Interesting is also that the hydrolysis kinetics of the two Ozi-based initiator salts show clear deviations from a linear dependency and therefore from a first order kinetic. This result is very unexpected as the hydrolysis should be a simple two component reaction, with water being present in a vast excess. Both phenomena line up with the unexpected reactivity seen in the copolymerization of Ozi with Ox, which were already discussed within this work (see section 4.1.2). Interestingly, while the hydrolysis reaction proceeds very slow, each of the resulting esters can be rapidly transformed into the respective amide by addition of a strong base. For instance, upon addition of $NEt_3$ directly to the NMR-tube containing the amino ester **2**, quantitative and rapid (under 5 min) conversion to the amide **1** was found (Figure 4.6 d).

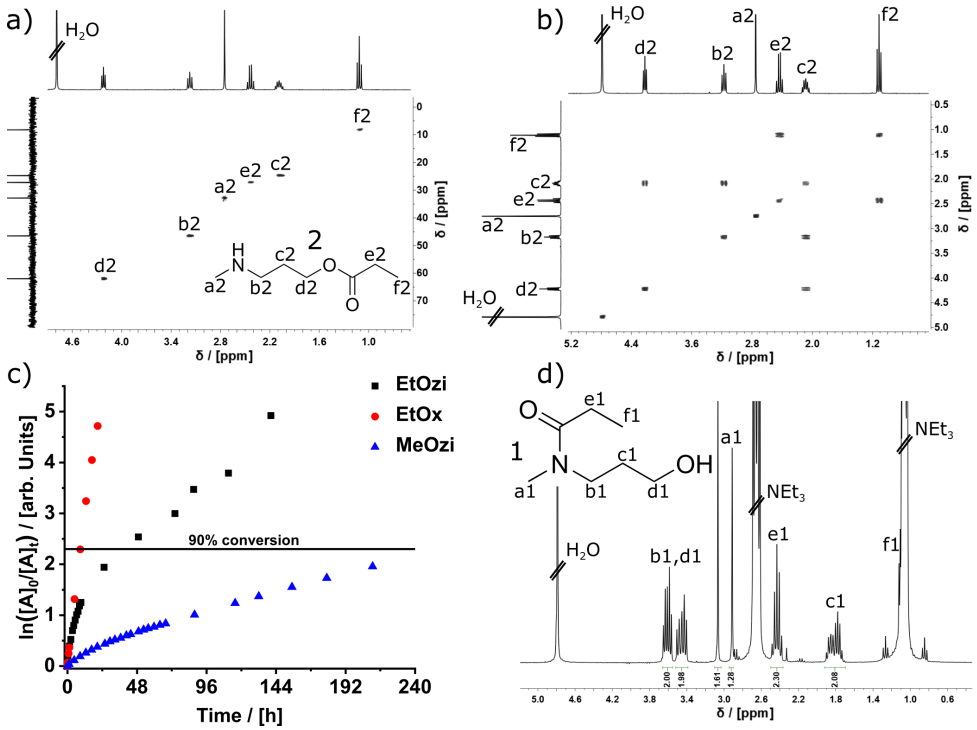


**Figure 4.6:** a) and b) HSQC- and COSY-spectrum of the initiator salt **I1** after full hydrolysis. All peaks can be assigned. The respective chemical shifts as well as the correlations derived from the COSY-spectrum support the formation of the amino ester **2**. c) Hydrolysis kinetics of the initiator salts **I1**-**I3** determined via $^1$H-NMR analysis. Plotted are the logarithmic values to verify a pseudo-first order reaction kinetic. d) $^1$H-NMR spectrum directly after addition of $NEt_3$ to the amino ester **2**. All solvent related signals are crossed out with a double line. Measurement parameters: 300 MHz, 298 K, $D_2O$.

The nucleophilicity of water is strongly increased under basic conditions and according to

literature, these conditions should result in termination at *6*-position (*5*-position for EtOx) leading to the formation of the amide product. All three salts investigated in this study reacted in accordance to this, which resulted in the rapid and quantitative formation of the respective amide. In all cases no trace of remaining initiator salt was found 5 min after addition of the 1 M aqueous KOH solution. This time, deuterated AN was used as solvent, and the termination reagent was added in a three-fold (molar) excess. Since it is most relevant for this thesis, the analysis of the reaction product of the salt **I1** is discussed in detail (Figure 4.7 a). For the analysis of this compound it is important to note that the amide bond rotation is hindered by an energy barrier. At RT, the syn and anti conformations of the compound **1** (Figure 4.7 b) and appendix Figure 8.4) can be observed by analytical methods like NMR. Protons located near this bond will give multiple signals, as both conformations have slightly different steric and electronic environments.[139] While this makes the resulting spectrum more crowded, it simultaneously simplifies the identification of the product as this syn/anti split is a strong indication for the presence of an amide bond. For the studied system, an amide bond is only formed for the product **1** (Figure 4.5 b). The syn/anti split can be observed very prominently for the N-$CH_3$ group **a1**, as this signal is split in two singlets at 2.94 ppm and 2.81 ppm respectively. The integrals of both peaks reveal roughly a 2:1 ratio of the anti and syn conformation in the product. The signals of the protons **b1** and **d1** overlap, but the correlation spectroscopy (COSY) spectrum allows clear identification of both (Figure 4.7 b). Interestingly, a much larger chemical shift difference can be found for the syn conformation. This could be due to the possibility of intramolecular H-bonding between the -OH group and the oxygen of the amide function. Furthermore, a syn/anti splitting is visible for all carbon and hydrogen atoms in the backbone, whereas the signals of the side chain are largely unaffected (Figure 4.7 c). From these results can be concluded that aqueous solutions of KOH are a reliable method for the transformation of Ozi-based initiator salts to their respective amide.

As all polymerizations in this project where conducted in BN, aqueous termination solutions have a critical disadvantage, which is the non-miscibility with BN. Upon addition of the terminating reagent to the polymer solution, a two-phase system is formed, which hinders the rapid and simultaneous termination of all polymer chains. This could potentially lead to undesired side reactions like chain transfer or irregular termination. According to literature, methanolic solutions of KOH are reported to reliably react with Ox-based polymers at *5*-position resulting in "OH" termini as well.[139] The advantage of this approach is that methanol is fully miscible with BN, which prevents phase separation upon termination. While studying the reaction of all three initiator salts with 1 M methanolic KOH it was found that the product spectra of all substances showed hints for unexpected

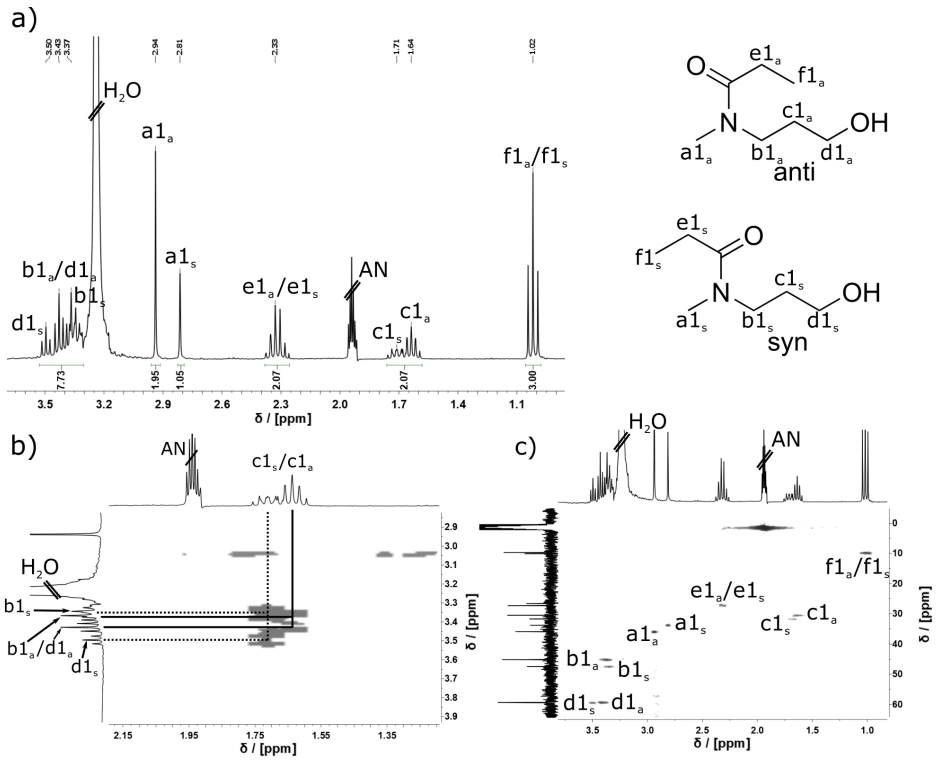


**Figure 4.7:** a) $^{1}$H-NMR, b) a section of the COSY and c) HSQC spectrum of **I1**, 5 min after addition of 1 M KOH in water. The syn and anti conformations of the resulting product are displayed on the right. All solvent related signals are crossed out with a double line. Measurement parameters: 300 MHz, 298 K, $CD_3CN$.

termination pathways and the presence of a product mixture. These deviations were more distinct for the initiator salt **I1**, than for the substances **I2** and **I3**. Since the reactivity of the salt **I1** was most relevant for this thesis, further studies were therefore focussed on the PEtOzi based initiator salt **I1**. Beside the expected amide **1** significant amounts of a second product were found (Figure 4.8 a, b). Additionally to the signals of **1**, five other peaks were observed in the $^{1}$H-NMR spectrum. Interestingly, the ratio of these two products was not constant but shifted with time to the side of the unknown product. For instance, by incubating the solution for 5 d at RT, the amount of amide decreased gradually from 85 to 50 %. Incubation of the reaction mixture over night at 50 °C had a very similar but accelerated effect. The additional peaks are an isolated triplet at 2.61 ppm **b3**, an overlaying triplet **d3** at 3.56 ppm and an overlaying multiplet **c3** at 1.63 ppm. These three proton groups show a correlation in the COSY spectrum and are therefore part of a consecutive chain of three carbons. A second isolated spin system consists only out of a singlet **a3** at 2.30 ppm. This signal overlays with the amide signal **c1**, and it can most likely be attributed to the "initiator" methyl group attached to the nitrogen atom. The last spin system consists out of a quartet at 2.05 ppm **f5** and a superimposed signal at

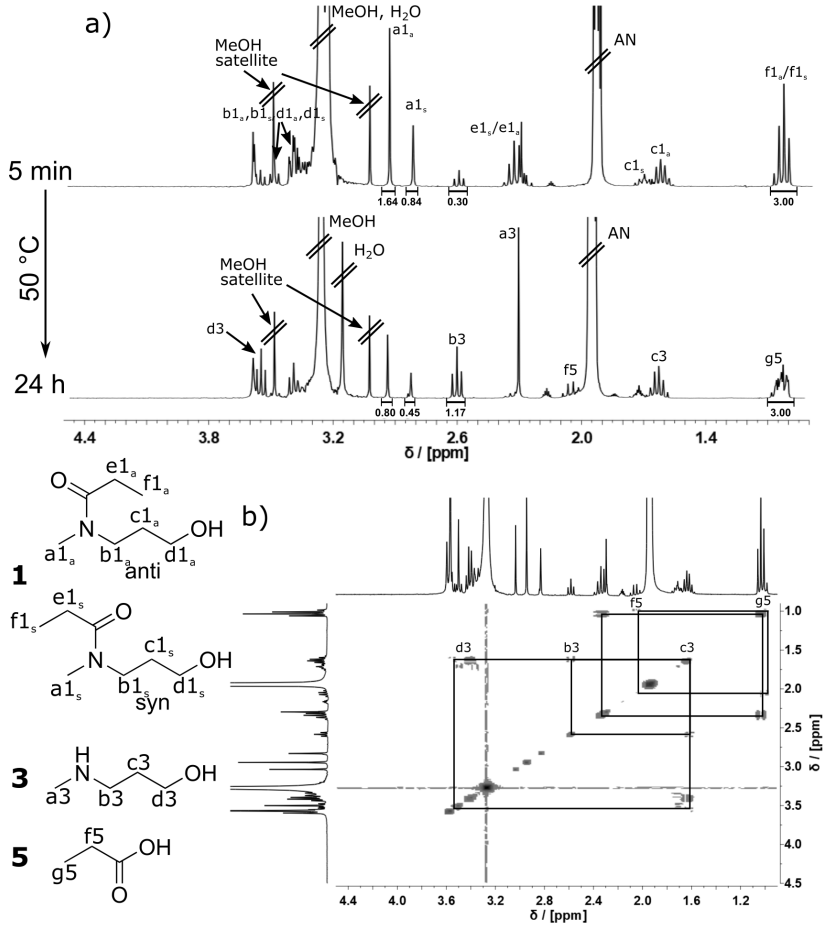


**Figure 4.8:** a) $^{1}$H-NMR spectrum of **I1** 5 min (top) after addition of 1 M KOH in MeOH and after incubation for 24 h at 50 °C (bottom). b) COSY spectrum of **I1** reacted with 1 M KOH in MeOH. Measurement parameters: 300 MHz, 298 K, $CD_3CN$.

1.01 ppm **g5**. This spin system can therefore be attributed to the ethyl chain. The absence of signals at ppm values greater than 4.0 ppm is a strong evidence for ruling out the amino ester **2** as a product. Therefore, three potential products remain, the amino-alcohol **3** with the corresponding carboxylic acid **5** and the two cyclic acetamide-acetal **6** and -hemiacetal **7** (Figure 4.5 b). Molecule **7** is not expected to be stable under the basic conditions of the reaction mixture. It should undergo ring opening, leading to the formation of the amino ester **2**. The product **6** however, due to the lack of an abstractable hydrogen, does not allow such ring opening. One factor that speaks against **6** is that no signal relating to the methoxy-group can be found in the spectrum. Due to the increased electron density at the methoxy-carbon in structure **6** compared to methanol, the signal should appear at lower ppm values than the methanol signal. Also due to the fact that this signal is a singlet, it should be just as prominent as the peak **a3**. The assumption that the product is a mixture of the amide **1** and the amino-alcohol **3** with the corresponding carboxylic acid **5** however, allows assigning of all peaks in the $^{1}$H-NMR as well as the COSY spectrum. It is there-

fore the most probable solution to this problem, yet at this point the observed dynamic within the product mixture is rather incomprehensible. There are two possible routes for the conversion of **1** to **3**: first, the simple hydrolysis of the amide bond, leading directly to the formation of **3** and **5**. However, amides are reasonably stable against hydrolysis and the cleavage of the bond should be much slower than what was observed here. This is supported by the fact that the reaction mixture containing aqueous KOH did show no signs of formation of a secondary product, even when it was heated to 50 °C for several days. The second route is a three step reaction pathway, starting with the re-cyclisation of the amide followed by ring opening at *2*-position leading to the amino ester **2**, which can then undergo hydrolysis into **3** and **5**. Despite the fact that an ester bond is much more susceptible to hydrolysis and can easily react to the amino alcohol, it is surprising that **3** was not found at any point in the experiments.

All in all, at the time these experiments were conducted, the amino alcohol was assumed to be the most probable product. It also needs to be highlighted that the conversion of **I1** with 1 M KOH in MeOH was repeated three times, and all experiments did show a comparable behaviour. A very important missing puzzle piece to possibly solve this matter would be an heteronuclear multiple-bond correlation spectroscopy (HMBC) spectrum. A strong correlation should be visible for the quaternary carbon **E6** with the protons **a6**, **b6**, **d6** and **f6**. Unfortunately the measured spectrum from the experiments presented above were all of poor quality and no information could be extracted from them. Striking is that when the attempt was made to reproduce the results about six months later and to analyse the matter in more detail, very different results were received. Above all, when seemingly nothing was changed in the termination procedure always one of these two different results was received, yet none of these matched the findings discussed above. This was a strong hint that the reaction of **I1** with 1 M KOH in MeOH is much more complex than expected previously. Such a behaviour also allows the hypothesis that the reaction is very sensitive towards its starting conditions. Therefore, in the next set of experiments special precautions were taken to ensure minimal variance between each experiment. To guarantee full control over the temperature at which the reaction proceeded, all reagents and the reaction vessel (NMR tube) were tempered in a water bath. A stock solution of the salt **I1** was prepared in anhydrous deuterated AN and the reagents were mixed in the reaction vessel using a micro-pipette preventing variations of the reagent concentration. Furthermore, two independently prepared batches of the termination reagent were used to investigate if slight changes in the KOH concentration would influence the reaction result. As the position for the attacking nucleophile onto the oxazinium ring is governed by thermodynamics, the reaction temperature should play a major role. Slight variations in the RT could be the

reason for the different reactivity observed in the reproduction of the experiments. The experiment was therefore split in two groups, each consisting out of 6 experiments, where the reaction was performed at 20 and 30 °C respectively. At each temperature three reactions per batch of terminating reagent were performed. This experimental setup revealed no significant differences within the two temperature groups, but major differences were observed between the 20 and 30 °C group (Figure 4.9 a, b). Considering the discussions above, the main product of the 30 °C group is easily identified by the $^1$H-NMR spectrum as the amide compound **1**. Additionally, traces (less than 10 % for all 6 experiments) of the amino alcohol **3** can be made out by the isolated triplet at 2.61 ppm (protons **b3**). The product composition 5 min after termination matches very well with the observations made in the first round of experiments with 1 M KOH in MeOH (Figure 4.8 a, top). Contradictory is that the product composition in this set of experiments was static, and no changes could be observed with time. When the reaction was performed at 20 °C, $^1$H-NMR analysis

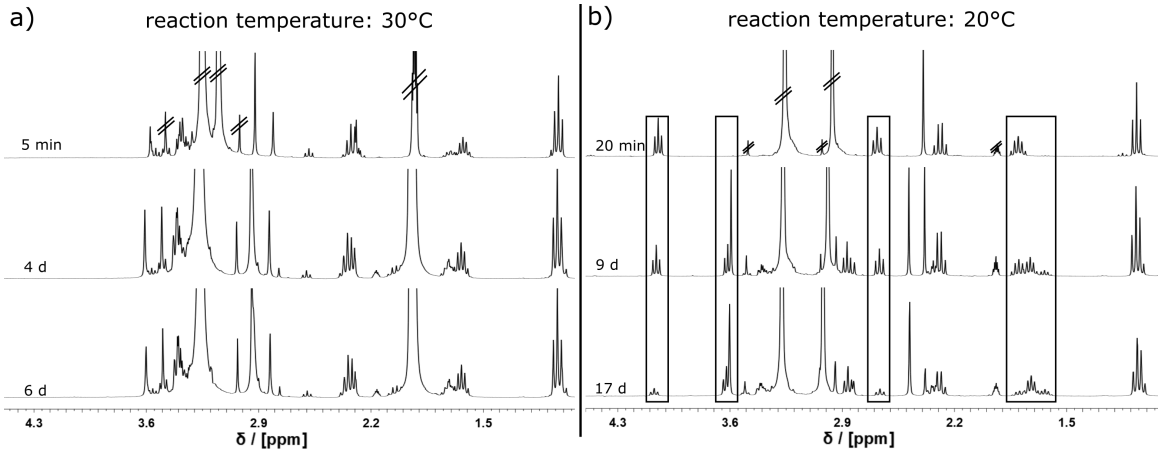


**Figure 4.9:** a) $^1$H-NMR spectrum of **I1** 5 min, 4 d and 6 d after addition of 1 M KOH in MeOH at 30 °C. b) $^1$H-NMR of **I1** 20 min, 9 d and 17 d after addition of 1 M KOH in MeOH at 20 °C. The most notable changes in the spectra are highlighted with black squares. Measurement parameters: 300 MHz, 298 K, $CD_3CN$.

revealed rapid conversion of the oxazinium salt, leading to one single product (Figure 4.9 b). Interestingly, this product was not stable under the basic conditions in the reaction mixture but slowly converted to a second product. Both products can be identified from the mixture by using 2D-NMR spectroscopy (Figure 4.10 a). Several indications suggest that the first product must be the amino ester **2**. For example, no signs of syn/anti splitting can be observed, which rules out the amide product **1**. Also an isolated triplet at 4.07 ppm was found, which can originate from the -$CH_2$-O group **d2** bound to the ester oxygen. Furthermore, the signal **d2** correlates with a low field shifted carbonyl carbon **E2** at 175.50 ppm (Figure 4.10 c). **E2** itself correlates in addition only with the -$CH_2$ and -$CH_3$ groups **f2** and **g2**. This rules out the cyclic products **6** and **7**. Finally, **d2** gives cross correlations with

the carbons **C2** and **B2** as well as **b2** correlating with **C2**, **D2** and the $CH_3$ carbon **A2** (Figure 4.10 c). In sum, all these aspects are only valid for the amino ester product **2**. For the second product a triplet **b3** appears at 2.88 ppm, and in the HMBC spectrum these protons correlate with the $CH_2$ carbons **C3**, **D3** as well as the $CH_3$ carbon **A3**. Contrary to the first product, the protons **d3** correlate only with the carbons **B3** and **C3** (Figure 4.9 c). No interaction was found with one of the low field shifted carbons in the ppm range above 116 ppm (Figure 4.9 b, inset). These findings are strong evidence that the second product is the amine **3**. Furthermore, significant amounts of methyl propionate are formed over the incubation period. This compound can be identified by the prominent -$CH_3$ singlet **h4** at 3.6 ppm, which correlates with the low field shifted carbon **E4** (Figure 4.9 a, b). **E4** itself additionally shows correlation with the protons **f4** and **g4**. This indicates that the ester **2** is slowly cleaved by a transesterification reaction with MeOH under the formation of the amino alcohol as well as methyl propionate. Additionally, traces of the amide **1** can be identified by the singlet peaks **a1** as a minor third product. Also the signals relating to **b1** and **b3** can be observed at the flank of the large methanol peak (Figure 4.9 b).

Two things remain conspicuous: first, the amino alcohol has also been identified as a product in other reaction mixtures. However, the protons **a3** and **b3** show significantly different chemical shifts between these experiments (2.49 and 2.88 ppm vs. 2.30 and 2.60 ppm). A possible explanation for this might be differences in the composition of these reaction mixtures and the availability of different H-bond partners. As both groups are directly bound to a secondary amine, the state of protonation as well as the presence of hydrogen-bonds can influence the chemical shift of neighbouring groups significantly. Second, two peaks appear in the $^{13}C$-NMR spectrum at 124.07 and 119.83 ppm (Figure 4.10 b). This is the ppm range, where the quaternary carbons **E6** and **E7** of the products **6** and **7** would be expected. However, these signals show no correlation with any protons of in the reaction mixture, nor do they change in intensity over the time scope of the experiment. This makes it unlikely that these peaks originate from a product in the reaction mixture and their origin is unknown.

This study highlights that the temperature at which the "termination" is performed has a very strong influence on the resulting product and therefore on the polymer end-group. Hints for unexpected reactivity of **I1** were also found for amine and carboxylic acid termination reagents. Considering the sensitivity of the reaction of **I1** with 1 M KOH in MeOH, a more detailed investigation of this matter would go well beyond the scope of this thesis. In this aspect it is also important to mention that although the preliminary studies of the reactivity of the initiator salts **I2** and **I3** with 1 M KOH in MeOH also resulted in reaction

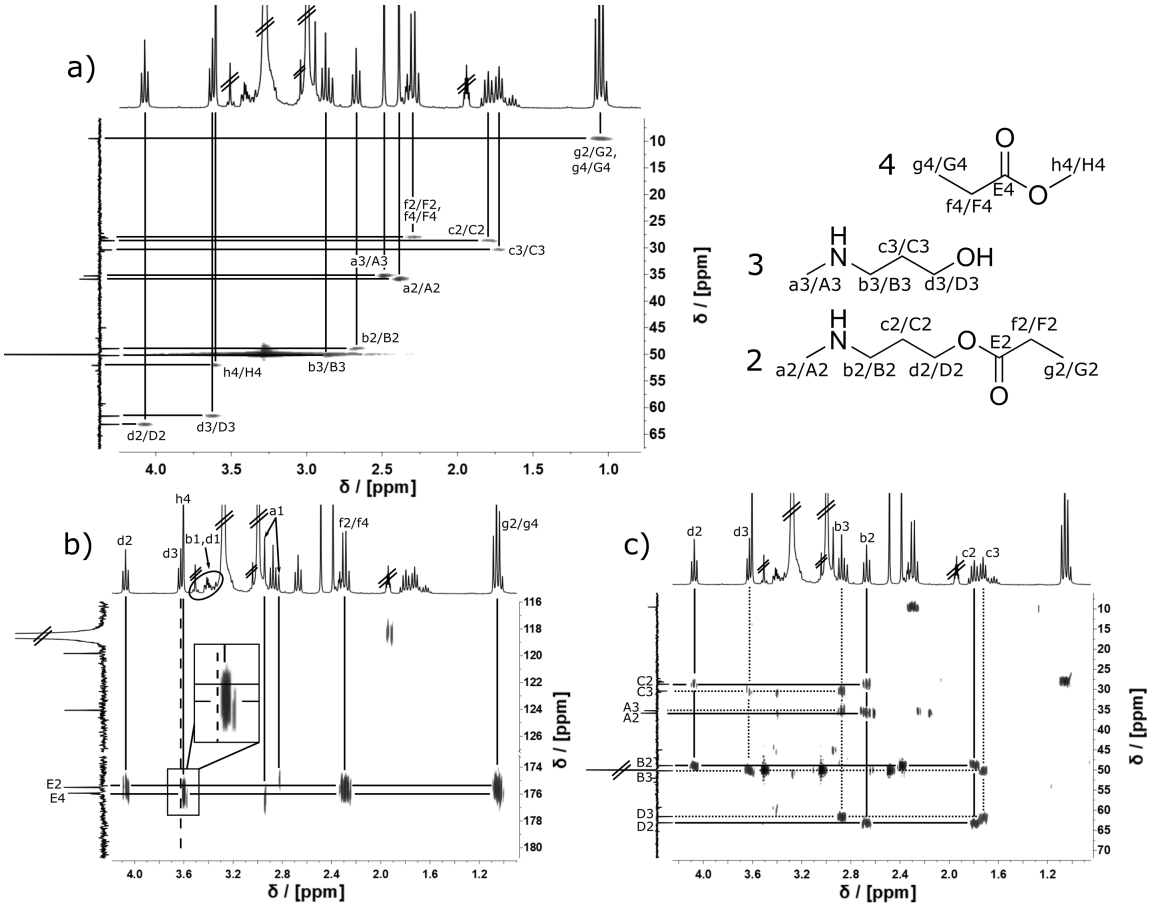


**Figure 4.10:** a), b) Sections of the HSQC spectrum of **I1** 4 d after addition of 1 M KOH in MeOH. Solid lines indicate existing correlations and the dashed line indicates a missing correlation. The chemical structures of the two main products are displayed on the left. All hydrogen and carbon atoms are labelled. b) For better visualization the important section, which shows the missing correlation of **d3** with **E2** and **E3**, is magnified in the inset. c) HMBC spectrum of **I1** 4 d after addition of 1 M KOH in MeOH. Solid lines indicate correlations of the product **2** and the dotted lines indicate correlations of the product **3**. All solvent related signals are crossed out with a double line. Measurement parameters: 300 MHz, 298 K, $CD_3CN$.

mixtures, similar issues with the reproducibility were found as with the initiator salt **I1**. Therefore, at this point it is unclear whether the above presented temperature dependency is limited to the EtOzi derived initiator salt **I1** or not. Further studies with the other initiator salts need to be conducted to elaborate on this question. In addition, the reader has to be aware that the initiator salts, as model components, do not fully reflect the situation during the termination of an active polymer end-group. Effects like end-group availability due to coiling or steric hindrance are not represented. In the case of Ox and Ozi also an intra-molecular polarization effect by neighbouring groups has been reported.[119] This is due to the formation of a six-membered (oxazoline) and seven-membered (oxazine) ring, where the carbonyl oxygen of the last repeating unit coordinates to the nitrogen of the cationic propagating end-group. This phenomenon can have a significant influence on

the electron density of the active chain end and therefore on its reactivity. It might be important to study the termination with either short polymers or at least a dimer. As a downside, this will make the analysis of the product mixtures considerably more difficult. While short polymers are accessible via standard LCROP, this method is due to the statistical nature of the reaction unsuited for the synthesis of defined dimers. As an alternative, the dimer might be accessible by conversion of the amide **1** with triflic anhydride resulting in the triflic acid derivative of **1**. This molecule could then be used for the synthesis of an oxazininum salt with one repeating unit attached to the nitrogen.

An important implication from the results presented above is that the end-group functionalization of the polymers, used in this thesis, might be compromised. Therefore, a significant ratio of the final repeating units might not be the desired amide function but an amino alcohol or an amino ester group. As a consequence, the polymer can contain secondary amines. This is of special importance as secondary amines will be used in the following for the polymer analogue modification with reactive chemical moieties allowing chemical crosslinking. In order to investigate this, a short PEtOzi polymer with 20 repeating units (**P6**) was synthesized and terminated with 1 M KOH in MeOH. The product was analysed using ninhydrin test, $^{1}$H-NMR analysis as well as acid-base titration (Figure 4.11). The ninhydrin test (or Kaiser test) allows the detection of primary (purple colour)

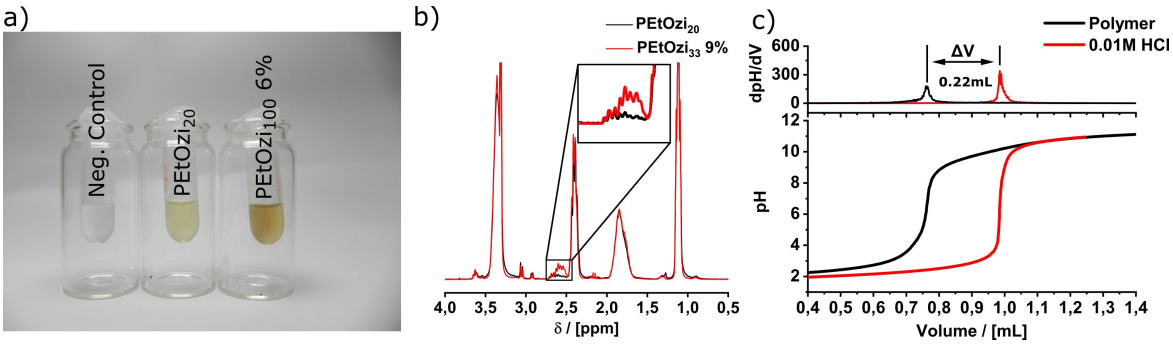


**Figure 4.11:** a) Ninhydrin test of the polymer **P6** (middle, PEtOzi$_{20}$), which was terminated with methanolic KOH. Water (left) served as negative control. A 6 % hydrolysed PEtOzi$_{100}$ (right, **P8**) served as positive control. b) $^{1}$H-NMR spectrum (300 MHz, 298 K, MeOD) of **P6** and **P7**. The peaks corresponding to the -$CH_2$ groups near the secondary amine are highlighted. c) Titration of **P6** compared to a 0.01 M HCl solution as reference. The $1^{st}$ deviation of both traces (top) visualizes the volume difference of the equivalence point caused by the amines in the backbone of **P6**.

and secondary amines (yellow/brown colour) by a colour change of the reaction mixture. For better visualization of the result, water served as negative control and the hydrolysed PEtOzi polymer **P7** (containing secondary amines, see section 4.2.1) as positive control. Even though, the **P8** positive control gave a much more pronounced colour change, **P6**

still resulted in visible colouring when being compared to the negative control (Figure 4.11 a). In addition, a broad peak between 2.73 ppm and 2.50 ppm was visible in the $^{1}$H-NMR spectrum of **P6**. This peak matches very well with the position and appearance of the signal relating to the -$CH_2$ group next to the amine in the partially hydrolysed polymer **P7** (Figure 4.11 b). Further evidence is given by acid-base titration (for details see section 4.2.1). The equivalence point for the sample containing 20 mg/ml of **P6** is significantly shifted to smaller volumes compared to the reverence. The volume difference allows the calculation of the amine concentration in the solution. This gives roughly 0.51 amines per polymer chain or a hydrolysis degree of 2.6 %. All in all strong evidence for the presence of secondary amines in the polymer sample **P6** were found. This must be attributed to a compromised end-group functionalization. It is important to point out that for all of the major polymer batches synthesized in this thesis, titration indicated the presence of amines (Table 4.3). In the following part of the thesis, this will be referred to as zero hydrolysis degree ($HD_0$). This finding is of importance as the hydrolysis degree will determine the DF and therefore govern the properties of the DA-based biomaterial ink. Further discussions can be found in section 4.2.1. Interestingly, the percentage of the alkanolamine end-groups varies on a wide range between 29 and 64 %, which could be attributed to temperature differences during the termination of those polymers (Table 4.3). Since the temperature sensitivity was not investigated by the time these polymers were synthesised, little focus was set on the termination temperature. Summing up this section, the reactivity of three

**Table 4.3:** Amine content in selected polymer batches determined via acid-base titration.

| ID | PC,theo | $HD_0$ [a] | Percent of end-group [b] |
|---|---|---|---|
| **P6** | $PEtOzi_{20}$ | 2.6 | 52 |
| **P9** | $PEtOzi_{100}$ | 0.29 | 29 |
| **P10** | $PEtOzi_{200}$ | 0.17 | 34 |
| **P11** | $P(EtOzi_{75}$-co-$EtOx_{25})$ | 0.64 | 64 |
| **P12** | $P(EtOzi_{75}$-co-$MeOx_{25})$ | 0.54 | 54 |

Determined by: [a] acid-base titration in [%]

Calculated as: [b] chain length$\times HD_0$ in [%]

initiator salts against commonly used reagents for the termination of POx- and POzi-based polymers was investigated. Using water under neutral conditions led to the formation of the ester product for all three salts. However, an unexpected reactivity difference was found, as the methyl-oxazinium salt reacted much slower than the ethyl-oxazinium salt. Furthermore, the reaction did not follow a pseudo-first order kinetic. Upon conversion with aqueous KOH, all three initiator salts reacted rapidly to their corresponding amide. In contrast, the reaction of the ethyl-oxazinium salt with methanolic KOH led to unexpected

and inconsistent results. It was shown that the product formation is very sensitive towards the starting conditions, especially the temperature. While at 30 °C the amid **1** is the main product and only traces of side products are formed. At 20 °C, the ester **2** is formed quantitatively. However with time, the ester is converted via transesterification to the amino alcohol **3**. Under these conditions, the amid **1** is only formed in small traces. To the best of my knowledge there are no reports in literature stating such a sensitivity to minor changes in the starting conditions for the termination of PEtOzi. Similar to the results seen for the polymerization kinetics discussed in section 4.1.2, the reactivity of oxazines with common terminating reagents also deviates from the results reported for oxazolines in literature. The end-group functionality is crucial for the control over the polymer properties. Therefore it is important for the Ox and Ozi community that this matter is investigated in more detail. Other reagents as well as a larger range of oxazinium and oxazolinium salts have to be investigated to gain a comprehensive understanding of the underlying mechanisms.

### 4.1.4 Melt Electrowriting of Poly(2-oxazoline) and Poly(2-oxazine)

As outlined above, the statistical copolymerization of EtOzi and EtOx allows the preparation of copolymers with defined molar mass distribution. The $T_g$ depends linear on the weight ratio of EtOzi/EtOx, and it was possible to synthesize polymers with a $T_g$ ranging from 25 to 61 °C. In the following section EtOzi and EtOx homo- and copolymers were assessed on their processability with MEW. In this context, the influence of the $T_g$ on the processability, the processing parameters as well as the morphology of the printed constructs will be of special interest. The aim of this was to identify the most promising polymer base for the $1^{st}$ generation of the DA-based biomaterial ink.

To evaluate the processability of each polymer, the materials were loaded into the printer head and the needle temperature (NT) and syringe temperature (ST) were gradually increased while the other printing parameters, pressure ($p$), voltage ($V$) and CS were kept at base values of 1.5 bar, 3 kV and 1000 mm/min. Once a stable polymer jet was established, the printing was optimized at constant NT and ST by tuning $p$, $V$ and CS. Using this procedure, parameter sets for the processing of all five polymers were found (Table 4.4). All printed constructs displayed in this thesis are labelled by a scaffold identification number (SID), and their respective MEW parameters are summarized in section 7.3. To

**Table 4.4:** MEW processing parameters for EtOzi and EtOx homo- and copolymers.

| **PC,theo** | ID | SID | NT[a] | ST[a] | p[b] | V[c] | CS[d] |
|---|---|---|---|---|---|---|---|
| $PEtOzi_{100}$ | **P1** | S22 | 120 | 100 | 1.5 | 3.2 | 1080 |
| $P(EtOzi_{75}$-co-$EtOx_{25})$ | **P4** | S23 | 130 | 110 | 1.6 | 3.6 | 1000 |
| $P(EtOzi_{50}$-co-$EtOx_{50})$ | **P3** | S24 | 140 | 120 | 1.25 | 3.5 | 1700 |
| $P(EtOzi_{25}$-co-$EtOx_{75})$ | **P2** | S25 | 160 | 140 | 1.25 | 3.1 | 1100 |
| $PEtOx_{100}$ | **P5** | S28 | 170 | 155 | 1.0 | 4.5 | 1500 |

Parameters in: [a] [°C]; [b] in [bar]; [c] in [kV]; [d] in [mm/min]

showcase the printability, box-like scaffolds with a fibre distance (FD) of 500 $\mu$m, a printing angle ($\alpha$) of 90° and at least 10 layers were printed (Figure 4.12 a). Due to the increased $T_g$ it was necessary to adjust the NT and ST from the moderate temperatures (120 and 100 °C) used for the PEtOzi homopolymer **P1** to higher temperatures (170 and 155 °C) used for the PEtOx homopolymer **P5**. To put this into perspective, PCL, the currently most used polymer for MEW, is usually processed around 80 °C.[51,62] Also, high molar mass PEtOx has been printed at very high temperatures of above 200 °C.[48] It has to be noted that this is the first report about the processing of Ozi-based homo- and copolymers

with MEW. A direct influence of the $T_g$ on both, the fibre morphology as well as the accuracy of fibre placement, was observed. While for **P1** fibres were placed accurately, the stacked fibres merged into a continuous polymer wall shortly after printing (Figure 4.12 b). This is caused by a low polymer $T_g$ around RT, allowing polymer flow post processing. Fibre placement was also accurate for the polymers **P4** and **P3**, yet for both the fibre morphology was retained after printing. When these structures were left at RT over night, the fibres lost their morphology and also merged. The hydrophilic nature of the polymers allows them to absorb moisture from the environment. Moisture acts as a plasticizer and lowers the $T_g$ of the polymer and facilitates material flow. In this context, the 50/50 copolymer **P3** was outstanding. This polymer showed remarkable accurate fibre placement capabilities up to 20 layers, while also maintaining fibre morphology for several hours. Increasing the EtOx content further, however drastically decreased fibre placement capabilities (Figure 4.12 d). This was caused by a rapid cooling of the polymer jet due to the large temperature difference between the collector temperature and the NT in combination with the high polymer $T_g$. Theses fibres solidify before touching the collector plate, leading to a "fall over" effect rather than a controlled deposition (Figure 4.12 e).

The fibres produced from the polymers with a high $T_g$ were also very brittle and sometimes even broke during deposition (Figure 4.12 g). This effect of too rapid solidification could be countered by heating of the collector plate. The influence of a heated collector on the processing of **P2** is shown in Figure 4.12 h), i). While at a collector plate temperature of 50 °C, solidification of the jet still hindered the printing process, at a collector plate temperature of 70 °C highly accurate placing was achieved. However, the increased collector temperature had a negative effect on the fibre shape fidelity. This is particularly noticeable for the 70 °C sample, where pronounced fibre fusing occurred. Interestingly, no major changes to the printing parameter had to be made for the printing on a hot surface (Table 7.12) and the printability improvements can be mainly attributed to the slower cooling of the jet. Figure 4.13 summarizes the relation of the polymer properties and the MEW processing. It is important to note that the polymer chain length was kept constant at 100 units for this comparative study. Also, the molar mass difference between the EtOzi (113 g/mol) and EtOx monomer (99 g/mol) is small. This means that the molar mass of the polymers ranges only from PEtOx (9938 g/mol) as the minimum value to PEtOzi (11350 g/mol) as the maximum value. Therefore, no major physico-chemical differences related to molar mass like chain entanglement are to be expected. Therefore, the $T_g$ should be the dominating factor determining the MEW processing temperature. As discussed in section 4.1.1, the $T_g$ of EtOzi and EtOx copolymers follows the Fox equation (Figure 4.2 b). In accordance with this, a similar linear trend of the NT was observed for the MEW

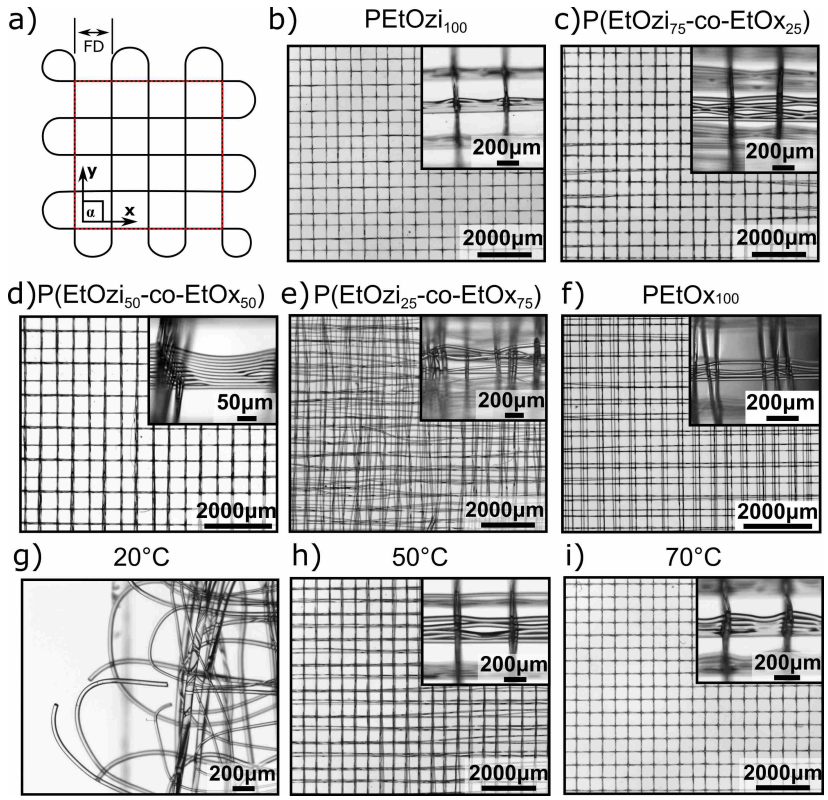


**Figure 4.12:** a) Schematic illustration of the MEW printing pattern used for the preparation of box-like architectures. Important attributes like scaffold size, printing angle ($\alpha$) and FD are visualized. b)- f) Representative MEW printed structures from the polymers **P1** (S22), **P4** (S23), **P3** (S24), **P2** (S25) and **P5** (S28). Inset pictures are taken under a tilted angle to visualize the fibre morphology. g) Fibres breaking during the deposition due to brittleness of the polymer. h), i) Structures printed using a heated collector plate at 50 (S26) and 70 °C (S27) respectively.

processing temperature of the PEtOx and PEtOzi homo- and copolymers (Figure 4.13 a). Very interesting is that plotting the NT against the $T_g$ reveals a linear dependency of both parameters (Figure 4.13 b). This shows very clearly the direct influence of the polymer $T_g$ on the MEW processing temperature. It also is a simple method for estimating the processing temperature of PEtOx- and PEtOzi-based copolymers based on the chemical composition. The shear viscosity of the homo- and copolymers was measured at the processing temperature via melt rheology. This revealed that the viscosity for all polymers ranged between 70 and 130 Pa$*$s. Considering that the processing temperature was determined empirically, this variance is surprisingly small. While currently little is known about the relationship of the polymer properties and the MEW processing parameters, this data suggests that stable MEW processing of POx and POzi polymers is possible, if the material has a shear viscosity of roughly 100 Pa$*$s at the printing temperature. For MEW processing, the CTS can be used as a sensitive measure to describe the processing of a polymer. Printing above this critical value, results in the deposition of a straight fibre.

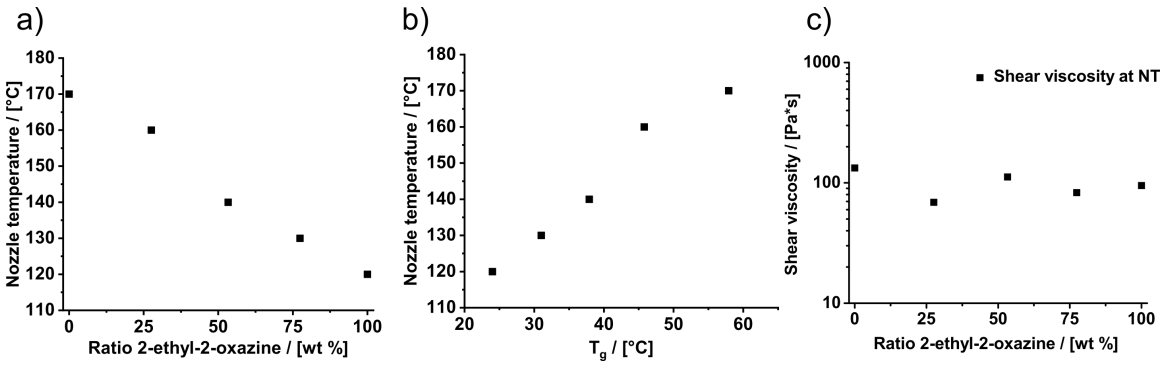


**Figure 4.13:** a) MEW processing temperature (NT) allowing stable processing of the polymers **P1**, **2**, **3**, **4**, **5**. b) MEW NT correlated to the $T_g$ of the respective P(EtOx-co-EtOzi) copolymer. c) Shear viscosity at a shear rate of $1\,1/s$ determined by rheology at the respective NT used for processing of the P(EtOx-co-EtOzi) copolymer.

Below the CTS, the deposited fibre is not straight but shows a loop or sinusoidal like pattern.[46,50] For polymers like PCL, the transition from loops to sinusoidals to straight fibres is smooth and usually takes place over a narrow CS range of 100-200 mm/min. The CTS is also a very sensitive measure to visualize changes of the material during the printing process. This could be thermal degradation over time or inhomogeneity within the material. To further investigate the processability of the P(EtOx-co-EtOzi) copolymers, CTS studies were performed. Therefore, a printing pattern consisting out of sets of four lines at the same CS, with an incremental increase of the CS between each set, was printed. This gave a set of 18 lines, produced at different CS, allowing to screen the printing behaviour over a wide range of CS (see Figure 4.14 a).

This revealed large fluctuations of the CTS over a wide range of CS for all polymers. As an example one CTS experiment with **P4** is shown in Figure 4.14 b). Within the CS range of 150 to 400 mm/min, the transition from an irregular fibre pattern consisting of loops and sinusoids to straight fibres takes place. Normally for higher CS only straight fibres are expected. However, a fall-back into sinusoids can be seen for a CS of 500 and 550 mm/min. A higher CS again produces straight lines, with an exception at the set at 950 mm/min. Moreover, the example shown in Figure 4.14 b) is not even very representative, as over a prolonged continuous printing experiment a wide variety of CTS progressions were observed. This also includes the extreme cases, were over the range of 150 to 1000 mm/min only straight fibres as well as no straight fibres at all could be produced (Figure 8.5). This inconsistent behaviour is also recognizable in Figure 4.14 c). In this graph the CTS resulting from a series of CTS prints, performed over a prolonged experiment, are plotted against time. For this experiment the CTS was determined as the first set, where all four fibres were straight and no major fall-backs occurred. Using this method the example shown in

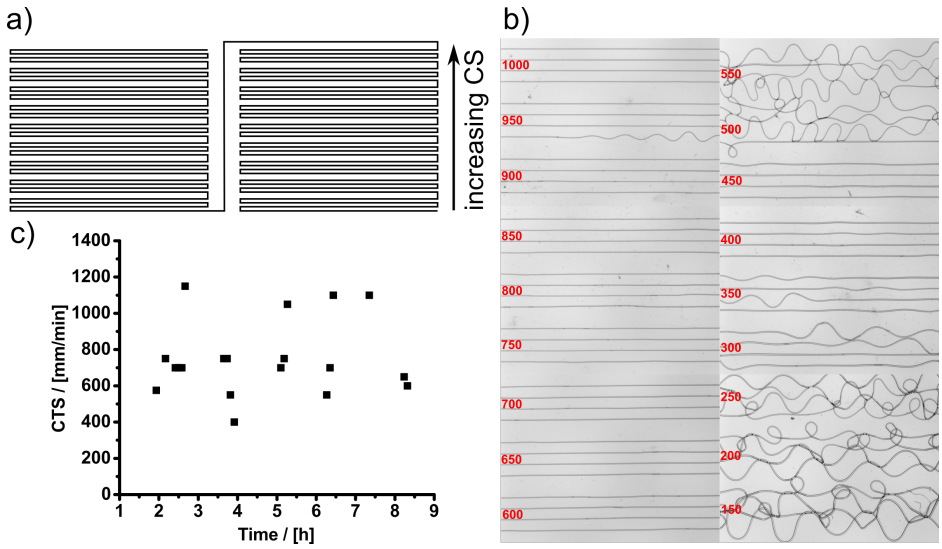


**Figure 4.14:** a) Schematic illustration of the printing pattern used to determine the CTS. b) Stereomicroscope images of a CTS experiment with **P4** using the MEW parameters: $p$ 1.4 bar; $V$ 3.5 kV; collector distance ($d$) 3.3 mm; NT 130 °C; ST 110 °C; collector temperature 40 °C. c) CTS development of **P4** over 9 h of continuous heating.

Figure 4.14 resulted in a CTS of 600 mm/min. This prolonged experiment revealed a wide range of CTS ranging from 400 to 1150 mm/min with no visible trend over the whole time period. It is important to note that the printing parameters like $V$, NT and ST were kept constant throughout the whole experiment. The velocity of the polymer jet produced during MEW depends upon several factors. These are among others, molar mass and related to this the melt viscosity, charge density in the material and impurities or inhomogeneities of the sample. Since no trend of the CTS was observed, it is likely that these fluctuations are not caused by thermal degradation of the polymer sample. This can be explained by the high degradation temperature of 356 °C, which is much higher than the used processing temperature. However, Hochleitner *et al.* reported about thermal degradation during the prolonged processing of high molar mass PEtOx even when the processing temperature was far below the degradation temperature of the polymer.[48] Such sudden changes in the jet velocity are more likely to be caused by fluctuations of the extruded material itself. It is unlikely that the samples still contain low molar mass impurities, as all polymers have been purified carefully by precipitation as well as dialysis. As it was discussed in the section before, the end-group functionalization of the polymers is compromised and the samples contain a mixture of molecules with amide or with amine end-groups. Since the workup procedure was performed in MilliQ water (neutral to slightly acidic conditions), some of these amines could be protonated and therefore charged. Such charged molecules can have a drastic influence on the MEW process. However, this can only explain the observed fluctuations, if there would be a non equal distribution of these polymer species within a

sample. As the samples where collected via lyophilisation of homogeneous aqueous solutions, such material gradients are not to be expected. In this context it is important to state that when the printing was performed with a CS above the range of the jet velocity fluctuation, it was still possible to print periodic patterns as they are shown in Figure 4.12.

Summarizing this section, it was shown that low molar mass PEtOx, PEtOzi as well as their copolymers can be processed via MEW into box-like structures. While fluctuations of the CTS were observed, these could be compensated by printing at a CS above the fluctuation range. A strong influence of the $T_g$ on the processing parameters was found. For instance a processing temperature corresponding to a shear viscosity of around 100 Pa$*$s has proven to allow processing for all polymers. It should be highlighted that the POzi/POx polymer system offers the straight forward option for tuning the $T_g$, while minimizing changes in physico-chemical properties like polarizability, thermal stability, chemical reactivity or dispersity. This makes the system an interesting candidate for an in depth study on how the polymer properties influence the MEW processing. Also, the large library of Ox and Ozi monomers reported in literature allows the tuning of the polymer properties on an even larger scale than what was discussed above.[266] With a NT of 120 °C, the PEtOzi homopolymer could be processed at the lowest printing temperature of all polymers. However, the printed fibres fused immediately after printing, which indicated polymer flow. This property is undesirable since it causes the loss of the printed microstructure. Besides, it can be expected that the polymer flow is drastically reduced by the addition of the DA functions. Since thermal degradation is expected to be a major challenge for the processing of the DA-based material, the purely EtOzi-based polymer was chosen for the synthesis of the $1^{st}$ generation of the biomaterial ink.

# 4.2 Microperiodic Hydrogel Constructs

## 4.2.1 Polymer Synthesis and Hydrolysis

In the previous chapter fundamental understanding of the polymerization, the termination as well as the physical properties of Ox and Ozi polymers was developed. Furthermore, the general MEW processability of several EtOx and EtOzi homo- and copolymers was established. Crucial for the fabrication of microstructured hydrogel scaffolds via MEW is the crosslinking of the polymer chains post printing. POx/POzi-based polymers generally do not allow crosslinking per se and the addition of functional groups is required. An exception to this are physically crosslinkable polymers like reported by Lorson and coworkers. [108]
This project aims to establish a biomaterial ink, allowing the spontaneous crosslinking of the polymer fibres post melt processing, using the DA chemistry. For this the very efficient DA pair of furan and maleimide was utilized. It is important to note that furan and maleimide are generally susceptible to a wide range of reactions. [206] Therefore, thermally induced side reactions can not be ruled out and might pose a major challenge in this work. The synthesis of monomer molecules with furan and maleimide side chains is rather challenging, especially with respect to the production of large quantities. Polymer-analogue modification however can be performed under very mild conditions and allows a wide range of functionalization degrees. Furthermore this technique was also already successfully established for POx homopolymers by Chujo *et al.* using the furan and maleimide pair. [200] Therefore, polymer analogue functionalization was identified as a promising synthesis route. Using the example of a PEtOzi homopolymer, the synthesis strategy for the DA biomaterial

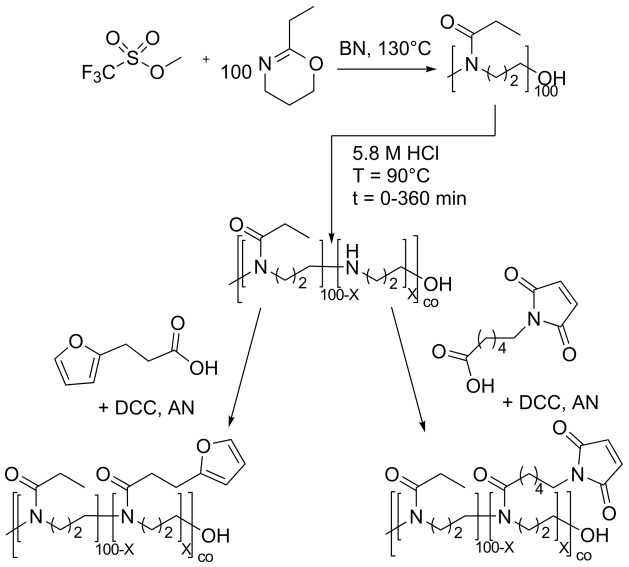


**Figure 4.15:** Schematic illustration of the synthesis path for the preparation of maleimide and furan functionalized poly(2-ethyl-2-oxazine).

ink is summarized in Figure 4.15. The polymers were synthesized by LCROP, using MeOTf as initiator. The following polymerization was carried out at 130°C in BN. As termination reagent a solution of KOH in methanol was used. After removal of the solvent and workup by dialysis, the recovered polymer was partially saponified using 5.8 mol/L HCl. Next, purification by dialysis was performed again to remove the vast excess of salts remaining from the hydrolysis step. Finally, DCC supported coupling of carboxylic acid derivatives of furan and maleimide gave the two components of the DA biomaterial ink. This reaction scheme (Figure 4.15) serves merely a guideline for the synthesis of all polymers discussed in the upcoming chapter. The synthesis and polymer structure was continuously altered with the aim of improving the processability by MEW. These changes will be discussed separately in the respective sections. Since the partial saponification step remained almost unchanged throughout the course of the work, it will be discussed in the following as a standalone chapter.

### Partial Hydrolysis

The partial hydrolysis of POx and POzi is an important part of the work presented in this thesis. Via hydrolysis it is possible to cleave the amide bonds in the polymer side chain, and introduce secondary amines to the polymer backbone. All hydrolysis reactions were performed using half concentrated HCl (5.8 mol/L) and a polymer concentration corresponding to a total amide concentration of 0.48 mol/L. Using similar conditions other research groups already successfully reported the (partial) hydrolysis of various oxazoline-based polymers.[180,184] Deviating from theses reports, the hydrolysis in this work was performed in round-bottom flasks heated by an oil bath. Compared to the literature reported microwave supported heating, this enabled the simple synthesis of larger quantities of hydrolysed polymers, and simultaneously the reaction speed was also reduced. In particular, for the synthesis of the polymers with very low hydrolysis degrees, a slower reaction speed was quite advantageous as it allowed a more precise adjustment of the reaction progress. The desired hydrolysis degree was adjusted by controlling the reaction duration. This required precise knowledge about the hydrolysis kinetics of every polymer investigated in the scope of this project. Therefore, in the following section the effect of the temperature, the chain length as well as the polymer structure on the hydrolysis kinetics will be evaluated and discussed.

For the determination of the reaction kinetics, a solution of the respective polymer with an amide concentration of 0.96 mol/L was preheated to either 75 or 90 °C. The solution temperature was measured inside of the reaction vessel and constantly monitored throughout the experiment. As soon as the desired temperature was reached, concentrated HCL was added. The added volume was hereby equal to the volume of water in the polymer solution. This resulted in a half concentrated HCL and a amide concentration of 0.48 mol/L. The addition of the HCL marked the starting point of the hydrolysis as no hydrolysis was observed during heating under neutral conditions. From here on, samples were taken from the reaction vessel at various time points. The samples were immediately quenched by cooling of the solution in an ice bath and by increasing the pH of the mixture to above 10 using 20 %wt NaOH solution. Following the removal of water via lyophilisation, the hydrolysis degree was determined using $^1$H-NMR analysis. All polymer kinetics were performed in triplicates. Great care was taken to carry out the reactions under identical conditions as far as possible. Upon partial hydrolysis of a PEtOzi homopolymer, all peaks in the $^1$H-NMR spectrum undergo a change in shape and or position (Figure 4.16 a). The black spectrum was taken after 0 min of hydrolysis and the red spectrum after 360 min. Most notably, the $CH_2$ integral of the ethyl side chain (peak **f**) decreases gradually throughout

the reaction. Alongside, new peaks corresponding to propionic acid (peak **h**) as well as the $CH_2$ group next to the newly formed amine (peak **d**) appear in the spectrum. The amount of formed propionic acid should theoretically be equal to the amount of hydrolysed side chains. However, it was noticed that the concentration of propionic acid, determined via $^1$H-NMR analysis, showed only poor correlation with the hydrolysis degree. The concentration was often either much lower or much higher than expected. Even though propionic acid is volatile and can easily evaporate, the immediate quenching of the samples with NaOH results in the formation of the non-volatile sodium derivative. Striking was that the propionic acid concentration also differed between multiple measurements of the same hydrolysis sample. It is therefore likely that the products are not homogeneously distributed throughout the lyophilised sample. This is probably caused by the poor solubility (due to a high salt concentration) and partial precipitation of the polymer during quenching. Thus, the signals of the propionic acid were not taken into account for the analysis of the hydrolysis degree. Furthermore, the signals corresponding to the $CH_3$ groups of the polymer side chain (peak **g**) and the propionic acid (peak **i**) appear superimposed in the spectrum. This makes the peak unreliable for determination of the hydrolysis degree and prevents normalization of the spectra. The signals of the protons **d** shift upon cleavage of the amide bond to lower ppm values. It is important to note that the position and shape of this peak is highly dependant on the pH. This makes the adjustment of the pH in the quenching step important in order to gain consistent results. Interesting is that the chemical shift of the central $CH_2$ group of the hydrolysed and non-hydrolysed backbone (peak **e** and **c**) remains almost unchanged throughout the reaction. The peak only broadens slightly and can be utilized for the normalization of the spectrum. The hydrolysis degree can therefore be accurately calculated by the ratio of the integral corresponding to the peaks **f** and **d**. For instance, in the displayed example a hydrolysis degree of 10.2 % can be calculated. Beside the PEtOzi homopolymers, the hydrolysis kinetics of P(EtOzi$_{75}$-co-EtOx$_{25}$) and P(EtOzi$_{75}$-co-MeOx$_{25}$) copolymers was also studied. While the hydrolysis degree of the P(EtOzi-co-EtOx) copolymers could be determined in a similar fashion to the PEtOzi homopolymer, slight adjustments had to be made for the MeOx containing polymers (for details see section 7.2).

It has been shown by Hoogenboom *et al.* that, for a large excess of HCl, the hydrolysis of POx homopolymers follows a pseudo-first order kinetic.[180] Therefore, very similar to the analysis of the polymerization kinetics discussed in Section 4.1.2, plotting $ln\left(\frac{[A]_0}{[A]_t}\right)$ vs. $t$ should give a linear dependency for the data collected for the hydrolysis kinetics. Fitting of a linear equation to the linearised data allows the calculation of the apparent hydrolysis rate ($k_h^{app}$) by using Equation 4.3. Figure 4.16 b) shows the first order hydrolysis kinetic

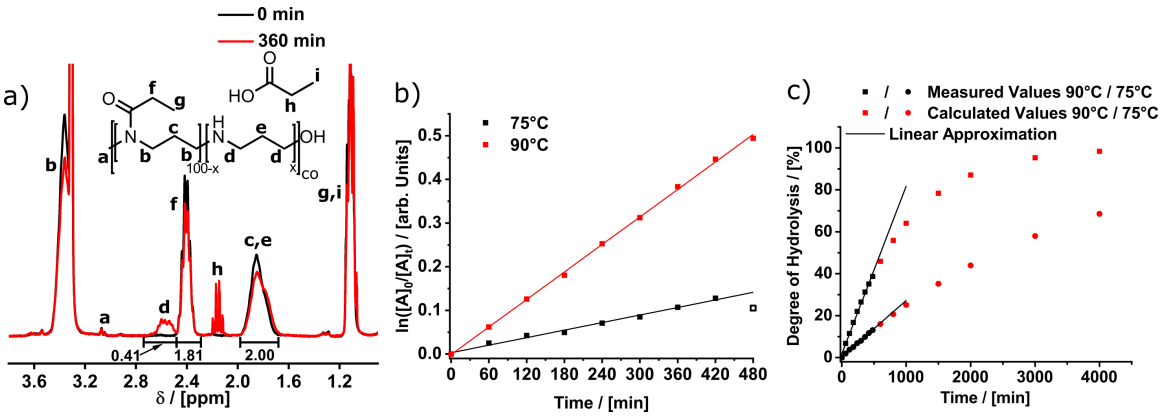


**Figure 4.16:** a) $^{1}$H-NMR spectrum (300MHz, 298 K, MeOD) of PEtOzi$_{100}$ after 0 min (black curve) and 360 min (red curve) of hydrolysis in acidic solution at 75 °C. All prominent peaks are assigned and the integrals of the 360 min sample are displayed below the curve. b) Linear pseudo-first order kinetic plots (n=3) of the hydrolysis of PEtOzi$_{100}$ at 75 and 90 °C. Open symbols have been masked for the linear fitting. c) Visualization of the linear approximation made for the exponential trend of the hydrolysis data at 75 and 90 °C. The black points represent measured data points (n=3) and the red points are calculated based on extrapolations of the respective pseudo-first order kinetic plots.

plot of PEtOzi$_{100}$ for the reaction temperatures of 75 and 90 °C. The data clearly follows a strict linear trend. This indicates that the hydrolysis of POzi homopolymers also follows pseudo-first order kinetics. The apparent rate constants $k_h^{app}$ are listed in Table 4.5. At 90 °C, a rate constant of $3.65\times10^{-5}\ \frac{l}{mol\times s}$ was calculated. Striking is the drastic difference to the values determined by Hoogenboom *et al.* for PEtOx, which are at 90°C more than 600 times higher ($23\times10^{-3}\ \frac{l}{mol\times s}$). Generally, when comparing the hydrolysis of POx and POzi polymers, a slower reaction speed is to be expected for POzi. The additional $CH_2$ group in the backbone makes the tetrahedral transition state during the amide-bond cleavage sterically more demanding. This will cause a decreased reaction speed. Furthermore, POzi is less hydrophilic than PEtOx, which results in a inferior hydration behaviour and a decrease of the reactivity.[184] However, the values reported by Hoogenboom *et al.* for PEtOx have to be viewed critically. While reading the publication one can notice that the shown first order kinetic plots do not correspond to the reported rate constants. To avoid speculations, no further comparison of absolute values will be made here. When decreasing the reaction temperature to 75 °C, a rate constant of $1.00\times10^{-5}\frac{l}{mol\times s}$ was found for PEtOzi$_{100}$. This corresponds to a more than three-fold deceleration of the reaction speed. This decrease corresponds well to the general rule of thumb in chemistry: "Increasing the reaction temperature by 10 °C will double the reaction speed and vice versa." The kinetics discussed here were only performed up to conversions of 15 % (75°C kinetics) and 40 % (90°C kinetics) due to a generally low reaction rate. Therefore, phenomena like decreasing solubility as well as reactivity changes due to neighbouring effects are unlikely to influence

**Table 4.5:** Summary of the rate constants as well as the fitting parameters for the hydrolysis kinetics of important polymers used in this thesis.

| PC,theo | $a$ | $b$ | $k_h^{app}$ |
|---|---|---|---|
| Hydrolysis temperature: 90°$C$ | | | |
| PEtOzi$_{33}$ | 0.249 | 0.084 | 3.44 |
| PEtOzi$_{100}$ | 1.671 | 0.080 | 3.65 |
| Hydrolysis temperature: 75°$C$ | | | |
| PEtOzi$_{33}$ | 0.591 | 0.026 | 0.87 |
| PEtOzi$_{100}$ | 0.240 | 0.027 | 1.00 |
| PEtOzi$_{200}$ | 0.178 | 0.026 | 0.94 |
| P(EtOzi$_{75}$-co-EtOx$_{25}$) | 0.002 | 0.041 | 1.41 |
| P(EtOzi$_{75}$-co-MeOx$_{25}$) | 0.188 | 0.050 | – |

Parameters in: a [arb. units]; b [1/s]; $k_h^{app}$ [$1 \times 10^{-5} \frac{l}{mol \times s}$]

the data, even though such effects are reported elsewhere.[180] As conversions are low, a non-logarithmic approximation of the hydrolysis degree vs. time plots using a simple linear equation can be made. This approximation is visualized in Figure 4.16 c). The measured values are in good agreement with both, the simple linear fit of the type $y = a + b \times x$ as well as the calculated exponential function. This confirms that the approximation is valid for such low conversions. The approximation allows the straight forward calculation of the reaction time required to reach a specific desired hydrolysis degree. As visualized in Figure 4.17 a) and b), the hydrolysis kinetics of low molar mass (n=33) and high molar mass (n=200) PEtOzi as well as the EtOx and MeOx containing copolymers, are also in good agreement with such a simple linear fit. The parameters resulting from the linear fits, the y-intercept (a) and the slope (b), are listed in Table 4.5. Using these values, the required reaction times for a specific hydrolysis degree can be calculated. In the course of these studies, it was observed that the samples collected at 0 min (immediately after addition of the concentrated HCL) often yielded hydrolysis degrees between 1 and 2 %. However, no clearly visible peaks were observed in the respective $^1$H-NMR spectrum. For the calculation of these values, the same integral ranges were applied as for samples taken at later time points, where the $CH_2$ signals **d** were clearly recognizable. This observation can be attributed to two reasons: first, due to the termination with methanolic KOH all parent polymers contain a certain percentage of secondary amines in the end-groups ($HD_0$ value, see Section 4.1.3). Second, even after applying a correction, the base line between the peaks **b** and **f** in the $^1$H-NMR spectra did not reach a level of zero. This is due to a natural broadening of polymer proton signals in $^1$H-NMR spectra. Also $^{13}$C satellite signals of **f** superimpose the integral range of the signals **d**. These phenomena resulted in y-intercept values (a) of the hydrolysis fits in the range of 1 to 4 %. Due to differences in

the peak shape, this effect was more pronounced for the copolymers than it was for the PEtOzi homopolymer. In the first parts of this thesis, exclusively PEtOzi polymers with comparably high hydrolysis degrees (5 and 15 %) were used. Therefore, for the $1^{st}$ and $2^{nd}$ generation of DA-material, uncorrected hydrolysis kinetics were applied and gave good results. However, in the later parts of this thesis ($3^{rd}$ generation) homo- and copolymers with lower degrees of functionalization between 2 and 4 % were synthesized. Due to the y-intercept values such hydrolysis degrees would be impossible to achieve with uncorrected fitting curves. Therefore, the average t=0 min integrals were subtracted from the integrals at the later time points of the kinetics. This gave corrected hydrolysis kinetics with the linear fitting parameters displayed in Table 4.5. It is important to note that only the data for the corrected hydrolysis kinetics will be presented in this chapter. This data can be applied universally and no additional information is gained from the non-corrected data.

The hydrolysis kinetics of PEtOzi with varying chain length from n=33 to n=200 are shown in Figure 4.17 a). No significant differences were found between the three polymers. This shows that the polymer length has no influence on the hydrolysis reaction within the studied molar mass range. Furthermore, it can be concluded that under these conditions the accessibility of the amide side groups does not depend on the polymer length. Similar results were found by Lambermont-Thijs *et al.* for PEtOx homopolymers.[184]

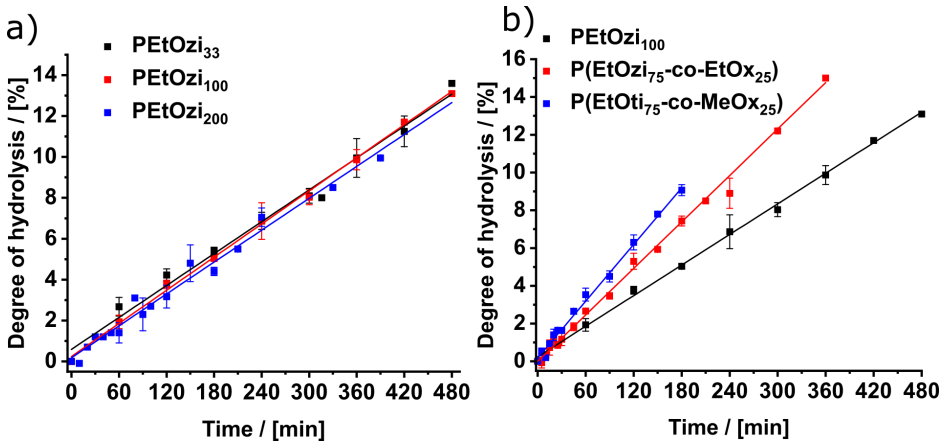


**Figure 4.17:** a) Comparison of the hydrolysis kinetics at 75 °C of PEtOzi with a chain length of n=33, 100 and 200. b) Comparison of the hydrolysis kinetics at 75 °C of the PEtOzi homopolymer as well as the copolymers containing EtOx or MeOx.

For the EtOx and MeOx containing copolymers, a more rapid hydrolysis was found compared to the EtOzi homopolymer (Figure 4.17 b), and the MeOx containing polymer showed the highest reactivity rate. This can be explained by an increase in the polymer hydrophilicity, resulting in an improved hydration of the Ox containing polymers.[184] Also, the

less flexible Ox backbone allows a sterically less hindered transition state during the amide bond cleavage. In the case of the MeOx containing polymer, the smaller side chain further decreases the steric demand of this transition state. These findings are in agreement with literature.[180] However, the increase in reactivity is relatively minor, which is probably due to the rather low Ox content in the polymers. Considering the complex structure of the Ozi/Ox copolymers discussed in section 4.1.2, the increased reactivity of the Ox monomer units favours a highly non-even distribution of secondary amines in the copolymers. Also, potential neighbouring effects would increase this phenomenon even further.[180] As the secondary amines will serve as binding site for the coupling of the DA functions, this can have an impact on the crosslinking efficiency of the DA functionalized copolymers.

Summarizing this section, the hydrolysis reaction of PEtOzi homo- and copolymers was studied. For all polymers a pseudo-first order kinetic was found. While the reaction kinetics were found to be independent from the molar mass of the polymers, the incorporation of Ox monomers resulted in a significant increase of the reaction speed. Furthermore, linear approximations, allowing the straight forward adjustment of the desired hydrolysis degree were established.

### 4.2.2 1st Generation

In the following, the results discussed in the previous sections on the chemical and physical properties as well as the partial hydrolysis of PEtOzi will be applied for the synthesis of the $1^{st}$ generation of DA functionalized PEtOzi. During MEW processing the printed fibres rapidly cool down to RT. This limits the mobility of the polymer chains within those fibres. This is of importance as both, the furan and maleimide component of the biomaterial ink, are macromolecules with a molar mass above 10 kg/mol. For a successful crosslinking of the fibres however, sufficient furan and maleimide units have to get in contact with each other. Both, the rapid cooling as well as the high molar mass will hinder this process. In the beginning of the project, little was known about the efficiency of the DA crosslinking within the bulk material. Furthermore, Chujo *et al.* reported that a mixtures of DA functionalized PEtOx with a degree of substitution lower than 4 % did not form stable gels, when these where cured in bulk.[200] Therefore, a high functionalization degree of 15 % was aimed at for these first experiments.

For the synthesis of the $1^{st}$ generation of DA material, the procedure described by Chujo *et al.* was followed closely. The characterization of the prepared polymers is summarized in Table 4.6. Based on the previously determined hydrolysis kinetic, **P1** was hydrolysed for 180 min at 90 °C under acidic conditions. This resulted in the polymer **P13** with a theoretical hydrolysis degree ($HD_t$) of 15 %. According to $^1$H-NMR analysis, an experimental hydrolysis degree ($HD_e$) of 13.9 % was achieved. Following the synthesis described in Scheme 4.15, two separate sets of the DA material (**P14**, **15** and **P16**, **17**) were prepared via DCC supported coupling of 3-(2-furyl)propionic acid and 3-maleimidopropionic acid. The $^1$H-NMR analysis of the functionalized polymers is summarized in Figure 4.18

**Table 4.6:** Selected analytical data of the hydrolysed and the furan and maleimide functionalized polymers of the $1^{st}$ generation of DA material.

| ID | PC,theo | $M_n^a$ | Đ | $ML^b$ 5% | $HD_t$ | Funct. | $HD_e^c$ | $DF_e^c$ | Eff. |
|---|---|---|---|---|---|---|---|---|---|
| | Parent polymer, $PEtOzi_{100}$ / **P1** | | | | | | | | |
| **P13** | $PEtOzi_{100}$-15% | 12.9 | | 281 | 15 % | – | 13.9 | – | 92 %$^d$ |
| **P14** | $PEtOzi_{100}$-15%-Fu | 8.0 | 1.19 | – | 15 % | Fu | 13.9 | 11.8 | 78 %$^e$ |
| **P15** | $PEtOzi_{100}$-15%-MaP | 9.6 | 1.27 | – | 15 % | MaP | 13.9 | 9.2 | 65 %$^e$ |
| **P16** | $PEtOzi_{100}$-15%-Fu | 7.5 | 1.20 | 334 | 15 % | Fu | 13.9 | 11.8 | 85 %$^e$ |
| **P17** | $PEtOzi_{100}$-15%-MaP | 8.8 | 1.22 | 307 | 15 % | MaP | 13.9 | 9.2 | 66 %$^e$ |

Determined by: $^a$ GPC(HFIP) in [kg/mol]; $^b$ TGA in [$^\circ C$]; $^c$ $^1$H-NMR in [%]

Calculated as: $^d$ $HD_e/HD_t$; $^e$ $HD_e/FD_e$

Abbreviations: Fu 3-(2-furyl)propionic acid; MaP 3-maleimidopropionic acid; Eff. efficiency

a) and b). For both, the furan and maleimide functionalized polymers all peaks in the spectrum can be assigned, and particularly the low field shifted unsaturated protons of the furan and maleimide rings are well resolved. The DF was calculated from the integral ratio of the signal originating from the $CH_3$ group in the side chain (signal e) and the signals of the furan (signals h, i, j) and maleimide rings (signal m). This revealed a functionalization efficiency between 65 and 85 %, which is very similar to the results reported by Chujo and coworkers.[200] It is important to note that Chujo and coworkers reported that the coupling has to be performed under inert condition using anhydrous AN. Here, no significant differences in the coupling efficiency were noticed when the reaction was performed under inert conditions or not. Therefore, all couplings were carried out under ambient conditions using non dried AN. This is a great advantage, as working under inert conditions as well as the drying of AN can be tedious. Further adjustments to the synthesis procedure were made for the $2^{nd}$ and $3^{rd}$ generation of DA material with the aim to increase the functionalization efficiency. An interesting trend of the molar mass determined via GPC can

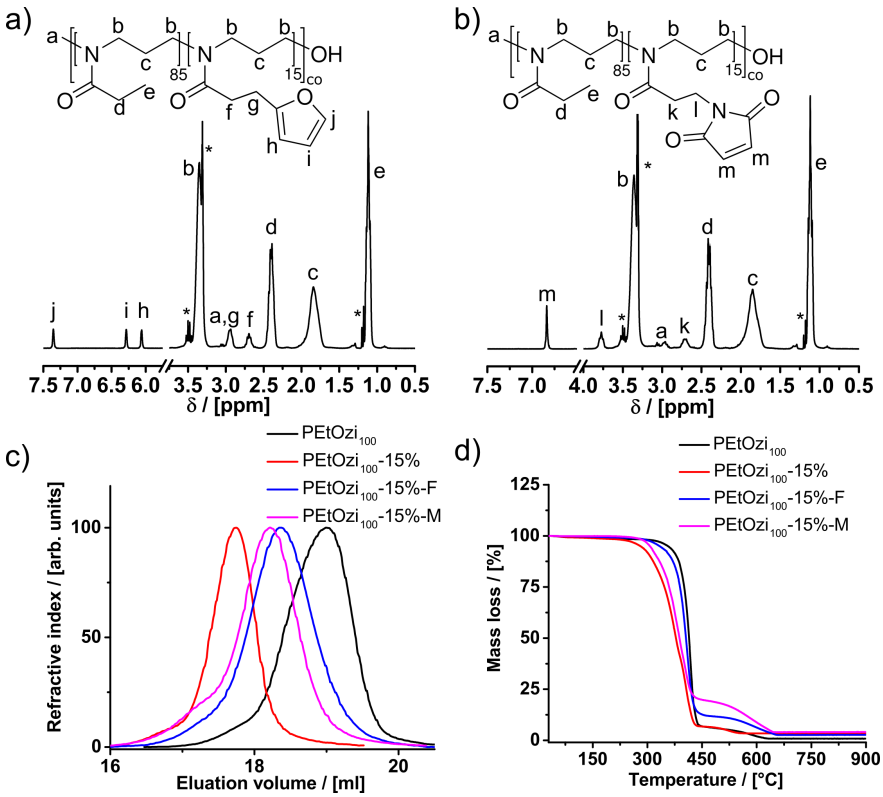


**Figure 4.18:** a), b) $^1$H-NMR spectrum (300 MHz, 298 K, MeOD) of **P16** and **P17** respectively. All peaks are assigned. Peaks marked with asterisks originate from residual solvent signals. c) GPC elugrams of **P1**, **13**, **16**, **17**. d) TGA traces of **P1**, **13**, **16**, **17**.

be observed for the polymers at the different stages on the synthesis route. In the case of the homopolymer **P1** the $M_n$ was with 5.1 kg/mol much lower than expected from the degree of polymerization (see discussion in Section 4.1.1). The $M_n$ increased significantly

after the hydrolysis step up to a value of 12.9 kg/mol for **P13** (see Table 4.6 and Figure 4.18 c). For the functionalized polymers the $M_n$ decreased to values between 7.5 and 9.6 kg/mol. A possible explanation for this is that the charges of the secondary amines have a significant effect on the coiling behaviour, resulting in an increased hydrodynamic radius. Due to the incomplete functionalization some secondary amines remain, which explains the intermediate $M_n$ values of the functionalized polymers. Furthermore, a slight high-molar mass shoulder corresponding to roughly double the molar mass can be observed in the GPC elugram of **P17**. This could be caused by side reactions during the functionalization process, leading to irreversible crosslinking of the maleimide functionalized polymer with itself (for discussion see below). TGA revealed a decreased thermal stability of the hydrolysed polymer **P13** as well as the maleimide functionalized polymer **P17**. Five percent of mass loss was observed for those polymers at 281 and 307 $^{\circ}C$ respectively. However, these temperatures are still well above the expected MEW processing temperatures.

DSC can give insight into the thermal dynamics of the reversible DA crosslinking. Therefore, **P14** and **P15** were separately dissolved in water, mixed and finally lyophilised. Three consecutive heating and cooling cycles between -50 and 200 $^{\circ}C$ were performed with this sample (Figure 4.19 a). The last two heating cycles revealed a $T_g$ at 37 $^{\circ}C$ as well as two broad endothermic peaks in the range of 84 to 120 $^{\circ}C$ and 120 to 160 $^{\circ}C$. At a slightly lower temperature range, the respective broad exothermic signals can be seen in the cooling cycles. These peaks can be attributed to the rDA (heating cycle) and the DA (cooling cycle) reaction of maleimide and furan. The two peaks in the heating curve originate from the dissociation of the endo- and exo-configuration of the bicyclic DA adduct respectively. In the case of the endo-product, the ring opening takes place at lower temperatures (84 to 120 $^{\circ}C$) as it is the less stable configuration.[267,268] Moreover, the two consecutive temperature cycles match very well, supporting the reversible nature of the DA reaction. Interestingly the $T_g$ of the mixture is higher than the $T_g$ of the two pristine polymers (see Table 7.6 and 7.7). This indicates an increased rigidity caused by the chemical crosslinking of the polymer chains.

While DSC clearly shows the presence of a reversible DA-reaction within the material, it was still unclear, if the crosslinking degree was sufficient to render the material insoluble and allow the formation of a hydrogel. Therefore, a solution of **P14** and **P15** (180 mg/mL) in methanol was cast into a dog bone mould, and the solvent was allowed to evaporate overnight (Figure 4.19 b, top). Immersion of the recovered polymer film into aqueous media resulted in significant swelling (EWC: 66 %) and the formation of a hydrogel material (Figure 4.19 b, bottom). In order to allow processing by MEW, the mixed and

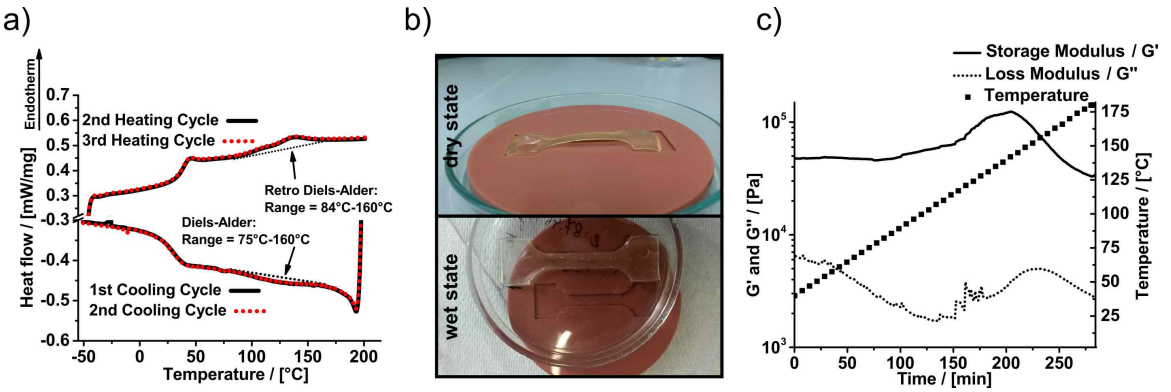


**Figure 4.19:** a) DSC analysis of a mixture of **P14**+**P15**, showing two heating and cooling cycles. b) Dog-bone prepared by casting a solution of **P14**+**P15** (180mg/ml) in MeOH. Top: After evaporation of the solvent an elastic film remains. Bottom: After swelling in water a significantly swollen hydrogel is formed. c) Rheological oscillation experiment of a mixture of **P16**+**P17** performed with a temperature ramp from 40 to 180 °$C$ (0.5 °$C$/s, amplitude: 0.5 %, frequency: 10 rad/s, geometry: plate/plate).

already crosslinked material must be liquefiable upon heating. To investigate this matter, methanolic solutions of **P16** and **P17** were mixed, cast into a mould, and the solvent was allowed to evaporate over night. The prepared film was analysed using continuous oscillatory rheology measurements, while simultaneously increasing the temperature from 40 to 180 °C (Figure 4.19 c). For low temperatures the $G'$ was found well above the $G''$. This shows that the material response was predominantly solid or elastic and that the film is well crosslinked. However, upon heating no intersection of $G'$ and $G''$ (gel point) was observed and the material response remained solid-like over the whole temperature range. In contrast, an opposing trend can be seen as the $G'$ increases for temperatures above 100 °$C$, while $G''$ decreases. Both factors indicate a stiffening of the material. Also visibly, no liquefaction of the polymer film occurred during the measurement. This result was rather unexpected as both, the discussed DSC measurements as well as the literature,[234] supports the reversibility of the DA reaction. It is important to note that while the DSC measurement was performed under nitrogen atmosphere, the rheological characterization was performed without the exclusion of air. Over the course of this work, it became apparent that the thermal stability of the DA material is strongly tied to the exclusion of air. This observation will be discussed in more detail at several occasions throughout this thesis. Therefore, one major factor for the controversial results of DSC and rheology can be attributed to the difference in the experimental conditions. Also, DSC shows merely the dynamics of the DA reaction, but allows no conclusion whether the material is liquefied in the heated state. In addition, irreversible side reactions might not be detected by DSC, but will prevent the liquefaction in the rheometry measurement. Reports about side reactions of furan and maleimide based materials in the heated state can also be found in the literat-

ure.[235] It is also important to pay attention to the details, when comparing the presented system with most of the commonly reported systems in literature. Most of the reported thermally reversible DA materials consist out of at least one or even two low-molar mass DA components.[235,249,257,269–271] Furthermore, the number of DA units per active molecule is usually in the range of 2 to 4. This means that even if a low percentage of DA adducts are dissociated, the formed molecule fragments tend to have a low molar mass and are easily released from the network, which allows the material to flow. In contrast, within this project both components have a molar mass above 10 kg/mol. Therefore, much smaller amounts of remaining DA adducts are sufficient to sustain an non-liquefiable interpenetrating network. The determined functionalization degree of the polymers converts to 9 and 11 DA units per chain respectively. Thus, in the most extreme case 11 DA bonds have to be broken to fully release a polymer molecule from the crosslinked network. Should this issue be responsible for the irreversible solidification, it can be easily addressed by lowering the functionalization degree of the polymers. Nonetheless, throughout the whole rheology measurement no significant convergence of $G'$ and $G''$ was observed. This is a clear sign for irreversible side reactions. It is known that in the heated, state side reactions, such as aromatisation of the DA adducts[252], ring opening of the furfuryl rings[253] as well as homopolymerization of the maleimide,[255] can occur. Furthermore, in the presented system additionally a Michael addition to the maleimide C=C double bond has to be taken into account. This is due to the considerable amount of residual secondary amines remaining in the material after the incomplete functionalization reaction. Michael addition can result

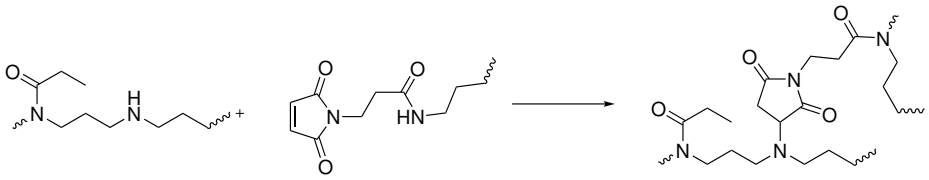

**Figure 4.20:** Schematic illustration of the Michael addition of a secondary amine in a PEtOzi backbone onto a maleimide.

in a thermally non-reversible chemical crosslink between two polymer chains (Figure 4.20). The strong electron deficit of the C=C double bond of the maleimide makes it highly susceptible to nucleophilic attacks.[206,234] This is especially important for the attack of thiols (thiol-ene click chemistry),[86] but also amines are known to undergo such reactions. Therefore, it was of utmost importance to improve the efficiency of the functionalization and fully remove the secondary amines from the DA material.

Summarizing this section, it was possible to successfully transfer the method reported by Chujo *et al.*[200] to the polymer class of POzi and to synthesize furan and maleimide func-

tionalized PEtOzi. Upon mixing these polymers, they spontaneously chemically crosslink, which allows the formation of POzi-based hydrogels. Contrarily, it was not possible to liquefy the already crosslinked material via heating and therefore no melt processing was possible. To allow melt processing, decreasing the crosslinking density as well as increasing the functionalization efficiency were identified as promising steps to improve the material.

### 4.2.3 2nd Generation

In chapter 4.1.4 it was shown that it is possible to process PEtOzi and its copolymers via MEW into defined structures. However, the first DA functionalized PEtOzi material, discussed in section 4.2.2, did not allow liquefaction of already crosslinking material and no melt processing was feasible. In this section the functionalization efficiency of the hydrolysed polymers was investigated and improved. Furan and maleimide functionalized PEtOzi with a lower degree of hydrolysis was synthesized, characterized and the processability via MEW was evaluated. Parts of this section have already been published in 2020.[272]

#### Coupling Efficiency

For the evaluation of the functionalization efficiency, the reverse reaction of the acid catalysed hydrolysis was chosen as model reaction (Figure 4.21 a). This allowed straight forward evaluation of the reaction performance using $^1$H-NMR spectroscopy. As illustrated in Figure 4.21 b), 100 % conversion is achieved, when the integral ratio of the signals corresponding to the two $CH_2$ groups is equal to 1. In the experimental setup the polymer concentration, the coupling agent and the excess of reactant (coupled acid) were varied. Finally, the procedure with the best performance was validated with 3-(2-furyl)propionic acid as reactant. The results of this study are listed in Table 4.7. A $PEtOzi_{100}$ with a $HD_e$ of 6.3 % (**P18**) was used in all reactions. For the first model reaction, **P19** was synthesized

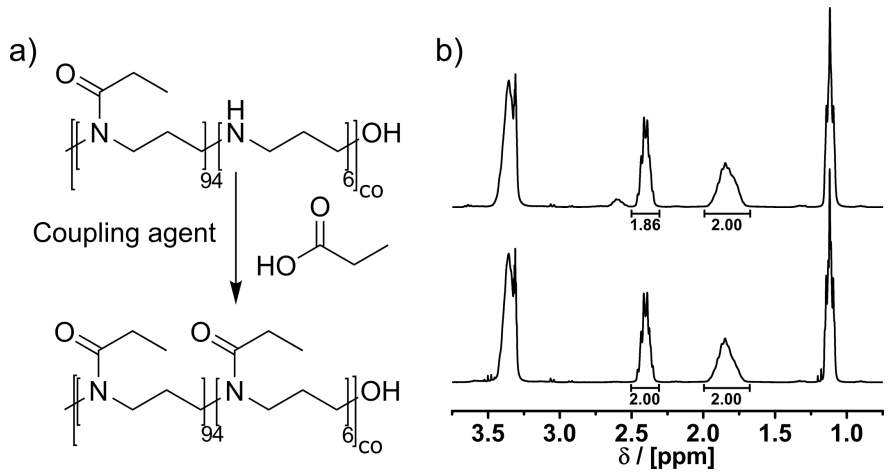


**Figure 4.21:** a) Schematic illustration of the model reaction for evaluation of the functionalization efficiency. b) Representative $^1$H-NMR spectrum (300 MHz, 298 K, MeOD) before (top) and after (bottom) conversion with propionic acid.

from **P18** using the same procedure used for the functionalization of the polymers **P14**, **15**, **16**, **17** in the preceding section. This resulted in a coupling efficiency of 65 %, which is very similar to the values achieved for the $1^{st}$ generation of DA material. Therefore,

propionic acid seems to be a viable test reactant. Changing the polymer concentration from 0.002 to 0.003 mmol/mL (synthesis of **P20**) increased the coupling efficiency to 81 %. Therefore, all following reactions were carried out with a higher polymer concentration. Increasing only the excess of the coupling agent from twofold to fourfold did not show any improvement to the functionalization reaction (**P21**: 81 %). However, when also the amount of reactant was increased to a fourfold excess (**P22**), a coupling efficiency of 103 % was found. Please note that efficiency values above 100 % can be attributed to the limited accuracy of the NMR measurement. In the direct comparison of different amine/acid coupling reagents, N,N'-diisopropylcarbodiimide (DIC) also enabled full conversion (**P23**), while for 1,1'-carbonyldiimidazole (CDI) (**P24**) a lower functionalization efficiency was found. Subsequently the two best performing conditions were again evaluated with 3-(2-furyl)propionic acid as reactant. Both conditions gave, within the error margin of the NMR measurement, the same coupling efficiency and both were close to full conversion. Due to the more facile removal of the side products produced in the DCC supported coupling compared to DIC, all upcoming functionalizations were performed using the conditions of **P25**.

**Table 4.7:** Investigation of the coupling efficiency.

| ID | Conc.[a] | Reactant | Coupling agent | [A][b] | [B][b] | Efficiency |
|---|---|---|---|---|---|---|
| **P19** | 0.002 | Propionic acid | DCC | 2 | 2 | 65[c] |
| **P20** | 0.003 | Propionic acid | DCC | 2 | 2 | 81[c] |
| **P21** | 0.003 | Propionic acid | DCC | 2 | 4 | 81[c] |
| **P22** | 0.003 | Propionic acid | DCC | 4 | 4 | 103[c] |
| **P23** | 0.003 | Propionic acid | DIC | 4 | 4 | 108[c] |
| **P24** | 0.003 | Propionic acid | CDI | 4 | 4 | 83[c] |
| **P25** | 0.003 | Fu | DCC | 4 | 4 | 95[d] |
| **P26** | 0.003 | Fu | DIC | 4 | 4 | 92[d] |

Parameter in: [a] [mmol/ml]; [c] [%]; [d] [%]

Calculated as: [b] in relation to the number of secondary amines in **P18** (6.3 %)
Calculated as: [c] ratio of the integral of the $CH_2$ groups in the side chain of the functionalized polymer and the backbone of hydrolysed polymer

Calculated as: [d] ratio of the furan signals in relation to the hydrolysis degree of **P18** (6.3 %)

Abbreviations: Fu 3-(2-furyl)propionic acid; [A] Excess of reactant; [B] Excess of Coupling agent

### Synthesis and Characterisation

Compared to the $1^{st}$ generation of DA material, several adjustments have been made for the synthesis procedure of the $2^{nd}$ generation. This includes the above discussed optimized coupling conditions, but also changes to the dialysis workup conditions for the hydrolysed polymers. Before, the dialysis was performed against MilliQ water at a neutral pH. This led to the partial protonation of the amino groups in the backbone, making them much less reactive for the following coupling reaction. For the $2^{nd}$ generation, the pH of the dialysis medium was adjusted between 9 and 10 using 1 M NaOH solution. This guaranteed full deprotonation and therefore full availability of the secondary amines for the coupling reaction. Furthermore, the acid derivative of the maleimide functionality was changed from 3-maleimidopropionic acid to 6-maleimidohexanoic acid. This step was required, since the synthesis of 3-maleimidopropionic acid was tedious and gave only low yields, which prevented the synthesis of larger batches. 6-Maleimidohexanoic acid however was commercially available in large quantities. Concerning the reactivity in the DA reaction, no notable changes are to be expected, while the hydrophilicity of the functionalized polymer will likely decrease due to the longer alkyl side chain of 6-maleimidohexanoic acid.

Implementing these changes to the synthesis procedure, three batches of DA crosslinkable polymers were synthesized. Selected analytical data of those polymers is listed in Table 4.8. GPC analysis of the polymers revealed a comparable molar mass around 4.2 kg/mol and a low dispersity of 1.1 for all batches. The determined $HD_e$ for all polymers was close to the aimed value of 5 %. Furthermore, functionalization efficiency generally reached values well above 90 % with the slight exception for **P31** and **P32**. Therefore, within the limitations of $^1$H-NMR analysis, little to none residual free secondary amines are expected in the prepared DA functionalized material. In the previous section, the mixing of the two

**Table 4.8:** Selected analytical data of the hydrolysed and the furan and maleimide functionalized polymers of the $2^{nd}$ generation of DA material.

| ID | PC,theo | $M_n^a$ | $Đ^a$ | $HD_t$ | $HD_e^b$ | $DF_e^b$ | Efficiency$^c$ |
|---|---|---|---|---|---|---|---|
| **P27** | $PEtOzi_{100}$-5%-Fu | 4.2 | 1.1 | 5 % | 5.4 | 5.0 | 93 |
| **P28** | $PEtOzi_{100}$-5%-Ma | 4.2 | 1.1 | | 5.4 | 5.0 | 93 |
| **P29** | $PEtOzi_{100}$-5%-Fu | 4.4 | 1.1 | | 4.8 | 4.6 | 96 |
| **P30** | $PEtOzi_{100}$-5%-Ma | 4.4 | 1.1 | | 4.8 | 4.7 | 98 |
| **P31** | $PEtOzi_{100}$-5%-Fu | 4.2 | 1.1 | | 4.8 | 4.3 | 90 |
| **P32** | $PEtOzi_{100}$-5%-Ma | 4.4 | 1.1 | | 4.8 | 4.1 | 85 |

Determined by: $^a$ GPC (HFIP) in [kg/mol]; $^b$ $^1$H-NMR analysis in [%]

Calculated as: $^c$ $HD_e/DF_e \times 100$ in [%]

polymeric components was generally achieved by dissolving both in methanol, mixing the two solutions and finally evaporate the solvent at RT. In this section, the mixing procedure was changed to either grinding the dry polymers in a liquid nitrogen filled mortar or to lyophilisation of an aqueous mixture. A detailed discussion of the procedures as well as the differences can be found in section 7.2.

In contrast to the $1^{st}$ generation, the $2^{nd}$ generation of DA material showed a distinct and reversible phase transition from an elastic solid to a viscous fluid upon simple heating at ambient conditions, using a heat gun. In addition, the liquefied material permitted threads to be pulled out of the mass, when it was brought into contact with a cooled object. This simple test is sometimes used to evaluate the melt electrospinning capabilities of a melt. These basic experiments already showed the significant impact of the improved synthesis procedure as well as the reduced DF. Furthermore, this allowed to study the thermal dynamics of the DA reaction in more detail. For instance infrared (IR) spectroscopy allowed visualization of the thermal equilibrium, depending on the temperature (Figure 4.22 a). The complete IR spectrum of the mixed polymers is relatively crowded (Figure 8.8), but it was possible to identify the stretching band of the maleimide double bond at 695 $cm^{-1}$. Therefore, the DA equilibrium can be easily followed by monitoring the intensity changes of this peak. A crosslinked polymer film was readily liquefied three times at ambient conditions without any notable change in the absolute maleimide peak intensity. After liquefaction at elevated temperatures, the material was cured for 2.5 h at 60 °C. After this period, no free maleimide could be observed as the peak intensity in the IR spectrum decreased essentially to baseline levels. Therefore, IR analysis indicated a rapid, efficient and most importantly reversible crosslinking. Thermal reversibility was also followed using DSC in seven consecutive heating cycles (Figure 4.22 b). As discussed in section 4.2.2, two broad endothermic peaks, attributed to the endo- and exo-conformation of the DA adduct, were observed between 100 and 160 °C. After excessive repetitions, a decrease in the total reaction enthalpy from 4.3 J/g in the first cycle and 4.0 J/g in the third to 2.6 J/g in the seventh cycle was observed. The reduced reaction energy shows a decrease of the total amount of DA crosslinks, being broken in each cycle. This could be either attributed to non-reversible effects or due to an incomplete reverse reaction in the cooling cycle. Very similar to the $1^{st}$ generation, the $T_g$ of the mixed DA polymers is with 29 °C higher than the $T_g$ of the respective polymers before mixing (21 °C). This indicates that the reduced number of DA crosslinks still has an influence on the rigidity and microstructure of the polymers in bulk. TGA measurements under synthetic air of the mixed DA material showed a high degradation temperature of above 400 °C for the polymers **P27** and **P28** (Figure 8.9).

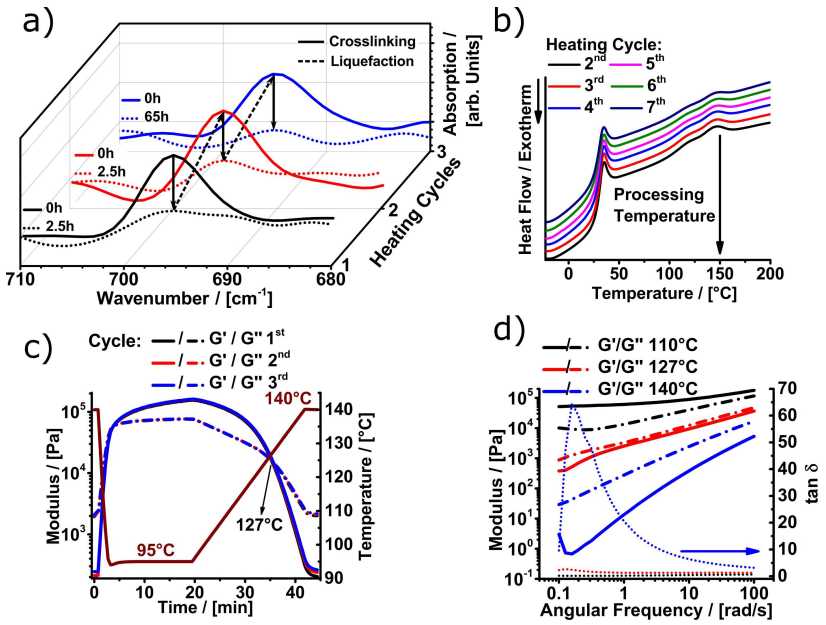


**Figure 4.22:** a) Monitoring the reversible crosslinking by IR-spectroscopy in three consecutive liquefaction cycles of a mixture of **P27** and **P28**. b) DSC thermograms with seven heating cycles of DA crosslinked poly(2-ethyl-2-oxazine) (**P27** + **P28**). c) Temperature-dependent viscoelastic properties of the dynamically crosslinked biomaterial ink, investigated by rheology measurements (**P29** + **P30**). d) Frequency dependency of the elastic and viscous moduli at temperatures below, near and above the gel point (**P29** + **P30**).[272] (Published by The Royal Society of Chemistry under Creative Commons licence CC BY-NC-ND 3.0)

In contrast to the $1^{st}$ generation, rheology showed full thermal reversibility over three consecutive heating cycles (Figure 4.22 c). This time the experiments were performed under oxygen and moisture free conditions. Upon cooling to 95 °C, a rapid inversion of $G'$ and $G''$ could be observed, indicating the solidification of the material. It is important to note that 95 °C is far above the $T_g$ of both functionalized polymers (see Table 7.6, 7.7), and the parent polymer $PEtOzi_{100}$ showed the properties of a medium viscous fluid at this temperature (Figure 8.6 a). Therefore, the solidification can be purely attributed to the chemical crosslinking of furan and maleimide caused by the forward DA reaction. During the gradual increase of the temperature to 140 °C (2 °C/min), the liquefaction point (crossing of $G'$ and $G''$) was found consistently at 127 °C for the three cycles. Above 127 °C $G'$ is much lower than $G''$, and the material shows a predominantly viscous behaviour. Strain sweeps at temperatures below (110 °C), near (127 °C) and above (140 °C) the liquefaction point reveal no strain dependency of the material in the range of 0.01 to 10 rad/s (Figure 8.6 b). The temperature dependent frequency sweeps at temperatures below the liquefaction point revealed a plateau of $G'$ for low frequencies (Figure 4.22 d), which is the typical behaviour of a crosslinked polymer. At higher temperatures a drastic decrease of $G'$ can be observed at low frequencies. $G'$ and $G''$ invert, which supports a fluid like behaviour.

It is important to stress that rheological analysis was only possible under inert conditions. Preliminary rheological experiments with the same material, but in the presence of oxygen and moisture, showed a pronounced thermal degradation of the material, when it was held at elevated temperatures for a period of several minutes. This became apparent by irreversible solidification as well as a colour change to red/brownish of the material at the edge of the rheology gauge head, respectively at the material-air interface (see Figure 8.7).

Summarizing, the physico-chemical characterization of the $2^{nd}$ generation of DA material showed good thermal reversibility of the chemical crosslinking, and little to no irreversible reactions were observed under inert conditions by the applied analytical methods. This thermal reversibility was essential for the melt processing via MEW and therefore the further progress of this project.

### Melt Electrowriting

For the first MEW experiments, the two polymer components were mixed under argon atmosphere using a liquid nitrogen cooled mortar. Following up, the mixture was annealed overnight at 40 °C and 300 mbar to remove residual moisture. This was important because the water evaporated in the heated polymer reservoir of the MEW device and caused the formation of gas bubbles. After this step, the 2-component biomaterial ink was crosslinked but ready for liquefaction and MEW processing. In general, gas bubbles had a drastic influence on the processability up to a point, where a continuous processing was prevented. Depending on the moisture content and the ambient temperature during the mixing process, the appearance of the mixture after tempering ranged from a continuous and clear polymer film to a granular and turbid material. In particular, in the case of the latter there were often still gas bubbles trapped in the molten polymer. Prior to the start of the printing process these were removed by applying a slight vacuum to the heated polymer reservoir. However, this often resulted in a noticeable reduction of the maximum printing time. This was caused by the influx of oxygen due to the applied vacuum. As mentioned above, oxygen appears to cause an acceleration of the irreversible solidification of the DA material. Thus an improved mixing method, allowing the full removal of gas bubbles without noticeable thermal degradation of the material, was developed in the later stages of this work. This is discussed in section 4.2.5 and 7.2.

Using MEW, microperiodic structures with defined fibre diameter, FD and number of layers could be obtained. As an example, scaffolds with 4 $cm^2$, 5 layers and a FD of 500 $\mu$m were direct-written (Figure 4.23 a). With the exception of some errors in the fibre stack-

ing, the structures were organized and well defined. A scaffold with these dimensions can be prepared within 7 min of printing time. Notable is the high processing temperature (NT: 150 °C; ST: 130 °C) required for a successful printing. This stands in contrast to the much milder temperatures used for the direct writing of non-functionalized PEtOzi$_{100}$ (NT: 120 °C; ST: 100 °C), and clearly demonstrates the impact of the DA equilibrium on the processing of the PEtOzi-based polymer. By DSC, the liquefaction point was found at 127 °C, yet the processing temperature (NT) was still more than 20 °C above this temperature. This indicates that the DA equilibrium still plays an important role on the material properties, even when the temperature is increased above the liquefaction point. The DSC data (Figure 4.22 b) supports this finding, since the signal of the rDA reaction was detected up to a temperature of 160 °C. While the printed structures were still soluble directly after printing, the forward DA reaction rendered them insoluble one hour post processing. However to ensure sufficient crosslinking, the scaffolds were typically stored at least overnight at RT. In contrast to non-functionalized PEtOzi the printed fibres maintain their morphology post processing (Figure 4.23 b) and even allowed bridging of the 500 $\mu$m gaps (Figure 4.23 b, inset). The crosslinking density caused by the DA reaction continuously reduces the mobility of the polymer chains, which in combination with the slightly higher $T_g$, retards polymer flow and the fibre shape is retained.

Immersing the printed structures into aqueous media induces immediate and rapid swelling. The timeline of the swelling process is visualized at selected time frames in Figure 4.23 d). Making use of the auto fluorescence of the PEtOzi backbone, the structure was illuminated with UV-light (365 nm) for better visualization. Shortly after the structure is fully covered with water, first signs of swelling can be observed by curling of the before straight fibres (14 s). Then, the distortion of the scaffold increases, causing it to buckle up and ultimately detach from the surface (26 s). After only 72 s the structure is fully released from the surface and no further swelling is observed. This fast swelling process can be attributed to the small fibre size and the high porosity of the architecture itself. This allows rapid and unhindered diffusion of water into the polymer fibres. Upon swelling, the box shaped pores increase in size from 500$\pm$20 to 690$\pm$40 $\mu$m and the total scaffold area from 4 to 9 cm$^2$. In the fully hydrated state, the architecture remained undistorted and no fibre delamination was observed (Figure 4.23 e). Also the fibre morphology was retained (Figure 4.23 f). The dynamic nature of the DA reaction allows the formation of chemical crosslinks between fibres at their junctions. The covalently reinforced fibre fusion greatly improves the interlayer adhesion of the 3D-printed constructs. It is important to note that interlayer adhesion is commonly the weakest point of 3D-printed objects.[273] This is a very advantageous intrinsic feature of this biomaterial-ink and has been reported for other DA-

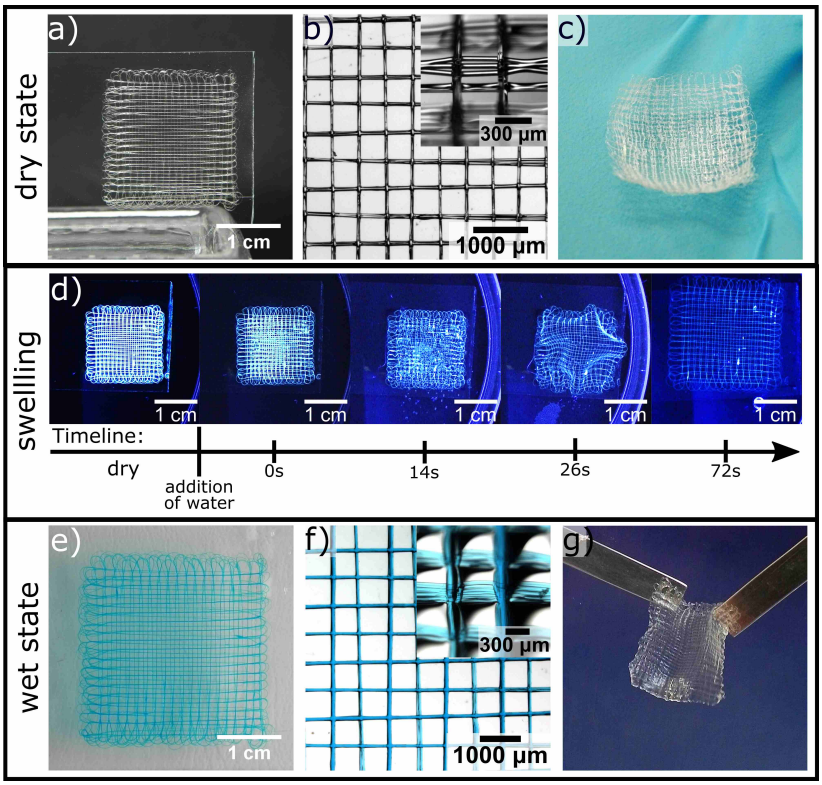


**Figure 4.23:** a) Picture of a MEW processed layered structure (S29). b) Stereomicroscope image of S29 in dry state. Inset shows the scaffold from a tilted angle to visualize the fibre morphology. c) Scaffold handling in dry state. d) Timeline of the swelling process illuminated under UV-light (365 nm). e) Picture of the fully swollen scaffold S29. The polymer was functionalized using a dye (DY-647P1-Maleimide) for better visualization. f) Stereomicroscope image of S29 in hydrated state. Inset shows the scaffold from a tilted angle to visualize the fibre morphology. g) Scaffolds allow handling outside of aqueous medium and are mechanically robust.[272] (a)- c) and e)- g) Published by The Royal Society of Chemistry under Creative Commons licence CC BY-NC-ND 3.0)

based materials as well.[235] The mechanical robustness of these MEW printed structures also allows the handling outside of aqueous solution (Figure 4.23 g). To get a more detailed view on the direct written structures in both, wet and dry state, environmental scanning electron microscopy (ESEM) experiments were performed (Figure 4.24 a- c).* In both conditions, the fibre surface appeared to be smooth and uniform. Under ESEM conditions, a significant increase of the mean fibre diameter from 45±5 to 89±12 $\mu$m was observed during swelling. This corresponds to a 290 % volume increase, which allowed to estimate the water uptake of the fibre and the calculation of an EWC of 74 %. A value of 84 % was found, when the EWC was determined gravimetrically in bulk. Of course, one has to consider that in ESEM the imaging parameters (a $H_2O$ partial pressure of 705 Pa and 100 % humidity) cannot fully reflect the hydration state of the scaffolds immersed in water. In fact, it was observed that the fully swollen scaffolds shrank significantly

*The ESEM experiments were performed in cooperation with Andreas Frank and Prof. Dr. Hans-Werner Schmidt from the Chair of Macromolecular Chemistry I at Bayreuth University.

within the first few minutes in the ESEM chamber. While images were taken quickly, the wet fibre diameters are likely underestimated. Since the solubility of PEtOzi in water is temperature dependant,[126] the 3D-printed structures should also show a temperature responsive swelling behaviour. At low temperatures of 2 °C, the scaffold shown in Figure 4.24 d) encompassed an area of 9 $cm^2$. Increasing the temperature to above 70 °C caused the scaffold to dehydrate as evidenced by a size reduction of 53 % to 4.8 $cm^2$, which is close to the size of the non-swollen structure (4.0 $cm^2$). Importantly, the swelling and de-swelling occured within seconds and was fully reversible. The temperature induced de-swelling was found to be a continuous process, and the relative area decreased rapidly in a linear fashion until 50 °C with a reduction of approximately 10 % relative area per 10 °C (Figure 4.24 f). This temperature compares well with the LCST of PEtOzi being 56 °C.[126] Beyond this temperature the relative area decreased notably slower. Considering the straight forward tunability of the LCST of POx and POzi (see Section 4.3), it could be possible to control the de-swelling profile for future applications.

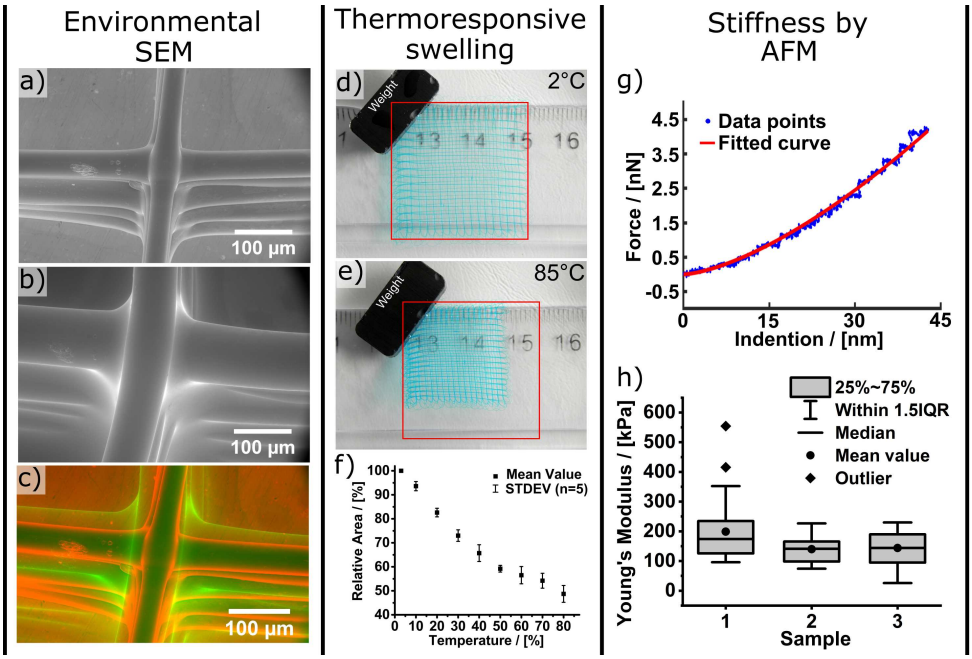


**Figure 4.24:** ESEM image of the dried a) and swollen b) 3D hydrogel scaffold (S4). c) Visualization of the volume decrease by superposition of the swollen and dried 3D hydrogel scaffold. Thermoresponsive de-swelling of the hydrogel architectures at d) 2 °C and e) 85 °C. The red square indicates the size of the scaffold at 2 °C. f) Relative area of the scaffolds depending on the temperature. g) Representative example of a force-distance curve measured on a swollen fibre using a FluidFM® setup. The red line shows the fitting curve using a Hertz Model. h) Young's modulus of three different swollen PEtOzi scaffolds (S5; S6; S7) determined using a FluidFM® setup.[272] (a)-c) Image by Andreas Frank, g), h) Image by Franziska Weigl, published by The Royal Society of Chemistry under Creative Commons licence CC BY-NC-ND 3.0)

A major aim of this project was to overcome a significant limitation that MEW currently suffers, namely the ability to fabricate soft structures. Therefore, the stiffness of the direct-written fibres was studied by colloidal indentation, using an atomic force microscope with the FluidFM® adapted technology.* For this two layered box-like structures were printed, and force distance curves were measured at more than 25 random spots per sample. The Young's modulus was received by fitting of a Hertz model to the traces (Figure 4.24 g). For three separate samples a stiffness ranging from $0.140 \pm 0.042$ to $0.20 \pm 0.10$ MPa was found (Figure 4.24 h). These values compare well to hydrogels with a similar EWC.[89] Putting this into perspective, the Young's modulus for PCL was calculated to be 365 MPa, which is more than three orders of magnitude higher than the DA-based hydrogel fibres. This marks the first time hydrophilic and soft but resilient structures were prepared via MEW.

As visualized in Figure 4.25 a), scaffolds with low amount of layers had little internal strength and collapsed immediately, when they were removed from the water. These structures had the tendency to form very thin strings, which, when being put back into the liquid, immediately unfolded to regain the sheet structure. The cause for this is probably the lack of internal strength in combination with the surface tension of the water. Interesting was that with more layers the prepared scaffolds maintained their shape when taken out of the liquid (see Section 4.3.4). This lack of internal strength allowed manipulation up to a remarkable extent. For example, a two-layered scaffold was easily aspirated into a cannula or glass capillary and also could be ejected again (Figure 4.25 b- d). This was repeated several times without any visible structural damage taken by the scaffold. Back

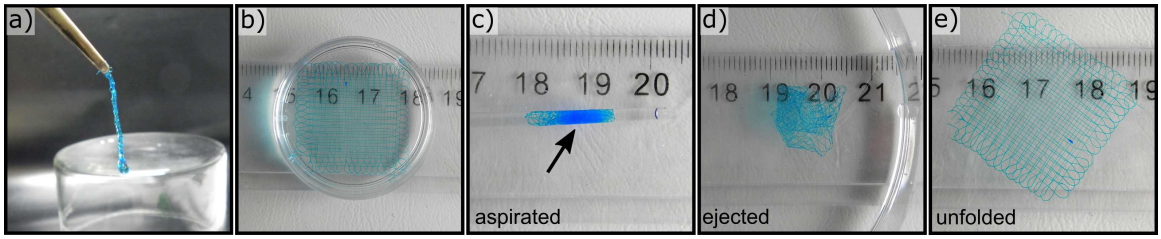


**Figure 4.25:** a) Collapsed swollen scaffold (S8) taken out of the liquid medium. b- e) Illustration of the robust character of the hydrogel scaffold. The swollen scaffold b) can be aspirated in a glass pipette (inner diameter 1.35 mm) c) and ejected again repeatedly d) without causing visible damage to the scaffold, which can be unfolded e) again. Please note that the structures were coloured with DY-647P1-Maleimide for better visualization.[272] (Published by The Royal Society of Chemistry under Creative Commons licence CC BY-NC-ND 3.0)

*The atomic force microscope experiments were performed in cooperation with Dr. Ana Sancho, Franziska Weigel and Prof. Dr. Jürgen Groll from the Department for Functional Materials in Medicine and Dentistry at the University Hospital Würzburg.

in the water, the scaffold could be unfolded and reverted to the sheet-like structure (Figure 4.25 e). It has to be highlighted again that this structure consisted of low-micron sized fibres with a EWC of 84 %. With such properties these structures could serve as injectable micro-structured hydrogel implants, which are highly desirable for ophthalmic or cardiac applications.[274,275] While the 3D-printed structures are mechanically stable, they are also found to be remarkably resistant against hydrolysis. Box scaffolds were incubated for 120 days in deionized water and PBS and were found to be visibly unaffected over this period of time (Figure 8.10). Other groups working with DA crosslinked hydrogels reported that especially the maleimide component is susceptible towards hydrolysis and that the speed of degradation is very much dependent on the pH.[206,243] Long term stability (months) was found in acidic pH, medium term stability (weeks) in neutral pH and short term stability (days) in basic pH. In comparison with these findings, the hydrolytic stability over 4 months in neutral pH was surprising. Therefore, a more detailed study about the degradability was performed and is presented in the section 4.3.

The dynamic nature of the DA reaction as well as the versatile reactivity of the maleimide and furan compound can be utilized in other useful ways. The crosslinking of the two polymeric components is sterically very demanding. Additionally, the molecular dynamics in the printed constructs are retarded by the rapid cooling of the fibres during printing. Both factors favour an imperfect crosslinking, and as a result free furan and maleimide units can be present in the crosslinked polymer fibres. Unfortunately, the generally low ratio of DA functions within the material did not allow direct detection of unreacted furan or maleimide by standard analytical methods like NMR- or IR-spectroscopy. However, it was possible to take advantage of this phenomenon, by modifying the scaffolds post processing, with chemical and biological cues. Demonstrating this, a dry scaffold was simply swollen in an aqueous solution of a maleimide functionalized dye (DY-647P1-Maleimide) and incubated over night. After extensive washing with water and ethanol, the scaffold retained a deep blue colour (Figure 4.26 b) and Figure 8.11 a). Proof for the presences and functionality of the dye gave visualization by both confocal- and two-photon confocal microscopy (Figure 4.26 c- e). Even though the scaffolds were kept in water during visualization, no leakage of the dye into the surrounding medium was noticed. To confirm that the dye is covalently bound and not physically adhered, a negative control experiment was conducted. For this, a different scaffold was incubated with a carboxylic acid derivative of the same fluorescent dye. This dye is therefore non-reactive towards the DA material. Interestingly, the blue colour was also retained even after extensive washing with water. It was however fully removed after washing with ethanol (Figure 8.11 b). In contrast, for the scaffold treated with the maleimide functionalized dye (Figure 8.11 a), the colour is

retained over the course of the whole process. This gave indirect conformation for the covalent bonding of the maleimide dye. It also highlights that the amphiphilic nature of the material prevents a fast release of amphiphilic molecules from the fibres into aqueous medium. Such properties are highly desirable for potential drug release applications. For instance, 3D-printed drug loaded depots or wound dressings are imaginable.

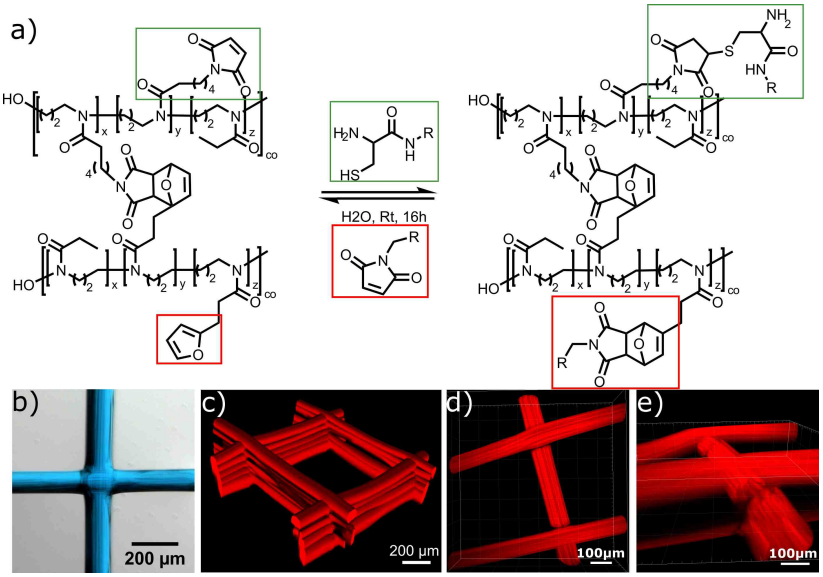


**Figure 4.26:** a) Schematic illustration of the chemical environment in the crosslinked MEW printed fibres. Unreacted DA functions allow the chemical functionalization with maleimide- (red squares) or thiol- (green squares) functionalized molecules post processing. b) Stereomicroscope image of a direct written fibre in hydrated state functionalized with DY-647P1-Maleimide. c) Confocal microscope image and d), e) two-photon confocal microscope image of a fluorescently labelled hydrogel scaffold (S9). The latter reveals a fibril like substructure within the direct written fibres. [272] (c) Published by The Royal Society of Chemistry under Creative Commons licence CC BY-NC-ND 3.0)

However, the chemical reactivity is not limited to maleimide functions but also allows reactions with thiols. To showcase this, scaffolds were incubated with a solution of a FITC dye, conjugated to a short cysteine containing peptide sequence (Cys-Gly-Gly-Lys(FITC)) at different pH (Figure 8.12). Very similar, after extensive washing with water and ethanol the fibres retain a visible yellowish colour and confocal microscopy confirms the presence of the FITC dye. It is important to note that the fluorescent dye was used for demonstrating this reactivity, and that this method will also allow functionalization with a wide range of chemical and biological cues. For instance, protein sequences with cell binding motives (e.g. RGD) can be introduced to control cell adhesion on the hydrogel fibres. Generally, the functionalization process is very straight forward and does not require special equipment or sophisticated chemical background. It is therefore an interesting alternative to other functionalization techniques used in the literature to introduce chemical or biological

cues to potential medical devices or implants. This includes UV induced reaction or conventional thiol-ene reaction.[86,276]

A closer look at the two-photon confocal images revealed a fibril like substructure within the direct written fibres (Figure 4.26 d- e).* Interestingly, these structures are also faintly visible under a normal light-microscope in the form of a stripe like appearance (Figure 4.26 b). This could be interpreted as a sign of flow induced phase separation of the two components of the DA material. Such effects have been reported for melt extrusion of other materials as well. However, in this case it was rather unexpected as the furan and maleimide content in the PEtOzi polymers is low and no major physico-chemical differences were observed during characterization (e.g. in the DSC). In this context it could be interesting to label one of the two components of the DA material with a fluorescent dye (e.g. through irreversible end group functionalization). Two-photon confocal microscopy of the printed fibres could then give information about potential microphase separation of the two components.

### Biological Evaluation

As it is envisioned to use the MEW printed hydrogels constructs for biomedical applications with a special focus on nerve regeneration, excellent biological compatibility is a important requirement. Importantly, PEtOzi is generally regarded to be cytocompatible and half maximal inhibitory concentration ($IC_{50}$) values between 10 and 100 g/L have been reported.[277] Also DA-based materials have been reported to be non toxic as well.[227] Therefore, the presented DA material is expected to show good biological compatibility. Nevertheless, the biomaterial ink was evaluated using a standard DIN-ISO 10993-5 WST-1 cell viability test. Testing the eluate of the bulk material, the viability of L929 mouse fibroblasts was $\geq 86 \pm 3\%$ after 48 h of incubation. This suggests the general safety for biological applications (Figure 4.27 a). Building up on the results presented above, it was also important to verify, whether the microperiodic scaffolds are also compatible with basic cell culture and staining procedures.** Therefore, HEK293 cell seeding and growth on MEW printed hydrogel scaffolds was investigated. Transfected HEK293 cells are a widely used platform in neurobiological research to investigate the expression and function of proteins. Ten-layered scaffolds were functionalized with a short cysteine containing RGD sequence to promote cell attachment. The functionalization was done according to the procedure for thiol coupling discussed above. Already after 4 h of seeding, first signs of cell attachment

*The two-photon confocal images were taken in cooperation with Prof. Dr. Katrin Heinze from the Rudolf Virchow Center for Integrative and Translational Bioimaging at Würzburg University.

**The cell experiments were performed in cooperation with Dr. Natascha Schaefer and Prof. Dr. Carmen Villman from the Institute for Clinical Neurobiology at the University Hospital Würzburg.

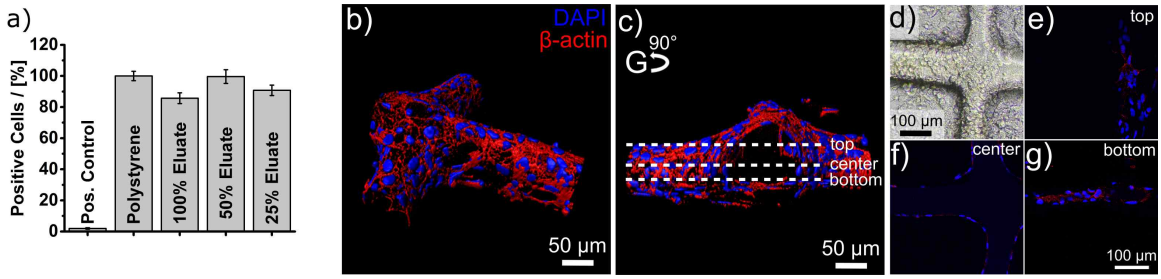


**Figure 4.27:** a) Results of the WST-1 cytotoxicity test of a mixture of **P29** + **P30**. b), c) 3D surface-reconstruction of HEK293 cells attached to a MEW printed scaffold (S10) based on confocal microscope images (Imaris 7.6 software). The cells were stained with the cytoskeletal marker protein $\beta$-actin (red) and nucleus staining DAPI (blue). d) Phase-contrast image of the scaffold seeded with HEK293 cells. The cells are attached along and around the fibres. e)- g) Representative images of one hydrogel filament within the whole scaffold. Pictures from the bottom, the centre and the top are shown and the respective imaging positions are marked in c).[272] (b)- g) Image by Natascha Schaefer, published by The Royal Society of Chemistry under Creative Commons licence CC BY-NC-ND 3.0)

were visible using a light microscope (Figure 4.27 d). Following 4 d of culturing on the scaffold, the cells were stained for the cytoskeleton protein $\beta$-actin (red) as well as the nucleus (blue). Using confocal microscopy, a 3D re-construction of the cell morphology around the fibres was prepared (Figure 4.27 b, c, e- g). This showed that the cells fully covered and wrapped around the fibres. Importantly, the fibres remain transparent after the staining procedure. Therefore, no significant uptake of the staining agents did occur. The transparency even enabled the visualization of cells spreading underneath the structures. These tests highlight that the MEW processed architectures are non-cytotoxic and allow the attachment of HEK293 cells. Furthermore, the scaffolds are compatible with standard cell culture procedures.

### Summary

Summarizing this chapter, the synthesis and characterization of a PEtOzi-based hydrogel platform was reported. It was possible to consolidate DA click chemistry with MEW processing and to manufacture chemically crosslinking hydrogel constructs. This is the first time, this important material class becomes available for this direct writing technique. Compared to the $1^{st}$ generation of the DA material, the absolute content of furan and maleimide was reduced and the functionalization conditions were optimized. The amount of residual secondary amines in the material was reduced and the liquefaction of already crosslinked material via rDA reaction was finally possible. This ultimately opened the way for MEW processing. Under inert conditions, IR analysis, DSC and rheology indicated good thermal reversibility of the material. However, during MEW processing, thermally induced changes were still observed, which ultimately limited the processing time window to 1-

2 h. This issue will be discussed in the following section. The prepared architectures were soft (0.140 MPa) yet remarkably robust. Post processing, the DA equilibrium offered the possibility to covalently bind molecules to the construct. This was shown exemplary with fluorescent markers, but the presented concept potentially allows to bind catalysts, biological cues or other entities of interest as well. The material was found to be non-cytotoxic to L929 mouse fibroblasts as well as HEK293 cells and the microperiodic architectures proved to be compatible with standard cell culture procedures.

### 4.2.4 Improving the Diels-Alder Material

Two phenomena impeded a continuous MEW processing in the experiments discussed in section 4.2.3. First, the presence of gas bubbles in the melt and second a gradual change of the processability of the DA material. All in all a short processing time window of 1-2 h was observed, which severely limited the applicability of the developed material. Improvements regarding both of these issues were required to allow a more reliable and predictable printing process.

It was noticed that gas bubbles can cause a complete interruption of the polymer jet as soon as these are extruded through the nozzle. This causes missing fibres or even whole layers in the printed construct. Following on the interruption of the jet, a droplet is formed at the printer nozzle and then deposited on the printed structure as soon as the jet is re-established. This droplet will cause further disruption of the subsequent fibre deposition, which also leads to stacking errors and misplaced fibres. Because of the oxygen sensitivity, a technique for the full removal of trapped gas bubbles under the full exclusion of oxygen from the melt was established. This method is described in detail in section 7.2 and it was used for every printing process described from hereon.

In the used MEW setup, the whole polymer reservoir is continuously heated for the full time period of the printing process. This creates a very demanding environment regarding the thermal stability of the processed polymer. Oppositional to this is the objective to chemically crosslink the printed constructs post processing, as this requires the incorporation of reactive molecules into the material. Generally, chemical reactivity can not be fully separated from thermal reactivity. Above all, the MEW process is very sensitive to degradation and changes of the processed polymer.[49,50] In the preceding section a detailed analysis of the thermal reversibility and stability was presented. Even though TGA under synthetic air showed no thermal degradation in the MEW processing temperature range, one has to be aware that reactions without a mass loss can not be detected by this method (Figure 8.9). DSC analysis (under $N_2$ atmosphere) showed a gradual decrease in the reaction heat in 7 cycles. Rheology under ambient conditions revealed irreversible solidification of the material at the polymer/air interface (Figure 8.7). In contrast, when performed under inert conditions, consecutive oscillation measurements showed good thermal reversibility. This gives the hint that these side reactions are oxygen induced or accelerated, although in the context of the DA reaction such reactivity is not well studied in literature. In contrast, there are reports of the maleimide/furan pair showing good reversibility even in the presence of oxygen.[238,278,279] Literature known side reactions of the maleimide/furan pair are

aromatisation of the adduct,[255,280] ring opening of the furfuryl ring[253] and homopolymerization of the maleimide.[257,281] Interestingly, none of these are reported in relation to the presence of oxygen. However, the oxygen radical initiated homopolymerization of maleimide is feasible under elevated temperatures. Even though special focus was set on the exclusion of oxygen during MEW, for instance by using nitrogen pressure to deliver the melt to the nozzle, the $2^{nd}$ generation of DA material allowed only a limited printing time window. During this time, a continuous deceleration of the polymer jet was observed and to counteract this, it was necessary to either decrease the CS or to increase the acceleration voltage. Otherwise extensive dragging of the jet was observed, which prevented a controlled deposition of the fibres. With a constant collector distance of 3.3 mm, the acceleration voltage had a upper limit of approximately 6 kV as arcing occurred at higher voltages. At this point it was necessary to increase the NT in small temperature steps of 2 °C, which caused temporary acceleration of the jet and allowed to decrease the acceleration voltage again. This process was usually iterated until no stable jet could be established anymore. For better visualization, a timeline of a mediocre printing experiment is displayed in Figure 4.28 a). In the beginning, reasonable printing results were achieved, yet over time the printing performance decreased significantly. After 50 min, severe instabilities, like breaking of the jet as well as longbeading, decreased fibre stacking capabilities and caused several missing layers in the printed scaffold. Increasing ST as well as NT allowed prolonging of the processing time, yet instabilities increased further and no reasonable structures were fabricated anymore.

In addition, the processability varied from batch to batch even though the synthesis procedures were kept identical and the analytical results varied only little (Table 4.8). While the mixture of **P27** + **P28** only allowed poor printing quality (Figure 4.28 a), the printing was generally more stable and well structured constructs were achieved with **P29** + **P30** (Figure 4.23 a) as well as **P31** + **P32** (Figure 4.28 a). Above all, when using the same batch of material, there were also printability variations observed on a print to print basis. While well structured constructs with little defects were prepared in one printing session (Figure 4.28 b), the same set of parameters gave only mediocre results in a following session (Figure 4.28 c). Noteworthy is also the difference in CS that had to be used in those two sessions. This indicates a drastic difference of the jet velocity, when the same material was processed on different days. These effects prevented the definition of a generalized parameter set, which would allow the stable processing of a PEtOzi$_{100}$-5% polymeric ink. Also the range of application was limited by this, as larger constructs were not accessible due to the limited processing time. Defects prevented a smaller fibre spacing and a precise control over the fibre diameter. Considering the preceding discussion, it was hypothesized that

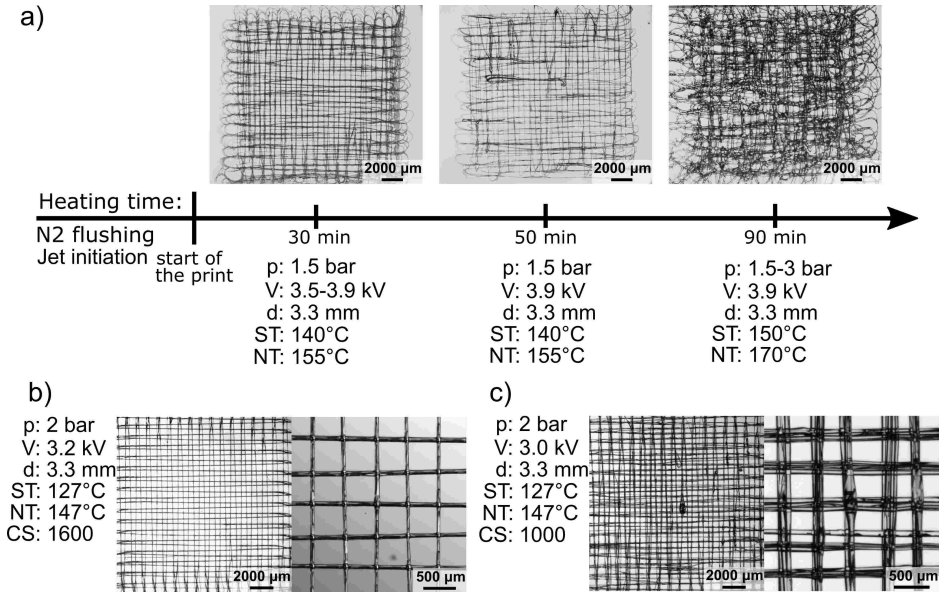


**Figure 4.28:** a) Timeline demonstrating the printability changes of a mixture of **P27** and **P28**. b), c) Box-scaffolds printed using a mixture of **P31** and **P32**. Despite the fact that the same material and processing parameters were used, the printing quality is noticeable different.

the thermal degradation and the processing inconsistencies of the DA material might be caused by impurities remaining within the material and not necessarily by a reaction of the maleimide/furan pair itself. Therefore, the synthesis scheme was revised and several steps with potential for improvement were identified (Figure 4.29). Post dialysis it was noticed that small amounts of yellowish residue, insoluble in water, would remain in the sample. During printing, such solids might cause clogging of the nozzle or disrupt the polymer jet. Therefore, from now on the polymer solution was concentrated post dialysis followed by removal of any non-dissolved particles via filtration. For both, the 3-(2-furyl)propionic acid as well as the 6-maleimidohexanoic acid, purification steps were added. 3-(2-furyl)propionic acid was synthesized from its ester derivative via hydrolysis under basic conditions. After purification via extraction, a crude mixture of yellowish and white crystals was recovered. Despite the fact that the $^{1}$H-NMR spectra showed no side products, according to literature reports a colourless/white appearance of 3-(2-furyl)propionic acid is to be expected. It was noticed that the raw solid is readily molten and distilled at 80 °C and 2x10$^{-3}$ mbar. Afterwards, the product was recovered as white and slightly transparent crystals, which indicated a successful purification. Still, no changes could be observed in $^{1}$H-NMR spectrum. 6-Maleimidohexanoic acid was purchased from Sigma-Aldrich and was used before without further purification. To ensure high purity, an additional recrystallization step was added. Post functionalization of the partially hydrolysed polymers, the reaction mixture contains a large variety of substances that require removal. Before, these were removed by centrifugation, filtration and precipitation. However, two compounds might still be partially present

after these steps. First, dicyclohexylurea is partially soluble in MeOH. Therefore, traces will remain in the sample post centrifugation and filtration. Also, as it is insoluble in diethyl ether, precipitation will not remove these traces. Full removal is assured as filtration is performed in concentrated aqueous solution (a non-solvent for dicyclohexylurea). Second, the hydrolysed polymers still contain traces of NaOH from the synthesis process. In the molten polymer, NaOH will be very reactive and cause side reactions, like ring opening of the maleimide. Therefore, as a final step in the purification of the functionalized polymers, dialysis against MilliQ water was performed.

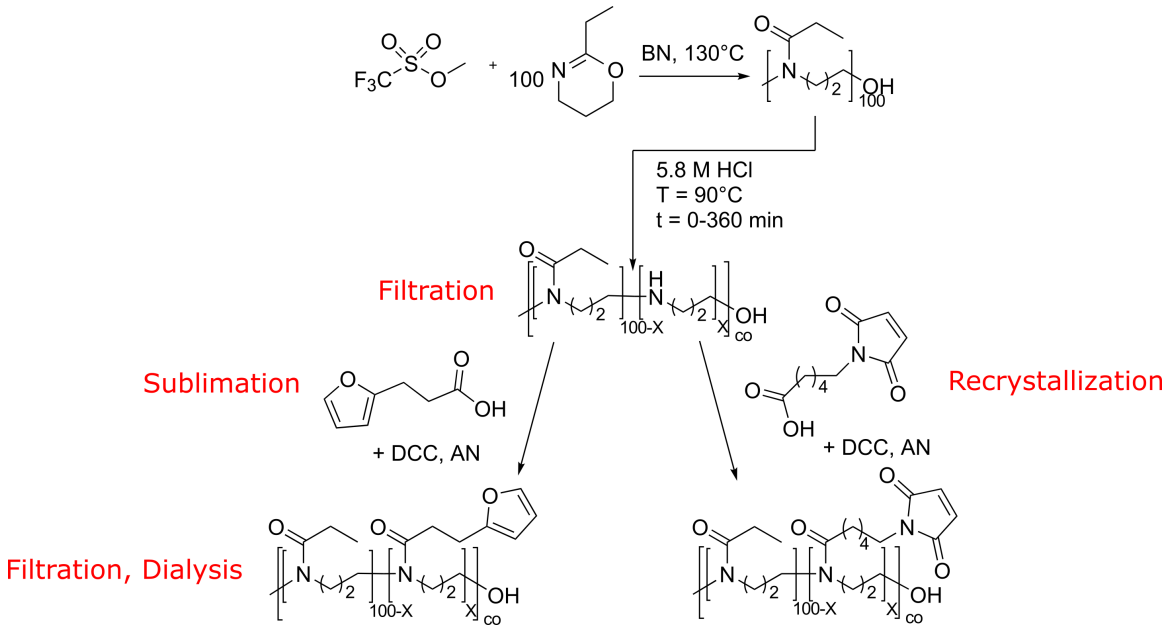


**Figure 4.29:** Schematic illustration of the synthesis path for the preparation of maleimide and furan functionalized poly(2-ethyl-2-oxazine). Highlighted in red are additional purification steps, potentially leading to improved thermal stability of the DA material.

### 4.2.5 3rd Generation

Applying these changes, a new generation of DA functionalized PEtOzi was synthesized (Table 4.9). All DA polymers synthesized according to the revised protocol will be referred to as the $3^{rd}$ generation. Additionally, for the polymers **P33** and **P34**, the targeted hydrolysis degree was decreased from 5 to 4 %. Interestingly, for both polymers the FD was found to be higher than the hydrolysis degree. This is potentially caused by partial functionalization of the "OH" termini in addition to the secondary amines. The rheology temperature sweep showed good thermal reversibility for the $3^{rd}$ generation of DA material (Figure 4.30 a). However, it also revealed slightly lower absolute values of both $G'$ and $G''$ as well as a lower temperature for the liquefaction point when compared with a mixture of **P31** and **P32** ($2^{nd}$ generation). Both factors indicate a slightly lower degree of crosslinking for the polymers **P33** and **P34**, even though, both material batches had a similar average FD. This was possibly caused by an imbalance of furan and maleimide, since the DF of **P33** differed from **P34** by 0.5 % (Table 4.9). To mimic the thermal stress in the MEW

**Table 4.9:** Selected analytical data of the hydrolysed and the furan and maleimide functionalized polymers of the $3^{rd}$ generation of DA material.

| ID | PC,theo | $M_n^a$ | Đ | $HD_t$ | $HD_e^b$ | $DF_e^b$ |
|---|---|---|---|---|---|---|
| **P33** | $PEtOzi_{100}$-4%-Fu | 3.2 | 1.09 | 4 % | 3.5 | 4.0 |
| **P34** | $PEtOzi_{100}$-4%-Ma | 3.5 | 1.11 | | 3.5 | 4.5 |

Determined by: $^a$ GPC (HFIP) in [kg/mol]; $^b$ $^1$H-NMR in [%]

device, the melt viscosity of the $2^{nd}$ and $3^{rd}$ generation of DA material was determined over 8 h at a constant temperature of 127 °C (Figure 4.30 b). This temperature was also used as ST in several of the above discussed MEW experiments. Furthermore, it is close to the liquefaction temperature of the materials and even small changes in the material should result in a noticeable increase of the melt viscosity. For both DA polymers, a steep increase of the viscosity was observed in the first 20 min of the experiment. This likely marks the time until the DA equilibrium was fully established. For the $2^{nd}$ generation, the viscosity continued to increase at a slower pace for 3 h, until the material solidified and the measurement was terminated. In contrast, the polymers of the $3^{rd}$ generation showed almost no change of viscosity over 8 h. This indicates an increased thermal stability of the $3^{rd}$ generation due to the improvements made to the synthesis procedure. Based on these results, the MEW processing performance for the $3^{rd}$ generation of DA material was investigated in a long term printing experiment. Therefore, at each time point a parameter set allowing stable processing was determined followed by the fabrication of a box-like scaffold with three x- and y-layers. The printing performance was evaluated qualitatively from

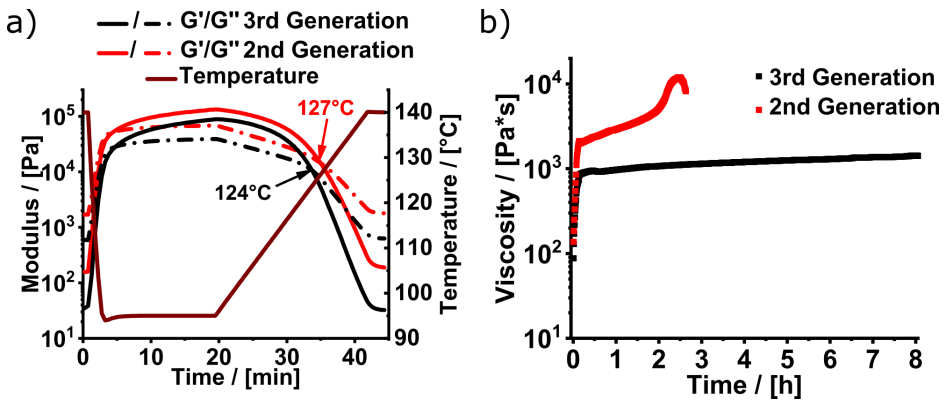


**Figure 4.30:** a) Comparison of the thermal dynamics of the $2^{nd}$ generation and $3^{rd}$ generation of DA material. The arrows indicate the liquefaction temperatures. b) Long term melt viscosity, determined at a constant shear rate of 1 1/s and a temperature of 127 °C.

stereomicroscope images of the structures. After reaching thermal equilibrium (0.5 h), the first printed structure showed excellent fibre stacking capabilities with only minor long-beading defects (Figure 4.31 a). Interestingly, even after 1.5 h it was possible to use the same parameter set, while maintaining a high structural accuracy (Figure 4.31 b). Even though, a deceleration of the polymer jet became noticeable, it is important to highlight that after such a time period already major disruptions were observed for the processing of the $2^{nd}$ generation of DA polymers. With increasing heating time, the acceleration voltage was gradually increased to 5.0 kV for 3.5 h of heating. Striking was that even after 8 h of continuous heating, the material was still processable and reasonable printing quality was achieved (Figure 4.31 d). Please note that due to arcing a maximal voltage of 5.7 kV was applicable. Therefore, the CS had to be decreased to 1350 mm/min in order to compensate for the continuous decreasing jet velocity. This already marks the longest continuous printing experiment achieved with a DA material throughout this thesis. Heating was continued over night and even after 22 h of prolonged heating, the polymer still remained liquefied and processable. However, at this point the jet velocity was drastically reduced. This becomes clearly visible, when comparing the first scaffold from this experiment with the scaffold printed after 22 h (Figure 4.31 a, e). While for both the same parameter set was used, the latter structure deviates strongly from the printing path given by the g-code. This is particularly noticeable by the cutting of the turns as well as the skewed fibre deposition. This qualitative study already shows major improvements of the thermal stability achieved in the $3^{rd}$ generation. While the improvements made to the synthesis procedure and the sample preparation allowed significant prolonging of the processing time, the continuous deceleration of the MEW jet velocity remained. To gain a more quantitative measure of this phenomenon, a second long term printing study was performed and the CTS of the material was determined over a period of 23 h (Figure 4.31 f). Again, the CTS

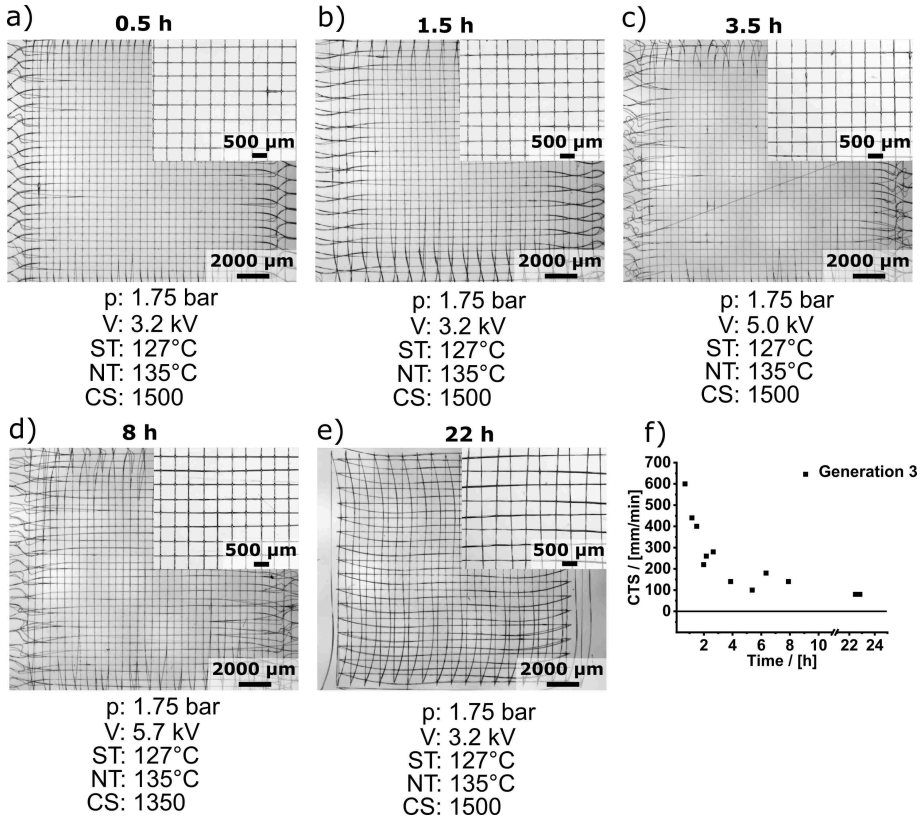


**Figure 4.31:** a)- e) Qualitative evaluation of the processing performance for the $3^{rd}$ generation of DA material (mixture of **P33** and **P34**). Stereomicroscope images of the scaffolds prepared via MEW at various time points. The printing parameters used for each scaffold are listed underneath the respective image. f) CTS development over 23 h of continuous heating. The applied printing parameters were: $p$ 1.75 bar; $V$ 3.2 kV; $d$ 3.3 mm; NT 135 °C; ST 127 °C.

was determined by applying the printing scheme presented in Figure 4.14. This revealed a very rapid deceleration process. The CTS dropped within two hours from its initial value of 600 mm/min to a value of 220 mm/min, and the CTS showed some fluctuations. For instance in the time frame of 2-2.5 h, it covered the range between 220 and 280 mm/min. Between 4 and 23 h the CTS approached a plateau around 100 mm/min. This clearly shows that thermally induced changes in the material still have a strong impact on the CTS, yet as shown in Figure 4.31 a)- d), printing quality can be maintained by adjusting the printing parameters. It has to be highlighted that this adjustment was done manually. Therefore, the automation of long term printing experiments remains an open challenge. A very interesting approach would be an optical feedback loop that automatically reacts to fluctuations in the polymer jet, maintaining a consistent processing. Such a system has already been reported for MEW, but was not available in the scope of this thesis.[282] Interesting would also be, if the material could be thermally annealed before printing. This could allow to omit the deceleration phase, and the printing process could be started in the more consistent plateau like region.

Very striking however, is the disconnection between the investigations of the material degradation with standard polymer analysis methods and the results gained from MEW processing. In this context it is important to note that the MEW jet velocity is believed to be influenced by more factors than the melt viscosity. Among others, these are polarisability, conductivity or ion content. No studies have explored the influence of these factors on the processing performance this far. The CTS development indicates that this phenomenon is rapid in the beginning of the heating process, but it slows down with prolonged heating times. It could be imaginable that a reactant is present in a limited amount and is used up with time. The purification procedure for the $3^{rd}$ generation was performed carefully to a point, where it was a rather time consuming and tedious process. Therefore at this point the cause of these observations is unclear.

Reducing the DF certainly helped to improve the printing quality and prolonged the printing time window. However, it was noticed that this simultaneously led to a reduced shape fidelity of the printed constructs (Figure 4.32 a). The low $T_g$ of the PEtOzi-based DA polymers still allows material flow until the DA crosslinking is sufficiently progressed. This caused the fibres to loose the cylindrical shape and merge with the underlying fibres to form a continuous polymer wall (Figure 4.32 a, inset). In a preliminary test, a small batch of DA material based on the MeOx containing copolymer **P12** with a comparable DF, was synthesized. It was possible to process this material with MEW as well, and the fibres showed excellent shape fidelity (Figure 4.32 b, inset). The $T_g$ of this polymer mixture was with 35.5 °C higher than the PEtOzi-based material, and this successfully reduced polymer flow.

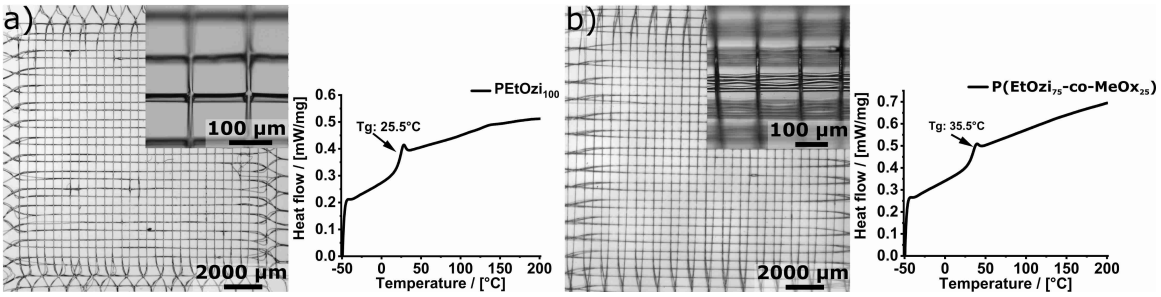


**Figure 4.32:** a) MEW printed mesh (S11) made from **P35**+**P36** based on a PEtOzi homopolymer with respective DSC data (arrow highlights the $T_g$). The inset shows the loss of shape fidelity of the printed fibres. b) MEW printed mesh (S12) made from **P37**+**P38** based on a P(EtOzi-co-MeOx) copolymer with respective DSC data (arrow highlights the $T_g$). The inset shows the retention of shape fidelity of the printed fibres.

Summing up this section, very noticeable improvements could be made for the $3^{rd}$ generation of DA material. Changes in the purification procedure and the sample preparation allowed a significant extension of the printing time. The processing performance was im-

proved, enabling a more precise fibre deposition and leading to more defined architectures. Despite thermally induced side-reactions were found to be retarded, they could not be fully prevented. Therefore, the CTS of the material is still decreasing over the course of a prolonged printing experiment. In contrast to the $2^{nd}$ generation, for the $3^{rd}$ generation of DA material, minor adjustments to the processing parameters allowed to maintain stable processing over several hours.

# 4.3 Expanding the Material Platform

## 4.3.1 The Polymer Platform

From the data presented in the preceding chapters, it became apparent that reducing the DF has a positive effect on the printability and thermal stability. However alongside, the shape fidelity of the printed constructs did decreased. Increasing the $T_g$ via copolymerization with EtOx and MeOx monomers could be a viable strategy to combine shape fidelity with long term processability. Also, changing the chemical composition of the polymer backbone will influence the hydrophilicity of the system and therefore increase swelling and decrease stiffness of the resulting constructs. Biologically relevant parameters like protein adsorption might be influenced in this manner as well. Furthermore, decreasing the DF will result in major changes of the swelling properties. The work presented in the following section aims to broaden the polymer platform of Ozi- and Ox-based DA materials (Figure 4.33). Effects on the processing performance and the resulting constructs will be investigated and discussed. Valuable correlations of the polymer and material properties with the MEW processing as well as the characteristics of the fabricated products will be displayed. Deriving the required hydrolysis times from the corrected kinetics described in section 4.2.1

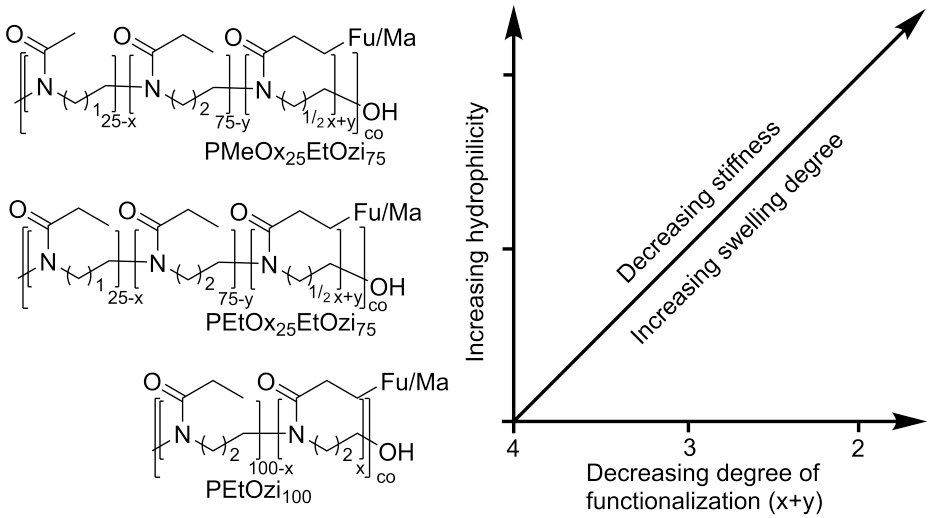


**Figure 4.33:** Schematic illustration of the polymers synthesized to expand the DA-based material platform (left). Postulation of the influence of the polymer structure on the material and construct properties (right).

allowed the precise hydrolysis of the three parent polymers **P9**, **P11** and **P12** to a $HD_t$ of 2, 3 and 4 %. The hydrolysis degree was then determined by $^1$H-NMR analysis as well as acid-base titration (see Table 4.10). Compared to the polymers of the $1^{st}$ and $2^{nd}$ generation, the hydrolysis temperature was reduced from 90 to 75°C. The experimental values determined via titration ranged with $\pm$ 0.3 % close to the $HD_t$ values of 3 and 4 %.

For the $HD_t$ values of 2 %, the experimental values showed a slightly higher and strictly positive deviation of +0.4 to +0.5 %. All things considered, slight positive deviations from the theoretically calculated values were expected, as the corrected hydrolysis kinetics do not account for the $HD_0$ (see Section 4.1.3) of the parent polymers.

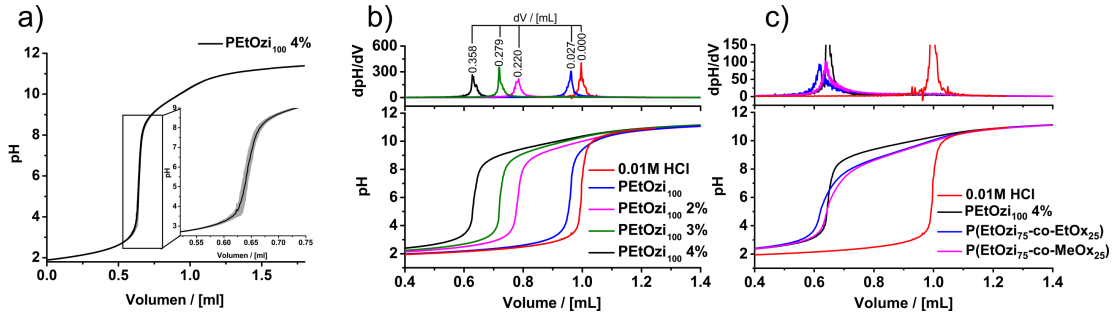


**Figure 4.34:** a) Acid-base titration of **P39**. The solid line represents the mean curve of five separate titrations. The grey band is one standard deviation. For better visualization, a magnified area around the equivalence point is shown in the inset. b) Comparison of the titration curves of the partially hydrolysed $PEtOzi_{100}$ batches **P9**, **39**, **40**, **41** with the master curve of 0.01 M HCL. The $1^{st}$-derivative of each curve with the receptive volume difference to the peak of the master curve is shown above. c) Comparison of the titration curves of the homo- and copolymers hydrolysed to 4 % (**P39**, **42**, **43**). The $1^{st}$-derivative of each curve is shown above.

Generally, titration has proven to be a very sensitive tool for determining the hydrolysis degree. Very low deviations were found between separate titrations of the same sample (Figure 4.34 a). For titration, the respective polymers were dissolved in 0.01 M HCL (10 g/L). 1 M NaCl was added, since this produced more defined pH transition steps. For each polymer, five samples were titrated against 0.1 M NaOH solution, and the hydrolysis degree was determined by finding the equivalence point of each titration curve, which is marked by a maximum in the $1^{st}$-derivative of pH by volume (Figure 4.34 b). The addition of partially hydrolysed polymers causes a shift or volume difference dV of the equivalence point with respect to the master curve (titration of 0.01 M HCL). This shift is caused by a partial "consumption" of the HCl by the secondary amines of the polymers. As the polymer molar mass as well as the concentration is known, one can easily calculate a mean hydrolysis degree of the polymer from the respective dV value. The titration of **P9** as well as the corresponding hydrolysed batches are displayed in Figure 4.34 b). For all hydrolysed polymers, a prominent volume shift of the equivalence point compared to the reference can be seen. Important to note is also the small but distinct shift, visible for the non-hydrolysed parent polymer **P9**, which is caused by the irregular termination (see Section 4.1.3). Very obvious is also the difference in buffer capacity between the hydrolysed polymers derived from the PEtOzi homopolymer compared to the polymers derived from the copolymers **P11** and **P12**. While **P39** (homopolymer) shows almost no buffer capacity, this was much

more pronounced for **P42** and **P43** (Figure 4.34 c). This effect could be explained by the polymer structure. Since MeOx and EtOx units are much more readily hydrolysed than the EtOzi units, it is likely that the majority of the hydrolysed units in the copolymers are MeOx and EtOx units. Moreover, due to the polymerization kinetics, the copolymers are expected to show a strong block character. This favours closer spatial proximity as well as cooperative effects of the amines in the copolymers.[283,284] Compared to this, a random distribution is expected in the homopolymers. However, the increased buffer capacity might also be due to a difference in the protonation behaviour of ethyleneimine (copolymer) and propyleneimine (homopolymer) groups. Full and partially hydrolysed POx are well-known polycations for the transfection of cells.[11] As the application range of PEI is hampered by its high toxicity, partially hydrolysed POx is investigated as a less toxic alternative. Currently, POzi is not included in these research efforts, although it might offer interesting capabilities for controlling the properties of these transfection agents. Compared to the

**Table 4.10:** Comparison of hydrolysed homo- and copolymers with respective analytical data.

| **ID** | $HD_t{}^a$ | Time | $HD_{e,tit}{}^b$ | $HD_{e,NMR}{}^c$ | $HD_{e,corr}{}^d$ | $HD_{e,corr}+HD_0{}^e$ |
|---|---|---|---|---|---|---|
| Parent polymer, $PEtOzi_{100}$ / **P9** | | | | | | |
| **P40** | 2 | 65 | 2.4 | 3 | 2 | 2.4 |
| **P41** | 3 | 102 | 3.2 | 3.7 | 2.7 | 3.4 |
| **P39** | 4 | 139 | 4.1 | 4.8 | 3.8 | 4.5 |
| Parent polymer, P($EtOzi_{75}$-co-$EtOx_{25}$) / **P11** | | | | | | |
| **P44** | 2 | 49 | 2.5 | 3.4 | 1.7 | 2.3 |
| **P45** | 3 | 73 | 3.1 | 4.2 | 2.4 | 3.0 |
| **P42** | 4 | 98 | 4.3 | 5.1 | 3.4 | 4.0 |
| Parent polymer, P($EtOzi_{75}$-co-$MeOx_{25}$) / **P12** | | | | | | |
| **P46** | 2 | 36 | 2.4 | 3.8 | 1.9 | 2.4 |
| **P47** | 3 | 56 | 3.1 | 4.3 | 2.4 | 2.9 |
| **P43** | 4 | 76 | 3.7 | 5.2 | 3.3 | 3.8 |

Parameter in: $^a$ [%]; $^e$ [%]

Determined by: $^b$ acid-base titration (n=3) in [%]; $^c$ $^1$H-NMR analysis (n=1) in [%]
Calculated as: $^d$ by subtraction of the average 0 min integral of the respective hydrolysis kinetic from the $HD_{e,NMR}$ value

values derived from titration, the non-corrected hydrolysis degrees determined via $^1$H-NMR analysis, showed much higher deviation from the targeted values (Table 4.10). It was found that these can be corrected by subtraction of the NMR baseline ($HD_{e,corr}$) and adding the $HD_0$ of the respective parent polymers. The resulting values are then comparable with the titration data. All in all the reduced reaction temperature allowed superior control over the hydrolysis degree, yet adjusting the hydrolysis degree by steps of 1 % seems to be close to the minimal step size for these hydrolysis parameters. In particular, for the copolymers

**P11** and **P12**, which show faster reaction kinetics, even lower hydrolysis temperatures of 60 or 50°C are advisable. For the low degrees of hydrolysis, the required reaction times are very short and slight deviations in the starting conditions (e.g. heating rate of the magnetic stirrer) can have a strong influence on the results.

Following hydrolysis, the polymers were functionalized using the improved procedure discussed in section 4.2.4. Notable was the positive deviation of the DF from the hydrolysis degree. While this difference was only minor for the batches based on the PEtOzi homopolymer, it was much more pronounced for the batches based on the EtOx and MeOx containing copolymers. Two factors can be made responsible for this deviation. First of all, due to the careful purification procedure remaining unbound furan or maleimide can be confidently excluded. A conclusive explanation however, is that the "OH" termini of the polymers were partially functionalized as well. While, "OH" functions are much less reactive than amines in DCC supported couplings, a large excess of DA functions and coupling reagent was used. Another factor is that the copolymers showed much broader signals in the $^1$H-NMR spectra, which leads to reduced precision in the determination of DF. Based on the available data, it is not possible to distinguish which effect played the primary role. However, for further experiments it is advisable to use a terminating reagent which results in non-nucleophilic end-groups, to exclude the possibility of end-group functionalization. Generally it is important to notice that the determination of a polymer structure based on $^1$H-NMR spectra is error prone and subjective. This is due to differences in the integration procedure as well as in the post-processing procedure of the spectra. Again, distinguishing between a DF of 2, 3 and 4 % is close to the resolution limit of the NMR method. It is well established that POx and POzi exhibit a pronounced LCST behaviour, and that the water solubility of the polymers is strongly temperature dependant.[11,126,149] The extend of this effect is controlled by the substituent on the 2-position of the monomer. While PMeOx shows no cloud point temperature ($T_{CP}$), a LCST of 94 and 25 °C has been reported for ethyl or *n*-propyl side chains respectively.[149] In this project, the $T_{CP}$ was used as a measure for the hydrophilicity of the parent polymers as well as the furan and maleimide functionalized polymers. It was hypothesized that the copolymerization of EtOzi with MeOx and EtOx allows adjusting of the hydrophilicity of the DA-based biomaterial ink. For this, the respective polymers were dissolved in MilliQ water with a concentration of 5 g/L, and UV-Vis spectra of the solutions were taken at different temperatures. The change of transmission at 600 nm was monitored and plotted against the temperature. The LCST was determined as the first measured temperature at which the transmission dropped below 90 % (Figure 4.35 a). For the EtOzi homopolymer **P9**, an LCST of 51°C was found. This compares well with the value reported in literature of 56°C.[149] Incorporation of 25% of

**Table 4.11:** Synthesized homo- and copolymers with respective analytical data.

| ID | PC,theo | Funct. | $HD_{e,t}{}^{a}$ | $DF_{e}{}^{b}$ |
|---|---|---|---|---|
| | Parent polymer, $PEtOzi_{100}$ / **P9** | | | |
| **P48** | $PEtOzi_{100}$-2%-Fu | Fu | 2.4 | 2.4 |
| **P49** | $PEtOzi_{100}$-2%-Ma | Ma | 2.4 | 2.4 |
| **P50** | $PEtOzi_{100}$-3%-Fu | Fu | 3.1 | 3.3 |
| **P51** | $PEtOzi_{100}$-3%-Ma | Ma | 3.1 | 3.4 |
| **P52** | $PEtOzi_{100}$-4%-Fu | Fu | 4.1 | 4.5 |
| **P53** | $PEtOzi_{100}$-4%-Ma | Ma | 4.1 | 4.3 |
| | Parent polymer, P($EtOzi_{75}$-co-$EtOx_{25}$) / **P11** | | | |
| **P54** | P($EtOzi_{75}$-co-$EtOx_{25}$)-2%-Fu | Fu | 2.5 | 3.2 |
| **P55** | P($EtOzi_{75}$-co-$EtOx_{25}$)-2%-Ma | Ma | 2.5 | 2.8 |
| **P56** | P($EtOzi_{75}$-co-$EtOx_{25}$)-3%-Fu | Fu | 3.1 | 4.1 |
| **P57** | P($EtOzi_{75}$-co-$EtOx_{25}$)-3%-Ma | Ma | 3.1 | 3.5 |
| **P58** | P($EtOzi_{75}$-co-$EtOx_{25}$)-4%-Fu | Fu | 4.3 | 4.3 |
| **P59** | P($EtOzi_{75}$-co-$EtOx_{25}$)-4%-Ma | Ma | 4.3 | 4.5 |
| | Parent polymer, P($EtOzi_{75}$-co-$MeOx_{25}$) / **P12** | | | |
| **P60** | P($EtOzi_{75}$-co-$MeOx_{25}$)-2%-Fu | Fu | 2.4 | 2.9 |
| **P61** | P($EtOzi_{75}$-co-$MeOx_{25}$)-2%-Ma | Ma | 2.4 | 2.8 |
| **P62** | P($EtOzi_{75}$-co-$MeOx_{25}$)-3%-Fu | Fu | 3.1 | 3.5 |
| **P63** | P($EtOzi_{75}$-co-$MeOx_{25}$)-3%-Ma | Ma | 3.1 | 3.6 |
| **P64** | P($EtOzi_{75}$-co-$MeOx_{25}$)-4%-Fu | Fu | 3.7 | 4.7 |
| **P65** | P($EtOzi_{75}$-co-$MeOx_{25}$)-4%-Ma | Ma | 3.7 | 4.5 |

Determined by: $^{a}$ acid-base titration (n=3) in [%]; $^{b}$ $^{1}$H-NMR analysis (n=1) in [%]

Abbreviations: Fu 3-(2-furyl)propionic acid; MaP 3-maleimidopropionic acid

EtOx or MeOx into the polymer increased the LCST to 59 and 85 °C respectively. While EtOx showed only moderate influence on the LCST, MeOx, being a strongly hydrophilic monomer, had a drastic influence on the water solubility of the copolymer. Very striking however, was the drastic decrease of the $T_{CP}$ upon incorporation of even small quantities of furan and maleimide into the polymers (Figure 4.35 b). For example, the functionalization of **P12** with 2.9 % furan resulted in a drop of 23 to 62 °C with respect to the parent polymer. A very similar but less pronounced decrease was seen for the functionalized polymers based on **P9** and **P11**. However, for all three polymer backbones, a roughly linear dependency of the LCST on the DF can be estimated in a range from 0 to 5 %. This highlights that by changing the chemical structure of the polymer backbone and the DF the hydrophilicity and thermoresponsiveness of the DA material can be controlled for potential applications. For the PEtOzi-based polymers functionalized to 4 % with furan and maleimide, an surprisingly low LCST of 34 °C was found. This does not relate well to the results presented in section 4.2.3, where it was found that the MEW printed scaffolds based on

a 5 % functionalized PEtOzi exhibit significant swelling well beyond 50 °C. It is imaginable that the hydrophobic influence of the furan and maleimide is significantly reduced by the formation of the bicyclic adduct as two hydrophobic moieties are combined to one. The LCST of an aqueous mixture of **P52** and **P53** was found at a similar temperature (31 °C) as the single components. However, it is likely, that the crosslinking efficiency in diluted solutions is much reduced compared to the bulk material. Therefore, aqueous mixtures can not fully reflect the situation of the melt processed material.

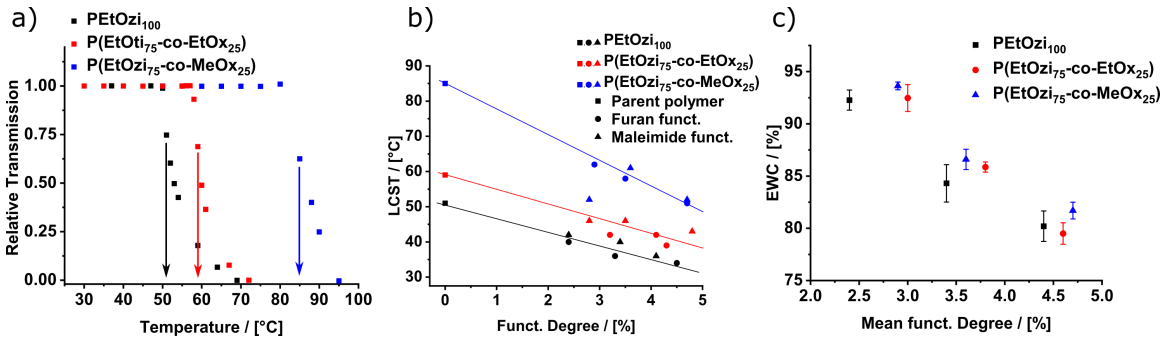


**Figure 4.35:** a) Relative transmission at 600 nm for 5 wt% solutions of the polymers **P9**, **11**, **12** depending on the sample temperature determined via UV-Vis spectroscopy. Arrows indicate the respective LCST temperature. b) LCST of furan and maleimide functionalized PEtOzi-based homo- and copolymers determined via UV-Vis. The lines do not represent linear fits, but are meant to guide the eye. c) Mean EWC (n=4) with one standard deviation of the DA crosslinked PEtOzi-based homo- and copolymers at 20°C.

Besides the hydrophilicity, the swelling properties of the DA crosslinked polymers are of major importance for the properties of the MEW printed constructs. Therefore, the DA functionalized PEtOzi-based homo- and copolymers were mixed using the $N_2$ technique. The mixed polymers were molten under inert conditions and cured at RT in order to mimic the MEW processing. The resulting films were then incubated in MilliQ water at 20°C for 48 h to ensure full hydration and negate variations caused by the temperature responsiveness. Measuring the sample weight in wet and dry state allowed calculation of the EWC of the hydrogels (Figure 4.35 c). Very obvious is a strong dependency of the EWC on the mean DF. This trend is visible in a similar extend for all of the three different polymer backbones. For instance, for the homopolymer-based samples, the EWC increased from the moderate value of 80.2±1.5 % up to a highly swollen state of 92.2±1.0 %, when the mean crosslinking degree was decreased from 4.4 to 2.4 %. On the first glance, the influence of the increased hydrophilicity of the copolymers seems to be insignificant. However, this effect is masked by the differences in crosslinking degree between each of the polymer batches. This means, for a material based on the P(EtOzi$_{75}$-co-MeOx$_{25}$) **P12** with an average DF of 2.4 %, a EWC beyond 95 % can be extrapolated from the visible trend.

Interestingly, in relation to the results of the LCST measurements, the difference between the DA polymers based on the copolymers **P11** and **P12**, is surprisingly small. Here, the complex chemical structure of the polymers, caused by the copolymerization and hydrolysis reactivity ratios, might result in a denser crosslinked network for the hydrogels based on **P12**, which results in a lower EWC.

Using cryogenic scanning electron microscopy (Cryo-SEM), it was possible to visualize the microstructure of the hydrogels in the swollen state (Figure 4.36).* Very noticeable is the comparably small pore size for all of the investigated samples. As expected, the sample with the lowest DF (2 %) shows the largest pores (approximately 500-700 nm), which can be explained by a smaller crosslinking density. These values are close to a recent report about a physically crosslinked and reinforced POx-based hydrogel.[285] Compared to this, the samples prepared from the 4 and 3 % functionalized polymers reveal very inhomogeneous pore size distributions with small ($\leq$100 nm) and large pores ($\geq$700 nm). Striking is also the difference between the samples prepared via melt casting and the MEW printed fibres. While the large pores on the surface of the fibres are common artefacts formed during the cryo-sample preparation (Figure 4.36 c, top), the pores inside of the fibres are with roughly 50 nm very small and much smaller than the pores in the melt cast sample (Figure 4.36 c, bottom). Generally, the observed pore sizes are close to the resolution

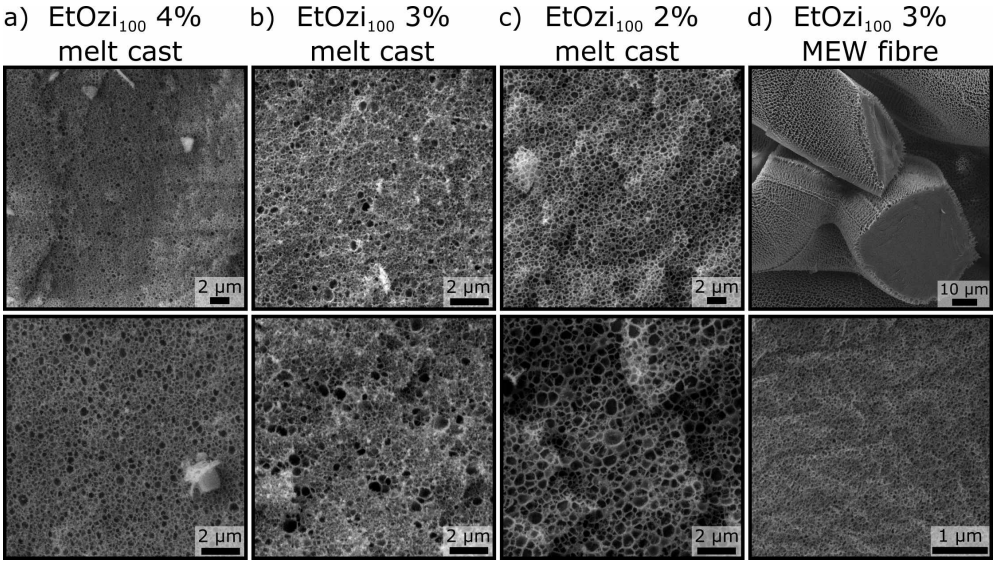


**Figure 4.36:** Comparison of Cryo-SEM pictures of the PEtOzi-based hydrogels with a functionalisation degree of 4, 3 and 2 %. The samples were prepared via melt casting a), b), c) or processed via MEW d). Please note the same scaling of b) top and bottom. (Images taken by Philipp Stahlhut)

*The Cryo-SEM images were taken in cooperation with Philipp Stahlhut from the Department for Functional Materials in Medicine and Dentistry at the University Hospital Würzburg.

limit of the Cryo-SEM technique, making the visualization very challenging. The imaging had to be repeated several times, to get samples where the pores were not fully covered with ice or deformed due to too extensive lyophilisation. As a result, the irregular pore size distribution seen for some of the samples might be due to insufficient removal of ice. Therefore, while the discussed trends are viable, the absolute values of the pore size have to be viewed critically. Overall the tiny pores point towards a very dense network formation during the curing of melt cast samples. Furthermore, the MEW processing seems to favour the formation of even smaller pores. Flow induced structuring of polymers during MEW has been observed before and could lead to the formation of asymmetric cylindrical pores, but no signs of such were found in Cryo-SEM. All in all, these pores are too small to allow biological activity like cell in growth or neovascularisation within the material, yet such activity is very much possible within the pores of the MEW printed structures themselves. [83]

It is crucial for the potential application of these hydrogels, to have information about their degradation behaviour. While qualitatively good structural stability was found for the MEW printed scaffolds in section 4.2.3, the overall small mass of the meshes prevented a meaningful quantitative analysis. Therefore, the degradation behaviour had to be studied in bulk even though a different microstructure has been observed in Cryo-SEM. For this, small chunks prepared from a melt cast mixture of **P50** and **P51** were incubated at 37°C in buffer solutions with a pH of 3.0, 7.3 and 11.0. At specific time points, three samples per condition were analysed upon their EWC and sol content (Figure 4.37 a, b). The difference in the hydrolytic stability found between the three conditions was striking. At pH 11.0 all samples were fully disintegrated after incubation for 11 d, leaving only a sticky gel drop behind. This loss of structural integrity made further analysis of these samples impossible and the experiments were terminated (Figure 8.13). In contrast, the samples at pH 3.0 and 7.3 remained visibly unchanged for several months. Please note that the EWC for all samples at day zero was only 61 % (incubation at 37°C) and therefore much lower than the 84 % (incubation at 20°C) reported above. This again highlights the thermoresponsive nature of the DA hydrogels, which needs to be taken into account for potential applications, especially in biological environments. Interestingly, in the pH 11.0 condition, roughly half of the samples lost their structural integrity already after 8 d while others remained intact until day 11. This is surprising as all samples were taken from the same polymer mixture, which was prepared via lyophilisation of an aqueous solution of **P50** and **P51**. While this should ensure a homogeneous mixing of both components, the results presented above, clearly show that even within a homogeneous mixture one has to expect some degree of sample to sample deviations. At pH 7.3, the sol content and EWC showed a slow but steady increase reaching 22.8±1.8 and 65.5±1.0 % respectively after

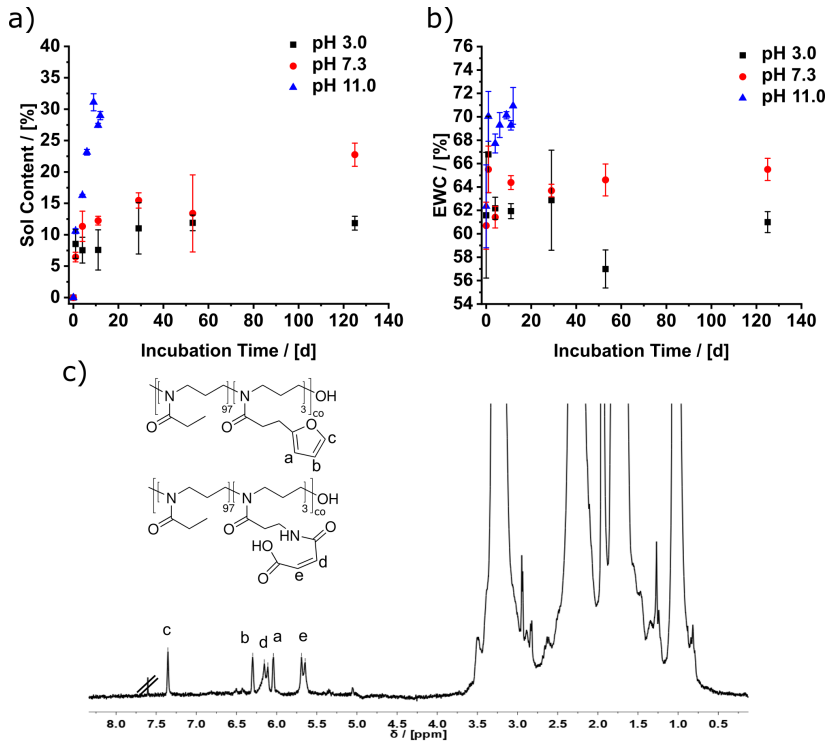


**Figure 4.37:** Development of the mean (n=3) sol content (a) and EWC (b) with the corresponding standard deviation of hydrogels prepared from a mixture of **P50**+**P51** after incubation at 37°C in buffer solutions with a pH of 3.0, 7.3 and 11.0. c) $^{1}$H-NMR spectrum (300 MHz, 298 K, $CD_3CN$) of the residue extracted from the supernatant of the disintegrated samples incubated for 11 d at pH 11.0.

continuous incubation for 125 d. At pH 3.0, both the sol content as well as the EWC seem to follow a plateau like trend and no further increase beyond 30 d of incubation was observed. While these observations are generally in-line with literature reports, the extent of structural stability of the DA hydrogels at neutral or acidic pH is still remarkable.[218,243] In particular, considering the low DF of the studied material. On average, one polymer chain has only three DA crosslinking units per molecule. Putting this into perspective, Kirchof *et al.* studied furan and maleimide functionalized eight-armed PEG molecules with a molar mass around 10 kg/mol. This means, the theoretical crosslinking density of the hydrogels studied by them was more than two times higher than the here presented PEtOzi-based material. Still they report a more rapid and complete degradation of the hydrogel network at pH 11.0 (after 4 d) and at pH 7.4 (after 25 d). In contrast, at acidic pH they also report excellent long term stability, observing only minor changes after almost one year of incubation. In this context, one has to be aware that the system studied by Kirchhof *et al.* was crosslinked in a 10 wt% aqueous solution, and therefore the initial water content was much higher than the PEtOzi-based hydrogel system presented here. The melt casting of the PEtOzi-based material favours a much denser network. Furthermore, linear polymers

have a much higher possibility to entangle than the star-like PEG molecules used in the literature. This would again favour a higher network strength. Kirchhof *et al.* identified a degradation pathway of the DA hydrogels via basic hydrolysis of the maleimide to maleamic acid. Maleamic acid is a much weaker dienophile preventing the formation of DA crosslinks at RT.[243] In line with these reports, the $^{1}$H-NMR spectrum of the polymer extracted from the supernatant of the disintegrated PEtOzi samples incubated for 11 d at pH 11.0, showed only signals of maleamic acid. No signs of maleimide were found in the spectrum, supporting a similar degradation pathway (Figure 4.37 c).

All in all, a library of DA-based biomaterial inks was successfully synthesized. This shows that the established synthesis procedure can be applied to a wide range of Ozi and Ox-based polymers. Via copolymerization important parameters like the hydrophilicity as well as the swelling degree are readily controlled. Furthermore, key knowledge about the structure and the degradation behaviour of the hydrogel materials was developed.

### 4.3.2 Processing via Melt Electrowriting

With the polymer library synthesized in the previous section, it should be possible to cover a large range of processing parameters as well as construct properties allowing to point out the polymers with the most potential for subsequent projects. In section 4.1.4, it was established that the $T_g$ has strong influence on the MEW processing performance. Therefore, the $T_g$ of the Ozi and Ox homo- and copolymers was determined via DSC measurements (Figure 4.38 a). The $T_g$ of the parent polymers increased from 24 °C for the PEtOzi$_{100}$ homopolymer to 31 °C for the EtOx containing polymer and 33 °C MeOx containing polymer. This is in-line with the results presented above as well as in the literature.[266] Also the formation of a single $T_g$ in the DSC trace supports good compatibility of the respective comonomer with EtOzi and the absence of micro phase separation. Even though some variations of the $T_g$ of the functionalized polymers were found for the different DF, the values were generally close to the $T_g$ of the respective parent polymer. Therefore, in this DF range the incorporated furan and maleimide functions showed only minor impact on the $T_g$.

Using temperature sweeps in oscillatory rheology measurements allows the determination of the liquefaction point of the DA crosslinked material (see Section 4.2.3 for a more detailed explanation). As representative examples, rheometry temperature ramps of the functionalized homopolymers are show in Figure 4.38 b). A distinct shift of the liquefaction point (highlighted with arrows) to higher temperatures was found, when the DF was increased from 2 to 4 %. A very similar trend was also found for the copolymer based DA materials (Figure 4.38 c). When comparing all polymers, it becomes apparent that the chemical composition of the polymers has little influence on the liquefaction point and that the DF is the governing factor. This is easily understood, as the liquefaction temperatures are in all cases far above the $T_g$ of the respective parent polymers, making the DA equilibrium the governing factor for the solidification. A approximately linear dependency of the liquefaction point was found in the DF range of 2 to 4 %. As MEW is a complex multi parameter process, several combinations of NT, pressure and voltage will allow the stable processing of single a polymer. In order to determine the influence of the PC as well as the DF on the processing temperature, the NT and ST were increased step wise until a stable process with a CS around 1200-1400 mm/min was achieved. The remaining MEW parameters were varied only slightly around the base values of 1.5 bar, 3 kV and a 3.3 mm collector distance. Doing so, the processing temperature for the MEW processing of the Ozi and Ox homo- and copolymers were found (Figure 4.39 c). A non-linear dependency of NT approaching the processing temperature of the respective parent polymers can be observed. Also, the samples with the higher $T_g$ tend to have a higher processing temperature.

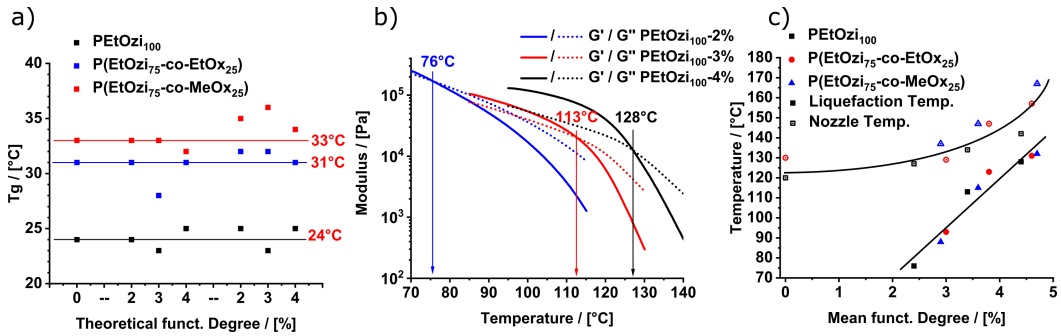


**Figure 4.38:** a) $T_g$ depending on the polymer composition for the furan and maleimide functionalized Ozi and Ox homo- and copolymers as well as their respective parent polymers. The values were determined via DSC analysis. The horizontal lines are meant to guide the eye and indicate the $T_g$ of the respective parent polymer. b) Temperature dependent viscoelastic properties of the dynamically crosslinked PEtOzi homopolymers with a DF of 2, 3 and 4 %. The respective liquefaction points are marked by the arrows. c) Comparison of the liquefaction point (closed symbols) and the MEW processing temperature (open symbols) for the Ozi- and Ox-based biomaterial inks.

The steep increase of the processing temperature depending on the DF suggests that the amount of DA functions in the material can not be increased much past the investigated range. Beyond this point, thermal degradation might become unmanageable and prevent any meaningful processing.

In order to compare the printing quality as well as the shape fidelity, five-layered box structures were printed from all nine polymer mixtures. Stereomicroscope images were taken within at least 30 min after printing (day 0) and after storage at 20 °C for 1 d and 7 d (Figure 4.39). Most importantly all polymers could be processed via MEW resulting in well structured box-scaffolds. Immediately after printing, the fibre stacks were well resolved and the fibre structure was clearly visible. Although only for the copolymers with a DF of 3 and 4 % a bridging of gaps was observed. For all polymers with a pure EtOzi backbone as well as for the copolymers with a DF of 2 %, the fibres partially merged upon contact, creating a dense stack with no openings. Drastic changes became visible for some samples after storing them overnight. The sample prepared from PEtOzi$_{100}$-2 % and P(EtOzi$_{75}$-co-MeOx$_{25}$)-2 % showed extensive polymer flow with the result of completely loosing the fibre shape and merging to a thin but broad band. A similar behaviour, but to a less drastic extend, was observed for PEtOzi$_{100}$-3 %. The polymers based on P(EtOzi$_{75}$-co-EtOx$_{25}$) were a noticeable exception. For these samples, regardless of the DF, all printed constructs showed either very little (DF: 2 and 3 %) or no polymer flow (DF: 4 %) post processing. For all samples no further changes were observed between the first and the seventh day. The two major properties of the DA materials which can prevent polymer flow post processing, are the $T_g$ and the DA crosslinks. With increasing DF, the critical

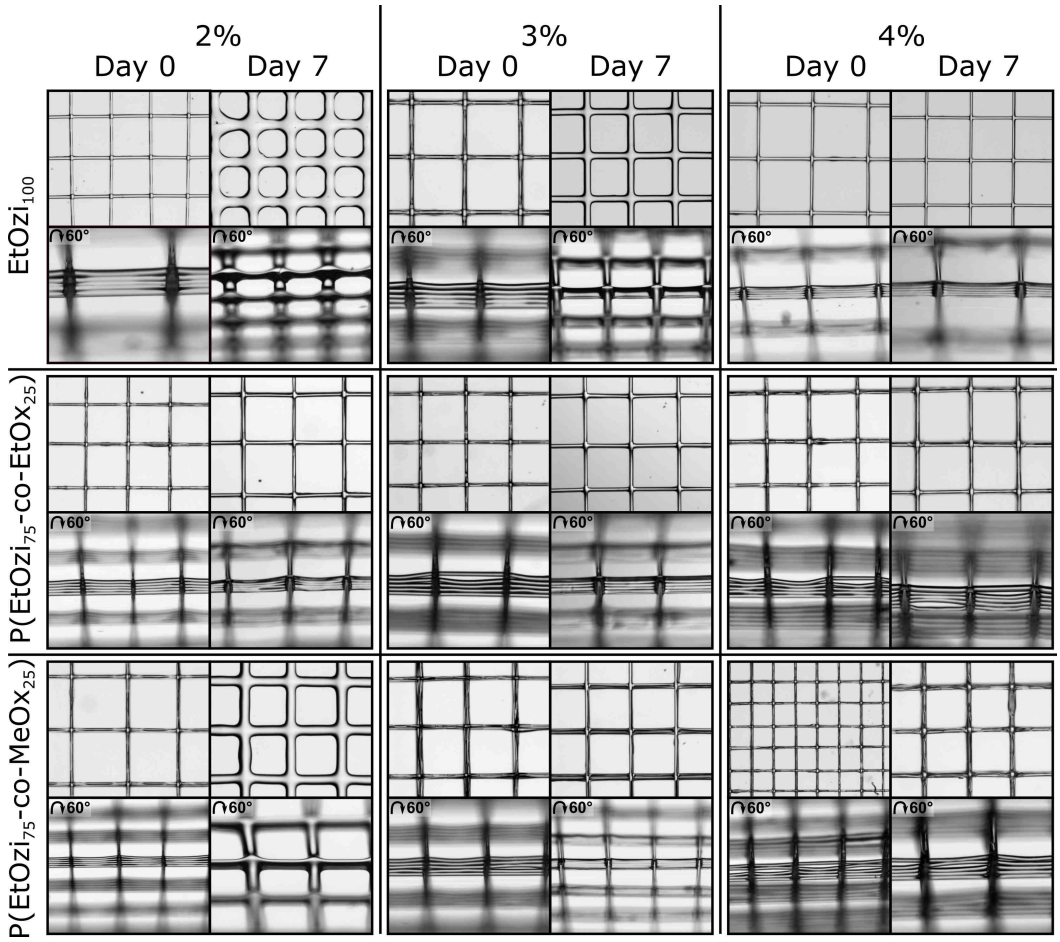


**Figure 4.39:** Stereomicroscope images of MEW printed box-like structures prepared from a large variety of Ozi and Ox homo- and copolymers. Images of the same scaffolds were taken directly after printing as well as after storage at 20 °C for seven days. The printing parameters for each scaffold can be found in Table 7.15.

crosslinking density required to solidify the material is reached more rapid. This effect can be observed best for scaffolds based on the PEtOzi$_{100}$ backbone, where shape fidelity was drastically increased for higher DF. Please note that the $T_g$ remains unchanged for those polymers. When comparing each of the scaffolds based on the homopolymer with the structures prepared from P(EtOzi$_{75}$-co-EtOx$_{25}$), the influence of the increased $T_g$ can be observed independently from the DF. All of the structures prepared from the EtOx containing copolymers show little to no polymer flow. Striking however, is the decrease of shape fidelity for the P(EtOzi$_{75}$-co-MeOx$_{25}$)-2 % sample, even though the $T_g$ is slightly increased compared to the P(EtOzi$_{75}$-co-EtOx$_{25}$) polymers. This is likely caused by the increased hydrophilicity of the MeOx containing polymers, which causes the material to draw water from the air much more rapid than the other polymers. The absorbed water acts as plasticizers, which lowers the $T_g$ and facilitates polymer flow. Therefore, P(EtOzi$_{75}$-co-MeOx$_{25}$)-2 % marks the "sweet spot", where the effect of the increased $T_g$ is

outweighed by the increased water uptake capability. It is important to note that the result of these experiments depends on the ambient conditions. While the curing temperature was easily controlled by an incubator, the air humidity was more challenging and for this set of experiments it varied between 40 and 50 %. Curing the structures at lower relative air humidity might result in less pronounced polymer spread in all cases. This study highlights very clearly both, the complexity and the versatility of the Ozi-based biomaterial inks.

Furthermore, all scaffolds regardless of the shape fidelity, allowed swelling in water and the formation of microperiodic hydrogel scaffolds (Figure 4.40). Even for the low DF, the fibres showed no signs of disintegration for several days. With the structures being detached from the printing substrate, it was possible to visualize the fibre stacks of the samples, which experienced significant polymer flow from the side (Figure 4.40 a, inset). This reveals the full extend of the polymer spread. The fibre stack had a flat band like shape with a diameter around 200 $\mu$m and a height around 40 $\mu$m. No signs of the individual fibres could be observed anymore. As shown by the two representative examples, the scaffolds with good shape fidelity in the dry state also retained their structure upon swelling and no signs of distortion or layer delamination were observed (Figure 4.40 b, c). To investigate the swelling properties in more detail, parallel stacks of lines were printed

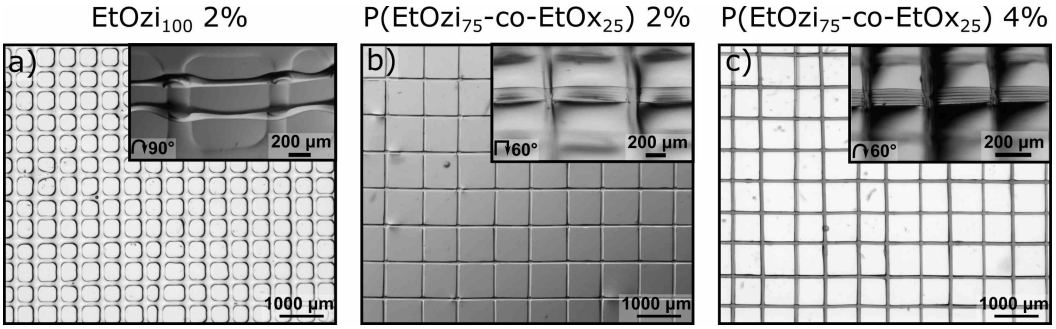


**Figure 4.40:** Representative examples of swollen scaffolds with different polymer backbone and DF (from left: S13, S14, S15). The inset pictures were taken at a tilted angle to visualize the fibre morphology.

from all of the homo- and copolymers discussed in this section (Figure 4.41 a). For each polymer mixture three scaffolds were prepared. For the propose of easier handling, each construct consisted out of three layers. The fibre length as well as the thickness in dry state was determined for at least 20 fibres per structure by using stereomicroscope and scanning electron microscopy (SEM) respectively (markers in Figure 4.41 a- d). For determining the fibre length, perpendicular lines in the architectures severed as points of orientation. Following hydration, the dimensions of the same fibres were measured again using stereomicroscope. From these values, the swelling ratio $SR = \frac{wet}{dry} \times 100$ was determined. The

resulting swelling ratios (SRs) of the fibre length with the respective standard errors after curing for 1 and 7 d are shown in Figure 4.41 e). As expected from the swelling degree in bulk, the longitudinal SR increases with decreasing DF. Striking is the difference in SR after 1 and 7 d of curing. For the samples with a DF higher than 3 % only negligible changes were observed, whereas the polymers with a lower DF showed large deviations. In these mixtures the reactive DA functions are so spare that the crosslinking kinetics are slowed down, and the equilibrium crosslinking density is reached much later as for the other samples. Therefore, if systems with a low DF are used, a storage longer than 24 h is advisable. Furthermore, the SR follows the trend expected from the hydrophilicity of the polymer backbone as it is consistently higher for the MeOx containing polymers compared to the EtOx containing copolymers (as illustrated by the dotted lines in Figure 4.41 e). In particular for the lower DF values, high SRs highlight the significant size increase that needs to be taken into account for the MEW printed constructs. For instance, a construct made from P(EtOzi$_{75}$-co-MeOx$_{25}$)-2 % (SR: 179 %) with a side length of 2 cm (4 cm$^2$) increases its area to almost 13 cm$^2$. This data shows very descriptive, how the material properties can be utilized to control the swelling properties of the MEW printed constructs.

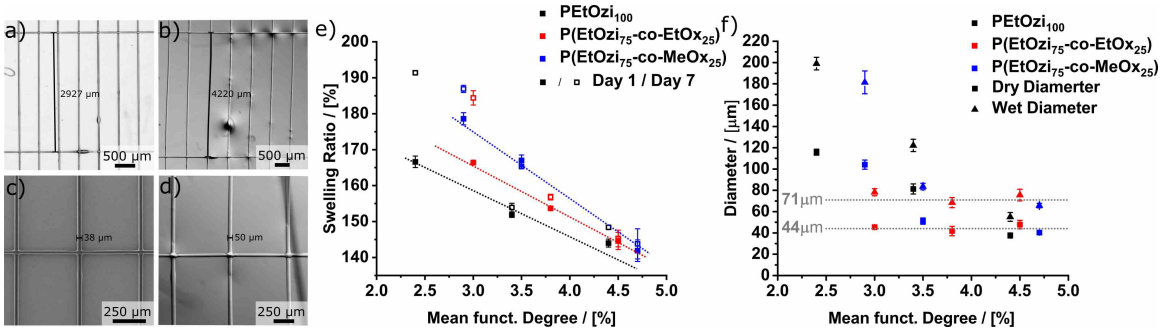


**Figure 4.41:** a), b) Stereo microscope image of the line printing setup used for the determination of the swelling ratio longitudinal to the fibre axis in dry and swollen state respectively. c), d) SEM (dry) and stereo microscope image (wet) of the line printing setup used for the determination of the swelling ratio transversal to the fibre axis. The length and thickness of one fibre is measured as an example. e) SR for the Ozi and Ox homo- and copolymers after 1 and 7 d of curing in dry state. Dotted lines do not represent linear fits, but are meant to guide the eye. f) Fibre diameter in dry and wet state of the Ozi and Ox homo- and copolymers after 7 d of curing in dry state.

Potential alignment of the polymer chains during MEW processing might induce a different SR transverse to the fibre axis (the diameter) compared to the longitudinal swelling. Unfortunately no clear trend of the transverse SR was found. This is likely caused by a combination of phenomena. Due to the difference in dimensions, measuring the fibre diameter resulted in a much larger relative error compared to the fibre length. While the diameter of each fibre in dry state could be determined with great precision using SEM, in wet state a stereomicroscope had to be used. Due to the fibres being transparent, it

was difficult to determine the edges of the single fibres in the stacks. Furthermore, due to pulsing instabilities in the MEW process, the fibre diameter showed great variance for some of the architectures. Therefore it has to be refrained from analysing the diameter SR and only the raw values are discussed in the following. According to the diameter in dry state, the material can be divided into the same two categories. When the structures retain their shape post printing, a mean diameter around 44 $\mu$m was found. After swelling, this increased on average to around 71 $\mu$m. The PEtOzi$_{100}$-based fibres showed a less pronounced swelling compared to the respective copolymers. For the materials which exhibit polymer flow post printing, significantly larger dry state diameters between 81 and 115 $\mu$m as well as 122 and 199 $\mu$m in the hydrated state were found.

In the preceding section, the MEW processing of several different PEtOzi-based biomaterial inks was investigated. All polymers allowed processing into defined box-like structures. Important relationships of polymer properties, the MEW processability as well as the characteristics of the resulting constructs were explored. It was shown that the P(EtOzi$_{75}$-co-PEtOx$_{25}$) backbone offers an ideal compromise of hydrophilicity, shape fidelity and processability. This polymer base is therefore a very promising candidate for further projects.

### 4.3.3 Other Crosslinking Units

Apart from the DA reaction, other pericyclic reactions have been used throughout literature for the crosslinking of polymers, and in this context two prominent examples are coumarin and cinnamic acid. Under illumination with light of a wavelength higher than 360 nm, both are able to undergo a [2+2] cycloaddition with another coumarin and cinnamic molecule respectively.[286,287] In this section, coumarin and cinnamyl functionalized PEtOzi will be explored as potential alternative to the DA-based crosslinking. Advantageous is that both functions are expected to be chemically less reactive than the maleimide and furan pair. Therefore less side reactions are to be expected during melt processing. Also, as these will form a homo-dimer, the polymeric ink will only consist out of one component. On the one hand, this simplifies and significantly shortens the synthesis procedure. On the other hand, processability changes related to the mixing of a two component system, like inhomogeneous mixing or mixtures with non ideal ratios, are circumvented. However, compared to a DA-based system light will be needed as an external stimuli to initiate the crosslinking.

Polymer analogue functionalization was used for the synthesis of coumarin and cinnamyl functionalized PEtOzi. Throughout this work, the DCC supported amine carboxylic acid coupling has proven to be a very mild but efficient method for the introduction of reactive functions to POx and POzi post polymerization. This procedure is outlined above and will not be discussed here. In the case of the cinnamyl functionalized polymer, the carboxylic acid derivative cinnamic acid was readily commercially available allowing the straightforward synthesis of **P66**. The successful and quantitative coupling was confirmed via $^1$H-NMR analysis (Figure 4.42 a). For the synthesis of the coumarin functionalized PEtOzi (**P67**), the acid derivative was first synthesized from 7-hydroxycoumarin using Williamson ether synthesis. Due to poor solubility of the coumarin-acid derivative in AN, dimethylformamide (DMF) was used as solvent for the following DCC supported coupling. $^1$H-NMR analysis of **P67** supported a successful coupling, yet very similar to the coupling with furan and maleimide, the functionalization efficiency was higher than 100 % with respect to the hydrolysis degree. During the work-up procedure it was noticed that both, **P66** as well as **P67**, were virtually insoluble in water. This prevented purification of the polymers via dialysis. While PEtOzi is hydrophilic and readily soluble in water, the introduction of a considerable amount of aromatic side groups rendered the polymers increasingly hydrophobic. This prevented the solubilisation in water. At this point, it already became apparent that these polymers were not suitable for the fabrication of hydrogels. However, as chemically crosslinked hydrophobic MEW-printed fibres can be utilized for potential biomedical applications as well[49,50], the processability using MEW was still evaluated. **P66**

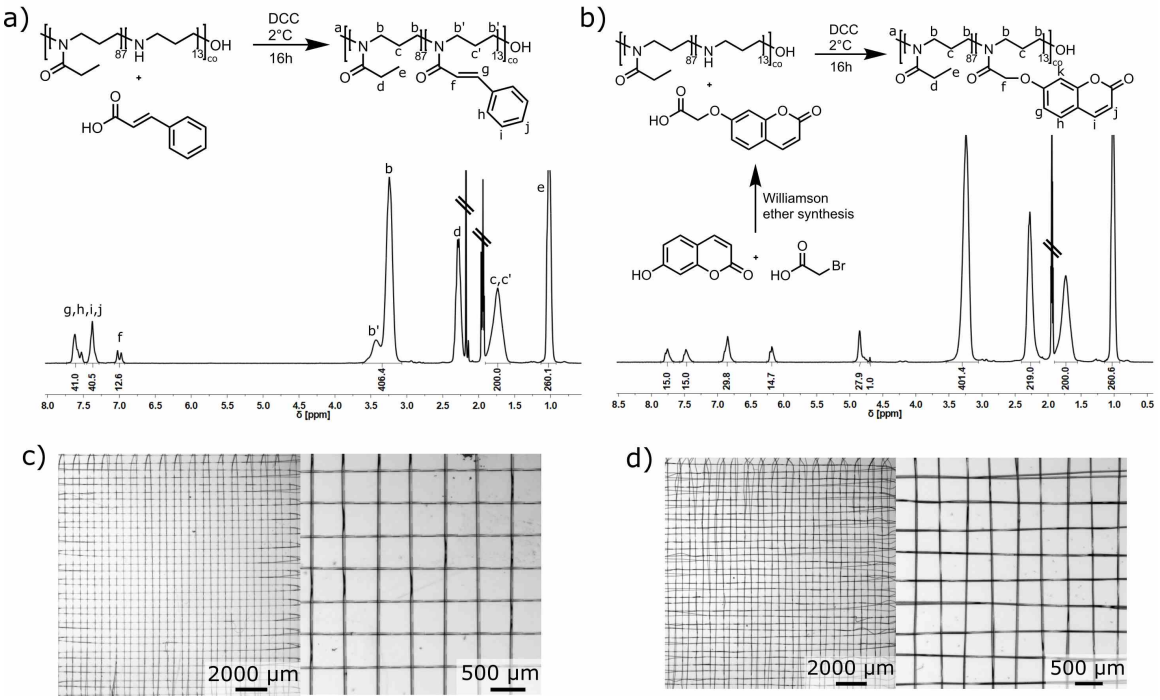


**Figure 4.42:** a) $^{1}$H-NMR spectrum (300 MHz, 298 K, $CD_3CN$) of the cinnamic acid functionalized PEtOzi (**P66**) as well as the schematic illustration of the synthesis path. b) $^{1}$H-NMR spectrum (300 MHz, 298 K, $CD_3CN$) of the coumarin functionalized PEtOzi (**P67**) as well as the schematic illustration of the synthesis path. c), d) Two-layered MEW printed box-like scaffolds made from **P66** (S41) and **P67** (S40) respectively.

was processed using a NT of 130°$C$ and a ST of 110°$C$. The MEW printing process was very stable and little defects were observed in the manufactured fibre mesh (Figure 4.42 c). Putting this into perspective, DSC reveals a $T_g$ of 32°$C$, which is 10°$C$ higher than the $T_g$ of the parent PEtOzi polymer and very close to the $T_g$ of the P(EtOzi$_{25}$-co-EtOx$_{75}$) copolymer **P4**. **P4** also allowed processing with the same set of printing temperatures. This highlights again that in contrast to the DA polymers the processing temperature of linear Ozi and Ox polymers is, due to the absence of thermally induced crosslinking, mainly governed by their $T_g$. For **P67** a $T_g$ of 42°$C$ was determined, and this samples allowed processing at a NT of 143°$C$ and a ST of 123°$C$. In contrast to the cinnamic acid functionalized **P66**, the structures made from **P67** show imprecise fibre placement. This is likely caused by the relativity high $T_g$, which causes the rapid solidification of the polymer jet during deposition.

After processing, the scaffolds were illuminated using a Dymax 5000 Flood UV-Chamber to induce the reaction of the cinnamyl and coumarin functions respectively. This should lead to the chemical crosslinking of the polymer chains in the MEW printed fibres. Due to the unknown reaction efficiency in the solid polymer fibres, five different scaffolds made

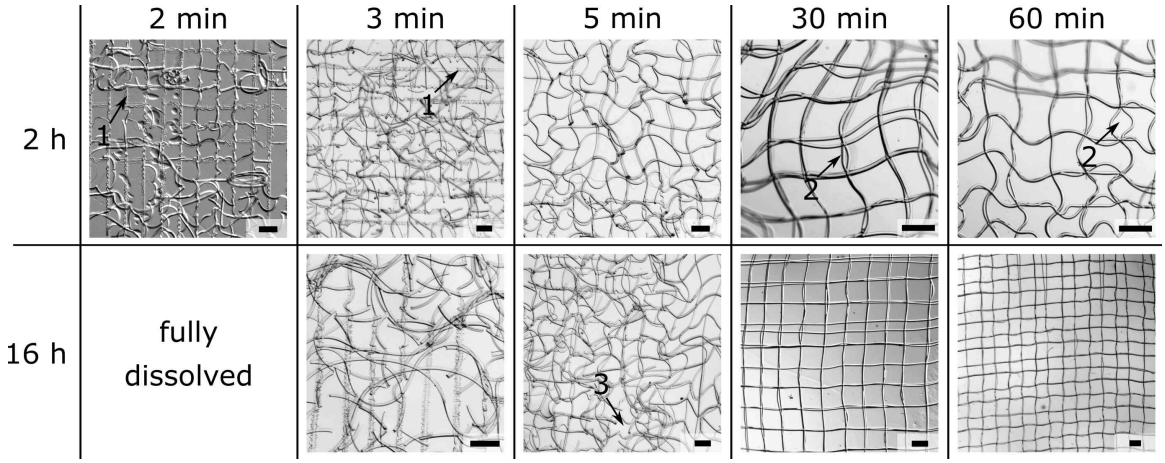


**Figure 4.43:** Two-layered MEW printed box-like scaffolds made from **P67**. Each structure was illuminated using a Dymax 5000 Flood UV-chamber for the time specified in the top row. The constructs were then incubated in AN. Stereo microscope pictures were taken after 2 and 16 h. Arrows indicate points of interest. 1: Residual material remaining on the glass slide after the fibres detached via swelling. 2: Stacked fibres that are not attached onto each other. 3: Fibres breaking at the junctions. Scale bars are 500 $\mu$m.

from **P66** as well as **P67** were illuminated for 2, 3, 5, 30 and 60 min. Subsequently, the scaffolds were immersed in AN and the swelling was evaluated using a confocal microscope. Surprisingly, all structures made from **P66** dissolved rapidly within 2 h, proofing that the crosslinking efficiency of the cinnamyl groups was rather poor. In contrast, the structures made from **P67** showed significant swelling in AN and did not dissolve within 2 h of incubation (Figure 4.43). The scaffolds illuminated for 2 and 3 min did not maintain the box-shape, and the fibres preferably broke at their junctions into small fragments. This indicated that the crosslinking was not sufficient to maintain the architecture during the swelling process. In contrast, the structures illuminated for 5, 30 and 60 min maintained their structure. The increasing crosslinking density with prolonged curing times was also reflected in the swollen fibre diameter. While the fibre diameter of the sample cured for 5 min increased from roughly 38 to 60 $\mu$m (57 % increase), the fibre diameter of the sample illuminated for 60 min increased from 34 to only 45 $\mu$m (32 % increase). It was further noticed that these architectures showed a strong tendency to stick onto the glass surface. For instance, for the samples with short curing times (2 and 3 min), small amounts of polymer remained stuck on the glass surface, while the majority of the material detached (highlighted with the arrow marker 1). Also, the scaffolds irradiated for 5 min and longer were still partially attached to the glass after 2 h of incubation. This stands in contrast to the DA-based scaffolds, as these detach without any signs of structural damage within 1 min of incubation. A possible explanation is that the samples experience high temperatures during the curing step, which causes them to partially liquefy and firmly attach to

the glass substrate. Very noticeable was also that the fibres were not well attached on their contact points. This led to partial disintegration of the mesh structure upon swelling (highlighted with the arrow marker 2). This indicates a poor interlayer adhesion and again stands in contrast to the DA-based scaffolds, where very strong interlayer adhesion was observed. After 16 h of incubation, the sample irradiated for 2 min was fully dissolved, while all others retained the fibre structure. However, the scaffold with only 5 min curing time started to visibly lose the box-structure (highlighted with the arrow marker 3). The structures irradiated for 30 and 60 min remained fully intact. This indicates that the minimal curing time, allowing a full retention of the printed architecture, is somewhere between 5 and 30 min.

All in all utilizing cinnamyl and coumarin-functions for a UV-light induced crosslinking of PEtOzi is not a viable alternative to the DA reaction. The cinnamyl-functions did not provide sufficient crosslinking and even after prolonged illumination times the fibres were still dissolved within short time periods. While the coumarin-functions rendered the printed constructs insoluble after 5 min of curing, a relatively high ratio of the UV-active functions was required. This made the material insoluble in water and unsuitable for the preparation of hydrogels. However, using the versatility of the Ox and Ozi chemistry, the used approach can easily be translated to a more hydrophilic polymer base for example PMeOx or PEtOx, but this would also required major adjustments to the processing conditions. The presented material could be utilized for the preparation of insoluble and though MEW printed scaffolds similar to the reports of Hochleitner and coworkers.[50]

### 4.3.4 Shape-Morphing Hydrogels

The fabrication of thin and wide sheet-like structures with a precise micro-structure is easily achieved via MEW.[59] However, the continuous character of MEW makes it challenging to control the macro-structure of the printed architecture. In contrast to FDM, the deposition of the filament cannot be readily or accurately stopped and restarted. Hence, commercially available tools, which convert 3D-structures into G-codes commands cannot be easily used for MEW, which was only recently addressed by Paxton and coworkers.[60] This, in combination with small fibre diameters makes the fabrication of large volumes challenging for MEW. A prominent technique for translating flat sheets into three-dimensional structures is often referred to as 4D-printing. Here, an external stimuli like swelling or temperature induces a strain mismatch in a structure causing it to deform into a more complex architecture.[288] Due to the lack of stimuli responsive materials explored for MEW, 4D-printing is currently not available for this direct writing technique. The work presented in the following section aims to explore the opportunities, Ox- and Ozi-based biomaterial inks offer for the fabrication of shape changing structures using MEW.

Throughout literature, there are several options, for inducing a strain mismatch in a 2D-dimensional structure, explored. The most common being layered structures made from a least two materials, which posses different swelling degrees.[288]. Manufacturing such a multi-material structure with MEW would require processing of more than one material, either sequentially or simultaneously. Both approaches have their advantages and disadvantages. For the processing of two materials simultaneously for instance, a multi-headed printer would be required, which would at the same time allow the fabrication of interpenetrated architectures. While this is rather easily achieved for simple extrusion-based 3D-printing techniques, the continuous character of MEW makes this more challenging. Printing two materials sequentially requires the exchange of the polymer reservoirs, each time a new material layer needs to be added. Even though this is a bit tedious it does not require a special printing setup nor a complex g-code. Interestingly, there are currently no reports about multi-material MEW printed scaffolds published.

Several properties of the POx- and POzi-based biomaterials make them an ideal candidate for the fabrication of multi-layered architectures with shape-morphing properties. As is was shown above, the versatility of the POx/POzi chemistry makes the adjustment of the swelling degree very straightforward. Also, the dynamic nature of the DA reaction allows a covalent bonding at the material interfaces, which will prevent delamination. Furthermore, the $T_g$ near RT makes the printed fibres flexible and still allows some degree of material

creep. This combination of properties can be used for very interesting interactions. When two scaffolds are brought in contact with each other after printing, they can partially fuse and the DA reaction will establish chemical bonds at the interface. To investigate this

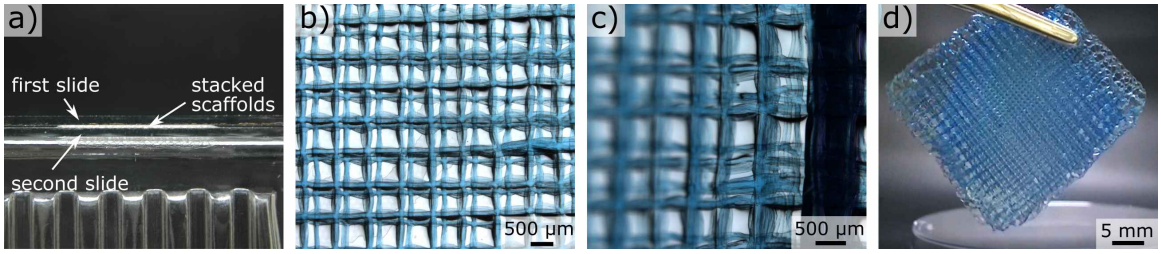


**Figure 4.44:** a) Two MEW printed scaffolds on a glass slide stacked on top of each other. b), c) Stereo microscope images of the swollen stacked scaffolds from the top and at a tilted angle respectively. d) The stacked structure does maintain its shape outside of a liquid medium.

matter, two scaffolds with 10 layers each, were printed on glass slides. Immediately after printing, the structures were stacked by gently pressing them onto each other (Figure 4.44 a). After storing the stack over night at RT, it could be swollen in water. No sign of delamination of the two stacked grids was observed (Figure 4.44 b), which highlights a strong adhesion force established at the interface of the two structures. This prove of principle was performed with two scaffolds made from the same polymer, and therefore no shape change can be observed. While printing scaffolds with a large number of layers using MEW can be challenging, this technique bypasses this. It offers a straight forward option for doubling the layer height of printed constructs post printing. A drawback is that it is rather difficult to stack two grids without any offset (Figure 4.44 c). Very noticeable was that the increased construct height reinforced the scaffold to an extent, where it retained its morphology outside of aqueous medium (Figure 4.44 d). In contrast, structures with layer numbers of 10 and lower collapsed upon removal from the liquid medium. It has to be noted that the successful binding of two scaffolds was only possible when they were stacked on the day of printing. Leaving them over night before stacking, probably drives the crosslinking reaction in both structures near completion and leaves no option for further chemical bonding. Nonetheless, this time window is still long enough to sequentially prepare a large number stacked scaffolds by using just one MEW printer.

In order to induce a shape change upon swelling, a difference in swelling degree is required. Therefore, the PEtOzi-based DA polymers **P48**+**P49** ($HD_t$=2 %; EWC: 92 %) and **P52**+**P53** ($HD_t$=4 %; EWC: 80 %) were used to produce scaffolds for the stacking experiments with a swelling mismatch. The geometries of the stacked constructs were selected with the aim to produce tube-like architectures. The ability for the formation of tubular structures is often used throughout literature to showcase the shape-morphing

potential of systems, because the underlying geometries are simple. In this setup one layer of each stack was printed into a box-like structure in order to give the constructs the required stability. The other, consisted out of parallel lines with the function to either bring up the force for deformation (Geometry 1, 2) or restrain the swelling of the mesh in one dimension (Geometry 3) (Figure 4.45). The constructs were stacked on the day of

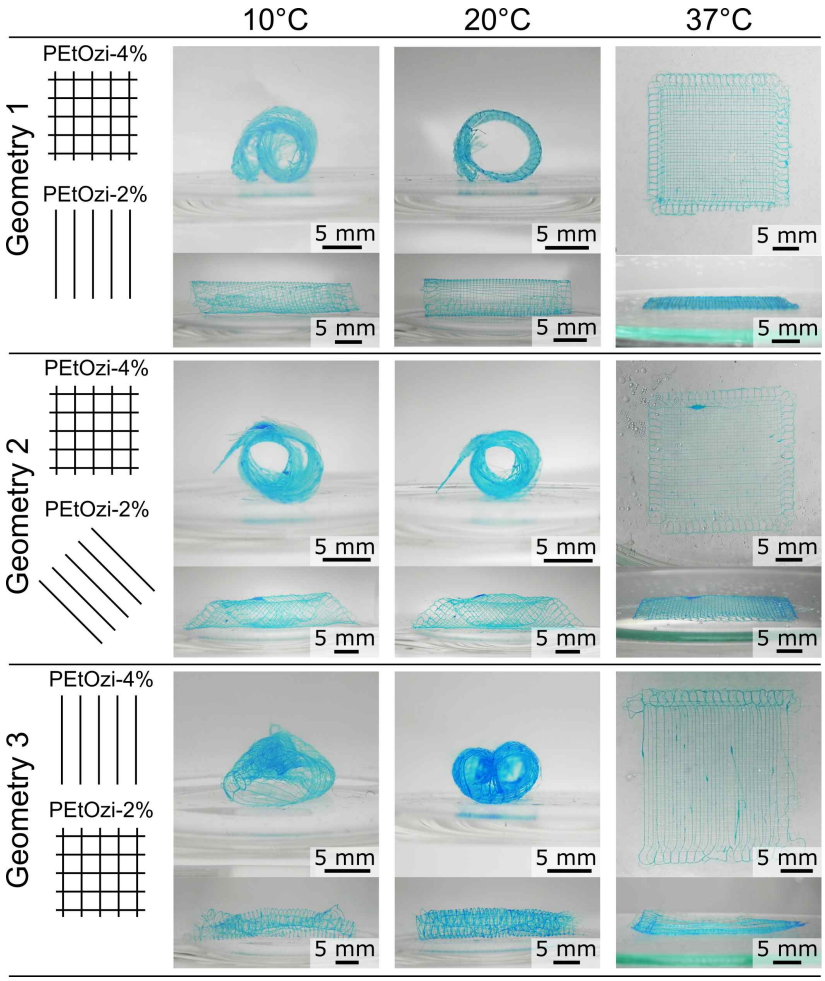


**Figure 4.45:** Shape-morphing hydrogel scaffolds made by stacking of constructs produced from the PEtOzi-based DA polymers **P48**+**P49** (PEtOzi-2 %) (from top: S16; S17; S18) and **P52**+**P53** (PEtOzi-4 %) (from top: S19; S20; S21). The stacking geometry is indicated on the left. Changing the temperature of the surrounding medium from 10 over 20 to 37 °C causes the architectures to gradually unfold from the tubular structure to the non-folded flat sheet.

printing and then left over night to ensure crosslinking. On the next day, the structures were incubated in an aqueous solution of DY-647P1-maleimide for better visualization. Upon swelling at 20 °C, all constructs immediately deformed from the flat sheet structure and large volume tube-like structures were established. Interestingly, the geometries of the stacks noticeably influenced the appearance of the resulting tube. Geometry 1 gave a large volume tube with a diameter of more than 8 mm (Figure 4.45 a). The tube was formed by

rolling of the stacked sheet over one of the long sides. Therefore, the fibres of the mesh were aligned transverse and longitudinal to the long axis of the tube. Geometry 2 caused the sheet to role over one of the edges. This led to a tube with a smaller diameter around 5 mm and the fibres were aligned at a 45 ° angle to the axis of the tube. For geometry 3 the most pronounced folding was observed. This resulted in a twofold tube with the fibres being aligned transverse and longitudinal to the axis of the architecture. While handling these structures, a very pronounced temperature dependency of the shape-morphing was noticed. To investigate this phenomenon further, the structures were also evaluated at 10 and 37 °C. Decreasing the temperature led to a more pronounced folding, which decreased the diameter of the tubes in geometry 1 and 2 and resulted in a unstructured distortion of the geometry 3. At 37 °C all geometries lost their tube shape and reverted back to a flat sheet. This is a clear indication that the extent of the swelling degree mismatch of the two DA materials is strongly dependant on temperature. The explored temperature range has special implication for potential biological applications of such shape-morphing structures. Large volume scaffolds with high porosity often suffer from the fact that upon cell seeding the cells just "fall" through the mesh. This prevents the full cell coverage of the whole construct. With the presented material, cells can be readily seeded and cultivated at 37 °C on a flat sheet. Afterwards, the temperature can be reduced to 20 °C (which many cell types can withstand for a limited time period) inducing the shape-change, giving a porous tubular structure with a homogeneous cell distribution on the wall. If the surrounding media can be crosslinked, the medium temperature can be increased again without the loss of the tube architecture. The trigger for the crosslinking of the medium could be the temperature increase itself. An ideal candidate would be for instance the recently reported POx/POzi-based bioink.[108] Such embedded cell-containing constructs could be beneficial for vascular or nerve guiding applications.

Very recently, Lewis *et al.* reported about a one layered approach to shape-morphing structures. They induced a swelling degree mismatch longitudinal vs. transverse of extruded hydrogel fibres. This was possible due to the incorporation of nanofibrillated cellulose, which aligned longitudinal to the fibre axis during extrusion and allowed the deformation of even simple one layer mesh structures. Interestingly, hints for flow induced alignment during MEW processing of DA functionalized PEtOzi were observed in this project as well (see Section 4.2.3). Furthermore, with MEW the extruded fibres are stretched during deposition. The extend of the stretching is dependant on the CS relative to the CTS of the polymer. This interaction can be used to control the fibre diameter during deposition without changing the other printing parameters like voltage or pressure[51]. Due to the stretching, the polymer chains within the fibres are more likely to be aligned along the fibre

axis, and therefore the swelling degree of the PEtOzi-based MEW printed fibres might be dependant on the printing speed. Very similar to the approach of Lewis and coworkers, this could be used to prepare scaffolds with shape-morphing properties made from just a single polymer.

To investigate this, box structures with three fibre layers were printed. For one scaffold group, the collector speed in x direction ($CS_x$) and the collector speed in y direction ($CS_y$) were equal (S36). For the other group the $CS_y$ was twice the speed of $CS_x$ (S37) (Figure 4.46 a, b). As expected with $CS_x$=$CS_y$, no significant diameter difference of the fibres in the x- and y-layer was found as both were around 36$\pm$1 $\mu$m (Figure 4.46 c). In contrast to this, for $CS_x$<$CS_y$, the fibre diameter in the y-layer was with 30$\pm$1 $\mu$m significantly smaller than in the x-layer (36$\pm$1 $\mu$m). Swelling of S36 in aqueous medium resulted (with exception of minor lifting at the edges) in a flat sheet. A potential reason for the lifting of the edges could be the deviation from the 90° fibre angle at the turns. In contrast upon hydration, S37 spontaneously deformed into a tubular structure (Figure 4.46 b). Interesting is that the sheet does not role up over one of the long sides but over the edge (Figure 4.46 b, bottom left). This indicates that the force vector, responsible for the folding, is not parallel to the fibres but is the combination of two force components. Therefore, structures with shape-morphing properties can also be prepared from the same polymer within one continuous print, just by altering the CS. This is a useful feature, since the CS can be easily changed during printing at specific locations in the manufactured construct. It could allow the fabrication of flat sheets, which upon swelling deform into more complex architectures, and this deformation would be determined by the printing pattern and the CS. It is therefore very important to investigate the influence of the CS on the swelling properties and therefore on a potential shape change. SR studies depending on the CS were performed similar to the ones described above. The resulting SRs with the respective standard errors are visualized in Figure 4.46 d). For the SR transverse to the fibre diameter, the resulting values are 146$\pm$2 % at a CS of 1400 mm/min and 147$\pm$2 % for 2800 mm/min. Thus, with respect to the standard error, no significant differences can be observed. The same applies for the longitudinal SR, where for both printing speeds a value of 143 % was found. Therefore, only a minor swelling degree mismatch was found for the fibres printed at different CS. Which means upon swelling, the fibre diameter increases slightly more than the fibre length. However, this mismatch seems to be independent of the CS and therefore no explanation for the shape-morphing of the scaffold S37 can be drawn from this experiment. It has to be pointed out that the transverse swelling ratio could not be determined with high accuracy (see discussion above), therefore these values have to be evaluated critically.

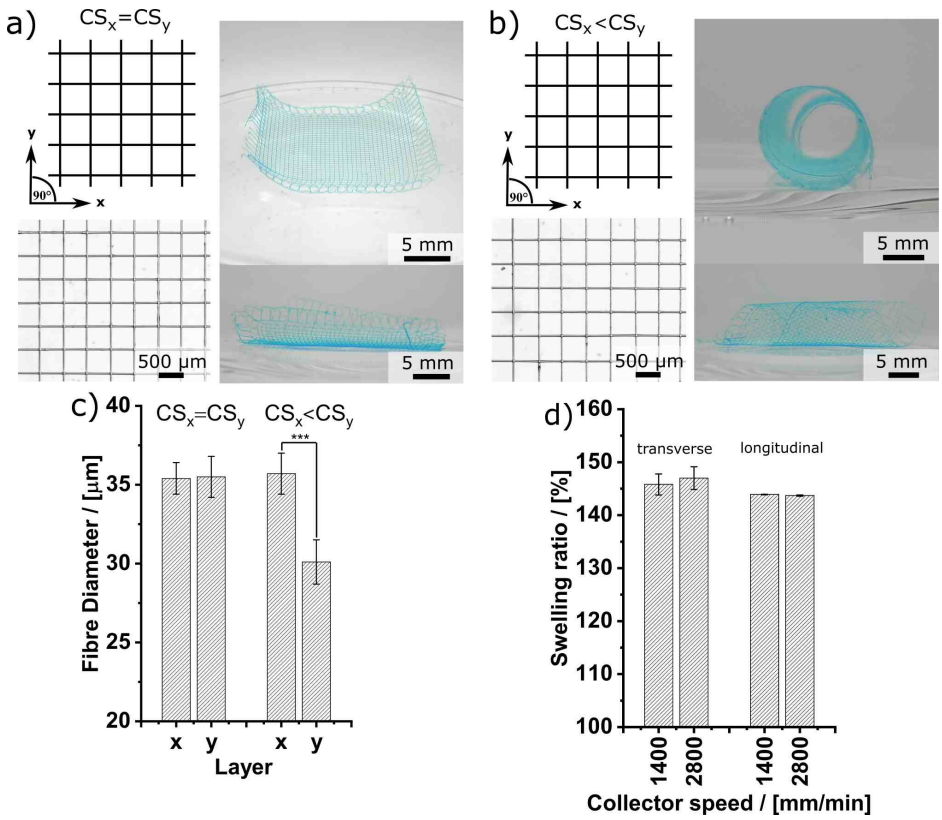


**Figure 4.46:** a) Counter-clockwise from top left: Schematic illustration of the MEW printing code with respective room coordinates. Stereo microscope image of the direct written structure with $CS_x$=$CS_y$ (S36). Side and top view of the structure after swelling. The scaffolds were coloured with DY-647P1-Maleimide for better visualization. b) Counter-clockwise from top left: Schematic illustration of the MEW printing code with respective room coordinates. Stereo microscope image of the direct written structure with $CS_x$<$CS_y$ (S37). Side and top view of the structure after swelling. The scaffolds were coloured with DY-647P1-Maleimide for better visualization. c) Average fibre diameter of the x- and y-layer of the structures S36 and S37 pre hydration. d) The calculated swelling ratio with its corresponding standard error depending on the CS.

Summing up this section, it was possible to utilize the dynamic nature of the DA reaction to produce stacks of MEW printed constructs, which are covalently attached to each other. This was used to prepare more rigid structures, which do not loose their shape outside of aqueous medium. Furthermore, by stacking structures with different EWC, a shape-morphing of the hybrid constructs was achieved upon swelling. The shape-morphing was found to be strongly temperature dependant. Furthermore, it was shown that shape change can be induced through a difference in the scaffold architecture. For instance, inducing a difference in fibre diameter between the x- and y-layers by printing at a different CS led to a shape change. Although, the mechanism responsible for some of the phenomena are not fully understood, this work highlights the potential for 4D-printing using MEW of PEtOzi-based biomaterial inks. Such systems are very interesting for applications like biological implants as well as soft robotics.[288–291]

### 4.3.5 Tubular Printing

In addition to flat collectors, MEW printing has also been performed on tubular collectors (rotating mandrels).[47] This allowed the fabrication of large volume tube structures with remarkable precision, which have been proposed for potential TE applications in bone, vascular or nerve regeneration.[59,292] In contrast to the shape-morphing of flat sheets, printing on a tubular collector gives closed architectures, which prevents undesired unwrapping upon temperature change or mechanical manipulation.*

The PEtOzi-based polymers **P68**+**P69** were used to validate, whether the DA-based biomaterial ink allows the printing of tubular constructs. Using the parameters NT:134 $^{\circ}C$, ST:134 $^{\circ}C$, p:3.25 bar, V:3.5 kV, d:3.4 mm well structured constructs with 20 layers and a fibre angle around 70 $^{\circ}$ could be prepared (Figure 4.47). Please note that these parameters are reasonably close to the parameters used for printing on a flat collector. This allowed the rapid transfer of the printing process to the new collector geometry. Except for occasional breaking of the jet, the printing was remarkably stable, which allowed the stacking of 20 fibre layers. Due to a strong adhesion of the fibres on the metal surface, it was not possible to remove the dry architectures from the mandrel without damaging them. Very similar

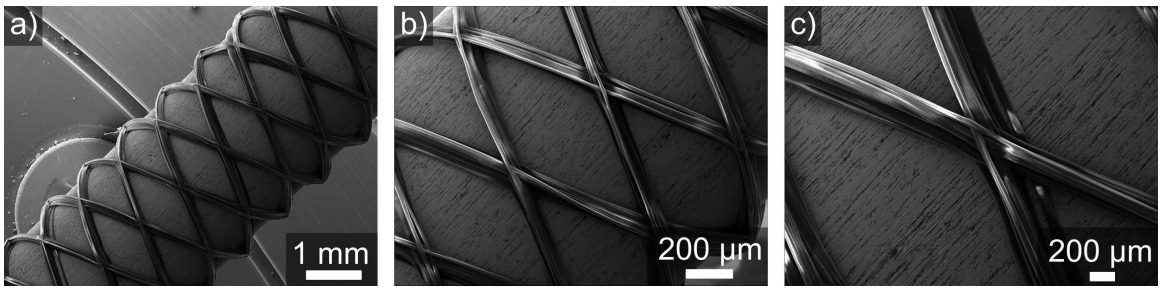


**Figure 4.47:** a)- c) SEM images of a melt electrowritten tubular scaffold (S42) produced from a mixture of **P68**+**P69**.

to the flat sheets discussed previously, the incubation of the scaffold together with the mandrel in MilliQ water resulted in rapid swelling of the printed tubular constructs. This caused the detachment of the architectures from the substrate surface without causing any damage. Furthermore, as long as the structures are immersed in aqueous medium, the tube architecture was fully retained (Figure 4.48 a). At 20 $^{\circ}C$ swelling resulted in a significant increase of the length (10.0 to 14.6 mm) and the diameter of the tubes (3.0 to 4.6 mm), while the fibre angle remained unchanged. This indicates an isotropic swelling of the whole architecture. Due to the thermoresponsive nature of the polymer backbone,

*The following printing experiments were conducted in cooperation with Michael Bartolf-Kopp and Dr. Tomasz Jüngst from the Department for Functional Materials in Medicine and Dentistry at the University Hospital Würzburg.

these dimensions decreased by approximately 20 % to 11.8 mm in length and 3.6 mm in diameter, when the bath temperature was increased to 50 °$C$. The immersed tubes (Figure 4.48 b) were readily compressed (Figure 4.48 c) and showed a "spring-like" behaviour, which causes them to "jump" (Figure 4.48 d), when the force is released quickly. This can be done repeatedly without any visible damage to the structures (Figure 4.48 e).

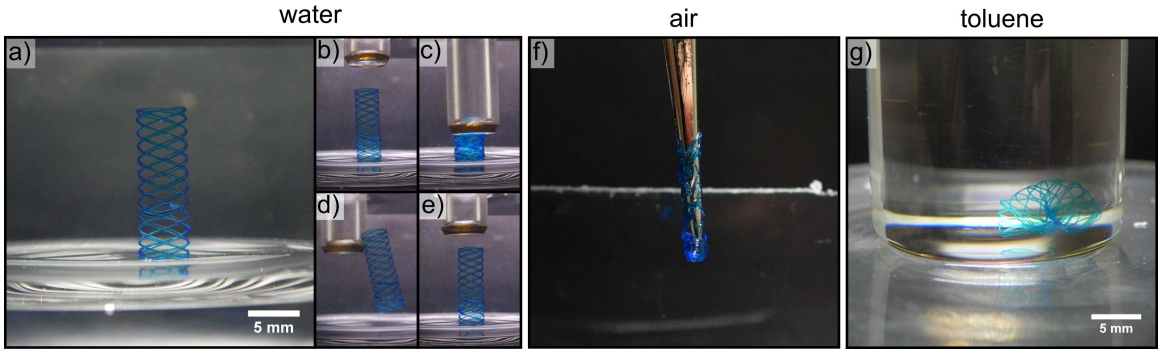


**Figure 4.48:** Images of a swollen melt electrowritten tubular scaffold (S42) produced from a mixture of **P68**+**P69**. While the tube structure is fully maintained in aqueous medium a), b) the tubes were readily compressed c) and show a "spring-like" behaviour when the compression force is released rapidly d). This causes no visible structural damage to the architectures e). The tube architecture is lost, when the scaffold is taken out of the liquid f) or when it is immersed into a non-solvent of the material (toluene) g). The scaffold is coloured with DY-647P1-Maleimide for better visualization.

However, very similar to the flat sheet structures discussed before, the tubular constructs have the tendency to collapse upon removal from the liquid medium (see Figure 4.48 f). Additionally, the nature of the solvent bath seems to have no influence on this phenomena. This was assessed with good solvents (water, ethanol), poor solvents (acetone) as well as non-solvents (toluene) of the DA polymers. For all solvents, the tube architecture collapsed upon removal from the medium. In the case of toluene, the tube structure was not even fully maintained, when the construct was immersed into the medium. This indicates that the swelling is the major driving force for maintaining the 3D-architectures of MEW printed hydrogel objects. In a non-solvent, the swelling force is lost and the printed geometry collapses. Another factor determining the rigidity of such PEtOzi-based constructs is the $T_g$ of the material. It was hypothesized that cooling of the architectures in a poor solvent might induce sufficient rigidity of the polymer fibres to allow subsequent removal from the liquid media. Therefore, S42 was immersed in pure acetone as well as a 1:1 mixture of acetone and toluene and cooled to -80 °$C$. In both solvents, the tube architecture was retained in the medium. However, upon removal of the structure from the respective solvent, the tubes still collapsed. Therefore, no enhanced structural rigidity could be induced by lowering the ambient temperature.

As the small diameter hydrogel fibres do not allow sufficient scaffold rigidity, the addition of an continuous film, which would fill the pores of the MEW scaffolds, might overcome this lack of structural integrity. In this context, SES is a straight forward and material efficient technique for the fabrication of such thin fibre fleeces. Therefore, it was hypothesized that either coating the MEW mandrel with SES followed by MEW tubular printing or vice verse could give microstructured tubular constructs, which allow handling outside of liquid media. Using the same material for SES as well as MEW will prevent the formation of a swelling degree mismatch and the deformation of the constructs upon swelling. Also as shown in section 4.3.4, the DA units will establish chemical bonds at the interface of the SES fleece and the MEW fibres, which will prevent delamination effects. Using a custom made SES device, it was possible to spin a 30 wt% solution of **P68**+**P69** in chloroform, directly on the rotating MEW mandrel. After 2 h of continuous electrospinning, a transparent and continuous polymer film was deposited on the mandrel (Figure 4.49 a). Interestingly, even

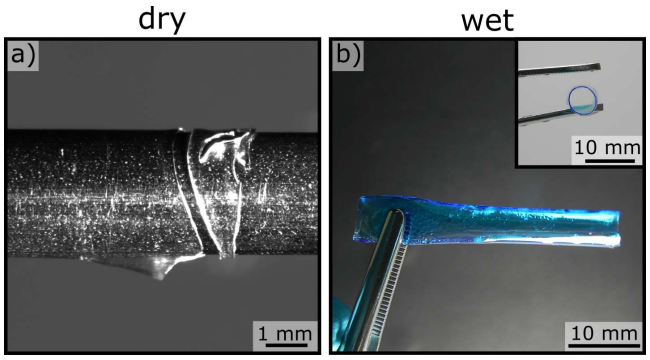


**Figure 4.49:** a) Stereo microscope image of a solution electrospun film on a MEW collector mandrel. The film was produced from a mixture of **P68**+**P69** in chloroform. The edge of the film with a defect was chosen for better visualization of the transparent coating, which is still intact on the left side of the image. The electrospinning parameters were: 0.3 mL/h; 8-10 kV; 19 mm collector distance; 3 mm mandrel diameter. b) Image of the swollen and detached solution electrospun film. The swollen film is coloured with DY-647P1-Maleimide for better visualization.

directly after the electrospinning process no signs of isolated fibres were found. The tendency of this material to flow after processing has been discussed before, yet such rapid merging of the fibres was still surprising. However, the large surface area of the small SES fibres likely promotes resorption of moisture from the surrounding, causing a more rapid plasticizing effect compared to the MEW scaffolds. Similar to the MEW printed scaffolds, the SES films show strong adhesion to the metal surface, preventing a removal in dry state. However, the film is readily detached by swelling in water. The detached films form stable tube architectures under water, but they still do fold to a flat rectangle structure upon removal from the fluid. However, by carefully removing the water film inside of the tube (e.g. with the help of a tissue paper), the tubes can be unfolded and are stable outside of a liquid medium. The structures do support their own weight and can be easily handled

with tweezers (Figure 4.49 b). The front view reveals a homogeneous film with a thickness of roughly 16 $\mu$m.

Based on these results, a tubular scaffold as shown in Figure 4.47 was MEW printed. Directly after, SES was performed and the MEW fibres were covered with a continuous polymer film. This caused the MEW fibres in the resulting construct to merge, lose their shape, and only the macroscopic structure was retained (Figure 4.50 a, b). After swelling, this gave a hybrid construct, which supported its own weight outside of the liquid medium and allowed handling. The solution electrospun material did flow into the MEW printed mesh and the film did not span over the pores. This resulted in a rough surface on the outside and a more smooth surface on the inside of the tubes (Figure 4.50 d). Moreover, the structures now are watertight and were perfusable with liquid media.

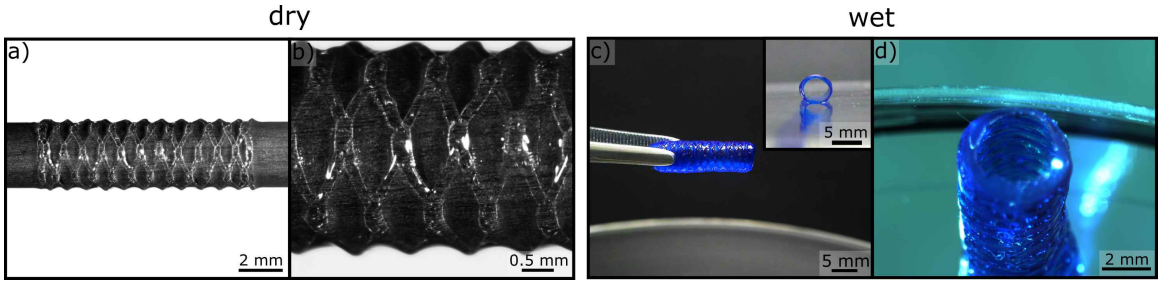


**Figure 4.50:** a), b) Stereo microscope image of a hybrid construct prepared by SES of a continuous polymer film onto a MEW printed tubular scaffold. c), d) Image of the swollen and detached hybrid construct, which retains its architecture outside of liquid medium.

All in all, this section presents the successful fabrication of microstructured tubular scaffolds using a custom made tubular MEW device. It was shown that the experience gained from printing on flat collectors, translates to the fabrication of these more complex structures. While the structures made from MEW alone collapse outside of liquid media, it was possible to incorporate SES into the fabrication process. The resulting MEW/SES hybrid structures are stable and readily handled. This also marks the first report about the SES of a PEtOzi-based material. While the structures prepared in these final experiments lack shape fidelity, this work still highlights the potential of the new DA-based biomaterial ink. These hydrogel tubes are very promising candidates for the mimicking tubular tissue like blood vessels or for nerve regeneration applications.

# 5 Summary and Outlook

Motivated by the chemical versatility as well as the excellent biological properties of POx and POzi, a new biomaterial ink was developed within this thesis. The properties of this material were tailored to the processing via MEW. MEW offers great potential for the field of biofabrication as well as scaffold-based TE. This new platform therefore expands its application range.

### Exploring the Polymer Platform

In the first chapter important basic research about the reactivity of Ozi monomers was conducted. Statistical copolymerization of EtOzi and EtOx resulted in defined polymers with narrow molar mass distributions. A detailed investigation of the polymerization kinetics revealed unexpected reactivity trends for the Ozi homopolymers as well as for the copolymerization of EtOzi and EtOx. It could be shown that during the polymerization the presence of EtOzi molecules drastically retards the reactivity of EtOx. This leads to deviations from a perfect statistical copolymer structure and favours the formation of polymers with a pronounced gradient. Furthermore, the termination behaviour of selected Ozi monomers with commonly used reagents was studied in relation to the reactivity of EtOx. For the termination with water and aqueous KOH solutions no differences between the two substance classes were found. In contrast, major deviations were revealed when methanolic KOH was used as reagent. At first, the conversion of EtOzi initiator salts with 1 M KOH in methanol led to inconsistent results. It was later shown that the result of this reaction is very sensitive to the reaction conditions, in particular the reaction temperature. When the reaction is conducted at 20 °C, termination occurs at *2*-position and 3-(methylamino)propyl propionate is formed as main product. In contrast, at 30 °C the reaction occurs at *6*-position and mainly the amide product is formed. Furthermore, it could be shown that for all major polymer batches, synthesized in this thesis, the unexpected reactivity with 1 M KOH in methanol led to the partial formation of secondary amines as end-groups. This work is also the first report about the MEW of EtOzi homo- and copolymers. It was possible to manufacture microstructured box-like scaffolds from all the investigated polymers. Also important relationships between the $T_g$, the melt viscosity, the

MEW process and the shape fidelity of the printed constructs have been explored. Taking recent publications into account, it becomes more and more apparent, that the POzi polymer class bears enormous potential for the synthesis of functional polymeric materials. However along with these reports, as well as the knowledge developed in this thesis, it is obvious that more in-depth fundamental understanding about the Ozi chemistry is required to gain full control over the polymer properties. The commonly stated assumption that Ozi reacts in the same way as its Ox counterpart needs to be revised. More detailed studies about the copolymerization as well as the termination behaviour have to be performed. In terms of studying the termination, it might be essential to mimic the chemical environment during the termination of the polymers more closely. This is not possible with the simple initiator salts used within this study as well as in literature. Unfortunately, with increasing complexity of the studied compounds the analysis, gets more and more tedious. An ideal compromise might be two- or three-membered oligomers. The influence of changes in the electronic environment of Ox and Ozi monomers is too complex to predict by common chemical principles. Therefore, along with more detailed experiments it is important to model the chemical reactivity of Ozi by computational chemistry. This could help to understand the experimental results as well as allow predictions for other monomers or termination conditions. It is also important to not neglect the influence of the initiator on the reactivity of Ox and Ozi. While this was beyond the scope of this project, it is essential for a thorough understanding of the chemistry.

**Microperiodic Hydrogel Constructs**

In the second chapter the synthesis and the stepwise improvement of the PEtOzi-based biomaterial ink is presented. This two-component material spontaneously chemically crosslinked upon mixing and due to its hydrophilic nature showed significant swelling in water. The crosslinking is based on the dynamic click chemistry of furan and maleimide. These two reactive functions are introduced to the polymer backbone via polymer analogue functionalization of partially hydrolysed PEtOzi. To allow sufficient control over the hydrolysis degree, detailed studies of the hydrolysis kinetics of POzi homopolymers as well as P(EtOzi-co-EtOx) and P(EtOzi-co-MeOx) copolymers were performed. It was found that under the studied conditions the hydrolysis kinetics followed a pseudo-first order kinetic. While the polymer length had no influence, a more rapid hydrolysis kinetic was found for the EtOx and MeOx containing copolymers. Based on the developed kinetics it was possible to control the hydrolysis degree of the polymers from 2 to 15 %. NMR analysis proofed to be sensitive enough for establishing the hydrolysis kinetics. However, the peak broadening as well as inconsistencies in the base line of the NMR spectra influenced the analytical results.

This was especially impactful for the analysis of polymers with a low degree of hydrolysis. Acid-base titration was found to be much more precise and for future studies it is advisable to use it as the main analytical tool. The DA reaction establishes a dynamic equilibrium, which is heavily influenced by the external temperature. In the heated state the equilibrium is significantly shifted to the side of the free furan and maleimide and therefore to the free polymer unimers. The material can flow and can be processed via MEW. In the cooled state (at RT) furan and maleimide react under the formation of a bicyclic adduct leading to the chemical crosslinking of the material. The $1^{st}$ generation of DA functionalized polymers allowed the formation of chemically crosslinked polymer films, which could be swollen in water resulting in hydrogels. However, it was not possible to revert this crosslinking and therefore no melt processing was feasible. The reasons for this were thermally induced side reactions leading to irreversible chemical bonds. These were caused by remaining secondary amines in the material as well as an overall high liquefaction point due to a high DF.

For the $2^{nd}$ generation the polymer analogue functionalization procedure was improved and the DF was reduced. This allowed the liquefaction of already crosslinked samples by simply heating them to above 120 °C. This was shown by DSC and IR analysis as well as melt rheology. It was possible to process these polymers by MEW, which resulted in well-structured constructs with low micron sized fibres. Upon incubation in water, these structures showed significant and rapid swelling leading to the formation of microstructured hydrogel scaffolds. The swollen architectures were soft but remarkably resilient, since they allowed aspiration and ejection through a metal cannula. The constructs showed extensive thermoresponsive properties as their size decreased by roughly 50 % upon a temperature increase of 80 °C. The dynamic nature of the DA reaction allowed straightforward chemical functionalization of the 3D constructs by DA and Michael-type chemistry. This was used for labelling them with fluorescent markers as well as biological cues. Biological evaluation showed excellent properties as well as the compatibility of the structures with standard cell culture techniques. This is the first report about the fabrication of microperiodic hydrogel scaffolds using MEW and parts of this work were published in the journal Materials Horizons.[272]

However, at this stage, the material was only processable for 1 to 2 h. During this time the printing performance decreased drastically, leading ultimately to irreversible solidification. This prevented a continuous fabrication of larger constructs and therefore drastically reduced the benefit of the DA material. Therefore, improvements of the platform were required. By establishing an improved purification method, further decreasing the DF as well as eliminating gas bubbles from the polymer melt, it was possible to extend the pro-

cessing time-window to above 24 h. While this improved the printing performance within this time-window, the reduced DF simultaneously decreased the shape fidelity of the printed constructs. Changing the polymer backbone from pure PEtOzi to a P(EtOzi-co-MeOx) copolymer increased the $T_g$ of the polymer system and allowed to counteract this effect. It has to be pointed out that the processability of this $3^{rd}$ generation of DA material still showed significant changes over prolonged heating times. Specifically, a continuous decrease of the MEW jet velocity as well as sudden and unpredictable fluctuations of the MEW jet were still observed. While no further improvements were made to this material within the scope of this project, it is of utmost importance to further increase the processing stability. These phenomena still prevent full control over the scaffold architecture, most notably a narrow fibre spacing or high number of layers. Considering the material purity, the urea derivative formed during the DCC supported coupling has proven to be difficult to remove from the samples. The use of other coupling agents like DIC or CDI could be considered. Decreasing the processing temperature further is another possibility to decrease thermally induced changes. Within this project, the crosslinking density was reduced to 2 %, which showed drastic influence on the printing temperature. In this context it is important to highlight that further decreasing the crosslinking degree will probably prevent the formation of stable hydrogels. However, using one low molar mass component, e.g. a small di-functional furan molecule, could allow further decrease of the processing temperature while still provide sufficient chain entanglement to maintain a stable jet. A third option is the use of less reactive DA molecules like cyclopentadiene or anthracene. However, this will most likely require major adjustments to the MEW processing conditions.

**Expanding the Material Range**

In this section the influence of the polymer backbone structure on the material properties, the MEW processing as well as the properties of the 3D hydrogel constructs was evaluated. For this, in addition to the PEtOzi homopolymers used before, P(EtOzi-co-EtOx) as well as P(EtOzi-co-MeOx) copolymers were used as parent polymers. All three different polymers were functionalized to 2, 3 and 4 % with furan and maleimide. Importantly, it was possible to transfer the synthesis procedure optimized for PEtOzi to the new polymer structures. By analysing the material, it was found that both, the different backbone as well as the DF had strong influence on the hydrophilicity and the LCST of the polymers. Within the investigated library, it was possible to cover a wide LCST range from 62 to 34 °C. Also the EWC of the crosslinked material could be controlled between 96 and 79 %. The hydrogel properties were further investigated using Cryo-SEM. This revealed overall rather small pores with a broad size distribution between $\leq$100 nm and $\geq$700 nm for melt

cast bulk samples. Interestingly, even smaller pores around 50 nm were found for swollen melt electrowritten fibres. Very surprising was the high stability of the DA hydrogels towards aqueous hydrolysis. Qualitatively, melt electrowritten structures were found to be unaffected over an incubation period of three months in MilliQ water and PBS solution. Quantitative studies showed rapid degradation of bulk samples within 11 d at pH 11. The degradation was found to proceed via basic hydrolysis of the maleimide ring. At neutral and acidic conditions, again long-term stability was found. Compared to the POzi homopolymers ($T_g$: 24 °C), the $T_g$ of the copolymers was found to be significantly increased to 31 and 33 °C for the EtOx and MeOx containing polymers respectively. All of the studied polymers allowed the fabrication of well-structured box-like architectures. It was found that the shape fidelity was strongly tied to the $T_g$, the crosslinking density but also the hydrophilicity. While all constructs were well structured immediately after printing, the structures prepared from polymers with a low $T_g$ and a low DF lost their microstructure within few hours post printing. This process was also dependant on the material hydrophilicity as well as the humidity in the surrounding air. Furthermore, the chemical structure of the polymers also had a strong influence on the MEW temperature, which ranged between 120 and 178 °C. It is important to note that a lower processing temperature is generally desired as processing instabilities were found to be increased at higher temperature. Unfortunately, within the studied library it was not possible to separate the MEW temperature from the polymer hydrophilicity. It would be interesting for future experiments to use low molar mass additives, as these could help to separate these two parameters.

While the lower functionalized polymers can be processed under gentle conditions, they do not provide sufficient shape fidelity. Either printing directly in a climate-controlled environment or curing the printed structures under dry and chilled conditions might help to overcome this issue. In addition to the thermally induced [4+2] cycloaddition of the DA reaction, light induced [2+2] reactions were investigated as potential alternatives. However, a high content of functional groups was required to allow enough chemical crosslinking, and this rendered the material insoluble in water. While these polymers cannot be used for the synthesis of hydrogels, they could be used for the fabrication of chemically reinforced hydrophobic MEW fibres. Using the dynamic nature of the DA reaction, it was possible to prepare multi-material constructs from melt electrowritten scaffolds. These structures showed potential for 4D-printing. By utilizing a swelling degree mismatch between the layers, it was possible to form hydrogel tubes upon swelling the constructs in water. The extent of the deformation was found to be strongly temperature dependent. Interestingly similar shape-morphing structures could also be prepared from a single material just by changing the conditions during printing. Using a higher CS in y-direction compared to x-

direction led to a spontaneous tube formation upon swelling the sheets in water. Compared to the two-material approach it is still unclear, where the driving force for this deformation comes from. Investigations of the swelling properties of fibres printed at different CS showed no significant differences. Generally, this is the first report about the use of melt electrowritten structures for 4D-printing. However, the ability to prepare self-folding structures with defined low micron sized features would be very beneficial for vascular applications or soft robotics. Due to the improved printing performance of the $3^{rd}$ generation of DA material, it was possible to transfer the printing process to a tubular MEW printer. This allowed the fabrication of defined microstructured hydrogel tubes. By combination of SES with MEW, the tubes were resilient enough to allow handling outside of liquid media. Such architectures are of immense interest for nerve guiding or vascular applications. Further steps should focus on improving the handling of these structures. While the combination with SES has proven to be a promising approach, this currently leads to the loss of the microstructure of the melt electrowritten constructs. Changes in the electrospinning protocol e.g. other solvents or polymers with a higher $T_g$ as well as longer curing times between the SES and MEW are good starting points.

With some final words I would like to recapitulate the work discussed in this thesis. The aim of this project was "the preparation of a biomaterial ink for the fabrication of chemically crosslinked hydrogel scaffolds with low micron sized features by using MEW". By using a functional polymeric material based on Ozi and Ox homo- and copolymers in combination with DA-based dynamic covalent chemistry, it was possible to achieve this goal. This marks an important step for the young AM technique MEW, as soft and hydrophilic structures become available for the first time. The use of dynamic covalent chemistry is a very elegant and efficient method for consolidating covalent crosslinking with melt processing. While there are still some challenges, most notably the persistent instabilities observed during processing, I am certain that these can be overcome. Furthermore it was shown that the high chemical versatility of the Ox and Ozi chemistry offers great potential to control the processing parameters. It was shown that the established platform offers straight forward potential for modification with biological cues and fluorescent markers. This is essential for advanced biological applications. The physical properties of the material are readily controlled and the potential for 4D-printing was highlighted as well. The developed hydrogel architectures are excellent candidates for 3D cell culture applications. In particular, the low internal strength of some of the scaffolds in combination with the tendency of such constructs to collapse into thin strings could be interesting for the cultivation of muscle or nerve cells. These cell types benefit from the directional cues of the aligned micro fibres as well as the soft nature of the material, and this could allow to mimic nerve or muscle

fibre bundles. In this context it was also possible to show that MEW printed hydrogel scaffolds can withstand the aspiration and ejection through a cannula. This allows the application as scaffolds for the minimally invasive delivery of implants or functional tissue equivalent structures to various locations in the human body. Specific examples could be the delivery of TE patches for the treatment of myocardial infarction. Also application in ophthalmology could be imagined, and the injected structure could serve as protection of the retina during ophthalmologic surgery. Considering the amphiphilic nature of the developed material and its ability to retain amphiphilic molecules for longer time periods, potential applications for the target specific drug delivery via drug-loaded scaffolds can be imagined. This could be promising for cancer treatment trough minimally invasive delivery, but also for non-invasive applications like drug-loaded wound dressings. Therefore, this work lays the foundation for a plethora of different applications in biomedicine and other fields.

# 6 Zusammenfassung und Ausblick

Motiviert durch die chemische Vielseitigkeit sowie die hervorragenden biologischen Eigenschaften von POx und POzi wurde im Rahmen dieser Arbeit eine neue Biomaterialtinte entwickelt. Die Eigenschaften dieses Materials wurden hierbei speziell auf die Prozessierung mittels MEW angepasst. Im Allgemeinen bietet MEW großes Potential für den Bereich der Biofabrikation sowie der gerüstbasierten Gewebezüchtung (engl. scaffold-based Tissue Engineering). Das hier entwickelte Material hat das Potential, den Anwendungsbereich von MEW deutlich zu erweitern und hydrophile und weiche Materialen zugänglich zu machen.

### Die Polymerplattform

Im ersten Kapitel dieser Arbeit wurden wichtige Grundlagen der Reaktivität von Oxazinmonomeren erarbeitet. Mittels statistischer Copolymerisation von EtOzi und EtOx war es möglich, definierte Polymere mit geringer Polydispersität zu synthetisieren. Hierbei wurden unerwartete, relative Reaktivitäten beobachtet. Zum Beispiel zeigte sich, dass die Reaktivität von EtOx in der Mischung mit EtOzi drastisch reduziert war. Während der Copolymerisation führte dies zu starken Abweichungen von der idealen statistischen Copolymerstruktur und es entstanden Polymere mit einem ausgeprägten Blockcharakter. Weiterhin wurde das Terminationsverhalten von EtOzi Initiatorsalzen mit gängigen Reagenzien untersucht und mit der Reaktivität von EtOx Initiatorsalzen verglichen. Hierbei wurden für die Termination mit Wasser und wässrigen KOH Lösungen keine Unterschiede zwischen den beiden Substanzklassen gefunden. Allerdings zeigten sich bei der Verwendung von methanolischem KOH als Reagenz größere Abweichungen. Zunächst führte die Umsetzung von EtOzi Initiatorsalzen mit 1 M KOH in Methanol zu schwer reproduzierbaren Ergebnissen. Später konnte gezeigt werden, dass das Ergebnis dieser Reaktion stark von den Ausgangsbedingungen, insbesondere der Reaktionstemperatur, abhängt. Wurde die Reaktion bei 20 °C durchgeführt, erfolgte die Umsetzung hauptsächlich an der *2*-Position, was zur Bildung von 3-(Methylamino)propanol führte. Im Gegensatz dazu reagierte das Initiatorsalz bei 30 °C ausschließlich an der *6*-Position und das Amidprodukt wurde gebildet. Darüber hinaus konnte gezeigt werden, dass bei allen in dieser Arbeit synthetisierten Polymeren die Termination mit 1 M KOH in Methanol zur teilweisen Bildung von sekundären Aminen als

Endgruppe führte. Im Rahmen dieser Arbeit wurden mehrere EtOzi Homo- und Copolymere auf ihre Prozessierbarkeit mittels MEW untersucht. Hierbei war es möglich, aus allen Polymeren mit hoher Präzision boxartige Konstrukte zu drucken. Zusätzlich wurden wichtige Zusammenhänge zwischen dem $T_g$ der Polymere, deren Schmelzviskosität, dem MEW Prozess und der Formtreue der 3D gedruckten Konstrukte hergestellt. Unter Berücksichtigung jüngster Publikationen und der in dieser Arbeit vorgestellten Ergebnisse lässt sich vermuten, dass die derzeit noch relativ unerforschte POzi Polymerklasse enormes Potential für die Synthese funktioneller polymerer Materialien birgt. Hierzu ist es allerdings unerlässlich, ein elementares Verständnis der Oxazinchemie zu erarbeiten. Offensichtlich ist hierbei auch, dass die Annahme einer vergleichbaren Reaktivität von Oxazolinen und Oxazinen zumindest hinterfragt werden muss. Weiterführende Arbeiten sollten sich darauf fokussieren, die Terminationschemie von Oxazinen besser zu verstehen. Es ist ratsam, von einfachen Initiatorsalzen auf komplexere Di- oder Trimere umzusteigen, da diese die chemische Umgebung der Polymere besser widerspiegeln. Als Ergänzung experimenteller Ergebnisse sollte die chemische Reaktivität von Oxazinen zusätzlich computergestützt modelliert werden.

**Mikrostrukturierte Hydrogelkonstrukte**

Im zweiten Kapitel wurden die Synthese der PEtOzi basierten Biomaterialtinte und die Optimierung der Schmelzprozessierbarkeit vorgestellt. Die Vernetzung der Polymere basierte dabei auf der dynamischen Klickchemie von Furan und Maleimide. Mittels polymeranaloger Funktionalisierung wurde teilhydrolisiertes PEtOzi jeweils mit Furan und Maleimide funktionalisiert. Diese zwei Komponenten vernetzen nach Vermischung spontan und anschließendes Quellen in Wasser führt zur Bildung eines Hydrogels. Um die kontrollierte Hydrolyse der Polymere zu ermöglichen, war es zunächst nötig, die Hydrolysekinetiken aller verwendeten POzi basierten Homopolymere sowie der P(EtOzi-co-EtOx) und P(EtOzi-co-MeOx) Copolymere zu untersuchen. Es zeigte sich, dass unter den angewandten Bedingungen die Reaktion einer Kinetik pseudo-erster Ordnung folgte. Während das Molekulargewicht der Polymere keinen Einfluss auf die Reaktionsgeschwindigkeit hatte, wurde eine deutliche Steigerung der Hydrolysegeschwindigkeit für die EtOx und MeOx basierten Copolymere festgestellt. Mittels der Hydrolysekinetiken war es anschließend möglich, Polymere mit definiertem Hydrolysegrad im Bereich von 2 bis 15 % zu synthetisieren. Die DA Reaktion zwischen Furan und Maleimide etabliert ein reversibles Gleichgewicht, dessen Lage stark temperaturabhängig ist. Bei hohen Temperaturen liegt das Gleichgewicht zum Großteil auf der Seite der Edukte. Für das DA basierte Biomaterial bedeutet dies, dass die Polymerketten zum Großteil als freie Polymerunimere vorliegen, wodurch sich das Material schmelzprozessieren lässt. Im abgekühlten Zustand verschiebt sich das Gleichgewicht zu der Seite

des bicyclischen Addukts, was zur Ausbildung von chemischen Bindungen zwischen den Polymerketten führt. Die erste Generation der DA funktionalisierten Poly(2-oxazolin)en ermöglichte die Synthese von chemisch vernetzen Polymerfilmen. Inkubation in Wasser führte zu einem starken Quellen des Materials und der Ausbildung eines Hydrogels. Allerdings war die Umkehr der Vernetzung durch Erhitzen des Materials nicht möglich. Durch die thermische Belastung bildeten sich durch ungewollte Nebenreaktionen nicht reversible chemische Bindungen. Aufgrund dessen wurde eine Schmelzprozessierung der Polymere unmöglich. Als Ursache dafür konnten Nebenreaktionen verantwortlich gemacht werden. Diese traten aufgrund unvollständiger Funktionalisierung im Material verbliebener, sekundärer Amine auf.

Für die zweite Generation des Biomaterials wurde zunächst, um die Anzahl an freien Aminen zu reduzieren, die Funktionalisierungsreaktion verbessert. Gleichzeitigt wurde ein niedrigerer Funktionalisierungsgrad verwendet, um die Verflüssigungstemperatur zu verringern. Durch diese Maßnahmen konnten zuvor vernetze Filme durch Erhitzen auf über 120 °C verflüssigt werden. Dies wurde sowohl visuell als auch mittels DSC, IR Analyse sowie anhand rheologischer Messungen gezeigt. Dadurch war es möglich, die Polymere mittels MEW in dreidimensionale, mikrostrukturierte Konstrukte zu verarbeiten. Anschließend konnten diese durch Inkubation in Wasser in mikrostrukturierte Hydrogelgerüste überführt werden. Die resultierenden Strukturen waren weich, aber gleichzeitig erstaunlich robust. Interessant war auch das ausgeprägte thermoresponsive Verhalten, welches dazu führte, dass der Quellgrad durch Erhitzen auf 80 °C um bis zu 50 % abnahm. Die dynamischen Eigenschaften der DA Reaktion ermöglichten es zusätzlich, die gedruckten Konstrukte mittels DA oder Michael Chemie zu funktionalisieren. Dies konnte sowohl mit fluoreszierenden als auch mit biologischen Markern gezeigt werden. Mittels Zelltests wurde die Zytokompatibilität nachgewiesen. Zusätzlich zeigte sich, dass die weichen Hydrogelkonstrukte mit Standardzellkulturtechniken kompatibel waren.

An diesem Punkt war die Verarbeitbarkeit der DA basierten Tinte jedoch auf maximal 1 bis 2 Stunden beschränkt. Während dieses Zeitraums konnte eine kontinuierliche Abnahme der Druckqualität beobachtetet werden und letztendlich verfestigte sich das Material schließlich irreversibel. Daher wurde die Herstellung größerer Konstrukte unmöglich. Durch die Etablierung einer verbesserten Aufarbeitungsprozedur sowie der weiteren Verringerung des Funktionalisierungsgrades war es allerdings möglich, den Druckzeitraum auf über 24 Stunden auszuweiten. Dies ging einher mit der generellen Verbesserung der Druckqulität in diesem Zeitraum. Die Verringerung des Funktionalisierungsgrades führte jedoch gleichzeitig zum partiellen Verlust der Formtreue der 3D gedruckten Konstrukte. Allerdings war es möglich,

diesem Effekt durch die Verwendung von Copolymeren mit einem höheren $T_g$ entgegenzuwirken. Die Verarbeitbarkeit dieser dritten Generation von DA Materialien wies weiterhin signifikate Veränderungen auf. Dies zeigte sich im Besonderen durch die kontinuierliche Abnahme der Geschwindigkeit des MEW Jets. Zusätzlich traten in unregelmäßigen Abständen plötzliche Fluktuationen des Jets auf. Im Rahmen dieses Projektes wurden keine weiteren Veränderungen der Biomaterialtinte vorgenommen. Um volle Kontrolle über die Faserablage und den Faserabstand zu erhalten, ist es von großer Bedeutung, die Druckqualität weiter zu steigern. Hinsichtlich der Aufarbeitung ist besonders die vollständige Entfernung des Harnstoffderivates, welches als Nebenprodukt in der DCC katalysierten Kupplungsreaktion anfällt, problematisch. Hier könnte die Verwendung anderer Kupplungsreagenzien wie DIC oder CDI in Betracht gezogen werden. Zusätzliche Verbesserung kann durch die weitere Senkung der Prozessierungstemperatur erreicht werden. Hinsichtlich dessen zeigte die Senkung der Vernetzungsdichte auf 2 % einen starken Einfluss. Allerdings würde eine weitere Verringerung vermutlich nicht mehr zu stabilen Hydrogelen führen. Die Verwendung von zumindest einer Komponente mit niedrigem Molekulargewicht, zum Beispiel eines difunktionellen Furanmoleküls, könnte jedoch die weitere Senkung der Prozesstemperatur ermöglichen. Zusätzlich kann auch die Verwendung von weniger reaktiven DA Molekülen wie Cyclopentadien oder Anthracen in Betracht gezogen werden. Vorraussichtlich würde dies größere Anpassungen des MEW Prozesses erfordern.

### Vergrößerung der Materialbasis

In diesem Kapitel wurde der Einfluss der Polymerstruktur auf die Materialeigenschaften, den MEW Prozess sowie auf die Eigenschaften der Hydrogelkonstrukte untersucht. Hierzu wurden, zusätzlich zu dem PEtOzi Homopolymer, P(EtOzi-co-EtOx) sowie P(EtOzi-co-MeOx) Copolymere zur Synthese des Biomaterials verwendet. Alle Polymere wurden jeweils zu 2, 3 und 4 % hydrolysiert und anschließend mit Furan und Maleimide funktionalisiert. Hier zeigte sich, dass sich die verwendete Syntheseroute direkt auf andere Polymerstrukturen übertragen lässt. Die verschiedenen Strukturen hatten großen Einfluss auf die LCST und die Hydrophilie der funktionalisierten Polymere. Innerhalb dieser Polymerbibliothek war es möglich, den LCST Bereich von 62 bis 34 °C abzudecken. Zusätzlich wiesen die vernetzten Hydrogele einen EWC von 96 bis 79 % auf. Mittels Cryo-SEM konnte gezeigt werden, dass alle Hydrogele aus kleinen, unregelmäßigen Poren aufgebaut waren. Die Porengröße nahm mit steigendem Funktionalisierungsgrad ab. Interessanterweise wurden sogar noch kleinere Poren, im Bereich von 50 nm, innerhalb MEW gedruckter Fasern gefunden. Das Degradationsverhalten ist von immenser Bedeutung für Biomaterialen. Überraschenderweise wiesen

die DA vernetzten Hydrogele hohe Stabilität gegenüber wässriger Hydrolyse auf. Qualitativ konnte an MEW gedruckten Konstrukten nach dreimonatiger Inkubation in MilliQ Wasser oder PBS keine Veränderung festgestellt werden. Nachfolgende quantitative Studien zeigten, dass sich das Material unter basischen Bedingungen (pH 11) innerhalb von 11 Tagen auflöste. Mechanistisch konnte dies auf die Öffnung des Maleimideringes durch $OH^-$ Nukleophile zurückgeführt werden. Unter neutralen und saueren Bedingungen wurden wiederum nur geringe Veränderungen über mehrere Monate beobachtet. Im Vergleich zu den POzi Homopolymeren ($T_g$: 24 °C) lag der $T_g$ der Copolymere mit 31 °C für die EtOx haltigen Polymere und 33 °C für die MeOx haltigen Polymere deutlich höher. Dies hatte sowohl Einfluss auf den MEW Prozess als auch auf die Eigenschaften der gedruckten Konstrukte. Alle untersuchten Polymere konnten mittels MEW versponnen werden. Während alle Architekturen unmittelbar nach dem Druck eine detaillierte Mikrostruktur aufwiesen, ging diese bei den Polymeren mit niedrigem Funktionalisierungsgrad und niedrigem $T_g$ innerhalb weniger Stunden verloren. Dieser Prozess war ebenfalls stark von der Hydrophilie des Materials und der Feuchtigkeit der Umgebungsluft abhängig.

Auch konnte ein großer Einfluss der Polymerstruktur auf die MEW Drucktemperatur beobachtet werden. Für die untersuchten Polymere reichte diese von 120 bis 178 °C. Im Allgemeinen ist eine niedrigere Drucktemperatur von Vorteil, da Prozessinstabilitäten bei hohen Temperaturen vermehrt auftraten. Leider war es im Rahmen dieser Studie nicht möglich, die MEW Drucktemperatur unabhängig von den hydrophilen Eigenschaften zu beeinflussen. Für nachfolgende Arbeiten wäre es interessant zu untersuchen, ob die Verwendung von niedermolekularen Vernetzungseinheiten es ermöglicht, hydrophilere Oxazine/Oxazolin Copolymere bei niedrigen Temperaturen zu verspinnen. Von Nachteil ist auch der Verlust der Mikrostruktur, welcher besonders bei niedrigfunktionalisierten Polymeren auftrat. Hierbei könnte es hilfreich sein, den MEW Druck in einer klimatisierten Umgebung durchzuführen. Dies könnte den weichmachenden Effekt durch Aufnahme von Feuchtigkeit aus der Luft verhindern und so zu einer erhöhten Formtreue führen. Zusätzlich zur thermisch induzierten [4+2] Cycloaddition der DA Reaktion wurden lichtinduzierte [2+2] Reaktionen als alternative Vernetzungsmethode untersucht. Jedoch war hier, um eine vollständige Vernetzung der Polymere zu gewährleisten, ein unerwartet hoher Funktionalisierungsgrad von Nöten. Aufgrund des hydrophoben Charakters der funktionellen Gruppen reduzierte sich die Wasserlöslichkeit der Polymere drastisch, was diese ungeeignet für die Synthese von Hydrogelen machte. Allerdings können diese Polymere zum Beispiel zur Herstellung von chemisch verstärkten, hydrophoben MEW Fasern verwendet werden. Die dynamische Natur der DA Reaktion machte es möglich, mehrschichtige MEW Strukturen aus zwei verschiedenen Materialen herzustellen. Wurden hierbei Polymere mit unterschiedlichem Quellgrad verwendet,

zeigten diese Strukturen Potential für 4D Druck Anwendungen. Als Beispiel wurden im Rahmen dieser Arbeit Hydrogelröhren erzeugt. Zusätzlich war das Ausmaß der Verformung stark temperaturabhängig. Interessanterweise konnten ähnliche strukturverändernde Konstrukte auch aus einem einzigen Material, allein durch Änderung der Druckbedingungen, hergestellt werden. Wurden beim Druck von Boxstrukturen in x- und y-Richtung unterschiedliche Kollektorgeschwindigkeiten verwendet, verformten sich die Konstrukte während des Quellens spontan. Im Gegenstatz zu den Multimaterialkonstrukten ist die Triebkraft für diesen Prozess noch unklar, denn die Untersuchungen der Quellungseigenschaften von Fasern, die mit unterschiedlicher Geschwindigkeit gedruckt wurden, zeigten keine signifikanten Unterschiede. Dies ist das erste Mal, dass MEW gedruckte Strukturen für den 4D Druck verwendet wurden. Selbstfaltende Konstrukte mit definierten Mikrostrukturen könnten jedoch äußerst interessant für vaskuläre oder Soft Robotik Anwendungen sein. Die verbesserten Druckeigenschaften der dritten Generation ermöglichten es, den Druckprozess auf einen MEW Röhrendrucker zu übertragen. Dadurch war es möglich, definierte, mikrostrukturierte Hydrogelröhren zu erstellen. Anschließend konnten diese durch Kombination mit SES mit einem dünnen Hydrogelfilm überzogen werden. Dies erhöhte die Stabilität der Konstrukte und ermöglichte deren Handhabung außerhalb von wässrigen Lösungen.

Abschließend möchte ich noch in ein paar Worten die in den vorangegangenen Kapiteln diskutierte Arbeit einordnen. Das Ziel dieses Projekts war „die Herstellung einer Biomaterialtinte, welche die Herstellung chemisch vernetzter, mikrostrukturierter Hydrogelgerüste mittels MEW ermöglicht“. Die Verwendung von speziell auf den schmelzbasierten 3D Druck angepassten polyoxazinbasierten Polymeren und die Anwendung von dynamisch kovalenter Chemie ermöglichte es, dieses Ziel zu erreichen. Dieses Projekt ist ein wichtiger Schritt für die aufstrebende, additive Fertigungstechnologie MEW, da nun erstmals weiche und hydrophile Strukturen erzeugt werden können. Speziell die Verwendung der dynamischen DA Chemie ist ein eleganter Weg, die Fertigung von kovalent vernetzten Strukturen mit der Schmelzprozessierung zu vereinen. Zwar gibt es noch einige Herausforderungen zu meistern, allen voran die Überwindung der weiterhin bestehenden Druckinstabilitäten, jedoch eröffnet die chemische Vielseitigkeit der Ox und Ozi Chemie viele Wege, das Material noch besser an den MEW Prozess anzupassen. Es wurde weiterhin gezeigt, dass die hier etablierte Materialplattform die Möglichkeit zur Modifikation mit biologischen und chemischen Markern bietet. Dies ist besonders für biologische Anwendungen unerlässlich. Die physikochemischen Eigenschaften des Materials lassen sich leicht auf potentielle Anwendungen anpassen und das Potential für den 4D Druck wurde ebenfalls hervorgehoben. Alles in Allem legt diese Arbeit den Grundstein für eine Vielzahl von verschiedenen Anwendungen sowohl in der Biomedizin als auch in anderen Bereichen.

# 7 Experimentals

## 7.1 Equipment

### Glovebox

A LabMaster 130 (MBraun, Garching, Germany) comprising nitrogen atmosphere (5.0, Linde AG, Germany) was used to store chemicals and to initiate polymerizations under inert conditions.

### Nuclear Magnetic Resonance (NMR) Spectroscopy

Nuclear magnetic resonance spectroscopy (NMR) measurements were performed on a Bruker Fourier 300 (1H 300.12 MHz) at 298 K, Bruker BioSpin (Rheinstetten, Germany). Spectra were referenced on the residual solvent signals (MeOD 3.31 ppm; $CD_3CN$ 1.94 ppm).

### Gel Permeation Chromatography (GPC)

Gel permeation chromatography (GPC) was performed of a Polymer Standard Service (PSS, Mainz, Germany) system (pump mod. 1260 infinity, RI-detector mod. 1260 infinity, precolumn GRAM 10 $\mu$m (50*8 mm), 30 Å PSS GRAM 10 $\mu$m (300*8 mm) and 1000 Å PSS GRAM 10 $\mu$m (300*8 mm). The device was calibrated against PEG standards and hexafluoroisopropanol (HFIP) (3 g/L potassium trifluoroacetate (KTFA), 313 K, 1 mL/min) was used as eluent.

### Infrared (IR) Spectroscopy

IR-Spectra were recorded on a Jasco (Gross-Umstadt, Germany) FT/IR-4100 equipped with an ATR-unit. A scan count of 64 with a resolution of 4 $cm^{-1}$ was used. All spectra were post-processed by baseline correction using the software Spektra Manager Version 2.

### Titration

Conductometric titrations were performed with a Metrohm 905 Titrando instrument. The titroprocessor was controlled by the software Tiamo 2.3.

### Rheology

Rheology experiments were performed on a Anton Paar (Ostfildern, Germany) Physica MCR 301 utilizing a plate-plate geometry (diameter 2 mm) and a measurement gap between 0.3 and 0.5 mm. All samples were added in powder state and then liquefied by heating to 140 °C followed by 2 min constant shear (10 1/s) segment to remove air bubbles. Strain sweeps from 0.01 rad/s to 10 rad/s were conducted at different temperatures to verify linear viscoelastic behaviour of the material. Frequency sweeps were performed from 0.1 to 100 rad/s with an amplitude of 1 %. For the reversibility studies, a strain of 1 % and a frequency of 10 rad/s was used.

### Thermogravimetric Analysis (TGA)

TGA was performed on a TG 209 F1 Iris from NETZSCH (Selb, Germany) with a heating rate of 10 K/min in synthetic air. Relative mass loss was calculated according to the absolute mass loss at 900 °C.

### Dynamic Scanning Calorimetry (DSC)

DSC measurements were performed on a SC 204 F1 Phoenix system from NETZSCH (Selb, Germany) equipped with a CC200 F1 controller unit.

### Confocal Laser Scanning Microscopy

Scaffolds functionalized with DY-647P1-Maleimide were visualized using a TCS SP8 SMD inverted confocal microscope from Leica. A illumination wavelength of 633 nm and a detection wavelength range from 650-694 nm was used. The image dimensions are 1162.5 $\mu$m x 1162.5 $\mu$m x 434.7 $\mu$m with a z-step number of 146.

### Matrix-Assisted Laser Desorption/Ionization Time-of-Flight Mass Spectrometry (MALDI-TOF)

The MALDI-TOF measurements were performed on a Autoflex II LRF from Bruker (Mannheim, Germany) and DCTB (trans-2-[3-(4-tert-Butylphenyl)-2-methyl-2-propenylidene]-malononitrile) was used as matrix. The polymers were dissolved in acetonitrile (1g/L) and

mixed with a matrix solution in acetonitrile (20mg/mL). 1$\mu$L of the mixture was crystallized on a smooth steel target.

### Scanning Electron Microscopy (SEM)

SEM and Cryo-SEM pictures were taken with a Zeiss Crossbeam 340 field emission SEM (Oberkochen, Germany).

### Environmental Scanning Electron Microscopy (ESEM)

ESEM images were taken using a scanning electron microscope (FEI Quanta FEG 250, Thermo Fisher Scientific). The imaging was conducted in the environmental scanning electron microscopy (ESEM) mode.

### Stereomicroscopy

Optical analysis was performed on a Discovery V.20 stereomicroscope from Carl Zeiss AG (Oberkochen, Germany). The device was equipped with a Zeiss icc 5 colour camera (5 MP, 12 bit), two lenses (0.63x and 1.5x Plan Apo) and a zoom range up to 20:1. All pictures were processed with the Zen2012 pro software.

### Melt Electrowriting

A custom-made MEW-printer was used as shown in Figure 2.1, which is similar to that presented in detail elsewhere.[49] Briefly, the MEW head is electrically-heated and has a nitrogen line to pressurize a glass syringe (the polymer reservoir). A high voltage is applied to the nozzle while the collector plate is grounded and can move freely underneath the MEW head on an x-y motion stage. The collector distance (z-axis) was adjusted manually.

### Solution Electrospinning

A custom-made SES device was used for the electrospinning experiments of the DA functionalized PEtOzi. A 1 mL BBraun plastic syringe equipped with a flat tipped 21 G metal needle served as polymer reservoir. The SES device consisted out of a syringe pump (wpi Ltd), a grounded rotating collector and a high voltage source.

## 7.2 Methods and General Procedures

### Mixing of the Diels-Alder Polymers

Three different mixing procedures have been utilized in the scope of this thesis.

- Mixing in Methanol: First, both polymers are dissolved in methanol and the solutions are thoroughly mixed, followed by evaporation of the solvent at RT. This results in an transparent and elastic polymer film. This polymer film often contains trapped gas bubbles, which are difficult to remove and can influence the analysis as well as disturb the MEW processing. Furthermore, due to strong adhesion to surfaces like glass or metal, the prepared film is difficult to remove without damage. Swelling in a solvent is a viable method but not always desirable.

- Mixing by grinding in liquid nitrogen: Most of the polymers used within this thesis have a $T_g$ near or below RT, which complicates the mixing in solid state. Reliable mixing can be achieved by grinding the two components in a liquid nitrogen filled mortar. During this procedure, moisture is rapidly adsorbed for the surrounding air causing a transition from a solid powder to a sticky paste soon after the liquid nitrogen is evaporated. Performing the mixing in a portable, argon filled glove bag allows prolonged and more thorough mixing. The resulting white powder can then be transferred into a disposable aluminium crucible and dried over night in an vacuum oven at 40 °C and 300 mbar. After this step, the two-component biomaterial ink is crosslinked yet ready for liquefaction and can be used for MEW processing. Depending on the $T_g$ of the polymer, the resulting material is either a clear colourless elastic polymer film or a brittle solid. Due to the flexibility of the aluminium crucible, the polymer is readily removed in both states.

- Mixing by dissolution and lyophilisation: Both polymers are dissolved in MilliQ water followed by thorough mixing of the solution using a vortexer. The solutions are then freeze dried over night resulting in a fluffy white material, which can be handled with ease. This material is also already crosslinked, insoluble in solvents and can be used for analysis or MEW processing.

The material recovered from the mixing procedures presented above usually contains a lot of gas bubbles upon liquefaction. These bubbles severely hinder the processability via MEW as they can cause jet breaking when being extruded through the nozzle. In the early stages of this thesis, these bubbles where removed directly at the MEW printer. For this, the polymer was heated and molten, the nozzle was blocked with a rubber stopper, and a gentle vacuum was applied to the gas supply of the printer head. Presumably due incomplete blockage

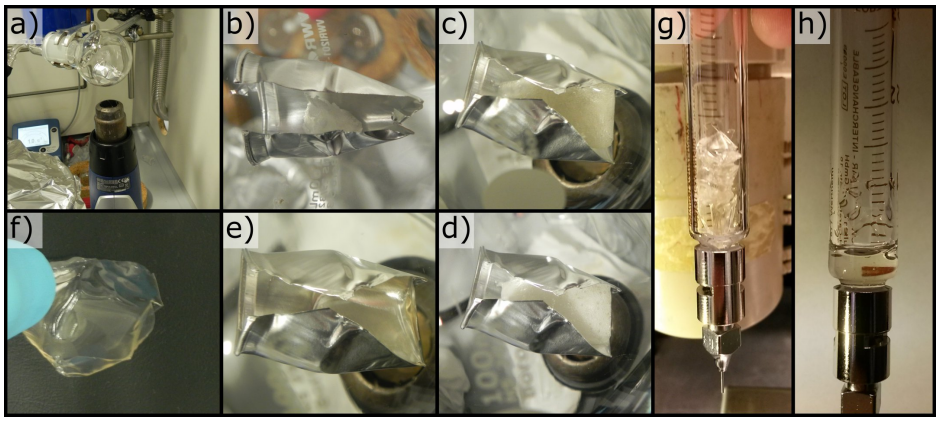


**Figure 7.1:** Schematic description of the preparation of the DA material for MEW processing. The polymer is placed in an aluminium crucible and put in a round bottom flask a), b). The flask is heated to 250 °C to liquefy the polymer c) vacuum is applied d) until all air bubbles are removed e). The polymer is cooled to RT and a clear colourless material can be recovered f). The polymer film is cut into small pieces and placed in a MEW glass syringe g). Upon heating the polymer melt is a clear colourless liquid without air bubbles h).

of the nozzle, air flow through the heated polymer reservoir could not be prevented. This caused degradation of the polymer and resulted in a shorter processing window. In the later stages of this thesis, another processing step was introduced allowing full removal of trapped gas from the mixtures, while ensuring minimal thermal decomposition (see Figure 7.1). For this the polymer recovered from either mixing by lyophilisation or by grinding in liquid nitrogen is put in an aluminium crucible, which is placed in an round bottom flask (Figure 7.1 a, b). The flask is evacuated and flushed with inert gas using a high vacuum line. The material is liquefied by heating to 250 °C under inert atmosphere using a heatgun. As soon as the polymer is liquefied, vacuum is applied until the gas bubbles are fully removed. The material is cooled to RT and a clear colourless polymer film can be recovered. For MEW processing the film is cut into small pieces and placed into a MEW glass syringe. Upon heating in the MEW printing head, a clear colourless liquid without air bubbles is received which allows improved processing.

### Melt Electrowriting

The following procedure was used for the $3^{rd}$ generation of DA material. Here the processing time was not limited and it was possible to thermally equilibrate the system. The polymer reservoir filled with the mixed DA polymer (see Section 7.2) was attached to the MEW pressure supply and flushed for at least 2 min with nitrogen at RT. If the printing temperature was known, the printer head was preheated to the respective NT and ST for at least 30 min prior to printing. If an unknown polymer was processed, the head was not preheated and heating was started as soon as the reservoir was loaded into the printer head. The collector distance was kept constant at 3.3 mm regardless of the used polymer. While, the acceleration voltage was varied between 2 and 4 kV and the feeding pressure was varied between 1.0 and 4 bar to allow a homogeneous fibre deposition depending on the polymer. A CS of 1200 mm/min was usually aimed at. For new polymers, the processing temperature was adjusted until a continuous process at a CS close to 1200 mm/min was established. For better handling, the scaffolds were printed on glass microscope slides. Usually, box like structures with a FD of 500 $\mu$m were printed, a typical g-code example is presented in Figure 7.3.

### Swelling of MEW Printed Constructs

After processing, the structures were allowed to rest for at least 16 h at RT. Afterwards, the scaffolds were incubated in MilliQ water and swelling occurred immediately. After a few minutes of incubation no significant further swelling was observed.

### Thermoresponsive Swelling

Five MEW printed PEtOzi hydrogel scaffolds are placed in water-filled Petri dishes. The scaffolds are incubated in a temperature control chamber (3-40 °C) or heated in a water bath (50-80 °C). The temperature inside the Petri dishes was monitored using a thermometer. Incubation is prolonged for at least 15 min once the respective temperature inside the Petri dishes was reached. A picture of the scaffolds is taken quickly. The dimensions of the scaffold were determined using the software ImageJ. The size reduction with increasing temperature was calculated with respect to the dimensions at 3 °C (set to 100 %).

### Environmental Scanning Electron Microscopy (ESEM)

The water swollen scaffold was placed in the sample chamber of the scanning electron microscope. The measurement was conducted in the ESEM mode. The sample holder was cooled to 2 °C and the chamber was purged twice with water vapour. Subsequently, the

chamber was stabilized for 30 min at a pressure of 730 Pa, which corresponds to a relative humidity of about 100 %. Under these conditions, the swollen state of the scaffold was maintained. By changing the pressure to 320 Pa, the relative moisture within the chamber is reduced and the fibres start to dry.

### Fibre Stiffness

The stiffness of the fibres was assessed as described elsewhere.[293] Briefly, the measurements were based on Single Cell Force Spectroscopy (SCFS) performed with an Atomic Force Microscope of the model Flex FPM (Nanosurf GmbH, Germany) combined with the FluidFM® technology (Cytosurge AG, Switzerland). The system was mounted on an inverted Axio Observer Z1 microscope (Carl Zeiss, Germany). Micropipette cantilevers with an aperture of 4 $\mu$m and a nominal spring constant of 0.3 N/m were used (Cytosurge AG, Switzerland). Polyethylene glycol coated polystyrene beads of 10 $\mu$m in diameter (Micrometer® 01-54-104, Micromod Partikeltechnologie GmbH, Germany) were used as indenter and immobilized at the aperture of the cantilever by applying under pressure. Before every experiment, the deflection sensitivity of the cantilever linked to a polystyrene bead was calibrated by using the Cytosurge software procedure. For the determination of the fibre elasticity, three independent two-layered scaffolds were investigated, generating 25 to 30 force-distance curves per scaffold. Indentations were performed on random spots of the fibres, omitting the intersections. The approach of the cantilever was done at 500 nm/s until a set point of 3 nN was reached. The data acquisition frequency was set to 6 kHz. The generated indentation curves were analysed by a custom program written in Matlab 2017b (Mathworks, USA). After several steps of data processing,[293] the curve is plotted in the form of force (nN) versus indentation (nm) and fitted according to the Hertz Model, to obtain the apparent Young's modulus. The model is based on the following Equation 7.1.[294]

$$F = \frac{4 * E * R^{\frac{1}{2}}}{3 * (1 - \nu^2)} * \delta^{\frac{3}{2}} \tag{7.1}$$

Here, F is the force, E the Young's modulus, R the radius of the spherical indenter, $\nu$ Poisson's ratio, which was set as 0.5 for these experiments, and $\delta$ represents the indentation.

### DSC

Around 10 mg of the respective sample was placed in an aluminium pan with a pierced lid. An typical measurement consisted out of three consecutive heating cycles to 200 °C (10 K/min) followed by cooling to -50 °C (10 K/min). All investigations were performed

under inert nitrogen atmosphere. The analysis of the traces was conducted using the NETZSCH proteus software. The $T_g$ was determined by the mean temperature of the turning point of the last two heating cycles. For the reversibility studies of the DA material, a temperature ramp from -50 to 200 °C with a heating rate of 10 K/min was performed under nitrogen atmosphere. Between each liquefaction cycle the material was cured at 60 °C for 1 h.

### Cytotoxicity Test

Cytotoxicity was evaluated according to DIN-ISO 10993-5. Briefly, the polymer sample was sterilized in 70 % ethanol for 1 h, followed by drying for 3 d at room temperature. The sample was incubated in medium (10 mL/mg) at 37 °C for 48 h. Next, the supernatant was transferred into a sterile vessel and the eluate medium was prepared by dilution to 100 (no dilution), 50 and 25 % with medium. L 929 CC1 mouse fibroblasts were seeded in medium in a 48-well plate (25,000 cells per well) and incubated for 24 h at 37 °C / 5 % $CO_2$. The cell culture medium was exchanged by the polymer eluate and the cells were again incubated at 37 °C / 5 % CO2 for 48 h. The cell medium was removed and the cells were incubated with WST-1 reagent for 30 min at 37 °C / 5 % $CO_2$. Cell count was determined using a Casy Cell Counter (OLS OMNI Life Science GmbH and Co KG).

### Equilibrium Water Content (EWC)

The bulk material was prepared in the same way as the samples used for MEW processing (see section 7.2). The resulting films were cut into specimen with a weight around 30 mg and cured at RT over night. For determining the swelling degree, at least three samples were incubated in MilliQ water for 48 h and 20 °C (weight equilibrium was reached after 24 h). During this time, the incubation medium was exchanged five times. The wet sample mass (MW) was then determined followed by drying of the samples for 40 h at 40 °C and 300 mbar. Finally, the dry mass (MD) was determined. The following equation was used for calculation of the EWC (Equation 7.2).

$$EWC = \frac{MW - MD}{MD} * 100 \tag{7.2}$$

### Functionalization of the Scaffolds

A dry scaffold was incubated overnight in 2 mL of a DY-647P1-Maleimide solution in MilliQ water (0.05 mg/mL, $6 \times 10^{-5}$ mmol/ml). This dye concentration will give a strong blue colouring of the fibres and can be used for better visualization under the light microscope. For the visualization under the fluorescence confocal microscope, a concentration of 0.5 $\mu$g/mL

is sufficient. The functionalized scaffold was then washed several times with MilliQ water and ethanol to ensure full removal of non-bound dye. The same protocol was used for the functionalization with peptides. Here, a concentration of $2.4 \times 10^{-4}$ mmol/ml resulted in a strong response of the seeded cells.

### Longterm Stability Tests

For the qualitative stability test, two scaffolds with 10 layers and 500 $\mu$m fibre spacing were printed as described above. The scaffolds were then incubated in Millipore water and PBS on a tilting table at 5 rpm and with the exclusion of light. Scaffolds were visualized using stereomicroscope, inspected for structural damage and the incubation was continued.

The quantitative degradation was studied under three different conditions: buffer solutions with a pH of 3.0, 7.3 and 11.0. Small specimen of the DA material with a weight of approximately 50 mg were prepared. The polymers were mixed using the method discussed in section 7.2. Before the experiment, all samples were washed extensively with the respective buffer solution. Afterwards, the samples were dried and the dry weight was determined. For each time point, three samples were incubated in 3 ml of the respective buffer solution in a separate small Petri dish at 37 °C. The EWC as well as the sol content were determined after 1, 4, 11, 29, 53, and 125 d for the conditions pH 3 and 7.3 and after 1, 4, 6, 9, 11, 12 d for the pH 11 condition.

### Cryogenic scanning electron microscopy (Cryo-SEM)

Small hydrogel samples were prepared by melt casting or MEW processing of the respective DA polymers and subsequent swelling in water. The swollen samples were flash-frozen in a nitrogen slush at -210 °C. Immediately after, the frozen samples were freeze fractured and freeze etched at -85 °C for 15 min and sputtered subsequently with platinum (3 nm) before observation (at -140 °C).

### Cultivation of HEK Cells

Cell line and transfection: Human embryonic kidney (HEK293) cells (ATCC® CRL-1573TM, Wesel, Germany) were grown in Minimum Essential Media (Life Technologies, Darmstadt, Germany). The medium was supplemented with 10 % fetal calf serum (FCS), glutaMAX (200 mM) and sodium pyruvate (100 mM), penicillin (10,000 U/ml) / streptomycin (10,000 $\mu$g/ml) at 37 °C and 5 % CO2. Cells were seeded in 10 cm plastic dishes with a density of 3 x 106 cells/dish. At 75 %, confluency cells were trypsinized, centrifuged, and seeded onto coated hydrogel scaffolds. Cells were imaged with the Leica S40/0.45 microscope, 20x/0.3 Objective and Leica 104550630 10x/23 Ocular.

Immunocytochemical staining: Scaffolds and cells were fixed with 4 % paraformaldehyde (PFA) and 4 % sucrose in phosphate-buffered saline (PBS) for 10 min at 21 °C. Scaffolds and cells were washed two times in PBS to remove the PFA. Following fixation, cells attached to the scaffold were blocked and permeabilized (0.1 % Triton-X 100, 5 % NGS in PBS) for 30 min at 21 °C. The primary mouse-monoclonal $\beta$-actin antibody (EnCor Biotechnology Inc., Gainesville, FL, USA) was supplied in a dilution of 1:500 for 45 min at 21 °C. Following, three washing steps with PBS, cells were incubated for 30 min with the secondary antibody goat-anti-mouse Cy3 (dilution1:500; Dianova, Hamburg, Germany). After washing with PBS, cells were incubated with DAPI (1:5,000) for 10 min and mounted on glass cover slips with mowiol.

Confocal microscopy, image acquisition and analysis of the scaffolds seeded with HEK293 cells: All images shown were acquired using an inverted IX81 microscope equipped with an Olympus FV1000 confocal laser scanning system, a FVD10 SPD spectral detector and diode lasers of 405 nm (DAPI) and 550 nm (Cy3). Images were acquired with an Olympus UPLSAPO 40x (numerical aperture: 1.35) objective. The images were further organized by Adobe Photoshop and Illustrator software (Adobe). The surface composition was obtained using Imaris 7.6 Software (Imaris v 7.6, Bitplane AG, software available at http://bitplane.com.)

### Hydrolysis Kinetics

The respective polymer was dissolved in 5 mL MilliQ water at a concentration corresponding to a total amide concentration of 0.96 mol/L. The solution was then placed in a preheated oil bath. The temperature within the hydrolysis vessel was monitored using a contact thermometer and the oil bath temperature was adjusted to correspond to a inner temperature of 75 or 90 °C. Once the desired inner temperature was reached and stable for at least

10 min, 5 mL of concentrated HCL were added. This marked the start of the hydrolysis experiment. From here on, samples (0.4 mL) were removed from the mixture in defined time intervals. The samples were immediately quenched by addition of 1 ml of ice-cold 20 wt% NaOH solution. These samples were then frozen and lyophilized over night. The hydrolysis degree was determined as discussed in section 7.2. Each hydrolysis kinetic in this thesis was performed at least in triplicates and the average value of all experiments was used to calculate the final hydrolysis kinetic.

### Determination of the Hydrolysis Degree via NMR

For the determination of the hydrolysis degree via NMR, the respective polymer was dissolved in deuterated MeOD (PEtOzi / P(EtOzi-co-EtOx) or in deuterated $CDCl_3$ P(EtOzi-co-MeOx). The samples must be basic to prevent an unpredictable shift of the peak corresponding to the $CH_2$ groups next to the secondary amines. Therefore, they were usually recovered from a aqueous solution with a pH of 10. The analysis was performed using the software MestreNova. The spectrum was referenced to the residual solvent signal and a phase correction was performed if required. The fix points for the baseline correction were always set at the ppm values 4.1 and 0.75 ppm. This was done to ensure consistent results. The spectra were then normalized to the integrals of the peaks c,h (PEtOzi) and $g_3$,$n_3$ P(EtOzi-co-EtOx) (see Figure 7.2 a, c). The hydrolysis degree for the polymers with the backbones PEtOzi and P(EtOzi-co-EtOx) was then calculated from these values using Equation 7.3.

$$HD(\%) = \frac{\frac{Int_{amin}}{4}}{\frac{Int_{amin}}{4} + \frac{Int_{amid}}{2}} * 100 \tag{7.3}$$

For P(EtOzi-co-MeOx) copolymer, no peaks with a constant integral can be found in the spectrum and the normalization was therefore based on the peaks $b_2$,$c_2$,$e_2$,$g_2$ (see Figure 7.2 b). The hydrolysis degree was then determined according to Equation 7.4. Please note that this method is an approximation and will result error prone values for higher degrees of hydrolysis.

$$HD(\%) = \frac{Int_{amin}}{Int_{amid}} \tag{7.4}$$

### Determination of the Hydrolysis Degree via Titration

Stock solutions with a concentration of 40 g/L of the respective polymer in MilliQ water were prepared. 584.4 mg NaCl were placed in a small glass vial and 2.5 mL MilliQ water, 2.5 mL polymer solution and 5 mL 0.02 M aqueous HCL were added. The solutions were

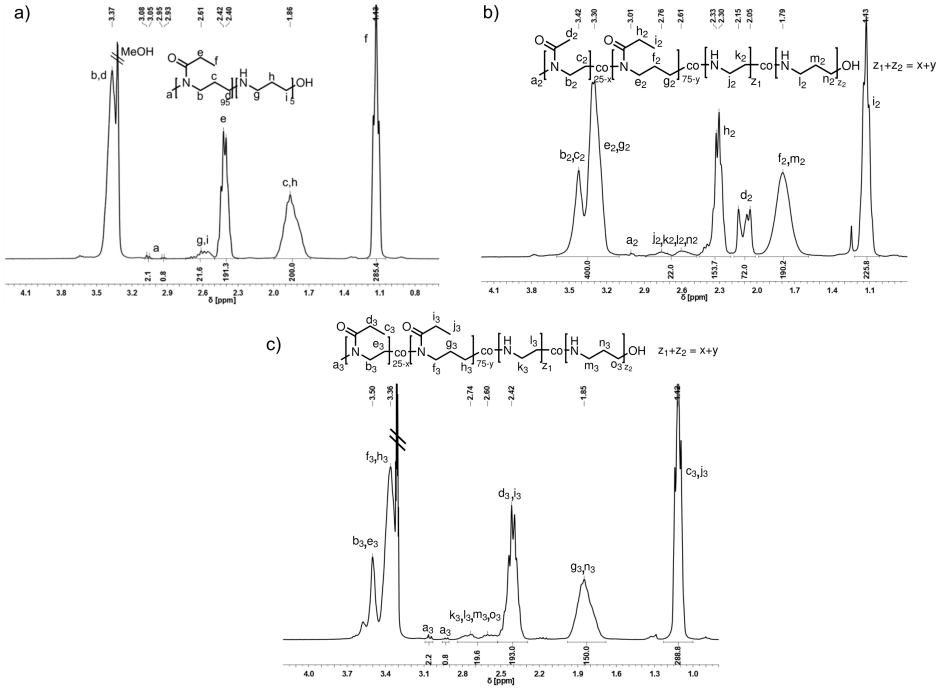


**Figure 7.2:** $^1$H-NMR spectra of the hydrolysed polymers **P70** (a) (300 MHz, 298 K, MeOD), **P43** (b) (300 MHz, 298 K, $CDCl_3$) and **P42** (c) (300 MHz, 298 K, MeOD) with the respective chemical structure. All peaks in the respective spectra are assigned.

stirred over night at RT. The samples were titrated on the following day using an aqueous 0.1 M NaOH solution, which was added at a speed of 0.03 mL/min. For every polymer, at least five separately prepared samples were analysed. Using Origin, the $1^{st}$ derivative of the pH against the volume was calculated and the maximum of the deviation marked the equivalence point. The average equivalence point was calculated from all titrations and multiplication of the volume at the equivalence point with the concentration of the NaOH solution (0.1 M), gave the total amount of amines in the solution. Using the theoretical molar mass of the respective polymer, allowed the calculation of the degree of hydrolysis from this value.

### Determination of the Lower Critical Solution Temperature

20 mg of the respective polymer were dissolved over night in 4 mL MilliQ water (5 wt%). This solution was transferred into a quartz cuvette and mounted into the UV-VIS device. A small stirrer bar was added and the solution was stirred over the course of the whole experiment. The temperature inside the cuvette was measured using a small cable-thermoelement. The temperature was increased stepwise, in steps of 1 to 5 °C and UV-VIS spectra were taken at each temperature. After each temperature step the solution was held for at least 5 min at the respective temperature before the measurement was performed,

which ensured full thermal equilibrium. The absorption at 600 nm was plotted against the temperature and the LCST was determined as the first measured value, where the absorption decreased to below 90 %.

### Polymerization Kinetics

Generalized procedure: In the following, a generalized procedure for the determination of the polymerization kinetics of all monomers, relevant for this thesis, is discussed at the example of EtOzi. In the glovebox, 44.1 mmol (4.986 g) EtOzi and 0.441 mmol (0.072 g) MeOTf were mixed with 9.65 mL BN. This results in a monomer concentration of 3 mol/L and a monomer to initiator ratio (M/I) of 100. The solution was gently shaken to ensure full mixture of all components and a $^1$H-NMR spectrum was taken to determine the initial monomer concentration ($A_0$). The mixture was then placed in a preheated oil bath and stirred at 120 °C. In defined time intervals $t$, 0.2 mL of the polymerization solution were removed from the reaction vessel and immediately transferred into an NMR tube containing 0.4 mL deuterated AN. $^1$H-NMR spectra were taken quickly thereafter. The residual monomer content was determined from the ratio of the proton signals of the BN solvent with the signals of the $CH_2$ groups at 6-position (5-position for oxazoline monomers) of the non-reacted monomers. This gave the evolution of the monomer content $A_t$ depending on the reaction time. This data was then linearised by using Equation 7.5.

$$ln\left(\frac{[A]_0}{[A]_t}\right) = k_p^{app}[I]_0 t \tag{7.5}$$

$Ln\left(\frac{[A]_0}{[A]_t}\right)$ was plotted against the reaction time $t$, and a linear equation was fitted to the data points. Dividing the slope of the fit by $I_0$ gave the apparent propagation rate ($k_p^{app}$) ($I_0$ was 0.3 mol/L for all experiments).

### Termination Studies

General procedure: For all termination experiments, 7 to 9 mg of the respective initiator salts were dissolved in 0.4 mL of the deuterated solvent (deuterated AN, $D_2O$ or $CDCL_3$). This resulted in a sample concentration of around 0.06 mol/L. Next, a three-fold excess of a termination reagent was added, and the samples were transferred into the NMR device. The first spectrum was usually measured 5 min after the addition of the termination reagent to the mixture. For the detailed analysis of the reaction results, $^1H$, $^{13}C$, COSY, HSQC and HMBC spectra were taken.

For the investigation of the batch to batch variation for the conversion of 2-ethyl-3-

methyloxaziniumtriflat with 1 M KOH in MeOH, a more careful procedure was applied. A stock solution (25 mg/mL) of the initiator salt in deuterated AN was prepared. The stock solution, the termination reagent as well as the NMR-tube were then temperated to 20 or 30 °C using a water bath. After reaching thermal equilibrium, 0.4 ml initiator salt stock solution were placed in the NMR tube, using a micro pipette. Then, 60 $\mu$L 1 M KOH in MeOH were added, the mixture was shaken extensively and immediately transferred to the NMR device. The first spectrum was usually measured 5 min after the addition of the termination reagent to the reaction mixture.

### Solution Electrospinning

0.446 mg of **P50** and **P51** were dissolved separately in 1 mL $CHCl_3$ (30 wt%). Both solutions were mixed shortly before the beginning of the SES processing, to prevent gelation caused by DA crosslinking. The solution was then loaded into a 1 mL syringe and a 21 G metal needle was attached. A MEW steel mandrel served as collector and was rotated with 92 rpm. An electrospinning voltage of 9 kV at a collector distance of 18-20 cm was utilized. In order to fully cover the mandrel with a sufficiently thick polymer layer, the electrospinning was performed for 2 h with a flow rate of 0.3 mL/h.

### Combination of Solution Electrospinning and Melt Electrowriting

A mixture of **P50** and **P51** was MEW printed onto a steel mandrel with a diameter of 3 mm. Directly after MEW, the mandrel was transferred to the SES device. A 30 wt% solution of **P50** and **P51** in $CHCl_3$ was electrospun on top of the MEW construct. SES was performed with a flow rate of 0.3 mL/h for 2 h. The structures were then cured for 2 d at RT.

## 7.2.1 Monomer Synthesis and other Procedures

### Synthesis of 2-Ethyl-2-oxazine

160 g of propionitrile (0.97 eq, 222 mL, 2.9 mol) and 16.5 g zinc acetate dihydrate (0.25 eq, 0.75 mol) were mixed in a nitrogen flushed flask and heated to 100 °C. 225 g aminopropanol (1 eq, 227 mL, 3 mol) were slowly added within 30 min. The mixture was stirred for 7 d. The raw product was purified by distillation under reduced pressure, dried over $CaH_2$ and finally distilled again.

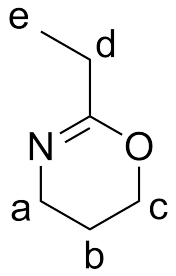


- Yield: 110 g (33 %, NHD001) / 323 g (46 %, NCL001)
- Boiling point: 72 to 74 °C (80 mbar)
- $^1$H-NMR ($CDCl_3$, 300 MHz) $\delta$ (ppm): 4.14 (t, 2H, c), 3.35 (t, 2H, a), 2.14 (q, 2H, d), 1.84 (q, 2H, b), 1.08 (t, 3H, e)

### 3-(2-Furyl)propionic Acid

2.5 g (2.38 mL, 14.9 mmol) Ethyl-3-(furan-2yl)propionate was dissolved in 10 mL THF and 20 mL of a solution of NaOH in a 1:1 (by volume) $H_2O$:MeOH was added. The mixture was heated to 80 °C for 1.5 h. After cooling to RT, 20 mL diethylether and 1 M aq. NaOH were added. The water phase was extracted three-times with 20 mL diethylether and the combined org. phase was washed three-times with 10 mL 1 M aq. NaOH. The combined water phase was acidified to pH=1 (1 M aq. HCl) and extracted four-times with 20 mL of diethylether. The organic phase was combined and washed with 10 mL water, dried over $MgSO_4$, filtered and the solvent was removed *in vacuo*. A crude mixture of yellowish and white crystals remained. For further purification the solid can be molten and distilled at 80 °C and 2x10$^{-3}$ mbar. The product solidified as white, slightly transparent, crystals. The purification via destillation was only applied for the synthesis of the $3^{rd}$ generation of DA polymers.

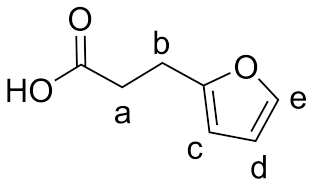


- Yield: 95% (1.98 g, 14.2 mmol) / 73% (11.04 g, 87.1 mmol)
- $^1$H-NMR (MeOD-d$^4$, 300 MHz) $\delta$ (ppm): 7.34 (d, 1H, e), 6.29-6.27 (q, 1H, d), 6.06-6.04 (d, 1H, c), 2.94-2.89 (t, 2H, b), 2.64-2.59 (t, 2H, a)

### Synthesis of 3-Maleimidopropionic Acid

$\beta$-Alanine (5.93 g, 66.6 mmol) and maleic anhydride (6.53 g, 66.6 mmol) were suspended in acetic acid (84 g, 80 ml) and allowed to react for 3 h at RT. The resulting white precipitate was collected by filtration, washed with cold water and dried. The recovered diacid precursor was suspended in toluene, and a two molar excess of triethylamine was added. The reaction mixture was stirred vigorously and heated to reflux, while the water by-product was collected using a Dean-Stark apparatus. After refluxing for ninety minutes, the hot toluene product mixture was decanted into another flask, separating it from a red-orange oil residue. The decanted toluene was removed via rotary evaporation to leave a pale yellow oily residue. Prior to acidification with 1 M HCl, the pale yellow residue was dissolved in approximately 100 mL of water. From the acidified mixture, the product 3-maleimidopropionic acid was extracted using 3x100 mL ethyl acetate. The combined ethyl acetate solutions were dried with sodium sulfate and the solvent was removed by rotary evaporation, yielding a pale yellow to white solid. The product still contained significant amounts of the educt $\beta$-alanine (around 40 %).

- Yield: 30%
- $^1$H-NMR (MeOD-d$^4$, 300 MHz) $\delta$ (ppm): 6.81 (d, 2H, c), 3.78-3.74 (t, 1H, b), 2.62-2.57 (t, 2H, a)

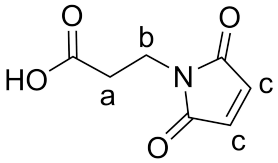


### Purification of 6-Maleimidohexanoic Acid

10 g 6-Maleimidohexanoic Acid were dispersed in 130 mL of a mixture of n-hexan and ethylacetate (3:1). The mixture was refluxed and additional n-hexan/ethylacetate (3:1) solution was added until the white flakes were fully dissolved. An oily yellowish substance precipitated on the bottom of the round bottom flask. The hot solution was decanted and chilled over night at 5 °C. The precipitated white crystals were recovered by filtration and drying under reduced pressure.

- Yield: 7 g (70 %)
- $^1$H-NMR ($CDCL_3$, 300 MHz) $\delta$ (ppm): 6.69 (s, 2H, f), 3.55-3.50 (t, 2H, e), 2.37-2.33 (t, 2H, a), 1.72-1.57 (m, 4H, d, b), 1.40-1.30 (m, 2H, c)

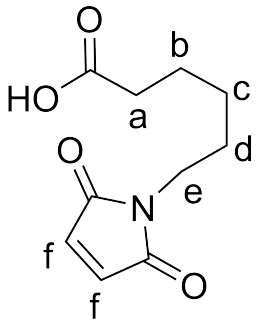

### 7-(Carboxymethoxy)coumarin

7-Hydroxycoumarin (2.0 g, 12.3 mmol), potassium carbonate (8.5 g, 61.5 mmol) and bromoacetic acid (8.5 g, 61.5 mmol) were dissolved in 250 ml acetone. Next, catalytic amounts of potassium iodide were added. The turbid and slightly yellowish mixture was then refluxed over night (70 °C oil bath temperature). Large amounts of a grey solid precipitated. The reaction progression was evaluated using TLC (10:1 EtOAc:PE) and no product was found. 200 mL of water were added and the pH of the mixture was adjusted to 3. The acetone was removed under reduced pressure and the remaining solid was recovered by filtration.

- Yield: 2.0 g (74 %)
- $^1$H-NMR (DMSO-d6, 300 MHz) $\delta$ (ppm): 8.00-7.97ppm (d, 1H, e), 7.64-7.61 ppm (d, 1H, d), 6.69-6.65 ppm (m, 2, b, c), 6.31-6.28 ppm (d, 1H, f), 4.82 (a, 2H, a)
- Solubility (10 mg/mL): DMF (rapid/complete), NMP (rapid/complete), THF(slowly/complete), BN (insoluble), AN (insoluble)

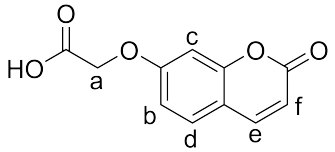


## 7.2.2 Initiator Salt Synthesis

### 2-Ethyl-3-methyloxaziniumtriflat

15 mL dry diethylether were placed in a dry round bottom flask and 2.58 g methyl trifluoromethanesulfonate (157 mmol, 1.2 eq) were added. The mixture was cooled using an ice bath. 1.48 g (130 mmol, 1.0 eq) 2-ethyl-2-oxazine were added slowly and a white precipitate formed immediately. The solvent was removed using a Schlenk frit and the precipitate was washed three-times with 12 mL dry diethyl ether. The product was dried under reduced pressure and stored under argon.

- $^1$H-NMR ($CDCl_3$, 300 MHz) $\delta$ (ppm): 4.68 ppm (t, J=5.4 Hz, 2H, d), 3.77 ppm (t, J=5.9 Hz, 2H, b), 3.43 ppm (s, 3H, a), 2.80 ppm (q, J=7.5 Hz, 4H, e), 2.43 ppm - 2.25 ppm (m, 2H, c), 1.25 ppm (t, J=7.4 Hz, 3H, f).

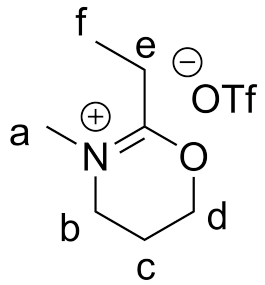

### 2,3-Dimethyloxaziniumtriflat

The synthesis was conducted according to the procedure of 2-ethyl-3-methyloxaziniumtriflat.

- Yield: 67.4 %
- $^1$H-NMR ($CDCl_3$, 300 MHz) $\delta$ (ppm): 4.60 ppm (t, J=5.5 Hz, 2H, d), 3.71 ppm (t, J=6.0 Hz, 2H, b), 3.40 ppm (s, 3H, a), 2.44 ppm (s 3H, e), 2.32 ppm (m, 2H, c).

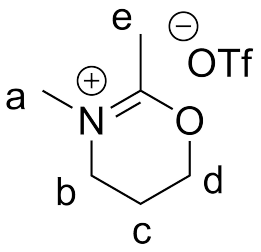


### 2-Ethyl-3-methyloxazoliniumtriflat

30 mL dry diethylether were placed in a dry round bottom flask and 2.79 g methyl trifluoromethanesulfonate (170 mmol, 1.2 eq) were added. The mixture was cooled using an ice bath. 1.41 g (142 mmol, 1.0 eq) 2-ethyl-2-oxazoline were added slowly and a slight clouding of the solution was observed. With time, an oily and slightly orange liquid phase formed. The diethyl ether phase was removed under reduced pressure, and the residual oil was further purified at 1 mbar for 10 h.

- Yield: 67.4 %
- $^1$H-NMR ($CDCl_3$, 300 MHz) $\delta$ (ppm): 4.85 ppm (t, J=10.0 Hz, 2H, c), 4.06 ppm (t, J=10.0 Hz, 2H, b), 3.22 ppm (s, 3H, a), 2.67 ppm (q, J=7.4 Hz, 1H, d), 1.21 ppm (t, J = 7.5 Hz, 2H, e).

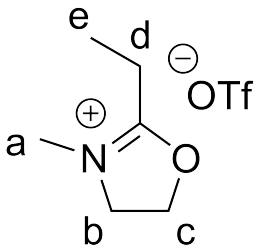

### 7.2.3 Polymer Synthesis

Generalized procedure: In the following, a generalized procedure for the synthesis of all polymers within this thesis is discussed at the example of $PEtOzi_{100}$. The polymer synthesis was carried out via an adapted procedure of Witte and Seeliger.[131] 99.7 g (100 eq, 0.88 mol) of 2-ethyl-2-oxazine were mixed with 193 ml of dry benzonitrile (4 mol/L). 1.45 g (1 eq, 0.088 mol) of the initiator MeOTf was added and the mixture was heated to 130 °C. The reaction progress was followed via $^1$H-NMR spectroscopy. As soon as full conversion was reached, the polymerization was terminated at 50 °C for 16 h using a three-fold excess of 1 M KOH in MeOH. The solvent was removed at 60 °C and under reduced pressure. Finally, the product was purified via dialysis against deionized water using a 1 kg/mol cut off cellulose membrane. Dialysis was performed for at least 24 h with regular water exchange. The product was recovered via lyophilisation. For the statistical copolymerization of two monomers, a very similar procedure was used. Here, both monomers were mixed in benzonitrile prior to the addition of the initiator. Also due to the lower boiling point of MeOx and EtOx, the reaction temperature was reduced to 120 °C. For the synthesis of PEtOzi with a M/I higher than 100, a M/I higher than required for the targeted molar mass was used, and the polymerization was terminated at a conversion around 95 %. For higher conversions, significant broadening of the molar mass destitution was observed. This was applied for the batch **P10**.

**Poly(2-ethyl-2-oxazine)**

- Yield: 4.5 g/91 %; NHD007
- $^1$H-NMR ($CDCl_3$, 300 MHz) $\delta$ (ppm): 3.43-3.08 (br, 400H, b), 2.97-2.81 (br, 3H, a), 2.44-2.21 (br, 202H, d), 1.88-1.58 (br, 202H, c), 1.16-0.91 (br, 300H, e)
- $^1$H-NMR ($CDCl_3$, 300 MHz): M/I=73
- GPC (HFIP): $M_n$=5.1 kg/mol; Đ=1.17
- MALDI-TOF (DCTB 5 % in $CHCl_3$): M/I=100; 11.4 kg/mol; Đ=1.01
- DSC: $T_g$=24.5 °C

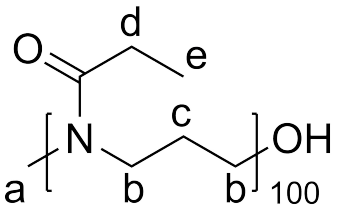

In the following, the characterization of all parent PEtOzi homopolymers is summarized.

**Table 7.1:** Summarized characterization of all PEtOzi homopolymers synthesized in this thesis.

| ID | Lab book-ID | Yield | $M/I_t$ | $M/I_e$ | $M_t$ | $M_n$ | Đ | $T_g$ [d] |
|---|---|---|---|---|---|---|---|---|
| **P1** | NHD007 | 4.5 g/91 % | 100 | 73[a]<br>100[b] | 11345 | 5.1[c]<br>11.4[b] | 1.17<br>1.01[b] | 24.5 |
| **P71** | NHD026 | 9.8 g/96 % | 100 | 74[a] | 11345 | 6.9[c] | 1.18[c] | 25.6 |
| **P72** | NHD041 | 27 g/91 % | 100 | 101[a]<br>96[b] | 11345 | 5.1[c]<br>10.8[b] | 1.1[c]<br>1.01[b] | 24.0 |
| **P73** | NHD080 | 49 g/98 % | 33 | 33[a] | 3765 | 1.89[c] | 1.06[c] | – |
| **P74** | NHD081 | 73 g/91 % | 100 | 103[a] | 11345 | 4.9[c] | 1.1[c] | 23.6 |
| **P10** | NHD097 | 48 g/95 % | 210 | 124[a] | 24071 | 8.74[c] | 1.14[c] | 24.5 |
| **P9** | NHD118 | 92 g/92 % | 100 | 70[a]<br>94[b] | 11345 | 5.1[c]<br>10.6[b] | 1.2[c]<br>1.01[b] | 24.0 |
| **P6**⋆ | ZgA03 | – | 20 | 23[a] | 2294 | – | – | – |

Determined by: [a] NMR end-group analysis; [b] MALDI-TOF in [kg/mol]; [c] GPC (HFIP) in [kg/mol]; [d] DSC in [°C]

Abbreviations: $M/I_t$, $M/I_e$ Theoretical and experimental monomer to initiator ratio

⋆ Synthesis was conducted by Andreas Züge in the course of a practical intercourse.

### Poly(2-ethyl-2-oxazine)-co-poly(2-ethyl-2-oxazoline)

- ID: **P11**; Lab book-ID: NHD128
- Yield: 48 g/96 %
- $^1$H-NMR ($CD_3CN$, 300 MHz) $\delta$ (ppm): 3.48-3.35 (br, 97H, f), 3.35-3.15 (br, 291, b), 2.98-2.94 (br, 1.8H, a), 2.87-2.83 (br, 1.23H, a), 2.45-2.16 (br, 219H, d, g), 1.90-1.59 (br, 149H, c) 1.15-0.95 (br, 291H, e, h)

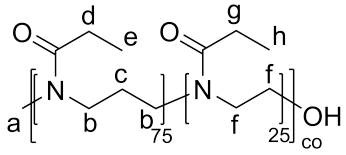


In the following, the characterization of all parent P(EtOzi-co-EtOx) copolymers is summarized.

**Table 7.2:** Summarized characterization of all P(EtOzi-co-EtOx) copolymers synthesized in this thesis.

| ID | Lab book-ID | Yield | Ozi/Ox$_t$ | Ozi/Ox$_n$ | M$_t$ | M$_n$ | Đ | $T_g$ [d] |
|---|---|---|---|---|---|---|---|---|
| **P2** | NHD015-A | – | 75/25 | 77/29 [a] | 10995 | 4.80 [c] | 1.15 [c] | 32.9 |
| **P11** | NHD128 | 48 g/96 % | 75/25 | 73/24 [a]<br>91 [b] | 10995 | 5.98 [c]<br>9.98 [b] | 1.13 [c]<br>– | 31.1 |
| **P3** | NHD009 | 4.4 g/89 % | 50/50 | 47/48 [a] | 10644 | 4.85 [c] | 1.20 [c] | 39.6 |
| **P4** | NHD015-B | – | 25/75 | 26/82 [a] | 10294 | 4.13 [c] | 1.22 [c] | 48.1 |

Determined by: [a] NMR end-group analysis; [b] MALDI-TOF in [kg/mol]; [c] GPC (HFIP) in [kg/mol]; [d] DSC in [°C]

Abbreviations: Ozi/Ox$_t$, Ozi/Ox$_e$ Theoretical and experimental oxazine to oxazoline ratio

### Poly(2-ethyl-2-oxazoline)

- ID: **P5**; Lab book-ID: NHD004
- M/I$_t$=100; M$_t$=9944 g/mol
- Yield: 4.8 /96 %
- $^1$H-NMR (MeOD, 300 MHz) $\delta$ (ppm): 3.65-3.21 (br, 323H, b), 2.96-2.90 (br, 2.3H, a), 2.83-2.79 (br, 0.70H, a), 2.40-2.12 (br, 162H, c), 1.04-0.84 (br, 243H, d)
- $^1$H-NMR ($CDCl_3$, 300 MHz): M/I=81
- GPC (HFIP): M$_n$=5.1 kg/mol; Đ=1.19
- MALDI-TOF (DCTB 5 % in $CHCl_3$): M/I=106; 10.5 kg/mol; Đ=1.00
- DSC: $T_g$=60.7 °C

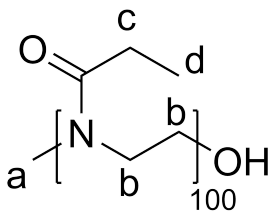


### Poly(2-ethyl-2-oxazine)-co-poly(2-methyl-2-oxazoline)

- ID: **P12**; Lab book-ID: NHD123
- M/I$_t$=75/25; M$_t$=10645 g/mol
- Yield: 46 g/92 %
- $^1$H-NMR ($CDCl_3$, 300 MHz) $\delta$ (ppm): 3.54-3.36 (br, 115H, f), 3.36-3.13 (br, 303H, b), 3.01-2.96 (br, 2.1H, a), 2.94-2.88 (br, 0.89H, a), 2.45-2.19 (br, 163H, d), 2.17-1.98 (br, 84H, g) 1.96-1.64 (br, 160H, c) 1.25-1.00 (br, 239H, e)
- $^1$H-NMR ($CDCl_3$, 300 MHz): M/I=76/29
- GPC (HFIP): M$_n$=3.71 kg/mol; Đ=1.12
- DSC: $T_g$=33.2 °C

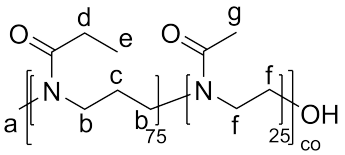

### 7.2.4 Polymer Hydrolysis

In the following a generalized procedure for the hydrolysis of all polymers relevant for this thesis is discussed at the example of PEtOzi$_{100}$-5 %. This procedure was applied for the 3$^{rd}$ generation of DA material, and the changes made compared to the former generations are listed below. The reaction time required for the desired hydrolysis degree was derived from the respective corrected hydrolysis kinetic (see section 7.2). The hydrolysis reaction was carried out via an adapted procedure reported by Van Kuringen and coworkers.[180] 20 g PEtOzi$_{100}$ were dissolved in 184.5 mL of deionized water (0.96 mol/L amide concentration), and the solution was heated to 75 °C. This temperature was measured inside the reaction mixture using a contact thermometer. 10 min after the inner temperature was reached and stable, 184.5 mL of 37 % HCl were added to the mixture. Heating was continued for 141 min. The heating was stopped and the reaction mixture was poured quickly into an ice cooled 20 wt% NaOH solution. The pH of the solution was adjusted to 10. After cooling to RT, this mixture was dialysed for 24 h against a NaOH solution with a pH of 10, using a 1 kg/mol cut off cellulose membrane. The solution was concentrated under reduced pressure and chilled over night at 5 °C. The precipitated yellowish solid was removed by filtration and product was recovered via lyophilisation.

- **1$^{st}$ generation:** Dialysis was performed at neutral pH, and uncorrected hydrolysis kinetics were used.
- **2$^{nd}$ generation:** The solutions were not concentrated or filtrated prior to the recovery via lyophilisation. Uncorrected hydrolysis kinetics were used.

The respective hydrolysis temperature, time as well as the applied procedure for each polymer are stated below.

### Partial Hydrolysed poly(2-ethyl-2-oxazine)

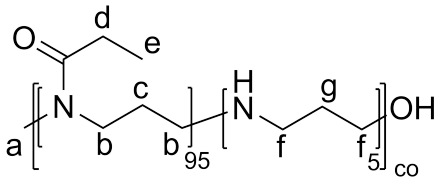


- ID: **P70**; Lab book-ID: NHD096
- $^1$H-NMR ($MeOD_3$, 300 MHz) $\delta$ (ppm): 3.49-3.23 (br, 432H, b and solvent), 3.08-3.02 (br, 2.1, a), 2.95-2.90 (br, 0.8H, a), 2.73-2.48 (br, 19.2H, f), 2.48-2.30 (br, 190H, d), 2.04-1.62 (br, 200H, c, g) 1.96-1.64 (br, 160H, c) 1.21-0.99 (br, 286H, e)
- Time/Temperature: 141 min/75 °C
- HD(theo): 5 %
- HD(NMR): 4.8 %
- HD(titration): 3.4 %

In the following, the characterization of all partially hydrolysed PEtOzi homopolymers is summarized.

**Table 7.3:** Summarized characterization of all hydrolysed PEtOzi homopolymers synthesized in this thesis.

| ID | Lab book-ID | Parent polymer | Yield$^a$ | Time/ Temp.$^b$ | $M_n^c$ | $Đ^c$ | $HD_t$ | $HD_e{}^d$ | $HD_e{}^e$ | $T_g{}^f$ |
|---|---|---|---|---|---|---|---|---|---|---|
| **P13** | NHD016 | **P1** | 1.7/60 | 180/90$^{nc}$ | 12.9 | 1.11 | 15 | 13.9 | – | 31.8 |
| **P18** | NHD031 | **P71** | – | 60/90$^{nc}$ | 9.7 | 1.10 | 5 | 6.3 | – | 21.2 |
| **P75** | NHD047 | **P72** | 8.4/95 | 73/90$^{nc}$ | 9.0 | 1.10 | 6 | 5.4 | 4.3 | – |
| **P8** | NHD055 | **P72** | 8.2/93 | 97/90$^{nc}$ | 7.5 | 1.16 | 8 | 7.5 | 5.6 | 19.4 |
| **P7** | NHD087 | **P76** | 4.0/80 | 239/75$^{nc}$ | – | – | 9.1 | 9.1 | – | – |
| **P77** | NHD088 | **P74** | 7.4/99 | 103/75$^{nc}$ | – | – | 4 | 3.7 | – | 21.0 |
| **P70** | NHD096 | **P74** | 7.1/95 | 141/75$^{nc}$ | 8.3 | 1.10 | 5 | 4.8 | 3.4 | – |
| **P78** | NHD117 | **P74** | 19/95 | 141/75$^{nc}$ | 7.8 | 1.11 | 5 | 4.8 | 3.4 | 20.8 |
| **P79** | NHD129 | **P9** | 4.5/90 | 147/90$^{nc}$ | 13.5 | 1.08 | 15 | 13.2 | – | – |
| **P80** | NHD143 | **P9** | 7.6/95 | 139/75$^c$ | – | – | 4 | 4.7 | 4.5 | 21.8 |
| **P40** | NHD162 | **P9** | 20/99 | 65/75$^c$ | – | – | 2 | 3.0 | 2.4 | 23.5 |
| **P41** | NHD176 | **P9** | 20/99 | 102/75$^c$ | – | – | 3 | 3.7 | 3.2 | – |
| **P39** | NHD155 | **P9** | 19/99 | 139/75$^c$ | 9.3 | 1.10 | 4 | 4.8 | 4.1 | – |

Parameters in: $^a$ [g]/[%]; $^b$ [min]/[°C]

Determined by: $^c$ GPC(HFIP) in [kg/mol]; $^d$ $^1$H-NMR in [%]; $^e$ acid-base titration in [%]; $^f$ DSC in [°C]

Abbreviations: $^{c}/^{nc}$ Specifies, whether the corrected or uncorrected hydrolysis kinetic was used.

## Partial Hydrolysed Poly(2-ethyl-2-oxazine)-co-poly(2-ethyl-2-oxazoline)

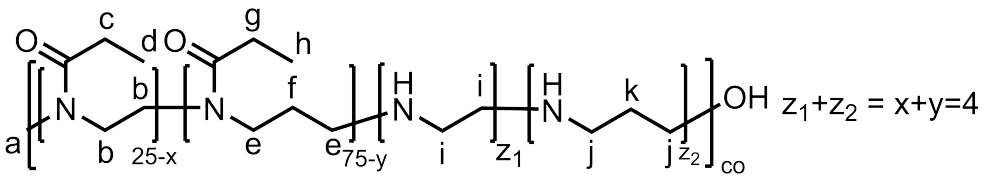


- ID: **P42**; Lab book-ID: NHD158
- $^{1}$H-NMR ($MeOD_3$, 300 MHz) $\delta$ (ppm): 3.62-3.45 (br, 93H, b), 3.45-3.26 (br, 369H, e and solvent), 3.09-3.03 (br, 2.2H, a), 2.96-2.91 (br, 0.81H, a), 2.84-2.53 (br, 20H, i, j), 2.53-2.29 (br, 193H, c, g) 1.98-1.68 (br, 150H, f, k) 1.23-1.00 (br, 289H, d, h)
- Time/Temperature: 79 min/75 °C
- HD(theo): 4 %
- HD(NMR): 5.1 %
- HD(titration): 4.3 %

**Table 7.4:** Summarized characterization of all hydrolysed P(EtOzi-co-EtOx) copolymers synthesized in this thesis.

| ID | Lab book-ID | Parent polymer | Yield$^{a}$ | Time/ Temp.$^{b}$ | $M_n^c$ | Đ$^{c}$ | $HD_t$ | $HD_d{}^{c}$ | $HD_e{}^{e}$ | $T_g{}^{f}$ |
|---|---|---|---|---|---|---|---|---|---|---|
| **P44** | NHD140 | **P11** | 14/100 | 49/75$^{c}$ | 8.2 | 1.13 | 2 | 3.4 | 2.5 | 28.5 |
| **P45** | NHD153 | **P11** | 9/67 | 79/75$^{c}$ | 8.6 | 1.13 | 3 | 4.2 | 3.1 | 28.6 |
| **P42** | NHD158 | **P11** | 14/107 | 98/75$^{c}$ | – | – | 4 | 5.1 | 4.3 | 27.7 |

Parameters in: $^{a}$ [g]/[%]; $^{b}$ [min]/[°C]

Determined by: $^{c}$ GPC(HFIP) in [kg/mol]; $^{d}$ $^{1}$H-NMR in [%]; $^{e}$ acid-base titration in [%]; $^{f}$ DSC in [°C]

Abbreviations: $^{c/nc}$ Specifies, whether the corrected or uncorrected hydrolysis kinetic was used.

### Partial Hydrolysed Poly(2-ethyl-2-oxazine)-co-poly(2-methyl-2-oxazoline)

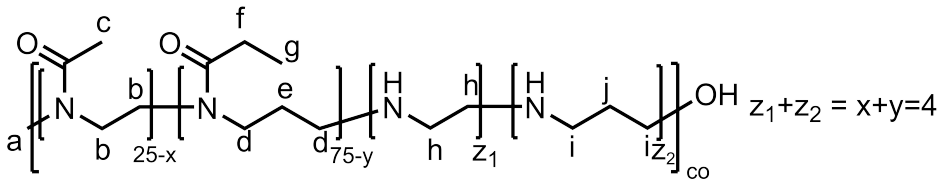


- ID: **P43**; Lab book-ID: NHD161
- $^1$H-NMR ($MeOD_3$, 300 MHz) $\delta$ (ppm): 3.6-3.1 (br, 400H, b, d), 3.02-3.96 (br, 2.2, a), 2.89-2.48 (br, 22H, h, i), 2.47-2.21 (br, 154H, f), 2.19-2.00 (br, 73H, c), 1.99-1.57 (br, 190H, e, j) 1.20-0.98 (br, 225H, g)
- Time/Temperature: 76 min/75 °C
- HD(theo): 4 %
- HD(NMR): 5.2 %
- HD(titration): 3.7 %

**Table 7.5:** Summarized characterization of all hydrolysed P(EtOzi-co-MeOx) copolymers synthesized in this thesis.

| ID | Lab book-ID | Parent polymer | Yield[a] | Time/ Temp.[b] | $M_n^c$ | $Đ^c$ | $HD_t$ | $HD_e{}^d$ | $HD_e{}^e$ | $T_g{}^f$ |
|---|---|---|---|---|---|---|---|---|---|---|
| **P81** | NHD130 | **P12** | 5.6/94 | $37/75^{nc}$ | 7.0 | 1.3 | 4 | 3.4 | – | 32.0 |
| **P46** | NHD149 | **P12** | 13/96 | $36/75^{c}$ | 6.8 | 1.29 | 2 | 3.8 | 2.4 | 30.4 |
| **P47** | NHD154 | **P12** | 10/100 | $56/75^{c}$ | 7.6 | 1.27 | 3 | 4.3 | 3.1 | – |
| **P43** | NHD161 | **P12** | 10/100 | $76/75^{c}$ | 7.6 | 1.27 | 4 | 5.2 | 3.7 | 29.0 |

Parameters in: [a] [g]/[%]; [b] [min]/[°C]

Determined by: [c] GPC(HFIP) in [kg/mol]; [d] $^1$H-NMR in [%]; [e] acid-base titration in [%]; [f] DSC in [°C]

Abbreviations: $^{c}/^{nc}$ Specifies, whether the corrected or uncorrected hydrolysis kinetic was used.

### 7.2.5 Functionalization with Furan and Maleimide

In the following, a generalized procedure for the functionalization of the partially hydrolysed PEtOzi-based homo- and copolymers is discussed using the example of the functionalization of the batch **P39**. The hydrolysis degree of this batch determined via $^{1}$H-NMR analysis was 4.8 %, and this value was rounded to 5 % for the calculation of the reagent masses. This procedure was applied for the $3^{rd}$ generation of DA material, and the changes made compared to the former generations are listed below. The synthesis procedure is adapted from a report by Chujo and coworkers.[200] 8 g (0.72 mmol polymer, 3.6 mmol amines) of hydrolysed polymer was dissolved in 242 mL (0.003 mmol/mL) acetonitrile , and the solution was chilled in an ice bath. A four-fold excess (with respect to the amines concentration) of N,N'-dicyclohexyl carbodiimide (3 g, 14.6 mmol) and either 3.1 g (14.6 mmol) 6-maleimidohexanoic acid for the synthesis of **P53** or 2.0 g (14.3 mmol) 3-(2-furyl)propionic acid for the synthesis of **P52** were added. The mixture was stirred for 16 h and a white solid precipitated. The precipitate was removed via centrifugation and decantation. The solvent was removed under reduced pressure and the remaining viscous liquid was dissolved in methanol (approx. 150 mg/ml with respect to the expected polymer mass). The polymer solution was precipitated three-times in ice cold diethyl ether. The precipitate was dried under reduced pressure, dissolved in small amounts of MilliQ water and chilled over night at 5 °C. Again, a white solid precipitated, which was removed via filtration. The product solution was further purified by dialysis against deionized water using a 1 kg/mol cut off cellulose membrane for 24 h. After concentrating under reduced pressure, the product was recovered via lyophilisation.

- **$1^{st}$ generation**: During functionalization, a lower polymer concentration of 0.002 mmol/mL as well as a lower excess (two-fold instead of four-fold) of the coupling agent DCC as well as the DA function furan and maleimide was used. Furthermore, the hydrolysed polymers were not recovered from a basic solution before the functionalization procedure.
- **$2^{nd}$ generation**: The product was used directly after precipitation and drying, and no further purification by filtration and dialysis was performed.

### Furan Functionalized PEtOzi$_{100}$ Polymers

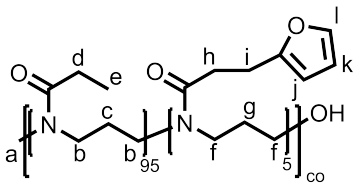


- ID: **P31**; Lab book-ID: NHD120
- $^1$H-NMR ($CD_3CN$, 300 MHz) $\delta$ (ppm): 7.35 (s, 4.3H, i), 6.30 (br, 4.4H, k), 6.05 (br, 4.33H, j), 3.34 (br, 398H, b, f), 2.96-2.80 (br, 12.1H, i, a), 2.70-2.54 (br, 9.3H, h), 2.42-2.21 (br, 192H, d),1.88-1.58 (br, 200H, c, g), 1.11-0.95 (br, 285H, e)
- DF(theo): 4.8 %
- DF(NMR): 4.3 %

In the following, the characterization of all furan functionalized PEtOzi homopolymers is summarized.

**Table 7.6:** Summarized characterization of all furan functionalized PEtOzi homopolymers synthesized in this thesis.

| ID | Lab book-ID | Parent polymers | Yield$^a$ | $M_n^b$ | Đ$^b$ | $DF_t$ | $DF_e{}^c$ | $T_g{}^e$ |
|---|---|---|---|---|---|---|---|---|
| **P14** | NHD021 | **P1**, **13** | 0.2/86 | 8.0 | 1.19 | 13.9$^c$ | 10.9 | 27.3 |
| **P16** | NHD024 | **P1**, **13** | 0.36/69 | 7.5 | 1.2 | 13.9$^c$ | 11.7 | – |
| **P27** | NHD063 | **P72**, **75** | 2.5/92 | 3.8 | 1.10 | 5.4$^c$ | 4.9 | 23.0 |
| **P35** | NHD098 | **P74**, **77** | 3.1/93 | 4.3 | 1.09 | 3.7$^c$ | 3.5 | 23.3 |
| **P29** | NHD103 | **P74**, **70** | 2.7/91 | 4.4 | 1.10 | 4.8$^c$ | 4.5 | – |
| **P31** | NHD120 | **P74**, **78** | 7.7/97 | 4.2 | 1.11 | 4.8$^c$ | 4.3 | 25.7 |
| **P33** | NHD144 | **P9**, **80** | 3.2/97 | 3.2 | 1.09 | 4.5$^d$ | 4.0 | 23.2 |
| **P48** | NHD180 | **P9**, **40** | 7.5/86 | 5.3 | 1.09 | 2.4$^d$ | 2.4 | 23.8 |
| **P50** | NHD178 | **P9**, **41** | 6.8/80 | 5.2 | 1.08 | 3.2$^d$ | 3.4 | 23.0 |
| **P52** | NHD172 | **P9**, **39** | 7.2/85 | 5.2 | 1.09 | 4.1$^d$ | 4.4 | 24.7 |

Parameters in: $^a$ [g]/[%]

Determined by: $^b$ GPC(HFIP) in [kg/mol]; $^c$ $^1$H-NMR in [%]; $^d$ acid-base titration in [%]; $^e$ DSC in [°C]

### Maleimide Functionalized PEtOzi$_{100}$ Polymers

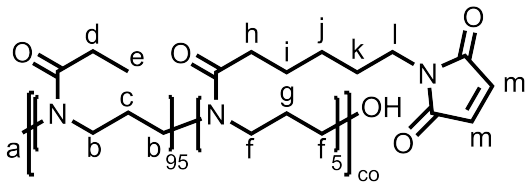


- ID: **P32**; Lab book-ID: NHD121
- $^1$H-NMR ($CD_3CN$, 300 MHz) $\delta$ (ppm): 6.74 (s, 8.1H, m), 3.48-3.38 (br, 13.5H, l), 3.37-3.10 (br, 394H, b, f), 2.96-2.92 (br, 1.6H, a), 2.86-2.80 (br, 1.1H, a), 2.38-2.20 (br, 197H, d, h), 1.88-1.60 (br, 200H, c, g), 1.60-1.47 (br, 19.7H, i, k), 1.36-1.18 (br, 11.7H, j), 1.12-0.87 (br, 286H, e)
- DF(theo): 4.8 %
- DF(NMR): 4.0 %

In the following, the characterization of all maleimide functionalized PEtOzi homopolymers is summarized.

**Table 7.7:** Summarized characterization of all maleimide functionalized PEtOzi homopolymers synthesized in this thesis.

| ID | Lab book-ID | Parent polymers | Yield$^a$ | $M_n^b$ | Đ$^b$ | $DF_t$ | $DF_e{}^c$ | Tg$^e$ |
|---|---|---|---|---|---|---|---|---|
| **P15** | NHD019 | **P1**, **13** | 0.27/113 | 9.6 | 1.27 | 13.9$^c$ | 9.5 | 38.1 |
| **P17** | NHD025 | **P1**, **13** | 0.46/85 | 8.8 | 1.22 | 13.9$^c$ | 9.2 | – |
| **P28** | NHD064 | **P72**, **75** | 2.6/96 | 4.1 | 1.11 | 5.4$^c$ | 5.0 | 23.3 |
| **P36** | NHD099 | **P74**, **77** | 3.3/100 | 4.5 | 1.11 | 3.7$^c$ | 3.6 | 23.6 |
| **P30** | NHD104 | **P74**, **70** | 2.8/92 | 4.6 | 1.11 | 4.8$^c$ | 4.8 | – |
| **P32** | NHD121 | **P74**, **78** | 7.8/98 | 4.4 | 1.15 | 4.8$^c$ | 4.0 | 26.2 |
| **P34** | NHD145 | **P9**, **80** | 3.1/97 | 3.3 | 1.09 | 4.5$^d$ | 4.5 | 25.1 |
| **P49** | NHD181 | **P9**, **40** | 7.6/87 | 5.4 | 1.09 | 2.4$^d$ | 2.4 | 25.2 |
| **P51** | NHD179 | **P9**, **41** | 7.3/86 | 5.3 | 1.10 | 3.2$^d$ | 3.4 | 23.1 |
| **P53** | NHD173 | **P9**, **39** | 7.3/86 | 5.5 | 1.10 | 4.1$^d$ | 4.3 | 24.7 |

Parameters in: $^a$ [g]/[%]

Determined by: $^b$ GPC(HFIP) in [kg/mol]; $^c$ $^1$H-NMR in [%]; $^d$ acid-base titration in [%]; $^e$ DSC in [°C]

### Furan Functionalized P(EtOzi-co-EtOx) Copolymers

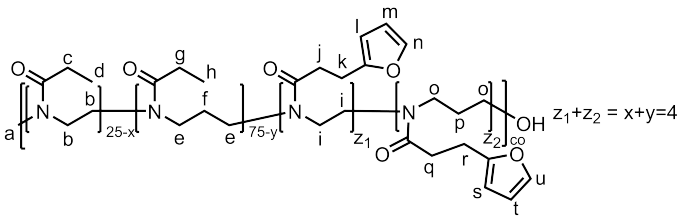


- ID: **P58**; Lab book-ID: NHD168
- $^1$H-NMR (MeOD, 300 MHz) $\delta$ (ppm): 7.36 (s, 4.8H, n, u), 6.29 (br, 4.8H, m, t), 6.07 (br, 4.8H, l, s), 3.66-3.45 (br, 102H, b, i), 3.44-3.21 (br, 394H, e, o, MeOH), 3.07-3.02 (br, 2.3H, a), 3.0-2.87 (br, 11.5H, k, r, a), 2.80-2.60 (br, 11.1H, j, q), 2.54-2.29 (br, 190H, c, g), 2.02-1.67 (br, 150H, f, p) 1.21-1.01 (br, 283H, d, h)
- DF(theo): 3.7 %
- DF(NMR): 4.7 %

In the following, the characterization of all furan functionalized P(EtOzi-co-EtOx) copolymers is summarized.

**Table 7.8:** Summarized characterization of all furan functionalized P(EtOzi-co-EtOx) copolymers synthesized in this thesis.

| ID | Lab book-ID | Parent polymers | Yield$^a$ | $M_n^b$ | Đ$^b$ | $DF_t$ | $DF_e{}^c$ | $T_g{}^e$ |
|---|---|---|---|---|---|---|---|---|
| **P54** | NHD146 | **P11**, **44** | 5.2/90 | 5.5 | 1.11 | 2.5$^d$ | 3.2 | 31 |
| **P56** | NHD156 | **P11**, **45** | 2.9/78 | 5.0 | 1.13 | 3.1$^d$ | 4.1 | 28 |
| **P58** | NHD168 | **P11**, **42** | 3.8/73 | – | – | 4.3$^d$ | 4.3 | 31 |

Parameters in: $^a$ [g]/[%]

Determined by: $^b$ GPC(HFIP) in [kg/mol]; $^c$ $^1$H-NMR in [%]; $^d$ acid-base titration in [%]; $^e$ DSC in [°C]

### Furan Functionalized P(EtOzi-co-MeOx) Copolymers

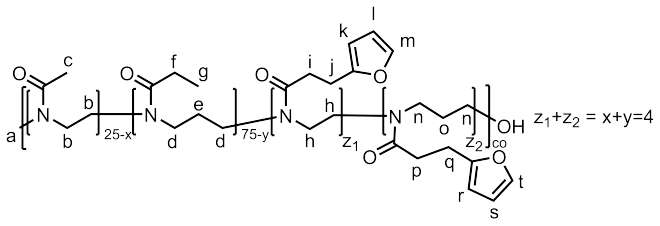


- ID: **P64**; Lab book-ID: NHD170
- $^1$H-NMR ($CD_3CN$, 300 MHz) $\delta$ (ppm): 7.36 (s, 4.7H, m, t), 6.30 (br, 4.8H, l, s), 6.04 (br, 4.9H, k, r), 3.53-3.01 (br, 400H, b, d, h, n), 2.98-2.82 (br, 14.1H, a, j, q), 2.77-2.55 (br, 11.2H, i, p), 2.43-2.21 (br, 145H, f), 2.07-1.97 (br, 61H, c), 1.89-1.58 (br, 153H, e, o), 1.14-0.91 (br, 217H, g)
- DF(theo): 3.7 %
- DF(NMR): 4.7 %

In the following, the characterization of all furan functionalized P(EtOzi-co-MeOx) copolymers is summarized.

**Table 7.9:** Summarized characterization of all furan functionalized P(EtOzi-co-MeOx) copolymers synthesized in this thesis.

| **ID** | Lab book-ID | Parent polymers | Yield$^a$ | $M_n^b$ | Đ$^b$ | $DF_t$ | $DF_e{}^c$ | $T_g{}^e$ |
|---|---|---|---|---|---|---|---|---|
| **P37** | NHD135 | **P12**, **81** | 1.9/95 | – | – | 3.4$^c$ | 3.9 | 33 |
| **P60** | NHD151 | **P12**, **46** | 4.8/85 | 4.0 | 1.30 | 2.4$^d$ | 2.9 | 33 |
| **P62** | NHD165 | **P12**, **47** | – | 4.3 | 1.20 | 3.1$^d$ | 3.5 | 33 |
| **P64** | NHD170 | **P12**, **43** | 3.7/87 | 4.2 | 1.28 | 3.7$^d$ | 4.7 | 32 |

Parameters in: $^a$ [g]/[%]

Determined by: $^b$ GPC(HFIP) in [kg/mol]; $^c$ $^1$H-NMR in [%]; $^d$ acid-base titration in [%]; $^e$ DSC in [°C]

### Maleimide Functionalized P(EtOzi-co-EtOx) Copolymers

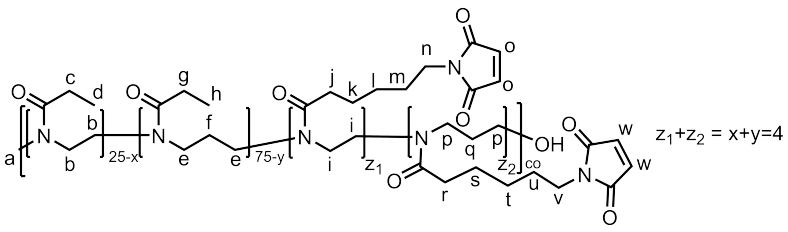


- ID: **P59**; Lab book-ID: NHD169
- $^{1}$H-NMR (MeOD, 300 MHz) $\delta$ (ppm): 6.81 (s, 9.0H, o, w), 3.63-3.44 (br, 114H, b, i n, v), 3.44-3.21 (br, 409H, p, e, MEOH), 3.09-3.03 (br, 2.6H, a), 2.94-2.91 (br, 0.8H, a), 2.54-2.29 (br, 201H, c, g, j, r), 2.01-1.71 (br, 150H, f, q), 1.71-1.51 (br, 20.8H, k, m, s, u), 1.41-1.24 (br, 12.0H, l, t), 1.21-1.02 (br, 288H, d, h)
- DF(theo): 4.3 %
- DF(NMR): 4.5 %

In the following, the characterization of all maleimide functionalized P(EtOzi-co-EtOx) copolymers is summarized.

**Table 7.10:** Summarized characterization of all maleimide functionalized P(EtOzi-co-EtOx) copolymers synthesized in this thesis.

| ID | Lab book-ID | Parent polymers | Yield$^{a}$ | $M_n^{b}$ | Đ$^{b}$ | $DF_t$ | $DF_e{}^{c}$ | Tg$^{e}$ |
|---|---|---|---|---|---|---|---|---|
| **P55** | NHD147 | **P11**, **44** | 5.4/94 | 5.6 | 1.13 | 2.5$^{d}$ | 2.8 | 32 |
| **P57** | NHD157 | **P11**, **45** | 2.9/78 | 5.2 | 1.15 | 3.1$^{d}$ | 3.5 | 32 |
| **P59** | NHD169 | **P11**, **42** | 3.9/74 | – | – | 4.3$^{d}$ | 4.5 | 31 |

Parameters in: $^{a}$ [g]/[%]

Determined by: $^{b}$ GPC(HFIP) in [kg/mol]; $^{c}$ $^{1}$H-NMR in [%]; $^{d}$ acid-base titration in [%]; $^{e}$ DSC in [°C]

### Maleimide Functionalized P(EtOzi-co-MeOx) Copolymers

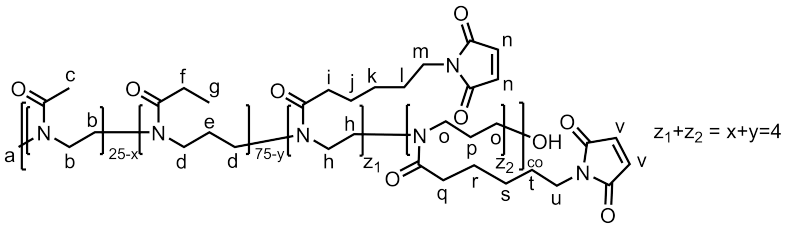


- ID: **P65**; Lab book-ID: NHD171
- $^1$H-NMR ($CD_3CN$, 300 MHz) $\delta$ (ppm): 6.74 (s, 9.0H, n, v), 3.50-3.14 (br, 400H, b, b, h, o, m, u), 2.96-2.91 (br, 1.67H, a), 2.85-2.81 (br, 1.02H, a), 2.94-2.91 (br, 0.8H, a), 2.45-2.21 (br, 153H, f, i, q), 2.07-1.96 (br, 62.6H, c), 1.88-1.61 (br, 151H, e, p), 1.61-1.47 (br, 22.7H, j, l, r, t), 1.34-1.20 (br, 13.2H, k, s), 1.10-0.95 (br, 213H, g)
- DF(theo): 3.7 %
- DF(NMR): 4.5 %

In the following, the characterization of all maleimide functionalized P(EtOzi-co-MeOx) copolymers is summarized.

**Table 7.11:** Summarized characterization of all maleimide functionalized P(EtOzi-co-MeOx) copolymers synthesized in this thesis.

| ID | Lab book-ID | Parent polymers | Yield[a] | $M_n^b$ | Đ[b] | $DF_t$ | $DF_e$[c] | Tg[e] |
|---|---|---|---|---|---|---|---|---|
| **P38** | NHD136 | **P12**, **81** | 1.9/95 | – | – | 3.4[c] | 2.7 | 34 |
| **P61** | NHD152 | **P12**, **46** | 4.9/87 | – | – | 2.4[d] | 2.8 | 35 |
| **P63** | NHD166 | **P12**, **47** | – | 4.5 | 1.24 | 3.1[c] | 3.6 | 36 |
| **P65** | NHD171 | **P12**, **43** | 3.7/87 | 4.6 | 1.33 | 3.7[d] | 4.5 | 34 |

Parameters in: [a] [g]/[%]

Determined by: [b] GPC(HFIP) in [kg/mol]; [c] $^1$H-NMR in [%]; [d] acid-base titration in [%]; [e] DSC in [°C]

### 7.2.6 Functionalization with Cinnamic Acid

1853 mg (9.0 mmol) DCC were dissolved in 58 ml AN and the solution was chilled using an ice bath. Next, 1330 mg of cinnamic acid (9.0 mmol) as well as 1900 mg (0.17 mmol) of **P79** were added. The mixture was stirred over night. The precipitated solid was removed by centrifugation and filtration. The AN was then removed under reduced pressure and the oily residue was taken up in a few millilitres of MeOH. The solution was then precipitated three-times in ice cold diethyl ether. The product was dissolved in AN and dried under high vacuum.

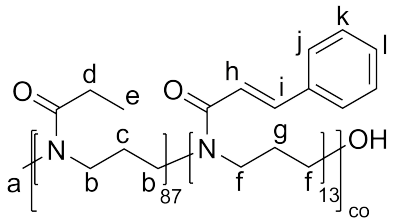


- ID: **P66**; Lab book-ID: NHD132
- Parent polymer: **P9**, **P79**
- Yield: 1.67 g/88 %
- $^1$H-NMR ($CD_3CN$, 300 MHz) $\delta$ (ppm): 7.73-7.28 (b, 81H, i, j, k, l), 7.07-6.93 (br, 12.6H, h), 3.62-3.07 (br, 406H, b, f), 2.97-2.91 (br, 1.9H, a), 2.86-2.79 (br, 0.9H, a), 2.39-2.20 (br, 173H, d), 1.91-1.56 (br, 200H, c, g), 1.13-0.92 (br, 260H, e)
- DF(theo): 13.2 %
- DF(NMR): 12.6 %
- $T_g$ (DSC): 35.0 °C

### 7.2.7 Functionalization with Coumarin

780 mg (3.79 mmol) DCC were dissolved in 24 ml DMF and the solution was chilled using an ice bath. Next, 832 mg of 7-(carboxymethoxy)coumarin (3.78 mmol) as well as 800 mg (0.07 mmol) of **P79** were added. The mixture was stirred over night, and the precipitated solid was removed by centrifugation and filtration. The DMF was removed under reduced pressure and the oily residue was taken up in a few millilitres of MeOH. A white solid precipitated and was removed via filtration. The solution was then precipitated three-times in ice cold diethyl ether. The product was dissolved in AN and dried under high vacuum.

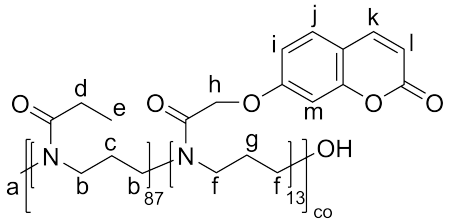


- ID: **P67**; Lab book-ID: NHD133
- Parent polymer: **P9**, **P79**
- Yield: 759 mg/95 %
- $^1$H-NMR ($CD_3CN$, 300 MHz) $\delta$ (ppm): 7.86-7.66 (b, 15H, k), 7.57-7.36 (br, 15H, j), 6.98-6.72 (br, 29.8H, i, m), 6.26-6.10 (br, 14.7H, l), 4.95-4.73 (br, 27.9H, h), 3.54-3.05 (br, 400H, b, f), 2.40-2.13 (br, 219H, d), 1.90-1.56 (br, 200H, c, g), 1.15-0.92 (br, 261H, e)
- DF(theo): 13.2 %
- DF(NMR): 15 %
- $T_g$ (DSC): 45.1 °C

## 7.3 Parameters for Melt Electrowriting

In the following section the printing parameters for the scaffolds presented in this thesis are specified. The printed constructs discussed in the main body are labelled with a scaffold ID of the type"SXX“, where "XX“ is a consecutive number. This allows the reader to find the printing parameters used for each polymer and scaffold discussed in this work. A typical example of a g-code used for the printing of box-like scaffolds is shown in Figure 7.3.

preamble

```
G17 G8 G91 g21 g71 g94 g69

%Stabilization Parameters

%Stabilization speed
#100=1400
%Stabilization turn speed
#101=600
%fiber spacing (stabilization)
#102=0.5
%scaffold size (stabilization)
#103=12

%number of lines
#104=[#103/2]
#104=[#104/#102]


% Scaffold Parameters

% Scaffold speed x-direction
#105=1400
% Scaffold speed y-direction
#112=1400
% Scaffold turnspeed
#106=600
%fiber spacing x-direction
#107=0.5
%fiber spacing y-direction
#110=0.5


%scaffold size (scaffold)
#108=18


%number of lines x
#109=[#108/2]
#109=[#109/#107]

%number of lines y
#111=[#108/2]
#111=[#111/#110]
```

main program

```
%main program
%-----------

%stabilization

m98 p5 l2

%move to printing field
g1 x[#103*1.5] y0 f[#105]

m98 p10 l3

g1 x0           y[#107*3]      f[#105]
g1 x[#108*1.5]          y0             f[#105]
g1 x0           y[#107*-3]     f[#105]

m98 p10 l3

%move to next slide
g1 x0           y[#107*3]      f[#105]
g1 x0           y[-27]         f[#105]
g1 x0           y[#107*-3]     f[#105]

m98 p10 l3

g1 x0           y[#107*3]      f[#105]
g1 x[#108*-1.5]         y0             f[#105]
g1 x0           y[#107*-3]     f[#105]

m98 p10 l3

%move collector away
g1 x0           y[#107*-7]     f[#105]

m30
```

subroutines stabilization

```
% X-line stabilization
o1
g91
g1      x[#103]         y0              f[#100]
g2      x0              y[#102*-1] r-1  f[#101]
g1      x[#103*-1]      y0              f[#100]
g3      x0              y[#102*-1] r-1  f[#101]
m99

% X-layer stabilization
o2
m98 p1 l[#104]
g2      x[#102*-1]              y0      r-1     f[#101]
g1      x0              y[#103*1]       f[#100]
g2      x[#102]         y0 r-1          f[#101]
m99

% Y-line
o3
g91
g1      x0              y[#103*-1]              f[#100]
g3      x[#102]         y0              r-1     f[#101]
g1      x0              y[#103*1]               f[#100]
g2      x[#102]         y0              r-1     f[#101]
m99

% y-layer stabilization
o4
m98 p3 l[#104]
g3      x0              y[#102*1] r-1   f[#101]
g1      x[#103*-1]      y0              f[#100]
g3      x0              y[#102*-1] r-1  f[#101]
m99

% multiple layers of boxes
o5
m98 p2 l1
m98 p4 l1
m99
```

subroutines scaffold

```
% X-line scaffold
o6
g91
g1      x[#108]         y0              f[#105]
g2      x0              y[#107*-1] r-1  f[#106]
g1      x[#108*-1]      y0              f[#105]
g3      x0              y[#107*-1] r-1  f[#106]
m99

% X-layer scaffold
o7
m98 p6 l[#109]
g2      x[#107*-1]              y0      r-1     f[#106]
g1      x0              y[#108*1]       f[#105]
g2      x[#107]         y0 r-1          f[#106]
m99

% Y-line scaffold
o8
g91
g1      x0              y[#108*-1]              f[#112]
g3      x[#110]         y0              r-1     f[#106]
g1      x0              y[#108*1]               f[#112]
g2      x[#110]         y0              r-1     f[#106]
m99

% y-layer scaffold
o9
m98 p8 l[#111]
g3      x0              y[#110*1] r-1   f[#106]
g1      x[#108*-1]      y0              f[#112]
g3      x0              y[#110*-1] r-1  f[#106]
m99

% multiple layers of boxes
o10
m98 p7 l1
m98 p9 l1
m99
```

**Figure 7.3:** Representative example of a g-code used for the printing of box-like scaffolds.

## MEW Printing Parameters Used for the Scaffolds Discussed in Section 4.1

**Table 7.12:** MEW processing parameters for non-functionalized PEtOzi and PEtOx homo- and copolymers.

| SID | polymer | size[a] | layer | angle | p[b] | V[c] | CD[a] | NT[d] | ST[d] | CS[e] |
|---|---|---|---|---|---|---|---|---|---|---|
| S22 | **P1** | 18 | 10 | 90° | 1.5 | 3.2 | 3.3 | 120 | 100 | 1080 |
| S23 | **P4** | 18 | 10 | 90° | 1.6 | 3.6 | 3.3 | 130 | 110 | 1000 |
| S24 | **P3** | 18 | 20 | 90° | 1.25 | 3.5 | 3.3 | 140 | 120 | 1700 |
| S25 | **P2** | 18 | 10 | 90° | 1.25 | 3.1 | 3.3 | 160 | 140 | 1100 |
| S26 | **P2** | 18 | 10 | 90° | 1.25 | 2.7 | 3.3 | 160 | 140 | 1100 |
| S27 | **P2** | 18 | 10 | 90° | 1.25 | 2.7 | 3.3 | 160 | 140 | 1100 |
| S28 | **P5** | 18 | 10 | 90° | 1.0 | 4.5 | 3.3 | 170 | 155 | 1500 |

Parameters in: [a] [mm]; [b] [bar]; [c] [kV]; [d] [°C]; [e] [mm/min]

Abbreviation: CD collector distance

## MEW Printing Parameters Used for the Scaffolds Discussed in Section 4.2

**Table 7.13:** MEW processing parameters for the $2^{nd}$ generation of DA functionalized polymers.

| SID | polymer | size[a] | layer | angle | p[b] | V[c] | CD[a] | NT[d] | ST[d] | CS[e] |
|---|---|---|---|---|---|---|---|---|---|---|
| S29 | **P29+P30** | 18 | 5 | 90° | 1.5 | 3.0-3.7 | 3.3 | 150 | 130 | 1300 |
| S4 | **P29+P30** | 18 | 5 | 90° | 1.5 | 2.7-3.1 | 3.3 | 150 | 130 | 1100 |
| S5 | **P29+P30** | 18 | 2 | 90° | 2.25 | 2.5-2.7 | 3.3 | 150 | 130 | 1500 |
| S6 | **P29+P30** | 18 | 2 | 90° | 2.25 | 2.5-2.7 | 3.3 | 150 | 130 | 1500 |
| S7 | **P29+P30** | 18 | 2 | 90° | 1.5 | 3.4 | 3.3 | 150 | 130 | 1300 |
| S8 | **P29+P30** | 18 | 2 | 90° | 1.5 | 3.4 | 3.3 | 150 | 130 | 1300 |
| S9 | **P29+P30** | 18 | 5 | 90° | 1.5 | 2.5 | 3.3 | 150 | 130 | 1300 |
| S10 | **P31+P32** | 18 | 5 | 90° | 2 | 3.1 | 3.3 | 147 | 127 | 1800 |
| S11 | **P35+P36** | 18 | 5 | 90° | 1.5 | 3.25 | 3.3 | 140 | 120 | 1000 |
| S12 | **P37+P38** | 18 | 5 | 90° | 2.25 | 3.9 | 3.3 | 140 | 120 | 1100 |

Parameters in: [a] [mm]; [b] [bar]; [c] [kV]; [d] [°C]; [e] [mm/min]

Abbreviation: CD collector distance

## MEW Printing Parameters Used for the Scaffolds Discussed in Section 4.3

**Table 7.14:** MEW processing parameters for the $3^{rd}$ generation of DA functionalized polymers.

| SID | polymer | layer | angle | p[b] | V[c] | CD[a] | NT[d] | ST[d] | CT[d] | CS[e] |
|---|---|---|---|---|---|---|---|---|---|---|
| | Scaffolds for shape fidelity assessment | | | | | | | | | |
| S13 | **P48+P49** | 5 | 90° | 1.25 | 3.3 | 3.3 | 127 | 120 | RT | 1400 |
| S30 | **P50+P51** | 5 | 90° | 1.5 | 3.2 | 3.3 | 134 | 125 | RT | 1400 |
| S31 | **P52+P53** | 5 | 90° | 1.25 | 3.7 | 3.3 | 141 | 127 | 40 | 1280 |
| S14 | **P54+P55** | 5 | 90° | 1.5 | 3.1-3.9 | 3.0 | 141 | 125 | RT | 1260 |
| S32 | **P56+P57** | 5 | 90° | 1.5 | 3.3 | 3.3 | 148 | 126 | RT | 1400 |
| S15 | **P58+P59** | 5 | 90° | 1.75 | 3.2 | 3.3 | 157 | 136 | 40 | 1400 |
| S33 | **P60+P61** | 5 | 90° | 1.5 | 3.9 | 3.3 | 138 | 118 | RT | 1260 |
| S34 | **P62+P63** | 5 | 90° | 1.25 | 3.4 | 3.3 | 149 | 129 | RT | 1260 |
| S35 | **P64+P65** | 5 | 90° | 1.5 | 3.5 | 3.3 | 167 | 140 | 40 | 1260 |
| | Stacked shape-morphing scaffolds | | | | | | | | | |
| S19 | **P52+P53** | 3 | 90° | 1.25 | 2.5-3.2 | 3.3 | 142 | 127 | 40 | 1400 |
| S20 | **P52+P53** | 3 | 90° | 1.25 | 2.5-3.2 | 3.3 | 142 | 127 | 40 | 1400 |
| S21 | **P52+P53** | 3 | 90° | 1.25 | 2.5-3.2 | 3.3 | 142 | 127 | 40 | 1400 |
| S16 | **P48+P49** | 3 | 90° | 1.5 | 3.1 | 3.3 | 127 | 120 | RT | 1260 |
| S17 | **P48+P49** | 3 | 90° | 1.5 | 3.1 | 3.3 | 127 | 120 | RT | 1260 |
| S18 | **P48+P49** | 3 | 90° | 1.75 | 3.1 | 3.3 | 127 | 120 | RT | 1260 |
| | One material shape-morphing scaffolds | | | | | | | | | |
| S36 | **P52+P53** | 3 | 90° | 1.25 | 3.5 | 3.3 | 142 | 127 | 40 | y=x=1400 |
| S37 | **P52+P53** | 3 | 90° | 1.25 | 3.5 | 3.3 | 142 | 127 | 40 | y=2x=2800 |
| S38 | **P52+P53** | 3 | 45° | 1.25 | 3.5 | 3.3 | 142 | 127 | 40 | y=x=1400 |
| S39 | **P52+P53** | 3 | 45° | 1.25 | 3.7 | 3.3 | 142 | 127 | 40 | y=2x=2800 |

**Table 7.15:** MEW processing parameters for cinnamyl and coumarin functionalized PEtOzi.

| SID | polymer | layer | angle | p[b] | V[c] | CD[a] | NT[d] | ST[d] | CT[d] | CS[e] |
|---|---|---|---|---|---|---|---|---|---|---|
| S40 | **P66** | 2 | 90° | 2 | 3.5 | 3.3 | 130 | 110 | RT | 1500 |
| S41 | **P67** | 2 | 90° | 2.5 | 4.8 | 3.3 | 143 | 123 | RT | 1800 |

**Table 7.16:** MEW processing parameters for the tubular printer.

| SID | Polymer | length[a] | d[a] | layer | angle | p[b] | V[c] | D[a] | ST[d] | NT[d] | CS[e] |
|---|---|---|---|---|---|---|---|---|---|---|---|
| S42 | **P50+P51** | 10 | 3 | 20 | 70° | 3.25 | 3.5 | 3.4 | 138 | 138 | 400 |

Parameters in: [a] [mm]; [b] [bar]; [c] [kV]; [d] [°C]; [e] [mm/min]

Abbreviation: CD collector distance; CT collector temperature

# 8 Appendix

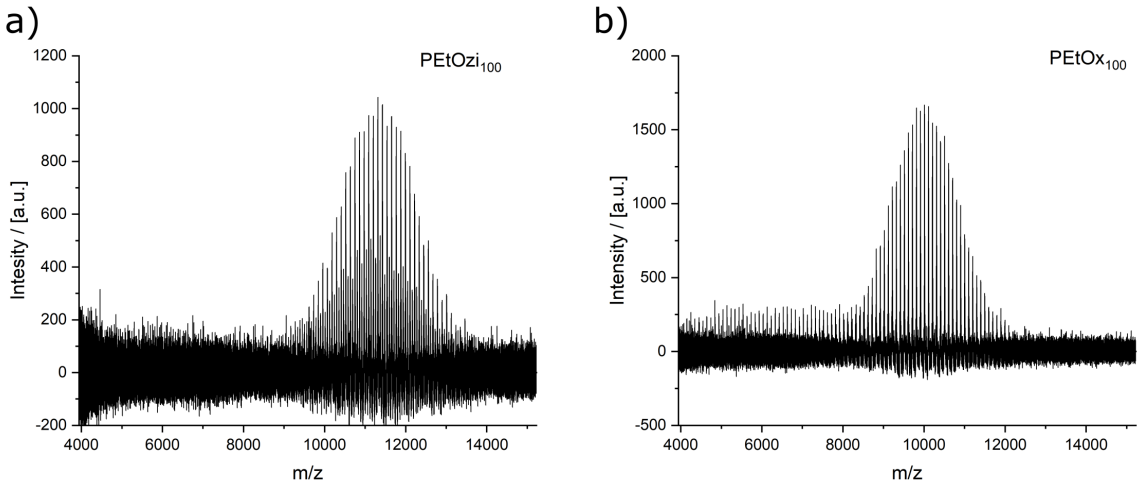


**Figure 8.1:** MALDI-TOF analysis of the $PEtOzi_{100}$ (**P1**) a) and the $PEtOx_{100}$ (**P5**) b) homopolymers.

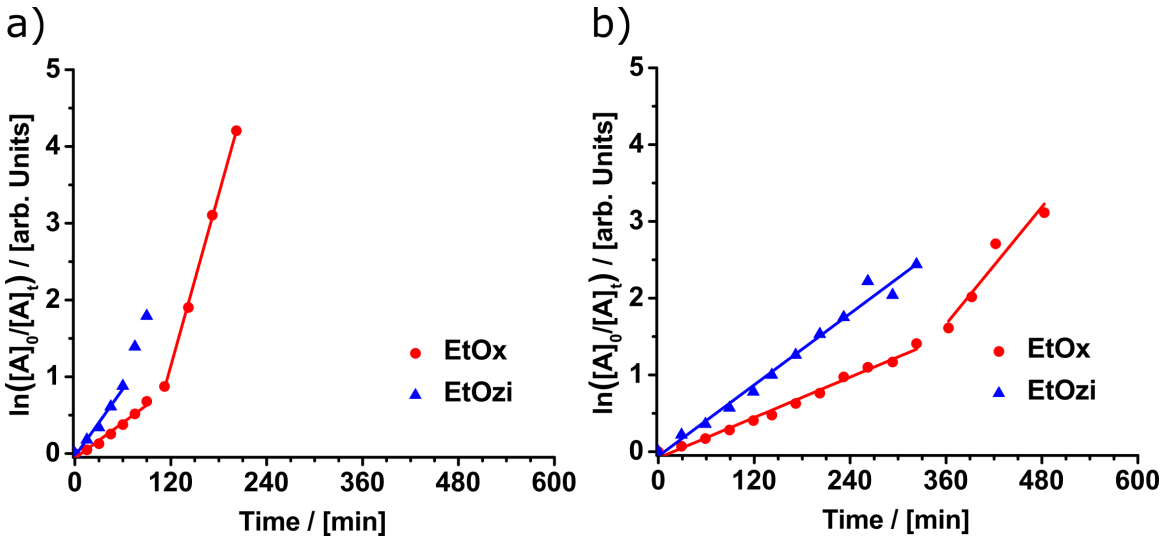


**Figure 8.2:** First order kinetic plot of the copolymerization of EtOzi and EtOx with a monomer ratio of 3:1 a) and 1:1 b).

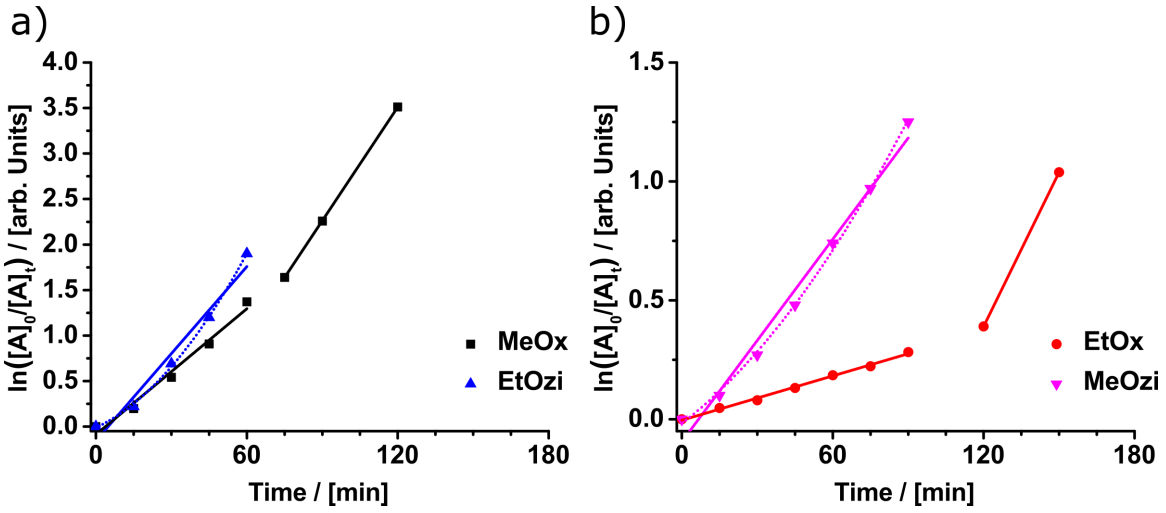


**Figure 8.3:** a) First order kinetic plot of the copolymerization of MeOx and EtOzi with a monomer ratio of 3:1. b) First order kinetic plot of the copolymerization of EtOx and MeOzi with a monomer ratio of 3:1.

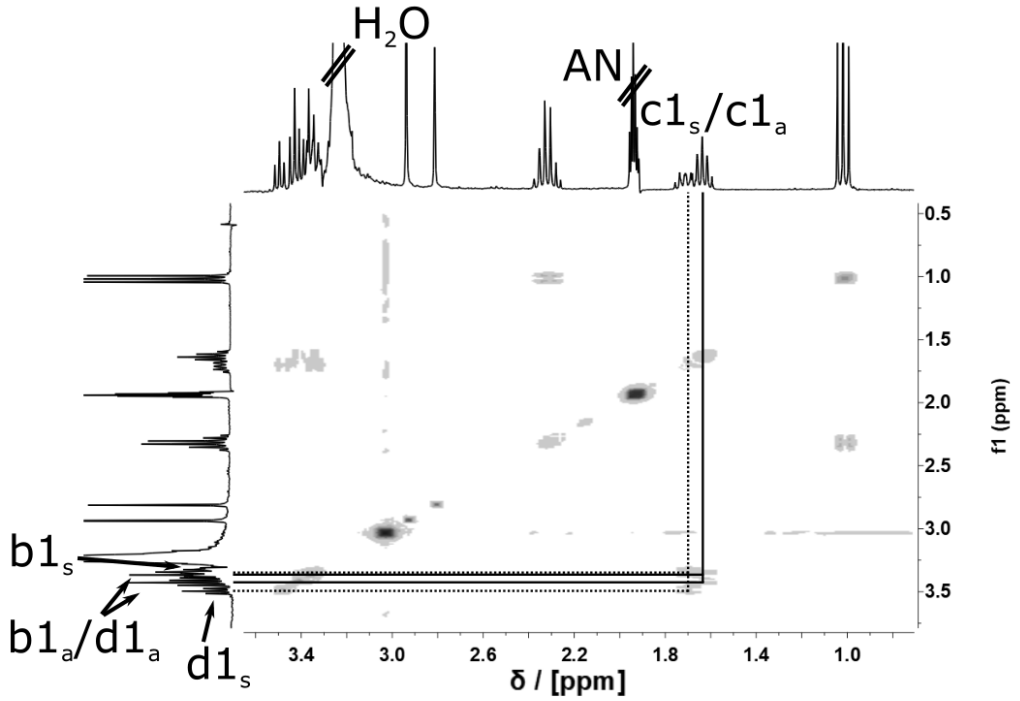


**Figure 8.4:** COSY spectrum (300 MHz, 298 K, $CD_3CN$) of **I1** 5 min after addition of 1 M KOH in water. The peaks relating to the syn and anti conformations of the resulting product are highlighted.

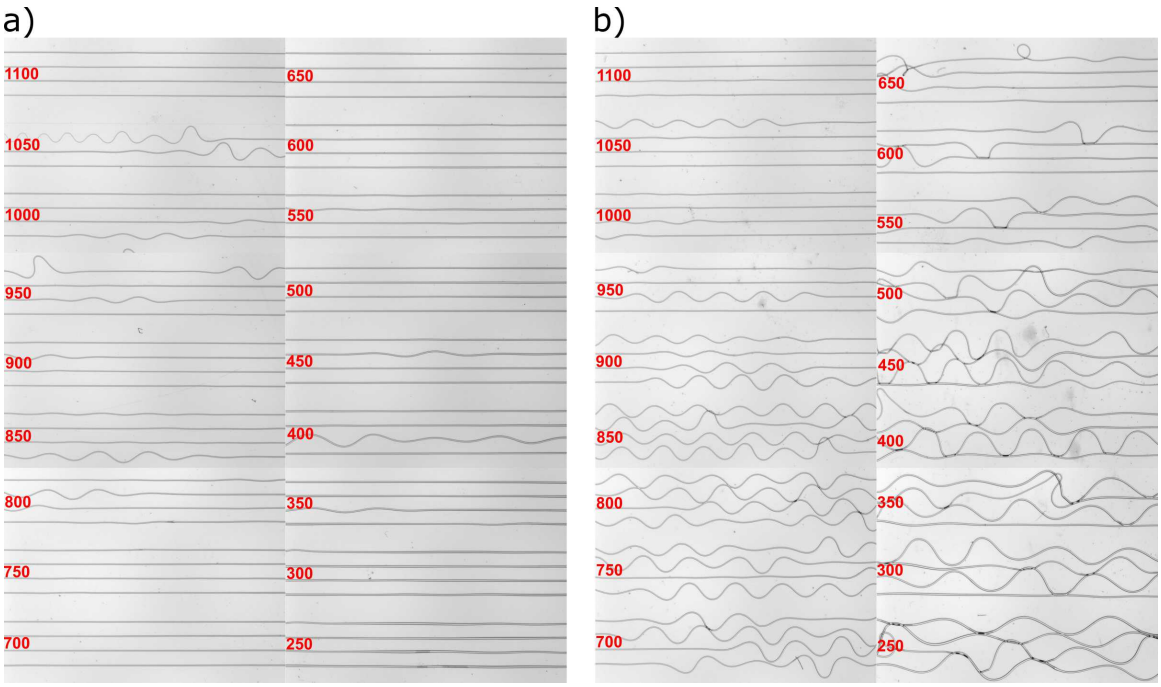


**Figure 8.5:** a), b) Stereomicroscope images of an CTS experiment of **P4**. While the printing parameters were kept constant, completely different results were obtained.

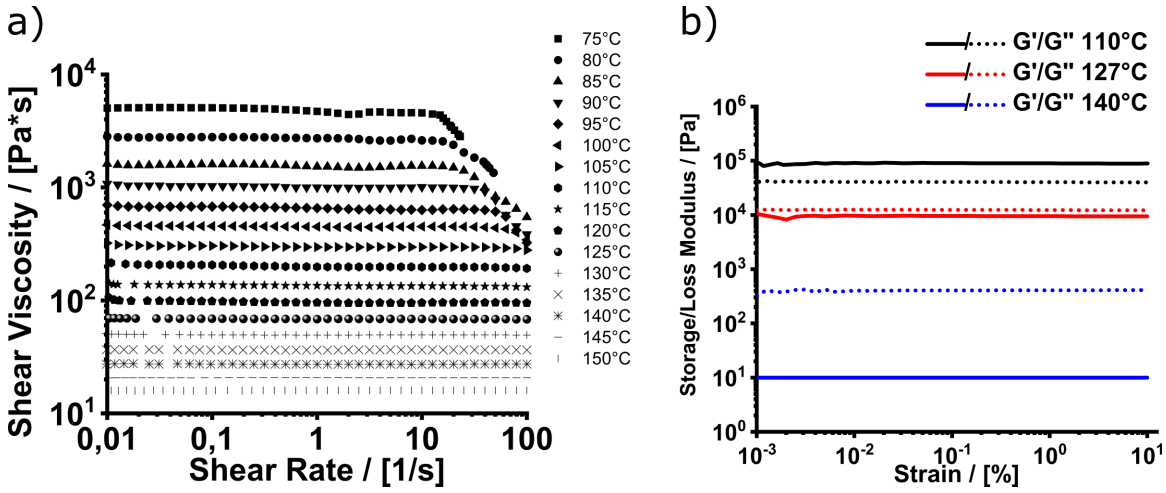


**Figure 8.6:** a) Shear rate sweep of **P1** between 75 and 150 °C. b) Rheology strain sweeps from 0.01 to 10 rad/s at below (110 °C), near (127 °C) and above (140 °C) the liquefaction point of a mixture of **P29** and **P30**.


**Figure 8.7:** a), b) Thermally degraded DA material after a rheology measurement at ambient conditions. The material experiences a colour change from colourless to a red/brownish colour. While at the air/polymer interface the material can not be liquefied by increasing the temperature, the polymer directly under the measurement head is still liquefiable.

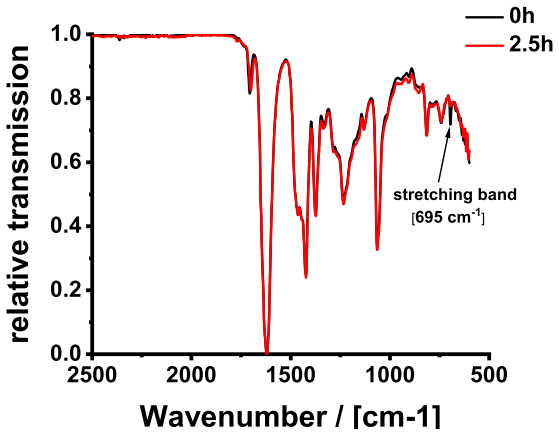


**Figure 8.8:** IR spectrum of a mixture of **P27** and **P28**, 0 and 2.5 h after liquefaction using a heat-gun.

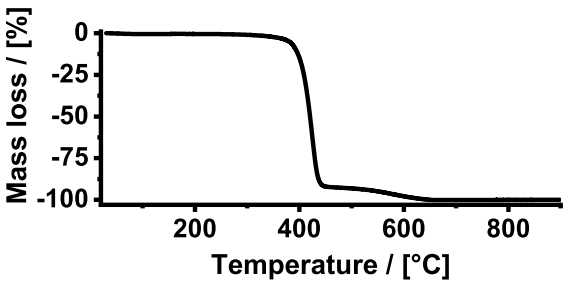


**Figure 8.9:** TGA measurement of a mixture of **P27** and **P28** under synthetic air.

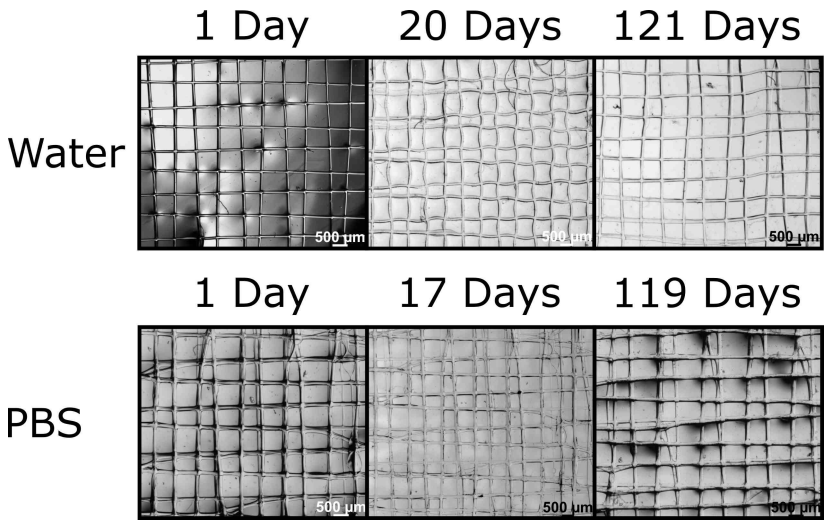


**Figure 8.10:** Stereomicroscope images of PEtOzi hydrogel scaffolds after incubation in water and PBS. No structural disintegration can be observed.

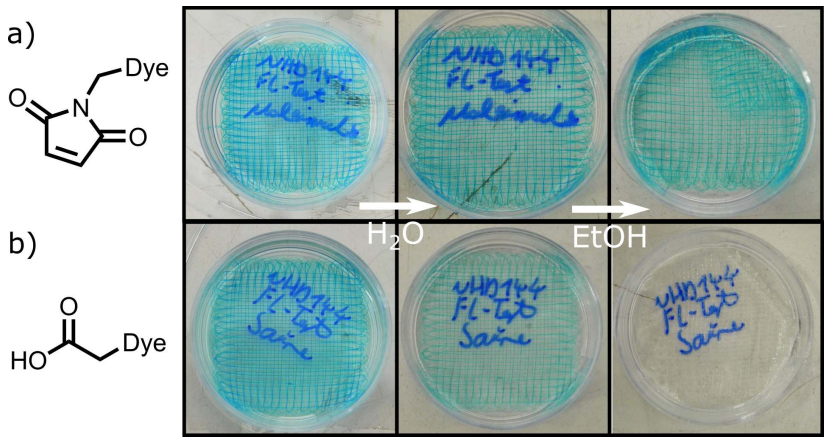


**Figure 8.11:** Incubation of PEtOzi hydrogel scaffolds with aqueous solutions of a fluorescent dye with a maleimide function (DY-647P1-Maleimide) a) and with a carboxylic acid function b). Both samples are first washed several times with water, followed by extensive washing with ethanol.

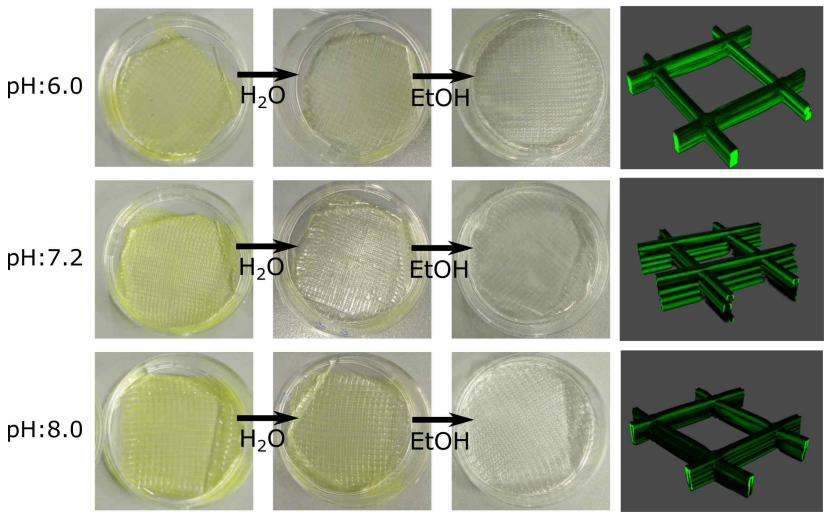


**Figure 8.12:** Incubation of PEtOzi hydrogel scaffolds with a solution of a FITC-dye tagged peptide sequence (Cys-Gly-Gly-Lys(FITC)). No notable differences were found between the incubation at the three pH conditions. Left to right: Scaffold incubated in peptide solution; after extensive washing with water; after extensive washing with ethanol; confocal image of respective washed scaffold.

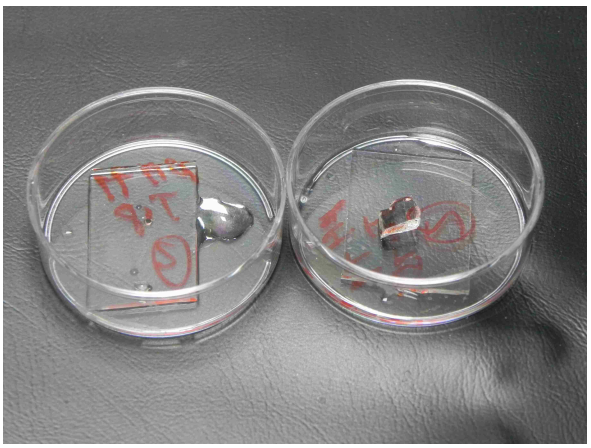

**Figure 8.13:** Two bulk hydrogel samples prepared from a mixture of **P50** + **P51** after incubation for 8 d in aqueous solution buffered to pH 11. While the sample on the left has lost its structural integrity, the sample on the right is still visibly unaffected.

# Bibliography


[1] H. Staudinger, *Ber. Dtsch. Chem. Ges.*, 1920, **53**(6), 1073–1085.

[2] S. C. Ligon, R. Liska, J. Stampfl, M. Gurr, R. Mülhaupt, *Chem. Rev.*, 2017, **117**(15), 10212–10290.

[3] B. Berman, *Bus. Horiz.*, 2012, **55**(2), 155–162.

[4] E. T. Pashuck, M. M. Stevens, *Sci. Transl. Med.*, 2012, **4**(160), 160.

[5] F. A. Probst, D. W. Hutmacher, D. F. Müller, H.-G. Machens, J.-T. Schantz, *Handchir. Mikrochir. Plast. Chir.*, 2010, **42**(06), 369–373.

[6] M. Gurven, H. Kaplan, *Popul. Dev. Rev.*, 2007, **33**(2), 321–365.

[7] B. M. Holzapfel, J. C. Reichert, J.-T. Schantz, U. Gbureck, L. Rackwitz, U. Nöth, F. Jakob, M. Rudert, J. Groll, D. W. Hutmacher, *Adv. Drug Delivery Rev.*, 2013, **65**(4), 581–603.

[8] S. V. Murphy, A. Atala, *Nat. Biotechnol.*, 2014, **32**(8), 773–785.

[9] A. Atala, F. K. Kasper, A. G. Mikos, *Sci. Transl. Med.*, 2012, **4**(160), 160–170.

[10] J. Henkel, D. W. Hutmacher, *BioNanoMaterials*, 2013, **14**(3-4), 171–193.

[11] T. Lorson, M. M. Luebtow, E. Wegener, M. S. Haider, S. Borova, D. Nahm, R. Jordan, M. Sokolski-Papkov, A. V. Kabanov, R. Luxenhofer, *Biomaterials*, 2018, **178**, 204–280.

[12] V. Mironov, T. Trusk, V. Kasyanov, S. Little, R. Swaja, R. Markwald, *Biofabrication*, 2009, **1**(2), 022001.

[13] W. Sun, *Biofabrication*, 2009, **1**(1), 010201.

[14] J. Groll, T. Boland, T. Blunk, J. A. Burdick, D.-W. Cho, P. D. Dalton, B. Derby, G. Forgacs, Q. Li, V. A. Mironov, L. Moroni, M. Nakamura, W. Shu, S. Takeuchi, G. Vozzi, T. B. F. Woodfield, T. Xu, J. J. Yoo, J. Malda, *Biofabrication*, 2016, **8**(1), 013001.

[15] F. Guillemot, V. Mironov, M. Nakamura, *Biofabrication*, 2010, **2**(1), 010201.

[16] B. Schon, G. Hooper, T. Woodfield, *Ann. Biomed. Eng.*, 2017, **45**, 100–114.

[17] B. Dhandayuthapani, Y. Yoshida, T. Maekawa, D. S. Kumar, *Int. J. Polym. Sci.*, 2011, **2011**, 290602.

[18] P. X. Ma, *Mater. Today*, 2004, **7**(5), 30–40.

[19] T. Jüngst, *Establishing and Improving Methods for Biofabrication* PhD thesis, Universität Würzburg, 2019.

[20] L. D. Harris, B.-S. Kim, D. J. Mooney, *J. Biomed. Mater. Res.*, 1998, **42**(3), 396–402.

[21] H.-W. Kang, Y. Tabata, Y. Ikada, *Biomaterials*, 1999, **20**(14), 1339–1344.

[22] J. M. Karp, K. Rzeszutek, M. S. Shoichet, J. E. Davies, *J. Craniofac. Surg.*, 2003, **14**(3).

[23] F. J. O'Brien, *Mater. Today*, 2011, **14**(3), 88–95.

[24] J. Ulbricht, R. Jordan, R. Luxenhofer, *Biomaterials*, 2014, **35**(17), 4848–4861.

[25] A. Karchin, F. I. Simonovsky, B. D. Ratner, J. E. Sanders, *Acta Biomater.*, 2011, **7**(9), 3277–3284.

[26] C. Colosi, M. Costantini, R. Latini, S. Ciccarelli, A. Stampella, A. Barbetta, M. Massimi, L. Conti Devirgiliis, M. Dentini, *J. Mater. Chem. B*, 2014, **2**, 6779–6791.

[27] A. J. Engler, S. Sen, H. L. Sweeney, D. E. Discher, *Cell*, 2006, **126**(4), 677–689.

[28] I. Levental, P. C. Georges, P. A. Janmey, *Soft Matter*, 2007, **3**, 299–306.

[29] J. P. Best, S. Javed, J. J. Richardson, K. L. Cho, M. M. J. Kamphuis, F. Caruso, *Soft Matter*, 2013, **9**, 4580–4584.

[30] D. Richards, J. Jia, M. Yost, R. Markwald, Y. Mei, *Ann. Biomed. Eng.*, 2017, **45**(1), 132–147.

[31] R. Y. Kannan, H. J. Salacinski, K. Sales, P. Butler, A. M. Seifalian, *Biomaterials*, 2005, **26**(14), 1857–1875.

[32] A. Y. Malkin, V. V. Goncharenko, V. V. Malinovskii, *Polymer Mechanics*, 1976, **12**(3), 439–444.

[33] K. Solc, W. H. Stockmayer, *J. Chem. Phys.*, 1971, **54**(6), 2756–2757.

[34] C. D. Han, R. R. Lamonte, Y. T. Shah, *J. Appl. Polym. Sci.*, 1972, **16**(12), 3307–3323.

[35] B. Wendel, D. Rietzel, F. Kühnlein, R. Feulner, G. Hülder, E. Schmachtenberg, *Macromol. Mater. Eng.*, 2008, **293**(10), 799–809.

[36] F. Pati, J. Jang, D.-H. Ha, S. Won Kim, J.-W. Rhie, J.-H. Shim, D.-H. Kim, D.-W. Cho, *Nat. Commun.*, 2014, **5**(1), 3935.

[37] G. I. Taylor, M. D. Van Dyke, *Proc. Math. Phys. Eng. Sci*, 1969, **313**(1515), 453–475.

[38] A. Greiner, J. Wendorff, *Angew. Chem. Int. Ed.*, 2007, **46**(30), 5670–5703.

[39] T. D. Brown, P. D. Dalton, D. W. Hutmacher, *Prog. Polym. Sci.*, 2016, **56**, 116–166.

[40] Z.-M. Huang, Y.-Z. Zhang, M. Kotaki, S. Ramakrishna, *Compos. Sci. Technol.*, 2003, **63**(15), 2223–2253.

[41] D. H. Reneker, A. L. Yarin, H. Fong, S. Koombhongse, *J. Appl. Phys.*, 2000, **87**(9), 4531–4547.

[42] D. Li, G. Ouyang, J. T. McCann, Y. Xia, *Nano Lett.*, 2005, **5**(5), 913–916.

[43] P. Katta, M. Alessandro, R. D. Ramsier, G. G. Chase, *Nano Lett.*, 2004, **4**(11), 2215–2218.

[44] D. H. Reneker, A. L. Yarin, *Polymer*, 2008, **49**(10), 2387–2425.

[45] P. D. Dalton, C. Vaquette, B. L. Farrugia, T. R. Dargaville, T. D. Brown, D. W. Hutmacher, *Biomater. Sci.*, 2013, **1**, 171–185.

[46] T. D. Brown, P. D. Dalton, D. W. Hutmacher, *Adv. Mater.*, 2011, **23**(47), 5651–5657.

[47] T. Jungst, M. L. Muerza Cascante, T. D. Brown, M. Standfest, D. W. Hutmacher, J. Groll, P. D. Dalton, *Polym. Int.*, 2015, **64**(9), 1086–1095.

[48] G. Hochleitner, J. F. Hümmer, R. Luxenhofer, J. Groll, *Polymer*, 2014, **55**(20), 5017–5023.

[49] F. Chen, G. Hochleitner, T. Woodfield, J. Groll, P. D. Dalton, B. G. Amsden, *Biomacromolecules*, 2016, **17**(1), 208–214.

[50] G. Hochleitner, F. Chen, C. Blum, P. D. Dalton, B. Amsden, J. Groll, *Acta Biomater.*, 2018, **72**, 110–120.

[51] A. Hrynevich, B. S. Elci, J. N. Haigh, R. McMaster, A. Youssef, C. Blum, T. Blunk, G. Hochleitner, J. Groll, P. D. Dalton, *Small*, 2018, **14**(22).

[52] L.-H. Zhang, X.-P. Duan, X. Yan, M. Yu, X. Ning, Y. Zhao, Y.-Z. Long, *RSC Adv.*, 2016, **6**, 53400–53414.

[53] T. D. Brown, F. Edin, N. Detta, A. D. Skelton, D. W. Hutmacher, P. D. Dalton, *Mater. Sci. Eng. C*, 2014, **45**, 698–708.

[54] C. Wei, J. Dong, *J. Micromech. Microeng.*, 2013, **23**(2), 025017.

[55] F. M. Wunner, M.-L. Wille, T. G. Noonan, O. Bas, P. D. Dalton, E. M. De-Juan-Pardo, D. W. Hutmacher, *Adv. Mater.*, 2018, **30**(20), 1706570.

[56] G. Hochleitner, A. Youssef, A. Hrynevich, J. Haigh, T. Jungst, J. Groll, P. Dalton, *BioNanoMaterials*, 2016, **17**.

[57] J. M. Meek, *Phys. Rev.*, 1940, **57**, 722–728.

[58] J. Lyons, F. Ko, *Polymer News*, 2005, **30**(6), 170–178.

[59] T. M. Robinson, D. W. Hutmacher, P. D. Dalton, *Adv. Funct. Mater.*, 2019, **29**(44), 1904664.

[60] N. C. Paxton, M. Lanaro, A. Bo, N. Crooks, M. T. Ross, N. Green, K. Tetsworth, M. C. Allenby, Y. Gu, C. S. Wong, S. K. Powell, M. A. Woodruff, *J. Mech. Behav. Biomed. Mater.*, 2020, **105**, 103695.

[61] J. Lyons, C. Li, F. Ko, *Polymer*, 2004, **45**(22), 7597–7603.

[62] G. Hochleitner, T. Jungst, T. D. Brown, K. Hahn, C. Moseke, F. Jakob, P. D. Dalton, J. Groll, *Biofabrication*, 2015, **7**(3), 035002.

[63] B. L. Farrugia, T. D. Brown, Z. Upton, D. W. Hutmacher, P. D. Dalton, T. R. Dargaville, *Biofabrication*, 2013, **5**(2), 025001.

[64] J. Visser, F. P. Melchels, J. E. Jeon, E. M. van Bussel, L. S. Kimpton, H. M. Byrne, W. J. Dhert, P. D. Dalton, D. W. Hutmacher, J. Malda, *Nat. Commun.*, 2015, **6**(1), 6933.

[65] P. D. Dalton, *Curr. Opin. Biomed. Eng.*, 2017, **2**, 49–57.

[66] F. Yang, J. Wolke, J. Jansen, *Chem. Eng. J.*, 2008, **137**(1), 154–161.

[67] S. M. Oliveira, N. M. Alves, J. F. Mano, *J. Adhes. Sci. Technol.*, 2014, **28**(8-9), 843–863.

[68] O. Bas, E. M. De-Juan-Pardo, C. Meinert, D. D'Angella, J. G. Baldwin, L. J. Bray, R. M. Wellard, S. Kollmannsberger, E. Rank, C. Werner, T. J. Klein, I. Catelas, D. W. Hutmacher, *Biofabrication*, 2017, **9**(2), 025014.

[69] A. Youssef, S. J. Hollister, P. D. Dalton, *Biofabrication*, 2017, **9**(1), 012002.

[70] A. S. Hoffman, *Adv. Drug Delivery Rev.*, 2012, **64**, 18–23.

[71] N. Peppas, J. Hilt, A. Khademhosseini, A. Langer, *Adv. Mater*, 2006, **18**(11), 1345–1360.

[72] N. Annabi, A. Tamayol, J. A. Uquillas, M. Akbari, L. E. Bertassoni, C. Cha, G. Camci Unal, M. R. Dokmeci, N. A. Peppas, A. Khademhosseini, *Adv. Mater.*, 2014, **26**(1), 85–124.

[73] O. Wichterle, D. Lim, *Nature*, 1960, **185**, 117–118.

[74] Q. Chai, Y. Jiao, X. Yu, *Gels*, 2017, **3**(1).

[75] L. Li, Y. Wang, L. Pan, Y. Shi, W. Cheng, Y. Shi, G. Yu, *Nano Lett.*, 2015, **15**(2), 1146–1151.

[76] B. Lorber, W.-K. Hsiao, K. R. Martin, *Curr. Opin. Ophthalmol.*, 2016, **27**(3).

[77] M. Manti, V. Cacucciolo, M. Cianchetti, *IEEE Robot Autom Mag*, 2016, **23**(3), 93–106.

[78] A. Kirillova, R. Maxson, G. Stoychev, C. T. Gomillion, L. Ionov, *Adv. Mater.*, 2017, **29**(46), 1703443.

[79] Y. Jiang, Q. Wang, *Sci. Rep.*, 2016, **6**, 34147.

[80] E. M. Ahmed, *J. Adv. Res.*, 2015, **6**(2), 105–121.

[81] Y. Li, J. Rodrigues, H. Tomas, *Chem. Soc. Rev.*, 2012, **41**, 2193–2221.

[82] E. Jabbari, J. Leijten, Q. Xu, A. Khademhosseini, *Materials Today*, 2016, **19**(4), 190 – 196.

[83] N. Annabi, J. W. Nichol, X. Zhong, C. Ji, S. Koshy, A. Khademhosseini, F. Dehghani, *Tissue. Eng. Part B Rev.*, 2010, **16**(4), 371–383.

[84] N. A. Peppas, E. W. Merrill, *J. Polym. Sci. Pol. Chem.*, 1976, **14**(2), 441–457.

[85] R. A. Perez, J.-E. Won, J. C. Knowles, H.-W. Kim, *Adv. Drug Delivery Rev.*, 2013, **65**(4), 471–496.

[86] C. M. Nimmo, M. S. Shoichet, *Bioconjugate Chem.*, 2011, **22**(11), 2199–2209.

[87] J. Malda, J. Visser, F. P. Melchels, T. Jüngst, W. E. Hennink, W. J. A. Dhert, J. Groll, D. W. Hutmacher, *Adv. Mater.*, 2013, **25**(36), 5011–5028.

[88] O. Okay, in *Hydrogel Sensors and Actuators: Engineering and Technology*, ed. G. Gerlach, K.-F. Arndt, Springer Berlin Heidelberg, Berlin, Heidelberg, 2010; pp. 1–14.

[89] C. Cha, S. Y. Kim, L. Cao, H. Kong, *Biomaterials*, 2010, **31**(18), 4864–4871.

[90] O. Bas, I. Catelas, E. M. De-Juan-Pardo, D. W. Hutmacher, *Adv. Drug Delivery Rev.*, 2018, **132**, 214–234.

[91] R. L. Truby, J. A. Lewis, *Nature*, 2016, **540**, 371–378.

[92] J. N. Hanson, M. J. Motala, M. L. Heien, M. Gillette, J. Sweedler, R. G. Nuzzo, *Lab. Chip*, 2009, **9**, 122–131.

[93] J. N. Hanson Shepherd, S. T. Parker, R. F. Shepherd, M. U. Gillette, J. A. Lewis, R. G. Nuzzo, *Adv. Funct. Mater.*, 2011, **21**(1), 47–54.

[94] S. N. Jayasinghe, *Adv. Biosyst.*, 2017, **1**(7).

[95] D. W. Hutmacher, T. B. Woodfield, P. D. Dalton in *Tissue Engineering (Second Edition)*, ed. C. A. V. Blitterswijk, J. D. Boer; Academic Press, Oxford, Second Edition, 2014; pp. 311–346.

[96] T. Jungst, W. Smolan, K. Schacht, T. Scheibel, J. Groll, *Chem. Rev.*, 2016, **116**(3), 1496–1539.

[97] R. R. Jose, M. J. Rodriguez, T. A. Dixon, F. Omenetto, D. L. Kaplan, *ACS Biomater. Sci. Eng.*, 2016, **2**(10), 1662–1678.

[98] J. M. Lee, W. Y. Yeong, *Adv. Healthcare Mater.*, 2016, **5**(22), 2856–2865.

[99] H. Kodama, *Rev. Sci. Instrum.*, 1981, **52**(11), 1770–1773.

[100] T. Frenzel, C. Findeisen, M. Kadic, P. Gumbsch, M. Wegener, *Adv. Mater.*, 2016, **28**(28), 5865–5870.

[101] J. R. Tumbleston, D. Shirvanyants, N. Ermoshkin, R. Janusziewicz, A. R. Johnson, D. Kelly, K. Chen, R. Pinschmidt, J. P. Rolland, A. Ermoshkin, E. T. Samulski, J. M. DeSimone, *Science*, 2015, **347**(6228), 1349–1352.

[102] A. K. Miri, D. Nieto, L. Iglesias, H. G. Hosseinabadi, S. Maharjan, G. U. Ruiz Esparza, P. Khoshakhlagh, A. Manbachi, M. R. Dokmeci, S. Chen, S. R. Shin, Y. S. Zhang, A. Khademhosseini, *Adv. Mater.*, 2018, **30**(27).

[103] C. J. Bloomquist, M. B. Mecham, M. D. Paradzinsky, R. Janusziewicz, S. B. Warner, J. C. Luft, S. J. Mecham, A. Z. Wang, J. M. DeSimone, *J. Controlled Release*, 2018, **278**, 9–23.

[104] J. Rolland, *J. Photopolym. Sci. Technol.*, 2016, **29**, 451–452.

[105] K. Schacht, T. Jüngst, M. Schweinlin, A. Ewald, J. Groll, T. Scheibel, *Angew. Chem. Int. Ed.*, 2015, **54**(9), 2816–2820.

[106] S. Stichler, T. Jungst, M. Schamel, I. Zilkowski, M. Kuhlmann, T. Boeck, T. Blunk, J. Tessmar, J. Groll, *Ann. Biomed. Eng.*, 2017, **45**, 273–285.

[107] N. E. Fedorovich, J. R. De Wijn, A. J. Verbout, J. Alblas, W. J. Dhert, *Tissue Eng. Part A*, 2008, **14**(1), 127–133.

[108] T. Lorson, S. Jaksch, M. M. Luebtow, T. Jüngst, J. Groll, T. Luehmann, R. Luxenhofer, *Biomacromolecules*, 2017, **18**(7), 2161–2171.

[109] P. S. Maher, R. Keatch, K. Donnelly, R. Mackay, J. Paxton, *Rapid Prototyp. J.*, 2009, **15**, 204–210.

[110] N. E. Fedorovich, I. Swennen, J. Girones, L. Moroni, C. A. van Blitterswijk, E. Schacht, J. Alblas, W. J. A. Dhert, *Biomacromolecules*, 2009, **10**(7), 1689–1696.

[111] R. Censi, P. J. Fieten, P. di Martino, W. E. Hennink, T. Vermonden, *Macromolecules*, 2010, **43**(13), 5771–5778.

[112] L. S. Moreira Teixeira, J. Feijen, C. A. van Blitterswijk, P. J. Dijkstra, M. Karperien, *Biomaterials*, 2012, **33**(5), 1281–1290.

[113] R. A. Barry, R. F. Shepherd, J. N. Hanson, R. G. Nuzzo, P. Wiltzius, J. A. Lewis, *Adv. Mater.*, 2009, **21**(23), 2407–2410.

[114] G. M. Gratson, M. Xu, J. A. Lewis, *Nature*, 2004, **428**(6981), 386–386.

[115] J. N. Haigh, Y. Chuang, B. Farrugia, R. Hoogenboom, P. D. Dalton, T. R. Dargaville, *Macromol. Rapid Commun.*, 2016, **37**(1), 93–99.

[116] O. Sedlacek, B. D. Monnery, S. K. Filippov, R. Hoogenboom, M. Hruby, *Macromol. Rapid Commun.*, 2012, **33**(19), 1648–1662.

[117] R. Luxenhofer, Y. Han, A. Schulz, J. Tong, Z. He, A. V. Kabanov, R. Jordan, *Macromol. Rapid Commun.*, 2012, **33**(19), 1613–1631.

[118] V. R. de la Rosa, *J. Mater. Sci.: Mater. Med.*, 2014, **25**(5), 1211–1225.

[119] B. Verbraeken, B. D. Monnery, K. Lava, R. Hoogenboom, *Eur. Polym. J.*, 2017, **88**, 451–469.

[120] W. Seeliger, E. Aufderhaar, W. Diepers, R. Feinauer, R. Nehring, W. Thier, H. Hellmann, *Angew. Chem. Int. Ed.*, 1966, **5**(10), 875–888.

[121] T. Kagiya, S. Narisawa, T. Maeda, K. Fukui, *J. Poly. Sci. Part B: Poly. Let.*, 1966, **4**(7), 441–445.

[122] D. A. Tomalia, D. P. Sheetz, *J. Polym. Sci. A Polym. Chem.*, 1966, **4**(9), 2253–2265.

[123] T. G. Bassiri, A. Levy, M. Litt, *J. Poly. Sci. Part B: Poly. Let.*, 1967, **5**(9), 871–879.

[124] K. Aoi, H. Suzuki, M. Okada, *Macromolecules*, 1992, **25**(25), 7073–7075.

[125] A. Levy, M. Litt, *J. Polym. Sci., Part B: Polym. Lett.*, 1967, **5**(9), 881–886.

[126] M. Bloksma, R. Paulus, H. Kuringen, F. Woerdt, H. Lambermont Thijs, U. Schubert, R. Hoogenboom, *Macromol. Rapid Commun.*, 2012, **33**(1), 92–96.

[127] M. M. Luebtow, L. Hahn, M. S. Haider, R. Luxenhofer, *J. Am. Chem. Soc.*, 2017, **139**(32), 10980–10983.

[128] R. Moreadith, T. X. Viegas, M. Bentley, J. M. Harris, Z. Fang, K. Yoon, B. Dizman, R. Weimer, B. P. Rae, X. Li, C. Rader, D. Standaert, W. Olanow, *Eur. Polym. J.*, 2017, **88**, 524–552.

[129] M. Beck, P. Birnbrich, U. Eicken, H. Fischer, W. E. Fristad, B. Hase, H.-J. Krause, *Angew. Makromol. Chemie*, 1994, **223**(1), 217–233.

[130] H. Wenker, *J. Am. Chem. Soc.*, 1935, **57**(6), 1079–1080.

[131] H. Witte, W. Seeliger, *Justus Liebigs Ann. Chem.*, 1974, **1974**(6), 996–1009.

[132] R. D. Puts, D. Y. Sogah, *Tetrahedron Lett.*, 1994, **35**(32), 5779–5782.

[133] C. Taubmann, R. Luxenhofer, S. Cesana, R. Jordan, *Macromol. Biosci.*, 2005, **5**(7), 603–612.

[134] S. Sinnwell, H. Ritter, *Macromol. Rapid Commun.*, 2006, **27**(16), 1335–1340.

[135] M. Glassner, D. R. Dhooge, J. Y. Park, P. H. V. Steenberge, B. D. Monnery, M.-F. Reyniers, R. Hoogenboom, *Eur. Polym. J.*, 2015, **65**, 29–304.

[136] R. M. Paulus, C. R. Becer, R. Hoogenboom, U. S. Schubert, *Macromol. Chem. Phys.*, 2008, **209**(8), 794–800.

[137] J. S. Hrkach, K. Matyjaszewski, *Macromolecules*, 1992, **25**(8), 2070–2075.

[138] B. Guillerm, S. Monge, V. Lapinte, J.-J. Robin, *Macromol. Rapid Commun.*, 2012, **33**(19), 1600–1612.

[139] O. Nuyken, G. Maier, A. Gross, H. Fischer, *Macromol. Chem. Phys.*, 1996, **197**(1), 83–95.

[140] M. W. M. Fijten, R. Hoogenboom, U. S. Schubert, *J. Polym. Sci., Part A: Polym. Chem.*, 2008, **46**(14), 4804–4816.

[141] T. Saegusa, Y. Nagura, S. Kobayashi, *Macromolecules*, 1973, **6**(4), 495–498.

[142] T. Saegusa, S. Kobayashi, Y. Nagura, *Macromolecules*, 1974, **7**(3), 265–272.

[143] T. Saegusa, S. Kobayashi, Y. Nagura, *Macromolecules*, 1974, **7**(3), 272–277.

[144] T. Saegusa, S. Kobayashi, Y. Nagura, *Macromolecules*, 1974, **7**(6), 713–716.

[145] M. M. Bloksma, U. S. Schubert, R. Hoogenboom, *Macromol. Rapid Commun.*, 2011, **32**(18), 1419–1441.

[146] T. Saegusa, H. Ikeda, H. Fujii, *Macromolecules*, 1972, **5**(4), 359–362.

[147] R. Hoogenboom, M. W. M. Fijten, H. M. L. Thijs, B. M. van Lankvelt, U. S. Schubert, *Des. Monomers Polym.*, 2005, **8**(6), 659–671.

[148] M. Miyamoto, K. Aoi, T. Saegusa, *Macromolecules*, 1991, **24**(1), 11–16.

[149] R. Hoogenboom, H. M. L. Thijs, M. J. H. C. Jochems, B. M. van Lankvelt, M. W. M. Fijten, U. S. Schubert, *Chem. Commun.*, 2008, pp. 5758–5760.

[150] R. Hoogenboom, H. M. L. Thijs, D. Wouters, S. Hoeppener, U. S. Schubert, *Macromolecules*, 2008, **41**(5), 1581–1583.

[151] S. Kobayashi, T. Igarashi, Y. Moriuchi, T. Saegusa, *Macromolecules*, 1986, **19**(3), 535–541.

[152] Y. Chujo, K. Sada, K. Matsumoto, T. Saegusa, *Macromolecules*, 1990, **23**(5), 1234–1237.

[153] R. Luxenhofer, *Novel Functional Poly(2-oxazoline)s as Potential Carriers for Biomedical Applications* PhD thesis, Technischen Universität München, 2007.

[154] G. Morgese, E. Benetti, *Eur. Polym. J.*, 2017, **88**, 470–485.

[155] M. Litt, A. Levy, J. Herz, *J. Macromol. Sci., Chemistry*, 1975, **9**(5), 703–727.

[156] F. Wiesbrock, R. Hoogenboom, M. A. M. Leenen, M. A. R. Meier, U. S. Schubert, *Macromolecules*, 2005, **38**(12), 5025–5034.

[157] J. F. Nawroth, J. R. McDaniel, A. Chilkoti, R. Jordan, R. Luxenhofer, *Macromol. Biosci.*, 2016, **16**(3), 322–333.

[158] R. Luxenhofer, R. Jordan, *Macromolecules*, 2006, **39**(10), 3509–3516.

[159] U. Mansfeld, C. Pietsch, R. Hoogenboom, C. R. Becer, U. S. Schubert, *Polym. Chem.*, 2010, **1**, 1560–1598.

[160] K. A. Kosakowska, P. Dimitrov, G. Panambur, S. M. Grayson, *J. Polym. Sci., Part A: Polym. Chem.*, 2017, **55**(8), 1303–1312.

[161] S. Kobayashi, E. Masuda, S. Shoda, Y. Shimano, *Macromolecules*, 1989, **22**(7), 2878–2884.

[162] E. F.-J. Rettler, J. M. Kranenburg, H. M. Lambermont-Thijs, R. Hoogenboom, U. S. Schubert, *Macromol. Chem. Phys.*, 2010, **211**(22), 2443–2448.

[163] V. V. Jerca, K. Lava, B. Verbraeken, R. Hoogenboom, *Polym. Chem.*, 2016, **7**, 1309–1322.

[164] K. Kempe, S. Jacobs, H. M. L. Lambermont-Thijs, M. M. W. M. Fijten, R. Hoogenboom, U. S. Schubert, *Macromolecules*, 2010, **43**(9), 4098–4104.

[165] K. Kempe, E. Rettler, R. Paulus, A. Kuse, R. Hoogenboom, U. Schubert, *Polymer*, 2013, **54**(8), 2036–2042.

[166] H. M. L. Lambermont-Thijs, M. J. H. C. Jochems, R. Hoogenboom, U. S. Schubert, *J. Polym. Sci., Part A: Polym. Chem.*, 2009, **47**(23), 6433–6440.

[167] H. Lambermont-Thijs, H. Kuringen, J. Put, U. Schubert, R. Hoogenboom, *Polymers*, 2010, **2**, 188–199.

[168] C. Weber, R. Hoogenboom, U. S. Schubert, *Prog. Polym. Sci.*, 2012, **37**(5), 686–714.

[169] T. X. Viegas, M. D. Bentley, J. M. Harris, Z. Fang, K. Yoon, B. Dizman, R. Weimer, A. Mero, G. Pasut, F. M. Veronese, *Bioconjugate Chem.*, 2011, **22**(5), 976–986.

[170] P. Lin, C. Clash, E. M. Pearce, T. K. Kwei, M. A. Aponte, *J. Polym. Sci., Part B: Polym. Phys.*, 1988, **26**(3), 603–619.

[171] D. Christova, R. Velichkova, W. Loos, E. J. Goethals, F. D. Prez, *Polymer*, 2003, **44**(8), 2255–2261.

[172] R. Luxenhofer, A. Schulz, C. Roques, S. Li, T. K. Bronich, E. V. Batrakova, R. Jordan, A. V. Kabanov, *Biomaterials*, 2010, **31**(18), 4972–4979.

[173] A. Schulz, S. Jaksch, R. Schubel, E. Wegener, Z. Di, Y. Han, A. Meister, J. Kressler, A. V. Kabanov, R. Luxenhofer, C. M. Papadakis, R. Jordan, *ACS Nano*, 2014, **8**(3), 2686–2696.

[174] M. Bauer, C. Lautenschlaeger, K. Kempe, L. Tauhardt, U. S. Schubert, D. Fischer, *Macromol. Biosci.*, 2012, **12**(7), 986–998.

[175] M. Bauer, S. Schroeder, L. Tauhardt, K. Kempe, U. S. Schubert, D. Fischer, *J. Polym. Sci., Part A: Polym. Chem.*, 2013, **51**(8), 1816–1821.

[176] M. N. Leiske, A.-K. Trützschler, S. Armoneit, P. Sungur, S. Hoeppener, M. Lehmann, A. Traeger, U. S. Schubert, *J. Mater. Chem. B*, 2017, **5**, 9102–9113.

[177] X. Pan, Y. Liu, Z. Li, S. Cui, H. Gebru, J. Xu, S. Xu, J. Liu, K. Guo, *Macromol. Chem. Phys.*, 2017, **218**(6), 1600483.

[178] L. Tauhardt, D. Pretzel, K. Kempe, M. Gottschaldt, D. Pohlers, U. S. Schubert, *Polym. Chem.*, 2014, **5**, 5751–5764.

[179] R. Shah, Z. Kronekova, A. Zahoranova, L. Roller, N. Saha, P. Saha, J. Kronek, *J Mater Sci: Mater Med*, 2015, **26**, 157.

[180] H. Van Kuringen, J. Lenoir, E. Adriaens, J. Bender, B. De Geest, R. Hoogenboom, *Macromol. Biosci.*, 2012, **12**(8), 1114–1123.

[181] P. Goddard, L. E. Hutchinson, J. Brown, L. J. Brookman, *J. Controlled Release*, 1989, **10**(1), 5–16.

[182] F. C. Gaertner, R. Luxenhofer, B. Blechert, R. Jordan, M. Essler, *J. Controlled Release*, 2007, **119**(3), 291–300.

[183] L. Wyffels, T. Verbrugghen, B. D. Monnery, M. Glassner, S. Stroobants, R. Hoogenboom, S. Staelens, *J. Controlled Release*, 2016, **235**, 63–71.

[184] H. M. L. Lambermont-Thijs, F. S. van der Woerdt, A. Baumgaertel, L. Bonami, F. E. Du Prez, U. S. Schubert, R. Hoogenboom, *Macromolecules*, 2010, **43**(2), 927–933.

[185] S. Kobayashi, *Prog. Polym. Sci.*, 1990, **15**(5), 751–823.

[186] T. Saegusa, H. Ikeda, H. Fujii, *Macromolecules*, 1972, **5**(1), 108–108.

[187] T. Saegusa, S. Kobayashi, A. Yamada, *Macromolecules*, 1975, **8**(4), 390–396.

[188] R. Tanaka, I. Ueoka, Y. Takaki, K. Kataoka, S. Saito, *Macromolecules*, 1983, **16**(6), 849–853.

[189] C.-H. Wang, K.-R. Fan, G.-H. Hsiue, *Biomaterials*, 2005, **26**(16), 2803–2811.

[190] O. Boussif, F. Lezoualc'h, M. A. Zanta, M. D. Mergny, D. Scherman, B. Demeneix, J. P. Behr, *Proc. Natl. Acad. Sci.*, 1995, **92**(16), 7297–7301.

[191] M. A. Mintzer, E. E. Simanek, *Chem. Rev.*, 2009, **109**(2), 259–302.

[192] T. Saegusa, Y. Nagura, S. Kobayashi, *Macromolecules*, 1973, **6**(4), 495–498.

[193] S. Janhom, P. Griffiths, R. Watanesk, S. Watanesk, *Dyes Pigm.*, 2004, **63**, 231–237.

[194] F. Dugonjic-Bilic, J. Plank, *J. Appl. Polym. Sci.*, 2011, **121**(3), 1262–1275.

[195] H. M. L. Lambermont-Thijs, J. P. A. Heuts, S. Hoeppener, R. Hoogenboom, U. S. Schubert, *Polym. Chem.*, 2011, **2**, 313–322.

[196] K. M. Kem, *J. Polym. Sci. A1*, 1979, **17**(7), 1977–1990.

[197] M. H. Litt, C. S. Lin, *J. Polym. Sci., Part A: Polym. Chem.*, 1992, **30**(5), 779–786.

[198] M. A. Mees, R. Hoogenboom, *Polym. Chem.*, 2018, **9**, 4968–4978.

[199] Y. Chujo, Y. Yoshifuji, K. Sada, T. Saegusa, *Macromolecules*, 1989, **22**(3), 1074–1077.

[200] Y. Chujo, K. Sada, T. Saegusa, *Macromolecules*, 1990, **23**(10), 2636–2641.

[201] Y. Chujo, K. Sada, A. Naka, R. Nomura, T. Saegusa, *Macromolecules*, 1993, **26**(5), 883–887.

[202] Y. Chujo, K. Sada, R. Nomura, A. Naka, T. Saegusa, *Macromolecules*, 1993, **26**(21), 5611–5614.

[203] Y. Chujo, K. Sada, T. Saegusa, *Macromolecules*, 1993, **26**(24), 6315–6319.

[204] Y. Chujo, K. Sada, T. Saegusa, *Macromolecules*, 1993, **26**(24), 6320–6323.

[205] T. Saegusa, S. Kobayashi, A. Yamada, *J. Appl. Polym. Sci.*, 1977, **21**(9), 2481–2488.

[206] M. Gregoritza, F. P. Brandl, *Eur. J. Pharm. Biopharm.*, 2015, **97**, 438–453.

[207] K. Luef, C. Petit, B. Ottersböck, G. Oreski, F. Ehrenfeld, B. Grassl, S. Reynaud, F. Wiesbrock, *Eur. Polym. J.*, 2017, **88**, 701–712.

[208] M. Hartlieb, K. Kempe, U. S. Schubert, *J. Mater. Chem. B*, 2015, **3**, 526–538.

[209] M. Hartlieb, S. Schubert, K. Kempe, N. Windhab, U. S. Schubert, *J. Polym. Sci., Part A: Polym. Chem.*, 2015, **53**(1), 10–14.

[210] V. Schenk, E. Rossegger, C. Ebner, F. Bangerl, K. Reichmann, B. Hoffmann, M. Hoepfner, F. Wiesbrock, *Polymers*, 2014, **6**, 264–279.

[211] A. Zahoranova, Z. Kronekova, M. Zahoran, D. Chorvat Jr., I. Janigova, J. Kronek, *J. Polym. Sci., Part A: Polym. Chem.*, 2016, **54**(11), 1548–1559.

[212] H. Uyama, S. Kobayashi, *Chem. Lett.*, 1992, **21**(9), 1643–1646.

[213] D. Christova, R. Velichkova, E. J. Goethals, *Macromol. Rapid Commun.*, 1997, **18**(12), 1067–1073.

[214] B. L. Farrugia, K. Kempe, U. S. Schubert, R. Hoogenboom, T. R. Dargaville, *Biomacromolecules*, 2013, **14**(8), 2724–2732.

[215] C. D. Hein, X.-M. Liu, D. Wang, *Pharmaceutical Research*, 2008, **25**(10), 2216–2230.

[216] H. C. Kolb, M. G. Finn, K. B. Sharpless, *Angew. Chem. Int. Ed.*, 2001, **40**(11), 2004–2021.

[217] E. Lallana, F. Fernandez-Trillo, A. Sousa-Herves, R. Riguera, E. Fernandez-Megia, *Pharm. Res.*, 2012, **29**(4), 902–921.

[218] S. Kirchhof, F. P. Brandl, N. Hammer, A. M. Goepferich, *J. Mater. Chem. B*, 2013, **1**, 4855–4864.

[219] S. Kirchhof, M. Gregoritza, V. Messmann, N. Hammer, A. M. Goepferich, F. P. Brandl, *Eur. J. Pharm. Biopharm.*, 2015, **96**, 217–225.

[220] O. Diels, K. Alder, *Justus Liebigs Ann. Chem.*, 1928, **460**(1), 98–122.

[221] K. C. Nicolaou, S. A. Snyder, T. Montagnon, G. Vassilikogiannakis, *Angew. Chem. Int. Ed.*, 2002, **41**(10), 1668–1698.

[222] S.-Y. Tang, J. Shi, Q.-X. Guo, *Org. Biomol. Chem.*, 2012, **10**, 2673–2682.

[223] U. M. Lindström, *Chem. Rev.*, 2002, **102**(8), 2751–2772.

[224] S. Otto, J. B. F. N. Engberts, *Pure Appl. Chem.*, 2000, **72**(7), 1365–1372.

[225] J. M. Palomo, *Eur. J. Org. Chem.*, 2010, **2010**(33), 6303–6314.

[226] I. Kosif, E.-J. Park, R. Sanyal, A. Sanyal, *Macromolecules*, 2010, **43**(9), 4140–4148.

[227] C. M. Nimmo, S. C. Owen, M. S. Shoichet, *Biomacromolecules*, 2011, **12**(3), 824–830.

[228] H.-L. Wei, K. Yao, Z. Yang, H.-J. Chu, J. Zhu, C.-C. Ma, Z.-X. Zhao, *Macromol. Res.*, 2011, **19**(3), 294–299.

[229] C. Garcia Astrain, I. Algar, A. Gandini, A. Eceiza, M. A. Corcuera, N. Gabilondo, *J. Polym. Sci., Part A: Polym. Chem.*, 2015, **53**(5), 699–708.

[230] R. Woodward, T. J. Katz, *Tetrahedron*, 1959, **5**(1), 70–89.

[231] J. Sauer, R. Sustmann, *Angew. Chem. Int. Ed.*, 1980, **19**(10), 779–807.

[232] K. Kumamoto, I. Fukada, H. Kotsuki, *Angew. Chem. Int. Ed.*, 2004, **43**(15), 2015–2017.

[233] R. Brueckner, *Reaktionsmechanismen*, 3, Springer Spektrum, 2004.

[234] A. Gandini, *Prog. Polym. Sci.*, 2013, **38**(1), 1–29.

[235] K. Yang, J. C. Grant, P. Lamey, A. Joshi-Imre, B. R. Lund, R. A. Smaldone, W. Voit, *Adv. Funct. Mater.*, 2017, **27**(24), 1700318.

[236] R. Breslow, U. Maitra, D. Rideout, *Tetrahedron Lett.*, 1983, **24**(18), 1901–1904.

[237] N. Baumhover, K. Anderson, C. Fernandez, K. Rice, *Bioconjug. Chem.*, 2010, **21**(1).

[238] X. Chen, M. A. Dam, K. Ono, A. Mal, H. Shen, S. R. Nutt, K. Sheran, F. Wudl, *Science*, 2002, **295**(5560), 1698–1702.

[239] A. D. de Araujo, J. M. Palomo, J. Cramer, M. Köhn, H. Schröder, R. Wacker, C. Niemeyer, K. Alexandrov, H. Waldmann, *Angew. Chem. Int. Ed.*, 2006, **45**(2), 296–301.

[240] W. Denissen, J. M. Winne, F. E. Du Prez, *Chem. Sci.*, 2016, **7**, 30–38.

[241] N. Yoshie In ed. H. Mark, *Encyclopedia of Polymer Science and Technology*, 4, pp. 493–510, 2014.

[242] Y.-L. Liu, T.-W. Chuo, *Polym. Chem.*, 2013, **4**, 2194–2205.

[243] S. Kirchhof, A. Strasser, H.-J. Wittmann, V. Messmann, N. Hammer, A. M. Goepferich, F. P. Brandl, *J. Mater. Chem. B*, 2015, **3**, 449–457.

[244] M. Gregoritza, V. Messmann, A. M. Goepferich, F. P. Brandl, *J. Mater. Chem. B*, 2016, **4**, 3398–3408.

[245] M. Gregoritza, V. Messmann, K. Abstiens, F. P. Brandl, A. M. Goepferich, *Biomacromolecules*, 2017, **18**(8), 2410–2418.

[246] W.-S. Yeo, M. N. Yousaf, M. Mrksich, *J. Am. Chem. Soc.*, 2003, **125**(49), 14994–14995.

[247] M. Proupin-Perez, R. Cosstick, L. M. Liz-Marzan, V. Salgueirimo-Maceira, M. Brust, *Nucleosides, Nucleotides & Nucleic Acids*, 2005, **24**(5-7), 1075–1079.

[248] M. Shi, M. S. Shoichet, *J. Biomater. Sci. Polym. Ed.*, 2008, **19**(9), 1143–1157.

[249] Y. Zhang, A. A. Broekhuis, F. Picchioni, *Macromolecules*, 2009, **42**(6), 1906–1912.

[250] K. K. Oehlenschlaeger, J. O. Mueller, J. Brandt, S. Hilf, A. Lederer, M. Wilhelm, R. Graf, M. L. Coote, F. G. Schmidt, C. Barner-Kowollik, *Adv. Mater.*, 2014, **26**(21), 3561–3566.

[251] R. K. Bose, J. Kötteritzsch, S. J. Garcia, M. D. Hager, U. S. Schubert, S. van der Zwaag, *J. Polym. Sci., Part A: Polym. Chem.*, 2014, **52**(12), 1669–1675.

[252] G. C. Tesoro, V. R. Sastri, *Ind. Eng. Chem. Res.*, 1986, **25**(3), 444–448.

[253] A. Gandini, M. N. Belgacem, *Prog. Polym. Sci.*, 1997, **22**(6), 1203–1379.

[254] B. Gotsmann, U. Duerig, J. Frommer, C. Hawker, *Adv. Funct. Mater.*, 2006, **16**(11), 1499–1505.

[255] J. Hao, W. Wang, B. Jiang, X. Cai, L. Jiang, *Polym. Int.*, 1999, **48**(3), 235–243.

[256] U. S. Sahu, S. N. Bhadani, *Makromol. Chem. Rapid. Comm.*, 1982, **3**(2), 103–107.

[257] B. J. Adzima, H. A. Aguirre, C. J. Kloxin, T. F. Scott, C. N. Bowman, *Macromolecules*, 2008, **41**(23), 9112–9117.

[258] A. A. Kavitha, N. K. Singha, *ACS Appl. Mater. Interfaces*, 2009, **1**(7), 1427–1436.

[259] J. Kötteritzsch, S. Stumpf, S. Hoeppener, J. Vitz, M. D. Hager, U. S. Schubert, *Macromol. Chem. Phys.*, 2013, **214**(14), 1636–1649.

[260] P. Yates, P. Eaton, *J. Am. Chem. Soc.*, 1960, **82**.

[261] B. H. Northrop, S. H. Frayne, U. Choudhary, *Polym. Chem.*, 2015, **6**, 3415–3430.

[262] S. E. Wheeler, D. H. Ess, K. N. Houk, *J. Phys. Chem. A*, 2008, **112**(8), 1798–1807.

[263] E. Schoolaert, R. Merckx, J. Becelaere, M. Everaerts, J. F. R. Van Guyse, O. Sedlacek, B. G. De Geest, G. Van den Mooter, D. R. D hooge, K. De Clerck, R. Hoogenboom, *Macromolecules*, 2020, **53**(17), 7590–7600.

[264] P. Bouten, K. Lava, J. Van Hest, R. Hoogenboom, *Polymers*, 2015, **7**(10), 1998–2008.

[265] O. Sedlacek, K. Lava, B. Verbraeken, S. Kasmi, B. G. De Geest, R. Hoogenboom, *J. Am. Chem. Soc.*, 2019, **141**(24), 9617–9622.

[266] M. Glassner, M. Vergaelen, R. Hoogenboom, *Polym. Int.*, 2018, **67**(1), 32–45.

[267] V. Froidevaux, M. Borne, E. Laborbe, R. Auvergne, A. Gandini, B. Boutevin, *RSC Adv.*, 2015, **5**, 37742–37754.

[268] J. Canadell, H. Fischer, G. De With, R. A. T. M. van Benthem, *J. Polym. Sci., Part A: Polym. Chem.*, 2010, **48**(15), 3456–3467.

[269] N. Yoshie, S. Saito, N. Oya, *Polymer*, 2011, **52**(26), 6074–6079.

[270] N. B. Sankaran, A. Z. Rys, R. Nassif, M. K. Nayak, K. Metera, B. Chen, H. S. Bazzi, H. F. Sleiman, *Macromolecules*, 2010, **43**(13), 5530–5537.

[271] G. Mantovani, F. Lecolley, L. Tao, D. M. Haddleton, J. Clerx, J. J. L. M. Cornelissen, K. Velonia, *J. Am. Chem. Soc.*, 2005, **127**(9), 2966–2973.

[272] D. Nahm, F. Weigl, N. Schaefer, A. Sancho, A. Frank, J. Groll, C. Villmann, H.-W. Schmidt, P. D. Dalton, R. Luxenhofer, *Mater. Horiz.*, 2020, **7**, 928–933.

[273] G. A. Appuhamillage, J. C. Reagan, S. Khorsandi, J. R. Davidson, W. Voit, R. A. Smaldone, *Polym. Chem.*, 2017, **8**, 2087–2092.

[274] M. Yoo, Y. Choi, J. Lee, W. Wee, C. Cho, *J. Drug Delivery Sci. Technol.*, 2007, **17**(1), 81–85.

[275] M. J. Seiler, R. B. Aramant, *Prog. Retin. Eye Res.*, 2012, **31**(6), 661–687.

[276] D. G. Karis, R. J. Ono, M. Zhang, A. Vora, D. Storti, M. A. Ganter, A. Nelson, *Polym. Chem.*, 2017, **8**, 4199–4206.

[277] Z. Kronekova, T. Lorson, J. Kronek, R. Luxenhofer, *ChemRxiv*, 2018.

[278] T. Defize, J.-M. Thomassin, M. Alexandre, B. Gilbert, R. Riva, C. Jerome, *Polymer*, 2016, **84**, 234–242.

[279] S. Magana, A. Zerroukhi, C. Jegat, N. Mignard, *React. Funct. Polym.*, 2010, **70**(7), 442–448.

[280] Y. S. Patel, H. S. Patel, *Int. J. Plast. Technol.*, 2013, **17**(1), 10–23.

[281] J. L. Hopewell, D. J. Hill, P. J. Pomery, *Polymer*, 1998, **39**(23), 5601–5607.

[282] F. M. Wunner, P. Mieszczanek, O. Bas, S. Eggert, J. Maartens, P. D. Dalton, E. M. De-Juan-Pardo, D. W. Hutmacher, *Biofabrication*, 2019, **11**(2), 025004.

[283] R. V. Benjaminsen, M. A. Mattebjerg, J. R. Henriksen, S. M. Moghimi, T. L. Andresen, *Mol. Ther.*, 2013, **21**(1), 149–157.

[284] J. D. Ziebarth, Y. Wang, *Biomacromolecules*, 2010, **11**(1), 29–38.

[285] C. Hu, L. Hahn, M. Yang, A. Altmann, P. Stahlhut, J. Groll, R. Luxenhofer, *J. Mater. Sci.*, 2021, **56**(1), 691–705.

[286] Y. Nakayama, T. Matsuda, *J. Polym. Sci., Part A: Polym. Chem.*, 1992, **30**(11), 2451–2457.

[287] J. P. Chesterman, F. Chen, A. J. Brissenden, B. G. Amsden, *Polym. Chem.*, 2017, **8**, 7515–7528.

[288] L. Ionov, *Adv. Healthcare Mater.*, 2018, **7**(17), 1800412.

[289] G. M. Gratson, J. A. Lewis, *Langmuir*, 2005, **21**(1), 457–464.

[290] C. Majidi, *Adv. Mater. Tech.*, 2019, **4**(2), 1800477.

[291] X. Kuang, D. J. Roach, J. Wu, C. M. Hamel, Z. Ding, T. Wang, M. L. Dunn, H. J. Qi, *Adv. Funct. Mater.*, 2019, **29**(2), 1805290.

[292] E. McColl, J. Groll, T. Jungst, P. D. Dalton, *Mater. Des.*, 2018, **155**, 46–58.

[293] A. Sancho, I. Vandersmissen, S. Craps, A. Luttun, J. Groll, *Sci. Rep.*, 2017, **7**, 46152.

[294] B. J. Briscoe, K. S. Sebastian, M. J. Adams, *J. Phys. D: Appl. Phys.*, 1994, **27**, 1156–1162.

# Affidavit

I hereby confirm that my thesis entitled "Poly(2-oxazine) Based Biomaterial Inks for the Additive Manufacturing of Microperiodic Hydrogel Scaffolds" is the result of my own work. I did not receive any help or support from commercial consultants. All sources and / or materials applied are listed and specified in the thesis.

Furthermore, I confirm that this thesis has not yet been submitted as part of another examination process neither in identical nor in similar form.

Place, Date Signature

# Eidesstattliche Erklärung

Hiermit erkläre ich an Eides statt, die Dissertation „Poly(2-oxazine) Basierte Biomaterialtinten für die Additive Fertigung von Mikroperiodischen Hydrogelstrukturen" eigenständig, d.h. insbesondere selbständig und ohne Hilfe eines kommerziellen Promotionsberaters, angefertigt und keine anderen als die von mir angegebenen Quellen und Hilfsmittel verwendet zu haben.

Ich erkläre außerdem, dass die Dissertation weder in gleicher noch in ähnlicher Form bereits in einem anderen Prüfungsverfahren vorgelegen hat.

Ort, Datum Unterschrift